Modelling of Microstructural Evolution in Austempered Ductile Iron

by

Duncan Colin Putman

Institute of Polymer Technology and Materials Engineering

Abstract

Austempered ductile iron (ADI) has a microstructure consisting mainly of high carbon austenite, bainitic ferrite and graphite nodules, produced by a two stage austenitisation and austempering heat treatment. The resulting microstructure gives these materials a combination of high strength and toughness, making them attractive for a wide range of applications. To increase surface hardness, ductile iron alloys can also be cast into chilled moulds to induce carbide formation in the required areas of components. These chilled ductile iron alloys can also be subjected to austenitisation and austempering heat treatments, therefore further improving the mechanical properties of the components core, whilst retaining the hard carbides present in the surface layers.

This work encompasses three main areas; two are concerned with the production of generic microstructure models, which work in conjunction with thermodynamic modelling software MTDATA, and one relates to high temperature X-ray diffraction experiments. The first modelling section details how a computer program was developed that can be used to investigate how chemical composition influences the chill tendency of ductile iron alloys. The model predictions were shown to be in good agreement with a wide range of experimental measurements.

The second modelling section considers ADI alloys. A computer program was developed which, given the chemical composition and austenitisation and austempering temperatures, produces a prediction of the microstructure of the alloy at the end of stage 1 of the austempering heat treatment, taking into account segregation of alloying elements. Experimental segregation profiles produced during this work showed good agreement with the model predictions. Furthermore, predictions of the stage 1 transformation kinetics as a function of alloying element segregation, are also made by the model. Therefore, the local microstructural transformation times during austempering can be predicted. Good agreement has been observed between phase volume fractions, transformation times and mechanical property predictions made using the model and those found in literature, therefore a useful tool for new alloy development has been produced.

High temperature X-ray diffraction experiments were also performed as part of this work. Microstructures typical of ADI alloys were produced during these experiments, although small quantities of pearlite were observed in the samples, and care was taken to minimise any effects of decarburisation and/or oxidation. The austenite carbon content was monitored during austenitisation and austempering, enabling comparisons to be made between high temperature and low temperature X-ray diffraction measurements in ADI alloys.

Acknowledgement

The work performed in this thesis was used for a number of journal publications, which are listed below:

D.C. Putman and R.C. Thomson, Microstructure and Mechanical Property Modelling of Austempered Ductile Iron, *International Journal of Cast Metals Research*, Vol. **16**, No.1, pp 191-196, (2003).
(also presented at SPIC7 Conference, Barcelona 2002)

P.A.S. Reed, R.C. Thomson, J.S. James, D.C. Putman, K.K. Lee and S.R. Gunn, Modelling of Microstructural Effects in the fatigue of Austempered Ductile Iron, *Materials Science and Engineering A*, Vol. **346**, pp 273-286, (2003).

R.C. Thomson, J.S. James and D.C. Putman, Modelling microstructural Evolution and mechanical Properties of Austempered Ductile Iron, *Materials Science and Technology*, Vol. **16**, pp 1412-1419, (2000).

List of Symbols and Abbreviations

a_{DH} = Austenite lattice parameter calculated using Dyson-Holmes relationship

a_m = Measured room temperature austenite lattice parameter

a_0 = Initial lattice parameter

$a_{0\gamma}$ = Lattice parameter of austenite at 298K

a_γ = Austenite lattice parameter

A = Atomic mass of Fe

Ae_3 = Temperature when α-iron transforms to γ-iron at equilibrium

A_1 = Eutectoid temperature

$\mathbf{b}$ = Burgers vector

bcc = body centred cubic

bct = body centred tetragonal

B_S = Bainite start temperature

$c = \Theta/T$

C^S_γ = C content of austenite carbon enriched austenite which is retained on cooling to room temperature

C^0_γ = C content of austenite after austenitisation (start of austempering)

d_{hkl} = Spacing between planes in a crystal

e^{-2M} = Temperature factor

fcc = face centred cubic

f = Scattering factor

f_s = Weight fraction of solid material in the bar

f_c = Scattering factor corrected because iron atoms are not independent of the wavelength of the scattered Cu radiation

F = Structure factor

G = Gibbs free energy

$G_{m[T]}$ = Gibbs free energy relative to a standard element reference state

G_N = Universal nucleation function of temperature

G^{XS} = Excess Gibbs free energy of mixing

G^{XS}_{IDEAL} = The ideal entropy and enthalpy change on mixing of two or more species in a phase

G_Z = Zener ordering energy

G^0 = Gibbs free energy of a species in its standard reference state

$H_m{}^{SER}$ = Enthalpy of a substance in its standard reference state

I = Nucleation rate of ferrite per unit volume

I_α = Integrated intensity a ferrite peak

I_γ = Integrated intensity a austenite peak

k = Partition coefficient

k = Thermal conductivity of a substance

K_1 = Empirical constant

K'_1 = Empirical constant

K_2 = Empirical constant

L = Mean linear intercept of bainitic ferrite/martensite plates

M_f = Martensite finish temperature

M_s = Martensite start temperature

P = Multiplicity factor

r = Empirical constant

R = Gas constant, 8.314 $JK^{-1}mol^{-1}$

SEM = Scanning electron microscope

t = time

t_α = Thickness of bainitic ferrite/martensite plate

T = Temperature

T_Q = Temperature alloy is quenched to after austempering

T^α = Austempering temperature

T^γ = Austenitisation temperature

u = Volume of a bainitic subunit

u_t = Subunit thickness

u_w = Subunit width

V = Volume of a unit cell of austenite or ferrite

Vf = Volume fraction

Vf_m = Volume fraction martensite

$Vf\alpha_b$ = Volume fraction bainitic ferrite

Vf_γ = Volume fraction austenite

w = Concentration of element (wt.%)

W_s = Widmänstatten ferrite start temperature

x = Mean carbon content of an alloy (mols)

x_i = Mole fraction of component I

x_γ = C content of the austenite in (wt.%)

X_E = Eutectic composition of an alloy bar

X_{Fit} = Fitted limiting austenite C content (wt.%)

X_L = Mole fraction solute in liquid

X_S = Mole fraction solute in solid

X_{T0} = limiting austenite C content (wt.%)

$X_{T0'}$ = limiting austenite C content, accounting for the stored energy of ferrite (wt.%)

X_{T*} = hypothetical limiting austenite C content (wt.%)

X_U = Mean composition of an alloy bar

X_0 = Composition of an alloy bar

X_α = C content of saturated ferrite (wt.%)

α = ferrite

α_b = bainitic ferrite

α_γ = Linear thermal expansion coefficient of austenite

α_{Exp} = *Linear thermal expansion coefficient*

β = Autocatalysis factor

β_m = Modified autocatalysis factor

Δa = Change in lattice parameter over a temperature range ΔT

$\Delta C = C^S_\gamma - C^0_\gamma$ (proportional to stage 1 austempering reaction driving force)

Δf = Correction of the scattering factor

ΔG = Gibbs free energy change

ΔG_{max} = Maximum free energy available for the nucleation of ferrite

ΔG^0_{max} = Initial value of ΔG_{max}

ΔG_I = Driving force for stage 1 austempering reaction

ΔG_{II} = Driving force for stage 2 austempering reaction

ΔG_2 = Free energy change for the formation of a mole of ferrite nuclei of composition x_α

$\Delta G^{\gamma \to \alpha}$ = Driving force for bainite transformation without a change in composition of the ferrite nucleus

$\Delta G^{\gamma \to \alpha'}\{T\}$ = Free energy change of austenite to martensite of the same chemical composition at a temperature T

$\Delta G^{\gamma \to \alpha*}$ = $\Delta G^{\gamma \to \alpha}$ + stored energy of bainitic ferrite (400 $Jmol^{-1}$)

$\Delta G_C^{\gamma \to \alpha'}$ = Critical value of $\Delta G^{\gamma \to \alpha'}\{T\}$ at which martensite formation becomes thermodynamically possible

ΔG^{*}_{max} = ΔG_{max} + stored energy of bainitic ferrite (400 $Jmol^{-1}$)

ΔH = Change in enthalpy

ΔS = Change in entropy

γ = austenite

γ_s = C enriched austenite which is retained on cooling to room temperature

γ_0 = metastable austenite

λ = Wavelength of the incident X-rays

λ_1 = Empirical constants

λ_2 = Empirical constants

μ = Shear modulus of iron

v = Actual volume fraction of bainite

θ = Half the angle between an incident and diffracted beam of X-rays

Θ = Debye characteristic temperature of Fe

ρ_d = Dislocation density of bainitic ferrite/martensite

σ_g = Strengthening of bainitic ferrite/martensite due to lath size

σ_p = Strengthening of bainitic ferrite/martensite due to dislocations

σ_{ssc} = Interstitial C strengthening of bainitic ferrite/martensite due to dislocations

σ_y = Yield strength of austenite

Ω = Maximum volume fraction of bainite

ξ = Normalised volume fraction of bainite

ADI = Austempered ductile iron

ASTM = American Society for Testing Materials

C.E.V = Carbon equivalent value

HTXRD = High temperature X-ray Diffraction

MTSol = Materials thermochemistry solutions database

SER = Standard element reference

SGTE = Scientific group thermodata Europe

TAL = Temperature of austenite liquidus

TCFE = Thermo-Calc Fe database

TEE = Temperature at which eutectic solidification is completed

TER = Eutectic recalescence temperature

TES = Temperature of eutectic solidification

TEU = Eutectic undercooling temperature

TEU_b = Eutectic undercooling temperature in an uninoculated iron

TEU_f = Eutectic undercooling temperature in an inoculated iron

TTT = Time temperature transformation

UAV = Untransformed austenite volume

UTS = Ultimate tensile strength

1 Introduction

Austempered ductile iron (ADI) alloys are a heat treated version of ductile cast irons that are becoming increasingly popular for a wide range of industrial applications. The popularity of these alloys stems from their outstanding mechanical properties of which their excellent combination of high strength and ductility, and therefore toughness, is the most prominent. These mechanical properties are obtained by performing a heat treatment consisting of two stages, austenitisation and austempering on ductile iron alloys.

Austenitisation, the first stage of the heat treatment, is carried out at temperatures of 850-1000°C, producing an austenite matrix with a uniform carbon content, which surrounds the graphite nodules. The iron is then quenched to the austempering temperature (440-250°C) for the second heat treatment known as austempering. During austempering, the metastable austenite is consumed by the formation of bainitic ferrite. The bainitic ferrite rejects carbon into the surrounding austenite during the transformation, resulting in the austenite becoming enriched with carbon. This transformation ceases when the austenite becomes so enriched with carbon that there is no longer a driving force for the formation of bainitic ferrite. The resulting microstructure is a mixed matrix of bainitic ferrite surrounded by high carbon austenite, that encircles the graphite nodules. The austenite is sufficiently enriched with carbon that it is usually retained upon quenching to room temperature. The presence of the bainitic ferrite phase gives the matrix strength, which when combined with the tough and ductile properties of the austenite results in the excellent mechanical properties of the alloys.

To increase the wear resistance of ADI components, these alloys can be cast into a chilled mould. Metal inserts known as chills, are placed in the mould at the required areas, and induce carbide formation upon solidification. During subsequent austenitisation and austempering heat treatments, most of these carbides are retained and therefore the local hardness of the component is increased. The resulting material is known as chilled austempered ductile iron and has the potential to be a useful material for the production of components such as automotive camshafts.

The successful production of the required microstructure requires a knowledge of the influence of a number of a intricate variables such as the alloy composition, heat treatment temperatures and times and extent of alloying element segregation. Indeed, although the potential of these alloys has been known for many years, their adoption by industry has been slow, due to the complexities in their production.

This work aims to help bridge this gap by reducing the uncertainty associated with the production of these alloys. Thermodynamic modelling techniques are used to produce accurate predictions of the microstructure, given simply the alloy composition and heat treatment details, enabling the influence of these production variables to be easily investigated.

The current work begins with a thorough analysis of the current understanding of ADI alloys such as the influence of austenitisation and austempering temperatures and times on the resulting microstructure, the effect of alloying elements on the system, and mechanical properties of the alloys. The concepts behind MTDATA, a thermodynamic software package which is used throughout this work are then discussed, and it is shown how this software package can be combined with computer languages such as Fortran enabling powerful computer programs to be produced, which are capable of predicting a wide range of material properties. The accuracy of predictions made by MTDATA are then compared to a series of reference systems, hence demonstrating the accuracy of the thermodynamic predictions.

A model which has been developed to predict the influence of alloying elements on the chill tendency of ductile iron alloys is presented in chapter 4. The model is tested against a range of experimental data to demonstrate its potential to accurately predict these effects. It is then shown how this model can be combined with cooling curve data to enable predictions of the microstructure through a section of a camshaft lobe.

A series of chapters then follow which outline and analyse a model which based on the thermodynamics of the system, is capable of predicting the microstructure, mechanical properties and austempering transformation rate of ADI alloys taking into account the important influence segregation has on local microstructure and transformation rate. Throughout these chapters, all the different aspects of the model are again tested thoroughly against a wide range of experimentally obtained data, demonstrating its true generic capabilities. Predictions made by the model are also validated by comparing them to a database of experimental measurements obtained from literature.

The final sections of this work detail high temperature X-ray diffraction experiments on ductile iron alloys, which were used to help validate predictions made by the model. Ductile iron alloys were subjected to austenitisation and austempering heat treatments and the phase transformations were monitored using high

temperature X-ray diffraction. Decarburisation of the samples during heat treatment was shown to have a strong influence on the results of these experiments. The measurements obtained were then compared to their corresponding low temperature values and model predictions.

2 Literature Survey

2.1 General Description of Cast Irons

Cast irons are iron carbon silicon alloys, typically containing 2-4 wt.% C and 0.5-3.0 wt.% Si, that pass through the eutectic reaction on solidification [1]. There are generally considered to be five different types of cast irons. These are grey cast irons, white cast irons, malleable cast irons, spheroidal graphite cast irons (also known as ductile irons) and compacted graphite cast irons. The origin of the formation of these different types of cast iron depends on the solidification kinetics, composition and the phase transformations that the alloy undergoes. A schematic of the Fe-C and Fe-Fe$_3$C phase diagrams is shown below in figure 2.1. The Fe-Fe$_3$C metastable system is highlighted by the blue lines and text, whereas the equilibrium system of Fe-C is shown by the black lines and text.

Figure 2.1. Schematic of the Fe-C and Fe-Fe$_3$C phase diagrams.
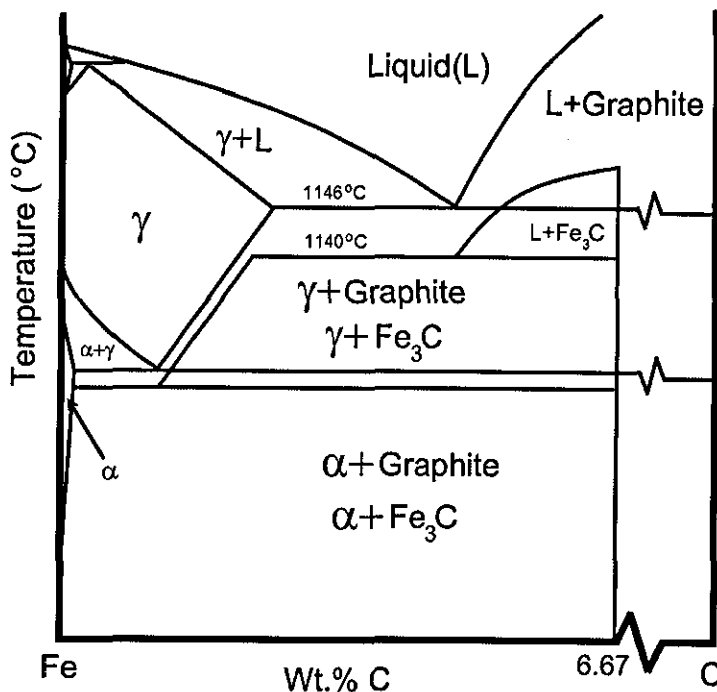
The eutectic reaction (L → γ + Fe$_3$C) of the Fe-Fe$_3$C system occurs at 1140°C for a simple iron carbon alloy. This reaction produces a white iron microstructure composed of Fe$_3$C and pearlite. However, this is the metastable system (blue lines in figure 2.1) and under truly equilibrium conditions the reaction is L → γ + Graphite

(black lines in figure 2.1). This occurs at 1146°C in a simple iron carbon alloy, and grey, ductile or compacted graphite iron would be produced [1]. In reality, an undercooling of greater than 6°C (the difference between the equilibrium and metastable eutectic temperatures) easily occurs and white iron forms. However, adding alloying elements such as silicon to a casting increases the temperature difference between the two eutectic reactions, allowing larger undercoolings to occur, and hence more time for graphite to nucleate and grow. Other elements such as chromium, have the opposite effect. Inoculants can also be added to aid graphite nucleation or the cooling rate can be reduced, such that more time is given for the formation of graphite in the alloy.

The way the austenite transforms during the eutectoid reaction determines the matrix structure and properties of the cast iron. Both the metastable ($\gamma \rightarrow \alpha + Fe_3C$) and the equilibrium ($\gamma \rightarrow \alpha +$ Graphite) reactions can occur. For example, silicon aids the equilibrium eutectoid reaction, and therefore during cooling of an iron containing silicon, the carbon atoms diffuse from the austenite to the existing graphite particles, leaving behind a low carbon ferrite matrix [1]. The control and manipulation of the eutectic and eutectoid reactions can produce cast irons with a wide range of different structures and hence mechanical properties. The five different structure types are discussed below.

2.1.1 Grey cast iron

Grey cast irons contain small interconnected graphite flakes that cause low strength and ductility [1]. They are the most common and cheapest to produce type of cast iron. Solidification produces graphite flakes, which are interconnected at the original graphite nucleus. Inoculation or rapid cooling produces finer graphite flakes. The graphite flakes are weak and brittle and behave like cracks in the microstructure, hence grey cast irons are very brittle. However, these flakes do not act as stress raisers under compressive loading, and the machinability of these irons is excellent, since the graphite flakes act as chip breakers. Resistance to sliding wear is good as the graphite flakes absorb and hold lubricants. Thermal conductivity is also high due to the interconnecting graphite flakes. This material is used extensively for engine

blocks due to its excellent vibration dampening characteristics and as machine tool bases for the same reason. Cooling rate can also affect the properties of grey irons. A fast cooling rate can produce a chilled microstructure, particularly on the surface. Carbides can then form and a white iron structure is produced making machining very difficult. Lowering the carbon content will increase the tensile strength as a smaller quantity of graphite flakes are produced [2].

2.1.2 White cast iron

White cast iron is a hard brittle alloy, containing large amounts of cementite [1]. These alloys have low carbon contents (approximately 2.5 wt.% C) and around 1.5 wt.% Si. They solidify rapidly, without graphite formation and produce a very hard material, which cannot easily be machined. Additions of Cr, Mo and Ni are made to the cast iron to make it even harder and more wear resistant by the formation of carbides. This also increases the hardenability of the alloy, hence a martensitic structure can be produced, which is an ideal material for excavators and other wear resistant applications. These irons are commonly heat treated to produce malleable cast iron.

2.1.3 Malleable cast iron

Malleable cast iron is formed by the heat treatment of white iron. During the heat treatment, graphite forms with the morphology of rounded clumps [1]. During the malleabilising heat treatment, cementite formed during solidification decomposes and graphite clumps are produced, which often resemble popcorn. Their rounded shape allows a good combination of ductility and strength to be produced in such irons. The malleabilising heat treatment has several steps, as shown in figure 2.2. Graphite nodules nucleate as the white iron is heated up. During first stage graphitisation, which is performed at approximately 900°C, cementite decomposes to austenite and graphite, as carbon in the Fe_3C diffuses to the graphite nuclei. During cooling, the austenite transforms. If the iron is cooled slowly through the eutectoid temperature

range (see figure 2.2), second stage graphitisation results and ferritic malleable iron is produced. This iron has good toughness due to its low carbon content and ductile ferrite matrix [1]. Alternatively, after first stage graphitisation is completed, the iron can be cooled in water to produce martensite, or simply air cooled to produce a pearlitic matrix. Both structures are hard and brittle, and are hence drawn at a temperature below the eutectoid to increase their toughness and ductility [1]. Drawing tempers the martensite and spheroidises the pearlite. Higher drawing temperatures decrease the strength, but increase the toughness. Typical applications include gears, wheel hubs and various tools such as hammers and wrenches [3].

Figure 2.2. Malleabilising heat treatments of white cast irons.
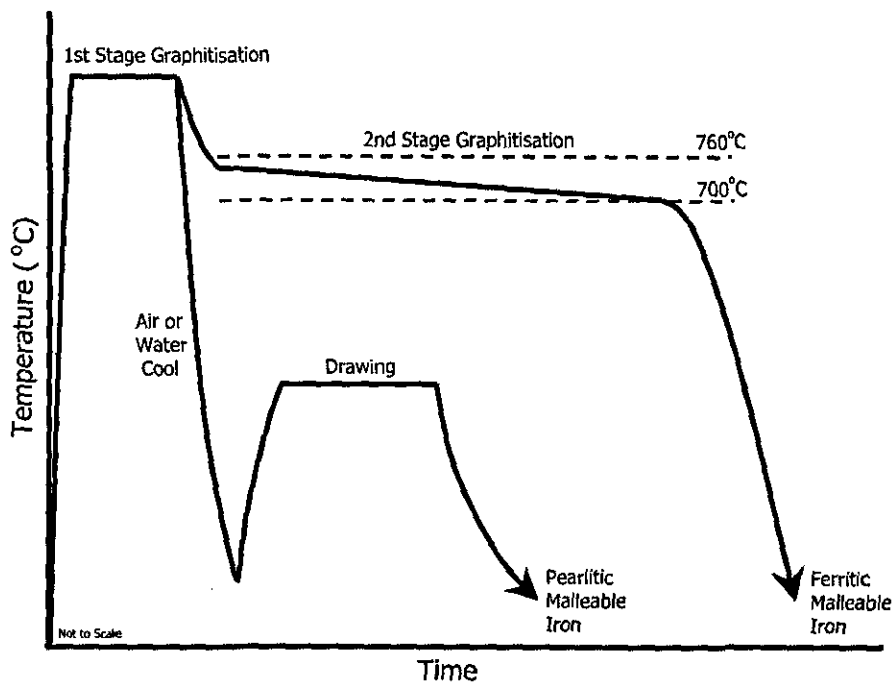
2.1.4 Spheroidal cast iron

Spheroidal cast iron, also known as nodular or ductile cast iron, contains spheroidal graphite particles that are obtained during solidification [1]. They contain high concentrations of carbon so that spheroidal graphite forms during solidification. To produce graphite with a spheroidal morphology, desulphurisation, nodulising and inoculation treatments must be performed. A desulphurisation treatment removes

sulphur from the liquid metal. This is needed because sulphur causes graphite to grow as flakes. Calcium carbide is commonly used [1]. Magnesium is added in the nodulising stage, to remove any sulphur and oxygen left in the liquid metal. Finally, inoculants are added just before casting to prevent white iron formation, since magnesium is a potent carbide stabiliser [1]. The inoculant causes the graphite to grow with a spheroidal morphology. FeSi is commonly used for this purpose [1;2]. The resulting irons have excellent strength and toughness as a result of the spheroidal graphite morphology.

2.1.5 Compacted graphite cast iron

Compacted graphite cast iron contains rounded, but interconnected graphite, which is produced during solidification [1]. The structure of the graphite in this iron is halfway between flake and spheroidal. These irons have reasonable mechanical properties, but still retain the good thermal conductivity and vibration dampening characteristics of grey iron. They are produced using a similar treatment to spheroidal iron, but less Mg is added during nodulising. Hence some flake graphite forms on solidification.

2.1.6 Solidification behaviour of cast irons

The solidification behaviour of a typical hypoeutectic cast iron alloy is shown in figure 2.3. The first solid forms at the temperature of the austenite liquidus (TAL). Austenite dendrites nucleate and start to grow at this temperature. As cooling continues, the temperature of eutectic solidification (TES) is reached. At TES, graphite nucleation commences, and eutectic cells of graphite and austenite form around the primary austenite dendrites. Nucleation continues accompanied by increased latent heat evolution until the eutectic undercooling temperature (TEU) is reached. Eutectic cell growth now becomes established. Due to the increased volume of solid being formed, a large amount of latent heat is produced and the temperature increases. This is known as recalescence. Steady state growth then

occurs at the eutectic recalescence temperature (TER). As eutectic growth nears completion, less latent heat is evolved and the temperature falls. Eutectic solidification is completed at temperature TEE [2]. A hypereutectic alloy follows the same solidification route, except primary graphite nucleation occurs instead of the formation of primary austenite dendrites.

Figure 2.3. Schematic diagrams illustrating the solidification of two cast irons cooled at different rates.

TAL = Temperature of Austenite Liquidus   TES = Temperature of Eutectic Solidification
TEU = Temperature of Eutectic Undercooling   TER = Eutectic Recalescence Temperature
TEE = End of Solidification

Not to scale
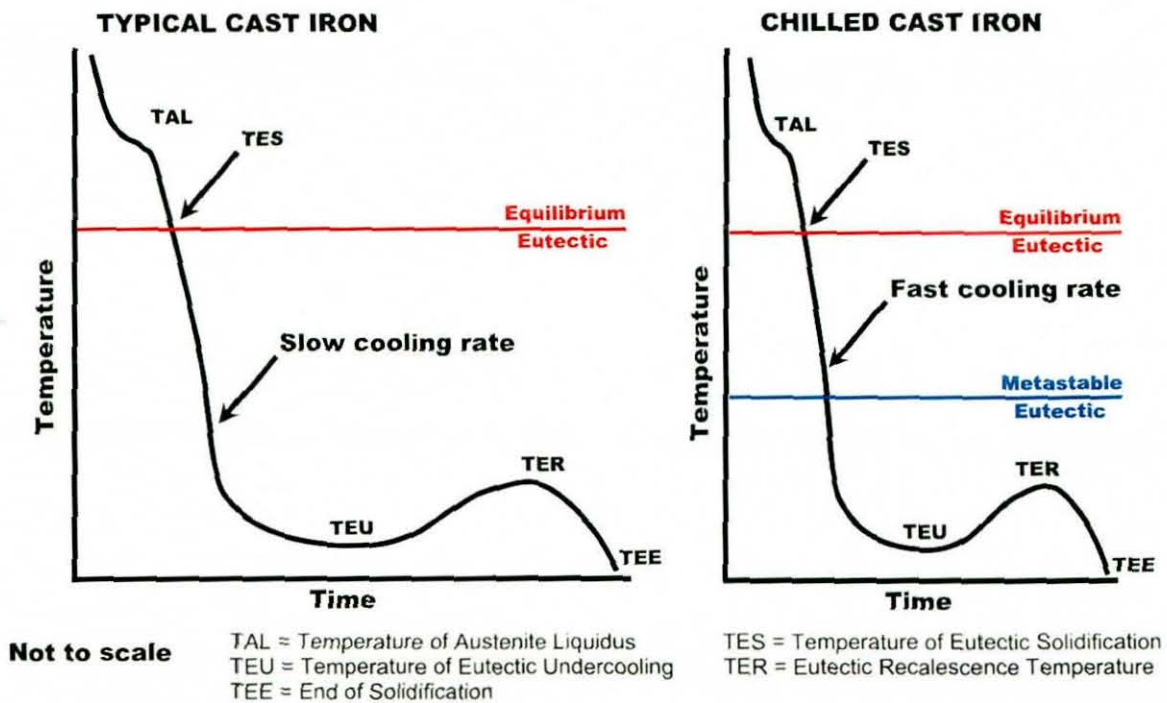
Figure 2.3 also shows the influence that chills have on the solidification of a hypoeutectic alloy. As with a normally cooled alloy, primary austenite dendrites are the first solid to form. However, due to the increased cooling rate induced by the chill, the dendrites are much finer [4]. The effect of the chill on the solidification of the surface layers of the alloy is to rapidly cool them well below the metastable γ-Fe_3C eutectic temperature (blue lines on figure 2.3). Therefore, there is little time for the equilibrium solidification of eutectic cells of austenite and graphite to occur. Hence the majority of the alloy solidifies as eutectic cells of austenite and cementite. The cell count is much greater than that of an alloy cooled normally, due to the greater number of fine primary austenite dendrites that host the eutectic cells [4]. As can be

seen in figure 2.3, the TEU and TER temperatures are suppressed well below the metastable eutectic temperatures. This type of solidification will produce a white iron microstructure with large volumes of carbide in the matrix.

Several theories exist regarding the formation of solidification cells in ductile iron alloys. These are highlighted in figure 2.4, in which the dark grey areas represent the last liquid to freeze. Cell formation has an important influence on the properties of ductile irons since segregation of alloying elements is thought to occur at the boundary between adjacent cells. The segregation can have a detrimental effect on mechanical properties and strongly influence subsequent heat treatments that the alloys are subjected too. The simplest model as seen in figure 2.4a is known as the uni-nodular model. It assumes that graphite nodules, which form in the liquid, are subsequently enveloped by austenite shells. Hence each nodule is at the centre of a single solidification cell, and segregation of alloying elements occurs at the boundary between these cells in the last to freeze areas of the microstructure. This model has traditionally been preferred by researchers involved in materials modelling due to its simplicity, but seldom agrees with actual microstructural observations [5;6].

Figure 2.4. Three models of ductile iron cell formation.

a) Uni-nodular Methodology   b) Multi-nodular Methodology   c) Boeri-Sikora Macrostructure   d) Boeri-Sikora Microstructure

☐ = Liquid   ☐ = First solid   ■ = Last solid
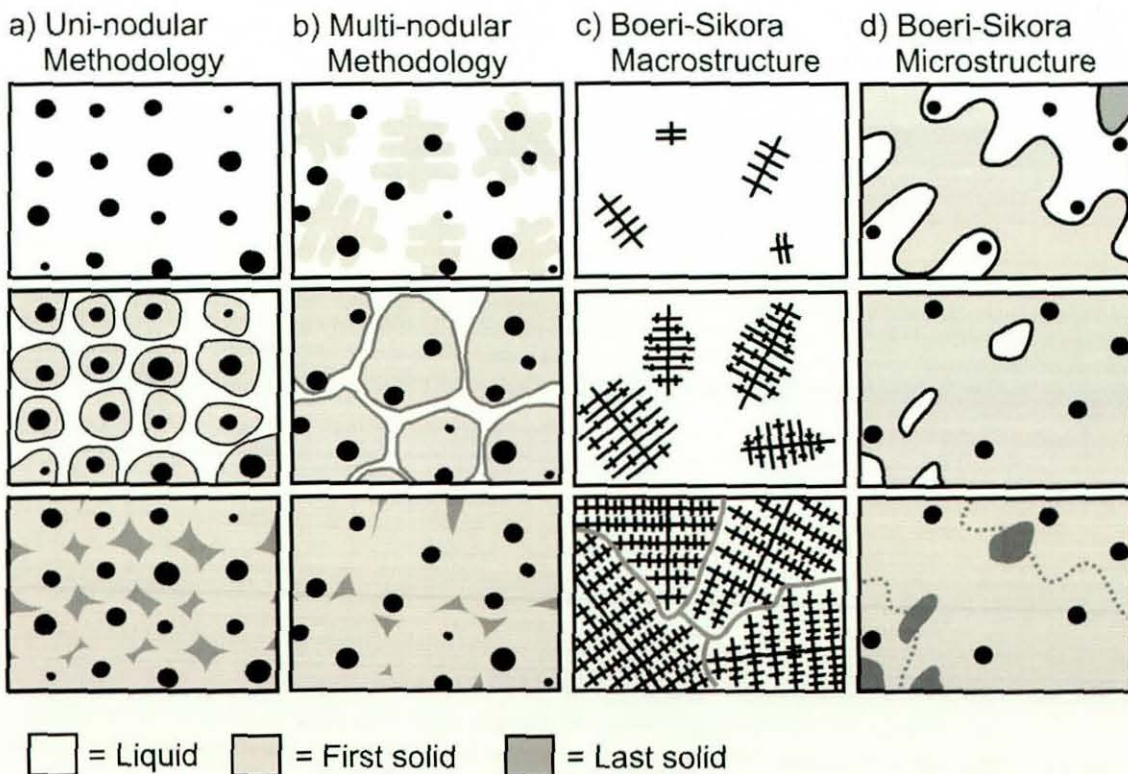
The multi-nodular model (figure 2.4b) assumes each cell contains several graphite nodules. It was developed in conjunction with actual microstructure observations of microsegregation patterns [7]. It considers that the austenite and graphite nodules nucleate independently. Subsequent austenite dendrite growth encompasses several graphite nodules and as in the uni-nodular model, segregation of alloying elements occurs between the cell boundaries. Although the multi-nodular model has been shown to agree with actual microsegregation profiles, the size of the solidification cells is much smaller than the grain size observed by macrography [8].

Recent work by Boeri and Sikora showed how new microstructural observation techniques have been used as supporting evidence for a new methodology for ductile iron solidification [8]. This is highlighted schematically macrographically and micrographically in figures 2.4c and d. They propose that austenite and graphite nucleate independently in the melt. In the macrostructure schematic (figure 2.4c) the graphite nodules are too small to be seen. As solidification progresses the austenite dendrites grow and contact, enveloping most of the graphite nodules. Further nodule growth is controlled by diffusion of carbon through the austenite envelope. However, significant amounts of melt remain trapped between the secondary dendrite arms. The grain size is defined as the point where the dendrites contact, but significant amounts of liquid still remain in the alloy at this time. The liquid trapped between secondary dendrite arms represents the last to freeze liquid and is highlighted by the dark grey regions in figure 2.4d. This theory that segregation occurs between secondary dendrite arms in grains accounts for the shortfalls of the multi-nodular theory because both the grain size and segregation pattern observed in microstructures can be accounted for using the Boeri and Sikora methodology.

2.1.7 Materials used in this work

All the different types of cast iron discussed in the preceding sections can be heat treated if need be, to tailor their microstructures to produce the properties required for their selected applications. One such material is known as austempered ductile iron. A spheroidal graphite casting is produced and is then given a two stage heat treatment to produce the required mechanical properties. This is the material that is used in this work and is discussed in detail in the following sections.

2.2 General Description of Austempered Ductile Iron

Austempered ductile iron (ADI) offers a wide range of mechanical properties. The most important and unique properties of these materials is their excellent ductility combined with high strength [9]. For example an ADI component can obtain a tensile strength of 900 MPa, and still retain 8% elongation. Hence ADI has more than twice the strength for a given level of ductility compared with other grades of ductile iron, and for a given hardness has superior wear resistance when compared with other materials [10]. These properties stem from the melt processing which controls the spheroidisation and distribution of graphite and from the austenitisation and austempering heat treatments in the solid state [11], see figure 2.5. Following the heat treatments a microstructure consisting of spheroidal graphite embedded in a complex matrix is produced. The heat treatments and composition of the alloy control the constitution of the microstructure. The resulting microstructure consists mainly of bainitic ferrite, high carbon austenite and graphite nodules. Martensite, ferrite, iron and other alloy carbides may also be produced [12].

The main alloying elements used are Mo, Mn, Cu, and Ni, which improve the hardenability of large castings [10]. This delays the formation of pearlite in the microstructure during cooling to the austempering temperature [10]. Pearlite is an unwanted phase as it reduces the mechanical properties of the alloys. ADI is 8 % less dense than steel due to the low density graphite in the matrix, and because of its excellent castability it can be produced nearer to the net shape than either a steel casting or forging. It also consumes 50% less energy in production than steel forgings. Its bainitic ferrite matrix, for a given level of hardness, exhibits significantly higher wear resistance than conventionally hardened steel [10]. The easy machinability and lower cost than either steel forgings or castings also makes ADI an attractive material. These properties make ADI an appealing material for use in a range of applications in the automotive industry. Uses include gears, suspension components, gearboxes, camshafts, wheel hubs and engine mounts. ADI is also used in numerous other applications such as civil, constructional and agricultural industries for components that combine high levels of tensile strength with good impact properties and wear resistance [13].

Figure 2.5. Schematic diagram of ADI production.
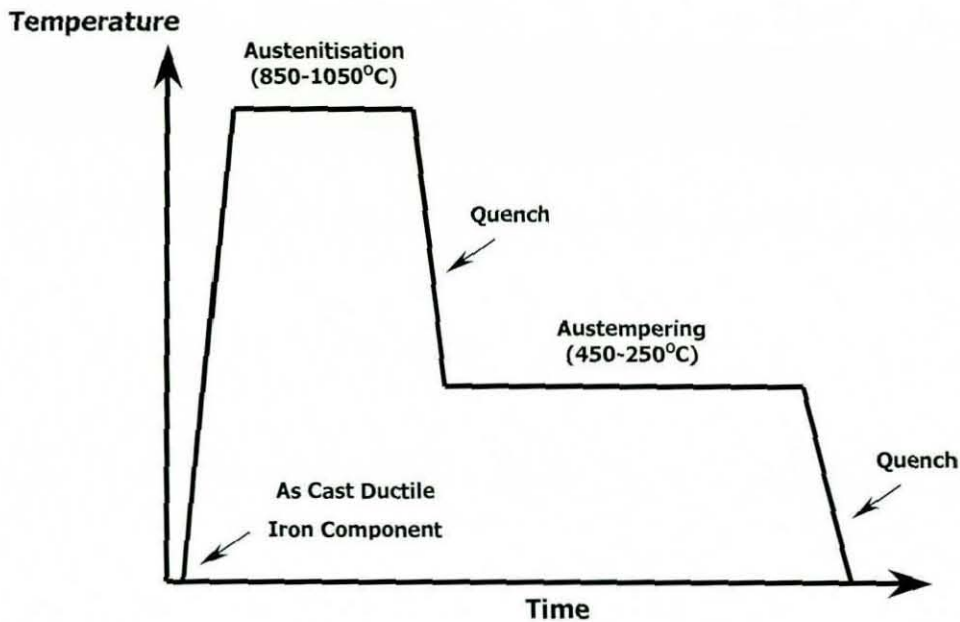
2.3 Microstructure of ADI

2.3.1 Austenite

Although some cast iron alloys have their cooling rate controlled so that the desired mechanical properties result directly from their solidification, ADI alloys undergo a two stage heat treatment after solidification. These heat treatments produce the excellent mechanical properties of ADI alloys. Austenitisation occurs as the alloy is heated to around 850-1000°C [14,15]. During this heat treatment a phase change results as the previous matrix transforms to austenite. Both the diffusion coefficient and the driving force for this change increase with temperature, so the overall rate of transformation increases as the temperature is raised [16]. The nature of this complex transformation depends on a number of factors since the initial microstructure can vary to a large degree. Particle size, phase distribution and chemistry, microstructural homogeneity and impurity levels all influence this sophisticated process [16].

However, austenite grains commonly nucleate on ferrite/cementite interfaces if the previous microstructure consisted mainly of pearlite [3]. The cementite then dissolves completely after a prolonged holding time at the austenitisation temperature. If the microstructure consisted mainly of ferrite before austenitisation, during the heat treatment the austenite grains will nucleate mainly on the ferrite grain boundaries [3]. Nucleation of austenite from bainitic microstructures, which are free from retained austenite, tends to occur at the prior austenite grain boundaries that formed during alloy solidification. However, if the driving force for the transformation is large then nucleation at other sites such as bainite plate boundaries may occur [16]. Nucleation of austenite from a mixed microstructure of bainitic ferrite and austenite is absent and the original austenite grain structure is regenerated during the heat treatment [16]. All these transformations are predominately diffusion controlled processes [3]. The austenite grows by a reconstructive mechanism with diffusion of substitutional solutes [16]. Upon completion of the heat treatment (approximately 2 hours for an ADI component of 40-60mm in diameter) the initial microstructure should be austenite containing a uniform distribution of carbon [17].

Figure 2.6. A typical ADI microstructure of bainitic ferrite in an austenite matrix [18].

Bainitic Ferrite
Sheaves

Graphite
Nodule

Austenite
(white)

20µm
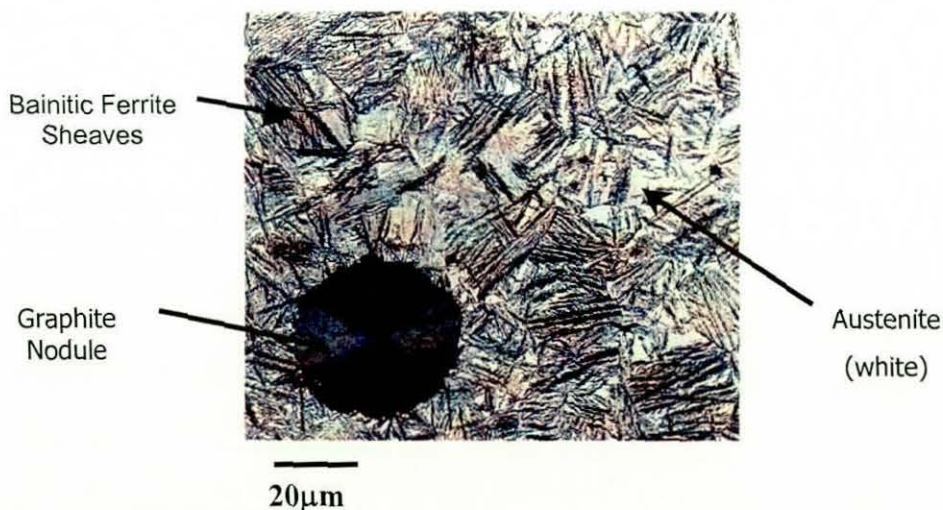
Figure 2.6 shows a typical ADI microstructure containing bainitic ferrite in an austenite matrix. As stated previously, austenite is formed during the high temperature austenitisation heat treatment stage of the production of ADI. By the end of the heat treatment the entire matrix is transformed to face centred cubic (fcc) austenite, which is saturated with carbon. The temperature of the austenitisation heat

treatment influences the solubility of carbon in the alloy and the austenite grain size. Increasing the austenitisation temperature will increase the carbon content of austenite, as more graphite is soluble in the matrix at higher temperatures [19]. Once the austenitisation heat treatment is completed the alloy is quenched to the austempering temperature. No transformation takes place on quenching (provided it is fast enough), and hence the austenite is metastable. Other factors that affect the carbon concentration in the austenite phase are the substitutional element concentration and the austenitising time, which determines how close the carbon content in the austenite gets to equilibrium [20].

During austempering bainitic ferrite nucleates on the graphite nodules or the interface between the nodule and the austenite matrix and the metastable austenite transforms to bainitic ferrite (figure 2.7a). Carbon is rejected from the bainitic ferrite into the remaining austenite (figure 2.7b). It is generally accepted that two kinds of austenite exist in ADI alloys [2;21]. The first type is austenite close to or trapped between bainitic ferrite plates, that quickly becomes enriched with carbon. The second type is blocky austenite, which is found between bainite sheaves. This is enriched with C at a slower rate. Due to segregation of alloying elements which influence the local microstructural transformation kinetics, carbon enrichment of this austenite may be additionally sluggish in some areas of the microstructure [22,23]. At the end of austempering, any remaining low carbon austenite is known as the untransformed austenite volume (UAV), and may transform to martensite on cooling to room temperature because of its low carbon content (figure 2.7c). 1.5-1.7 wt.% C is required to stabilise the austenite and prevent the transformation to martensite during cooling to room temperature [19]. To make the austenite mechanically stable at room temperature the austenite carbon content must be even higher (1.8-2.2 wt.% C)[24]. The desired microstructure at the end of the austempering heat treatment is islands of bainitic ferrite surrounded by a continuous matrix of high carbon austenite. The austenite is fcc in structure and crystals of this type are inherently more ductile than body centred cubic (bcc) crystal structures, making ADI alloys tough and ductile. The continuity of the austenite phase is important and also plays a key role in the ultimate ductility of the alloy by restraining the propagation of cracks through the cast iron [9, 25].

Figure 2.7. a schematic diagram illustrating the evolution of microstructure during austempering.
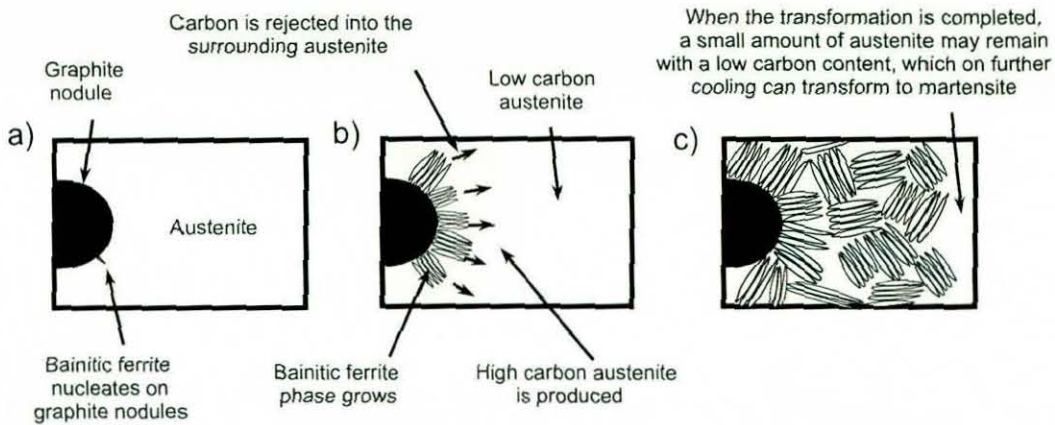
2.3.2 Bainitic ferrite

Bainite forms by a displacive mechanism, with diffusion of carbon following soon afterwards [26]. Bainitic ferrite in steels is commonly described in literature to be 'sheaf-like' in appearance. The sheaves nucleate on austenite grain boundaries because these are the most potent defects for nucleation. The sheaves are separated by regions of residual phases such as cementite or austenite [27]. Nucleation of new plates onto the sheaves allows them to grow. The nucleation of new plates is most common on the tip of the sheaf due to the stress field at the tip favouring the nucleation of the same variant [27]. This results in a wedge shape growth from the nucleation site on the austenite grain boundary out into the austenite grain. The width of the sheaves decreases with temperature.

In steels, two types of bainite can be differentiated depending on the temperature of the system. At high temperatures, upper bainite forms. The higher transformation temperature allows the diffusion of carbon out of the sheaves and into the surrounding austenite to lower the free energy of the system. The resulting plates of bainitic ferrite contain no carbides [27]. Carbides can occur in the austenite adjacent to the plates if the carbon content of the austenite is high enough [16]. Upper bainite sheaves also have a coarse, plate like appearance.

At lower temperatures the bainite forms using the same mechanism as with upper bainite, but diffusion of carbon is more difficult [16]. Therefore carbon finds it increasingly more difficult to diffuse out of the lower bainitic plates. As a result of this, carbides such as cementite and ε carbide may be found within the ferrite plates. These carbides precipitate from the super saturated lower bainite. The carbides found in lower bainite also tend to have a single crystallographic orientation [27]. η carbides have also been reported to form in bainite in high silicon cast irons [28]. Lower levels of carbides are found in the surrounding austenite, due to the larger volume fraction of carbon being accommodated in carbides within the bainite plates [16]. Alternatively, it is thought that cementite could nucleate and grow at the austenite-ferrite interface. This is known as interphase precipitation [27]. Carbon is thought to be taken from the surrounding austenite and the ferrite does not have to be supersaturated. Due to the lower levels of diffusion that takes place in lower bainite (only the small carbon atoms are mobile), the concentration of any substitutional alloying elements in the bainite are not found to differ from the concentration in the bulk material [27]. The morphology of lower bainite also differs from upper bainite in that the sheaves display a fine acicular appearance.

The sheaves upon closer examination consist of a series of laths or plates of ferrite separated by regions of residual phases such as cementite or untransformed austenite [27]. The plates in the sheaves may not be isolated from each other, therefore grain boundary formation occurs where plates come into contact [16]. Grain boundary formation is further aided by the fact that the sheaves tend to have a common crystallographic orientation. The resulting strains imposed on the material by the transformation to bainite do not seem to cause nucleation of other plates (as with martensite). However, stress induced autocatalysis may occur if adjacent plates form in such a way as to accommodate each others shape transformation [27].

It is well known that since there is a large quantity of graphite nodules and high concentrations of silicon and retained austenite in ADI, that the morphology of bainitic ferrite is different from the bainite found in steel [24,25,29]. Carbide formation can be suppressed due to the high silicon content in ADI alloys austempered at temperatures greater than 350°C [30]. This differs from the bainite found in steels where carbide formation occurs in short periods of time after the formation of the bainite plates. The combination of carbide free ferrite and stable austenite produced

during the first stage of austempering at high temperatures in ADI alloys is industrially referred to as 'ausferrite' by many authors [24;29;31], but will be known as bainitic ferrite in this work. At lower austempering temperatures, carbide formation can no longer be suppressed and carbides precipitate during the first stage of transformation [24;29;30]. Interestingly, this combination of bainitic ferrite and carbides, which is akin to lower bainite in steels [30] is also often refereed to as ausferrite[24;29;31]. The microstructural changes that occur upon austempering are highlighted for two different austempering regimes below:

High austempering temperatures (approximately ≥350°C):

$$\text{Stage I} \qquad \gamma_0 \ (C_\gamma^0) \ \rightarrow \ \alpha_b \ + \ \gamma_S (C_\gamma^S) \qquad\qquad [2.1]$$

$$\text{Stage II} \qquad \gamma_S \ (C_\gamma^S) \ \rightarrow \ \alpha \ + \ \text{carbide} \qquad\qquad [2.2]$$

Low austempering temperatures (approximately ≤350°C):

$$\text{Stage I} \qquad \gamma_0 \ (C_\gamma^0) \ \rightarrow \ \alpha_b \ + \ \text{carbide} \ + \ \gamma_S (C_\gamma^S) \qquad [2.3]$$

$$\text{Stage II} \qquad \gamma_S \ (C_\gamma^S) \ \rightarrow \ \alpha \ + \ \text{carbide} \qquad\qquad [2.4]$$
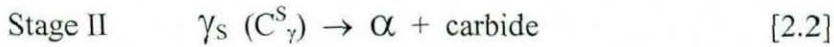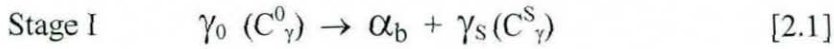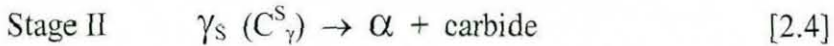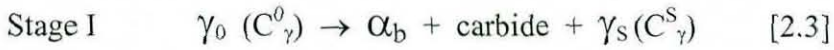
where γ_0 is the metastable austenite at the start of austempering with a carbon content of C_γ^0, α_b is bainitic ferrite, α is ferrite and γ_s represents stable austenite with a carbon content of C_γ^S.

After austenitisation the alloy is quenched to the austempering temperature and nucleation of bainitic ferrite occurs. The formation and growth of bainitic ferrite plates commences in the areas that were first to solidify which are around the graphite nodules [31]. They then proceed to grow out towards the last liquid to solidify. This occurs because of segregation of silicon in the alloy towards the first liquid to solidify and the opposite effect of elements like manganese and molybdenum. This segregation pattern results in an increase in the driving force for the transformation to bainitic ferrite in these areas, and lowers the driving force in areas away from the nodules [31,32].

For both regimes carbon from the bainitic ferrite is rejected into the surrounding austenite. As this process continues, the austenite carbon content increases and eventually it becomes thermodynamically impossible for austenite to

transform into bainitic ferrite. The austenite at this stage should have a carbon content high enough to make it stable on cooling to room temperature. At high austempering temperatures, carbon diffuses swiftly out of the bainitic ferrite plates, hence carbide formation is largely or totally avoided (equation 2.1). At lower austempering temperatures, carbon diffusion is more sluggish and carbides are found to precipitate within the bainitic ferrite plates (equation 2.3). If the austempering process continues for time periods longer than stage 1 the high carbon austenite can decompose into a mixture of ferrite and carbides (equations 2.2 and 2.4) [15;22;24].

The austempering temperature affects the structure of the bainitic ferrite. At low austempering temperatures the bainitic ferrite plates are fine and continuous, whilst at high austempering temperatures, the plates have a much coarser appearance and larger quantities of austenite are retained in the structure. The difference in the appearance of the bainitic ferrite can be seen in the two microstructures in figure 2.8.

Figure 2.8. Microstructure of an ADI alloy austempered at different temperatures [20].
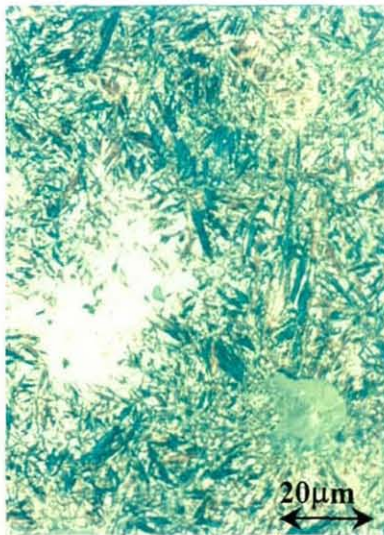
a) 950°C/250°C   b) 950°C/400°C
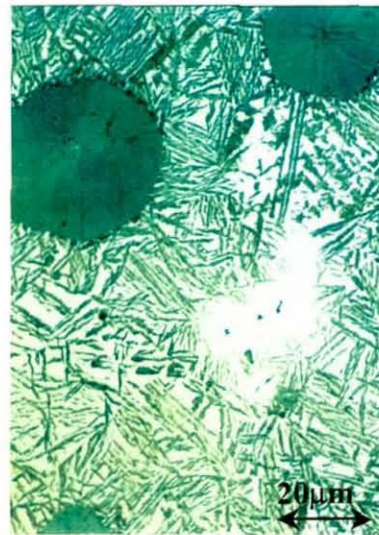
The microstructure content with respect to austenite/bainitic ferrite, strongly influences the mechanical properties of ADI alloys. The mechanical properties of a lower bainitic steel are generally more favourable than those of upper bainitic steel. Carbides in lower bainitic steel are finer than those in upper bainite and precipitate both inside and between the plates, whilst in upper bainitic steels carbides precipitate

just between the plates. The combination of these effects results in upper bainitic steels having a lower toughness than their lower bainitic counterparts [33]. The smaller plate size in lower bainitic steels also gives them a higher strength. The opposite is true for ADI even though the lower bainitic ferrite platelets are generally finer than those of upper bainitic ferrite. Although upper bainitic ferrite plates (produced by austempering at 350-400°C) are thicker than those of lower bainitic platelets, they are still fine and well dispersed. Accordingly the network of austenite throughout the matrix, including the spans between the bainitic ferrite sub units, is fine and continuous. This ductile continuous austenite matrix is the key to the mechanical properties of ADI, so a combination of high strength and ductility are observed in these alloys. Within lower bainitic ferrite platelets, the spans of austenite are very fine. Hence, the propagation of cracks can not be restrained effectively. Moreover, the lower bainitic ferrite platelets that are in contact with each other cut the network of the ductile austenite matrix altogether, producing a brittle ADI alloy [25].

However, austempering ADI alloys at very high temperatures (420°C) not only produces a bainitic ferrite microstructure with large platelets, but more importantly the austenite between the bainitic ferrite platelets decomposes more readily. Therefore, the tensile strength and toughness of the austenite decreases dramatically, resulting in poorer mechanical properties of the alloy [25].

2.3.3 Graphite

The graphite in ADI alloys is in the form of spheres and is known as spheroidal or nodular graphite. To enable spherical graphite formation to occur in a cast iron, a three stage treatment process must be performed on the liquid iron [1]. The iron melt must first undergo a desulphurisation treatment. High sulphur levels cause the graphite to grow with a flake morphology [1]. Nodulising follows, which removes any sulphur or oxygen left in the melt. Finally, an inoculation treatment is needed which promotes the growth of graphite with a spherical morphology [1].

Magnesium or cerium are added to the iron to make the graphite form a spheroidal morphology, magnesium being the most economical [2]. Oxygen and sulphur contents must be kept low because magnesium is a deoxidizer and desuphurizer. Carbon, silicon and aluminium in alloys help ensure a low oxygen

content, but a desulphurization process maybe needed to reduce the sulphur content. However, if sulphur levels become too low the nodule count can reduce because the sulphur present in the alloy can act as a nuclei for graphite formation [2].

The nucleation rate of graphite in ADI is influenced by composition, cooling rate and inoculation [34]. Increasing the additions of inoculants increases the nucleation and therefore the number of nodules at any cooling rate [34]. Inoculation is the process of adding small quantities of alloying elements to induce the eutectic graphite nucleation [2]. Its effectiveness is a measure of the initial nucleation potency and its ability to maintain effectiveness during eutectic solidification. Inoculants tend to be most effective immediately after addition and then their influence tends to fade. Therefore, they are added to the melt late in the production of the iron to prolong their effect. They are rarely effective for more than 20 minutes [2]. Ferrosilicon is the most popular inoculant, but a combination of minor elements is also needed for it to be successful. Barium is commonly used in spheroidal graphite inoculants and also increases fade resistance [2].

The graphite nucleates in either the liquid or on solid metal and subsequent growth occurs by the addition of diffusing carbon atoms onto the graphite nucleus [34]. The nucleation process is difficult due to the high surface energy between the graphite and surrounding phases. Therefore heterogeneous nucleation is the dominating nucleation process [34]. The heterogeneous nucleation sites provide a solid or substrate upon which the graphite can nucleate with a lower surface energy resulting between the liquid metal and graphite. Indeed, each graphite spheroid is a result of a distinct nucleation event, as is evidenced by the presence of a substrate particle at the growth centre of each spheroid [35].

Current understanding of the substrate responsible for graphite nucleation involves the formation of a complex non-metallic inclusion having sufficient crystallographic symmetry to essentially match that of graphite [35]. Effective nucleation requires two criteria. The two structures must have similar crystallographic structure, and the interfacial energy of the liquid embryo on the nucleation particle must be minimised. The degree of acceptable crystallographic mismatch between the two structures increases with undercooling, therefore a wider range of particles become active nucleation agents for graphite as undercooling increases [35].

Once nucleated, the growth of the spheroidal graphite occurs from the centre of the spheroids outwards in a radial manner until they are enveloped by austenite [2].

Proeutectic graphite will grow unimpeded until the start of eutectic solidification. The eutectic austenite may then co-precipitate with graphite, in the form of a solid shell of austenite. This separates the graphite from the liquid, therefore carbon must diffuse through the austenite to enable the graphite to grow [35]. Since the majority of spheroidal graphite growth occurs by carbon diffusion through the austenite shell, increased shell thickness will result in increasingly slower solidification rates and final solidification will occur at lower temperatures [35]. Undercooling of approximately 30°C is associated with the growth of normal spheroidal graphite structures. If the undercooling is less, the new graphite growths may form with rod or pyramid-like instabilities [2]. In commercial processes the required graphite morphology is obtained by controlling the undercooling by careful balance of the minor alloying additions. Uniformly round spheroids are produced by the kinetic undercooling effect. If the undercooling is too high then imperfect spheroids are produced, whilst if it is too low, intermediate graphite formations result [2]. A large undercooling also risks the nucleation and growth of cementite if the metastable eutectic temperature is reached.

Several other factors must be taken into account when selecting the minor element balance to obtain spheroidal graphite growth [2]:

- Minor elements may interact in the liquid iron resulting in a lower concentration of a particular element in solution (Mg can react with O or S, producing a deficiency in spheroidizing agents).
- Minor elements can display a dual effect during solidification (Cu after interacting with spheroidizing agents can promote undercooling if present in excess).
- The influence of spheroidizing agents is additive.
- Slow cooling in large sections is conducive to macro and micro segregation.

The graphite distribution is an important parameter. The aim is to produce a uniform distribution of fine perfectly shaped spheroids, which promotes good mechanical properties [2]. The distribution is quantified as the number of spheroids per mm^2, known as the nodule count, and can be measured by ultrasonics, magnetic techniques or simply by using an optical microscope [2]. The nodule count can vary from 1550 for very thin sections of highly nucleated alloys to 5 for castings of very large sections. As the casting section size increases and the nodule number

decreases, a significant reduction in properties occurs [36]. This is an important parameter as the graphite morphology influences the austempering kinetics, because graphite particles act as a substrate for bainitic ferrite nucleation [37]. The high nodule counts produced by effective inoculation result in a more uniform distribution of elements in the casting. This leads to a reduction in carbide formation tendency, as the distance between nodules will be smaller, hence there is less opportunity for segregation to occur [35]. Some quantitative line scan measurements made between nodules spaced different distances apart in two alloys are shown in figure 2.9 [38]. As can be seen in the figure, the severity of the segregation is shown to increase with a reduction in nodule count for both alloys.

Figure 2.9. Quantitative line scan measurements made between nodules spaced different distances apart in two alloys [38].
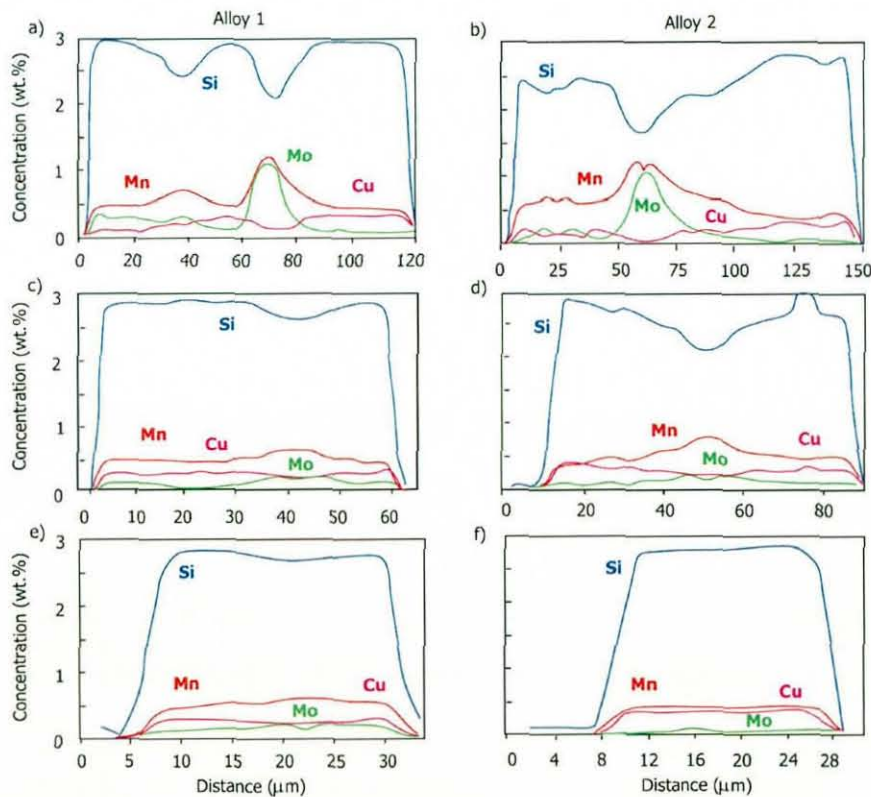
Increasing the carbon equivalent value (C.E.V) of the alloy also increases the spheroid count. The C.E.V is the amount of carbon in the alloy plus the amount of carbon equivalent of the added elements (all wt.%) [2].

$$C.E.V = \%C + 0.32\%Si + 0.33\%P \qquad\qquad [2.5]$$

A minimum C.E.V of 4.3 is accepted as the prerequisite for a good spheroid quantity and a carbide free structure. Too high a C.E.V can result in spheroid degeneracy and too low a level results in a low graphitizing potential [2].

The graphite nodules in ADI change little through either the austenitisation or the austempering of the ADI alloys. During austenitisation some carbon may however diffuse out of the graphite nodules and dissolve into the surrounding austenite enriching it with carbon. The extent of this carbon diffusion depends on the phase stability of the graphite as a function of temperature. This relationship is shown in figure 2.10 in the multicomponent phase diagram.

Figure 2.10. A multicomponent phase diagram for an ADI alloy [20].
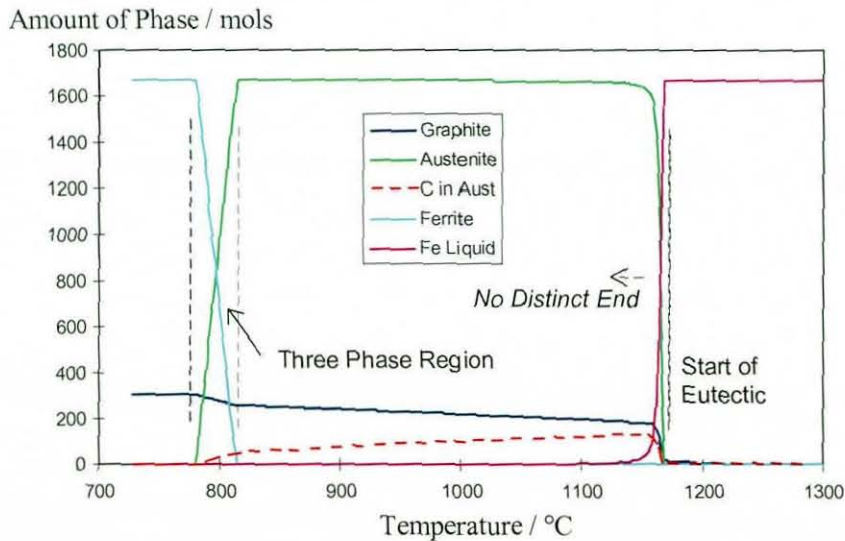
As the temperature falls the amount of graphite increases slightly, as the solubility of carbon in the austenite matrix decreases. The distribution of the graphite can also have an effect on the transformation kinetics of the austempering phase of the heat treatment and the mechanical properties of the alloy. A low graphite nodule density leads to greater alloying element segregation in the areas between the nodules and the possibility of a delayed phase transformation to bainitic ferrite [15]. This effect is generally overcome as the austempering reaction proceeds.

2.3.4 Carbides

Carbide formation in ADI can occur especially at lower austempering temperatures, but is also dependent on the alloy composition and transformation times [39,40]. Carbides in ADI are generally based on iron. At early transformation times essentially two phases exist in the microstructure, bainitic ferrite and high carbon austenite. At longer austempering times after the growth of bainitic ferrite and the high carbon austenite has stopped the high carbon austenite will decompose to form the equilibrium product of ferrite and carbides.

Carbides may also form during the initial solidification of the casting [9]. These are known as primary carbides, and tend to occur in the last liquid to solidify approximately halfway between the graphite nodules [9]. If the graphite nodule count in an ADI alloy is low, a greater degree of segregation of alloying elements will occur in the areas between the nodules, and this increases the probability of carbides forming in these segregated areas of the matrix. It has been observed that very little of this carbide phase is removed during a low temperature austenitisation heat treatment, and hence the resulting ADI alloys show decreased elongation values [41]. Studies on high manganese ADI alloys have shown that due to segregation of manganese during solidification the precipitation of a carbides containing Fe, Mn, Si and Cr with a metal to C ratio of 2.5-2.9 are possible [42]. Some carbides found in ADI alloys are summarised in table 2.1 below.

Table 2.1. Carbides found in ADI alloys.

Precipitate	Formula	Structure	Reference
θ-carbide (Cementite)	Fe_3C	Orthorhombic	43,30
ε-carbide	$Fe_{2.4}C$	Orthorhombic	30,39
η-carbide	Fe_2C	Orthorhombic	44,30
χ-carbide (Hägg)	Fe_5C_2	Monoclinic	43,44, 45
Titanium carbide	Ti_2C_2SP	Unknown	42
Eutectic carbide	$(Fe, Mn, Si, Cr,)_{2.5-2.9}C$	Orthorhombic	42

2.3.5 Martensite

Martensite forms from austenite by a sudden shear process without a change in chemical composition [2]. This process is generally triggered by rapid cooling, but can also be induced by the application of stress. The metastable austenite is rapidly cooled and reaches the martensite start temperature (M_s), before any bainite or pearlite formation occurs. The shear transformation of the fcc austenite results in a new body centred tetragonal (bct) structure. The carbon that was in solid solution in the austenite remains in solid solution in the bct structure. Each austenite grain transforms by this sudden shear process into laths of martensite. An orientation relationship exists between the new laths and the austenite [2]. The temperature range in which the reaction occurs can be precisely defined for a particular alloy. The reaction commences once the metastable austenite reaches the M_s temperature and finishes at the martensite finish temperature M_f [33]. At the M_f temperature all the metastable austenite should have transformed to martensite. However, in practice a small proportion of the austenite phase, known as retained austenite does not transform [33]. If the M_f temperature is well below room temperature, as occurs in alloys with a large proportion of alloying elements, a large volume of austenite can be retained [33].

Martensite is generally regarded as an unwanted phase in ADI. The martensite in ADI is not identical to that which forms in steels. The difference is the martensite in ADI can have a carbon concentration as high as 1.6 wt.%, compared to 0.8 wt.% maximum for steels. This makes ADI martensite much harder, and as a result, very difficult or almost impossible to machine. The hard martensite will wear the tools out in seconds, so these parts are machined by grinding only. Martensite is also particularly detrimental to the mechanical properties of ADI if it forms a continuous path in the matrix [15].

Martensite formation in ADI alloys is usually a result of unsuitable heat treatments or compositions. Martensite can form from the untransformed austenite volume (UAV) areas in the matrix during the fast cooling from the austempering temperature. The UAV is austenite that has a low carbon concentration. It forms in the microstructure as a result of a poor austempering heat treatment that has not been performed for a long enough time period or as a result of segregation of alloying elements, which slow the local transformation rate. Carbon levels in some

areas of austenite will not have had enough time to reach adequate levels for the prevention of martensite formation on cooling, and hence these areas of the microstructure may transform to martensite. Increasing the austempering time favours the redistribution of carbon in austenite and hence impairs the formation of marternsite [46].

2.3.6 Pearlite

Pearlite is a lamellar product of eutectoid decomposition found in steels and various other alloys such as ADI [3]. It comprises of multiple colonies of parallel lamellae, which are orientated in a different direction to adjacent colonies. Pearlite can nucleate on austenite grain boundaries, or on ferrite or cementite depending on the composition and transformation temperature and then grow with a roughly constant radial velocity [3,33].

The first stage in the formation of pearlite is the nucleation of either cementite or ferrite on the austenite grain boundaries. The phase that nucleates first depends on the grain boundary structure and composition [33]. If cementite is the first phase to nucleate it will try to minimise its free energy by forming with an orientation to the austenite grains. The surrounding austenite will be depleted of carbon increasing the driving force for it to transform to ferrite, hence a ferrite nucleus will form adjacent to the nucleus of cementite with the same orientation [33]. Carbon rejected from the growing ferrite travels through the austenite to the front of the growing cementite [33]. A redistribution of other alloying elements also occurs at or near the reaction front [3]. The growth continues and a lamellar structure results which is in contact with austenite [33]. It can be seen therefore that the formation of pearlite requires the cooperative growth of ferrite and cementite to form the pearlite lamellae [3,33]. In some cases this cooperation does not become established and the ferrite and cementite grow in a non-lamellar manner producing degenerate pearlite [33].

The rate of transformation depends on the nucleation rate of the pearlite nodules and their subsequent growth rate [3]. The nucleation rate is structure sensitive and is influenced by austenite grain size and impurities [3]. At temperatures just below A_1, the degree of undercooling is small and therefore pearlite growth is slow. As the temperature reduces further, the undercooling increases, hence the

driving force for the pearlite nucleation increases and therefore the growth rate increases, reaching a maximum at the nose of the time temperature transformation (TTT) curve. Below the nose of the TTT curve as the temperature drops further, diffusion becomes more difficult and therefore the growth rate slows [2].

Pearlite is detrimental to the strength of ADI. The most significant effect of the presence of pearlite in the microstructure is a reduction in the ductility of the ADI alloy. The ultimate tensile strength, 0.2% proof strength, impact energy and hardness also reduce as the amount of pearlite increases in the microstructure of ADI alloys[17]. Additions of Mo, Mn, Ni and Cu are added to ADI alloys in order to increase their hardenability, and hence suppress pearlite formation [17]. Pearlite in ADI forms when the pearlite promoting and/or stabilising elements segregate into areas around the graphite nodules. Hence any pearlite formation in ADI is normally found around the graphite nodules. If pearlite forms, it will occur during the continuous cooling of a casting from the austenitisation temperature to the austempering temperature. Consequently it forms initially in the centre of the component, then in any localised hot spots and finally formation of pearlite will occur on the outside of the casting [17]. Pearlite also tends to form after longer austempering times as described in section 2.5.2.

2.4 Alloying Additions

Alloying additions in ADI are needed for a number of reasons. They must give the casting adequate hardenability, produce a high count of uniformly shaped graphite nodules, counteract the effects of element segregation, and produce a sufficiently wide processing window, as will be discussed in section 2.6.3 [2].

2.4.1 Carbon

There has to be sufficient carbon in the alloy to enable both the formation of graphite nodules and allow the matrix of the alloy to be saturated with carbon during the austenitisation heat treatment. The latter will result in the formation of bainitic

ferrite on quenching to the austempering temperature and hence diffusion of the carbon will occur during austempering, enriching the austenite with carbon. The result is the production of the high carbon austenite phase during austempering, which is one of the phases that gives ADI its combination of excellent properties. The carbon in ADI can also form a variety of carbides, as shown in section 2.3.4. A typical ADI alloy contains 3.5 wt.% C. Increasing the carbon content lowers the strength, due to the fact that more of the weak graphite phase will be bearing load [2]. However, little change in hardness or elongation to failure is observed.

2.4.2 Silicon

Silicon is needed in quantities greater than 2 wt.% in order to obtain graphite instead of iron carbide during the solidification of ADI [32]. It increases the graphitisation potential of cast iron alloys strongly [2]. It is also present in large quantities in ADI alloys to prevent the formation of carbides in the bainitic ferrite phase. It tends to segregate towards the graphite nodules because it is one of the first elements to solidify in the first solid to form. Silicon also promotes the stability of the metastable phases of austenite and bainitic ferrite [32]. As the silicon content increases, yield strength decreases and ductility increases [2]. It has also been shown to counteract the deleterious effects of manganese.

2.4.3 Manganese

Additions of manganese can offset the segregation effects that high nickel contents produce in ADI alloys [47]. The segregation effects of a number of different alloying elements are shown in figure 2.9a and b, in which it can be seen that Si and Mn behave in opposite ways. The lines on the figure were taken along a path between two graphite nodules in the matrix of an ADI specimen. The effects of segregation can clearly be seen for manganese and some other elements. Manganese itself tends to segregate and is found in higher quantities in the last solid to form [22]. Manganese also increases the hardenability of ADI by slowing down the

nucleation and growth rates of ferrite needles in the microstructure, therefore delaying the austempering reaction [37]. Hence during the austempering reaction in segregated areas that contain high manganese levels, the austenite may not contain enough carbon to prevent it transforming to martensite on cooling from the austempering temperature. It is also a strong carbide former and therefore easily promotes the formation of carbides in the matrix, especially in segregated areas [2]. Therefore, it can be seen that the manganese levels must be carefully controlled or it can have a serious effect on the mechanical properties of the alloy. Its levels should therefore be kept below 0.25 wt.% [2]. Manganese also reduces the graphitisation potential of cast iron alloys [2].

2.4.4 Molybdenum

The hardenability of ADI is enhanced by the addition of molybdenum, which delays the formation of the undesirable pearlite phase in the ADI microstructure [47]. It is the single most effective element at increasing the hardenability of ADI alloys. This effect can also be increased because molybdenum combines synergistically with copper, nickel and chromium to enhance hardenability [2]. It also slows down the bainitic transformation. This element is often found in higher quantities in the last solid to form, which can lead to problems in processing and also increases the likelihood of formation of primary molybdenum carbides in the last solid to form [22]. It has been observed that increasing the molybdenum content in an ADI alloy leads to an increase in the amount and continuity of carbide at the intercellular boundaries [41]. It can also have a detrimental effect on the microstructure by disturbing the delicate equilibrium between additions of manganese and nickel in the matrix [47]. Molybdenum also reduces the graphitisation potential of cast iron alloys [2]. Tensile strength, hardness and elongation all fall progressively as molybdenum content is increased [2]. Hence molybdenum quantities must be limited to no greater than 0.3 wt.% because of its strong segregation and carbide forming tendencies [2].

2.4.5 Nickel

Nickel is a common alloying element in ADI and is primarily used due to its superior effect on structure, ease of addition and absence of carbide formation characteristics. Nickel also slows down the bainite transformation and in high concentrations can limit the formation of bainitic carbides [47]. Nickel has also been reported to shift down the transformation temperature range, hence influence the morphology of the bainitic ferrite phase [47]. A high nickel content causes differences in the rates of bainitic ferrite transformation at different locations in the austenite phase, due to segregation. Therefore, nickel should be added along with an element that compensates for this segregation such as manganese. Hence, a more uniform bainitic ferrite microstructure can be obtained throughout the austenite matrix [47]. Nickel also increases the graphitisation potential of cast iron alloys [2]. It has been reported that for nickel contents of over 1 wt.% tensile strength and elongation both reduce [2]. Nickel tends to segregate towards the graphite nodules in ductile iron alloys [7;48].

2.4.6 Copper

Copper is primarily added to ADI to promote hardenability, and combines well with molybdenum to increase this effect. The improved hardenability suppresses the formation of pearlite in the microstructure and also increases the size of the processing window (see section 2.5.3), which is the stage during the austempering heat treatment where the properties of ADI are most attractive to the engineer [47]. It also promotes the formation of graphite in a similar, but less potent manner as silicon[2]. Elongation increases progressively as copper levels increase. It has also been suggested that copper may suppress the formation of carbides in lower bainite, which would account for the increased effect copper has on ductility [2].

2.4.7 Magnesium

Magnesium additions are important for ADI alloys as they act to promote the formation of spheroidal graphite in the ADI matrix, instead of other graphite morphologies [2]. However, additions of greater than 0.1 wt.% can be detrimental because these high levels can result in intercellular flakes or flake projections from the graphite spheroids, which reduces the mechanical properties of the alloy [2].

2.4.8 Others

Other alloying elements that are found in smaller quantities or are less frequently added to ADI alloys. These include small quantities of phosphorous, sulphur, chromium, tin, titanium and aluminium. Sulphur causes graphite to grow with a flake morphology, so desulphurisation techniques are need to be performed to obtain low sulphur contents of ADI alloys [1]. Tin is an excellent pearlite promoting element [2]. Titanium, chromium, sulphur and phosphorous have also been found as elements in carbides and phosphides in the ADI microstructure [20]. The major influences of alloying additions to ADI alloys are summarised in table 2.2 below.

Table 2.2. Influence of alloying additions on ADI alloys.

Element	Carbide Promoting?	Pearlite Promoting?	Segregate Towards?	Comments	Ref.
C	✓	✗		Needed for graphite formation	2
Si	✗	✓	Nodules	Promotes graphite, suppresses carbides	2,22, 32
Mn	✓	✗	Between Nodules	Offsets nickel content	2,32, 47
Mo	✓	✗	Between Nodules	Potent austenite stabiliser	2,32, 47
Ni	✗	✓	Nodules	Shifts down transformation temperatures	7,47, 48
Cu	✗	✗	Nodules	Promotes graphite	47,23
Mg	✗		Between Nodules	Needed for spheroidal graphite inoculation	2
Cr	✓	✗	Between Nodules	Strong carbide former	2,47

Additions of various alloying elements are known to influence the stable and metastable eutectic temperatures in different ways as shown in figure 2.11. Graphitizing elements such as Si increase the graphite eutectic temperatures and decrease the carbide eutectic temperature, whilst elements that stabilise carbide such as Cr have the opposite effect. Some elements also influence the chill depth in cast irons [2]. V and Cr, are known to increase the chill depth, whereas Si and Ni have the opposite effect.

Figure 2.11. The influence of alloying additions on the eutectic temperatures [2].
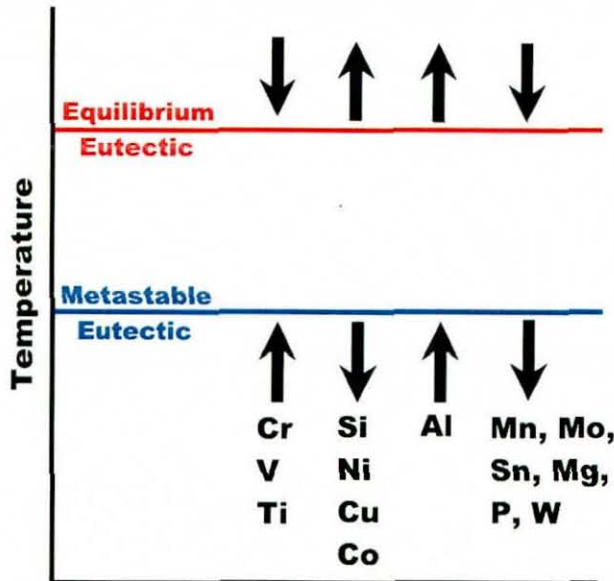
2.5 Austenitisation

The austenitisation heat treatment is carried out in the austenite phase field normally at temperatures between 850-950°C [14,15], but temperatures as high as 1000°C [49] have been used. It is held at these temperatures for between 1-4 hours. As the cast bcc ferrite and pearlite component is heated to these temperatures the matrix transforms to fcc austenite. At higher austenitisation temperatures more austenite will be produced and at a higher rate [9]. This austenite will also have a higher concentration of carbon if it is austenitised at a higher temperature and the saturation level for carbon will be higher, as seen in the Fe-C equilibrium diagram in

figure 2.12, due to the high temperature equilibrium between austenite and graphite. The austenite grain size also increase with austenitisation temperature [26]. However, as the austenitisation temperature increases, it has been found that the stage one reaction of the austempering process (see section 2.6.1) is delayed and the processing window narrows (see section 2.6.3), hence increasing the risk of producing ADI components that do not satisfy ASTM standards [41].

Figure 2.12. Fe-C binary equilibrium phase diagram [50].
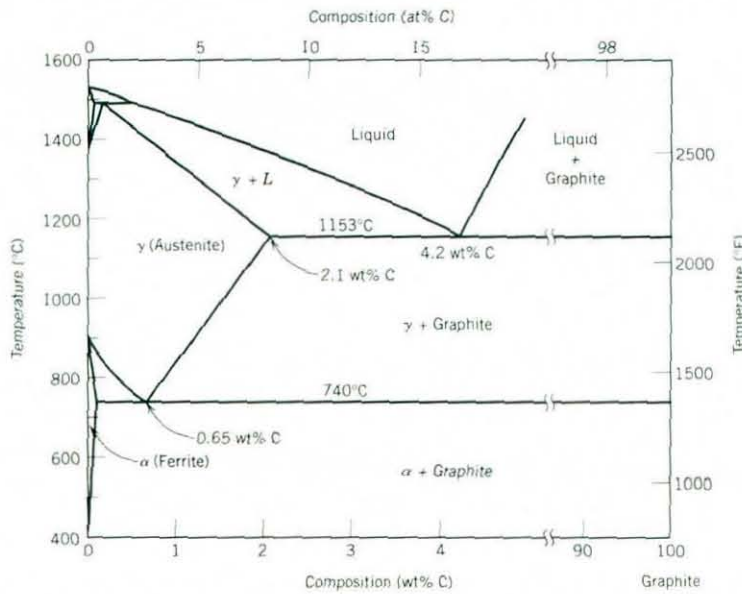
Darwish and Elliot [51] report that increasing the austenitisation temperature of low manganese ADI alloys has four effects:

- A coarser austempered structure is produced, with the length of the bainitic ferrite plates which corresponds closely to the austenite grain size increasing, and their number and uniformity of distribution decreasing.

- An increase in the volume fraction of retained austenite is produced.

- It leads to the formation of two types of retained austenite. A film which forms in between adjacent bainitic ferrite plates forms at low temperatures and a blocky type (the proportion of which increases with increasing austenitisation temperature) with austenite surrounded by bainitic ferrite growing in different directions.

- It enhances the formation of martensite in intercellular regions and in the centre of the blocky austenite.

The actual carbon concentration in the austenite increases with austenitisation time until the saturation equilibrium level is reached. Increasing the carbon content of the austenite during austenitisation also decreases the driving force for austenite to transform to bainitic ferrite during austempering, and reduces the likelihood of martensite formation on quenching to the austempering temperature.

The austenitisation heat treatment requires a significant time to generate a uniform matrix carbon concentration. It has been a general rule of thumb that two hours for a typical component size of 40-60 mm is needed at the austenitisation temperature for this goal to be reached [17]. At austenitisation times of less than two hours, an incomplete transformation to austenite may occur with large amounts of ferrite remaining in the matrix, or carbon gradients which are left in the austenite, dependent on component size.

After the austenitisation heat treatment the specimen is quenched to the austempering temperature. The rate of the quenching affects the structure of the matrix at the austempering temperature. If the quenching of the casting is too slow then pearlite may be produced. This is of particular importance in castings with large sections as the centre of the casting may cool at considerably slower rates than the surface of the casting producing a pearlite core in the cast. To help overcome this additions of Mn of Mo are added to the composition of the ADI to reduce the rate of pearlite formation by increasing the alloy hardenability. Increasing the austenitisation temperature has also been found to increase the hardenability of ADI alloys and hence limit the formation of martensite [17,41]. However, this slows the rate of austempering and increases the probability of non uniform austempered microstructure that could contain martensite when it is cooled to room temperature[49].

2.6 Austempering

During this stage of the heat treatment of ADI alloys, the bainitic ferrite, high carbon austenite and possibly carbides are produced [17]. Austempering is typically

carried out at temperatures ranging from 260-440°C [49,52] although temperatures between 300-400°C are most common [17,23,53]. Austempering times can vary from 5-600 minutes depending on the austenitisation and austempering temperatures and alloy composition [53,54]. In order to avoid the formation of martensite on cooling after austempering, enough time has to be given for the austenite present to have a carbon content high enough to give a M_s temperature below room temperature [22]. The austenite carbon content should also be high enough to ensure the austenite is mechanically stable at room temperature [24].

Low austempering temperatures promote high strength. This is due to a combination of factors. Less retained austenite is produced during austempering but it contains a high carbon content. The low austempering temperature also produces a fine bainitic ferrite phase with a small lath size. The small lath size and high carbon content in the matrix austenite increase the strength of the alloy. Alternatively, a high austempering temperature produces an ADI with good ductility. When austempered, more retained austenite is found in the matrix so the alloy is weaker, but more ductile due to the greater volume fraction of the ductile austenite phase. The high austempering temperature also facilitates the production of coarse upper bainitic ferrite, which is more ductile but lower in strength than bainitic ferrite that forms at low temperatures. These two factors combine to produce a weaker but more ductile alloy.

Austempering is often considered to happen in two stages. In stage one, the formation of bainitic ferrite and high carbon austenite are the main transformations. During stage two, the high carbon austenite decomposes to ferrite and carbides. Figure 2.13 shows the amount of each phase present in the microstructure during the two stages of austempering for two different austempering temperatures. After the austempering heat treatment the ADI alloy is quenched to room temperature. If the combination of alloy composition and heat treatment was optimised, the alloy will contain no martensite and few carbides and hence have a combination of high strength and good ductility.

2.6.1 Stage 1

After quenching to the austempering temperature stage one begins. During stage one the metastable austenite transforms to bainitic ferrite. Ferrite nucleates

and then grows on the graphite/austenite interface, or at austenite grain boundaries [9]. During this transformation carbon is rejected from the bainitic ferrite into the austenite. As the stage 1 reaction progresses, the volume fraction of reacted austenite increases, as it receives carbon that is rejected from the bainitic ferrite. Hence, the volume fraction of untransformed austenite decreases. The carbon level of the reacted austenite continues to increase as the reaction progresses [41]. The carbon the austenite receives increases its stability, causing the martensite start temperature to fall below room temperature [37]. At lower austempering temperatures it is generally observed that the formation of carbides during stage one is possible, as shown in figure 2.13b. This carbide formation however is so sluggish that the austenite will have had enough time to be enriched by carbon diffusion to substantial values [22].

Figure 2.13. Schematic diagram of the microstructural changes that occur during austempering at a) high temperatures and b) low temperatures.

a) High Austempering Temperature (> 350 °C)

b) Low Austempering Temperature (< 350 °C)
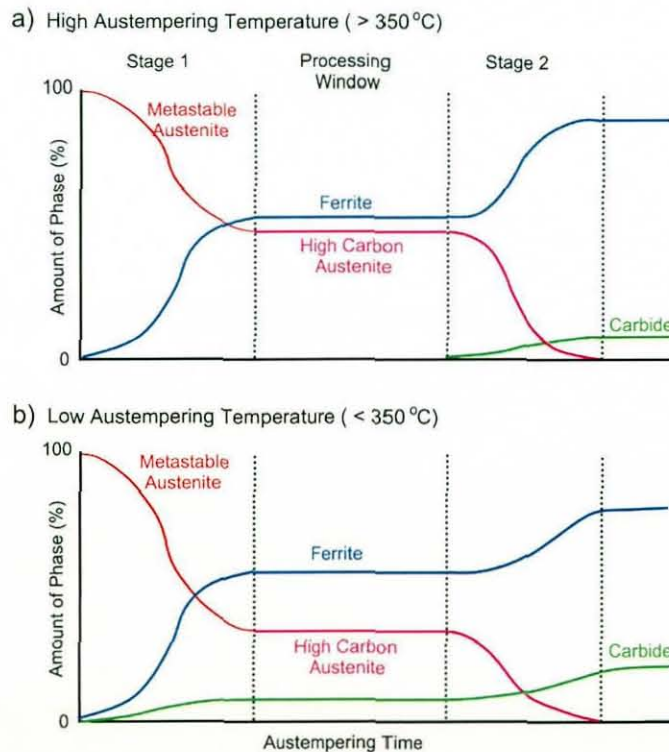
Towards the end of the stage one reaction the bainitic ferrite growth will slow, and then eventually stop and hence the diffusion of carbon into the surrounding austenite also ceases. The reaction stops because the austenite is enriched with

carbon to such a level that it becomes thermodynamically impossible for the reaction to proceed. This is the point where stage one of the austempering reaction ends. The optimum mechanical properties of ADI are observed at the end of the stage one reaction when the level of high carbon reacted austenite is at a maximum [2;15;22]. This austenite is known as retained austenite because it remains stable on cooling to room temperature. Alloying additions delay the stage 1 reaction and the time for stage 1 completion increases with decreasing austempering temperature [15].

The rate of the stage one reaction is influenced by alloy composition, and the austempering and austenitisation temperatures. At a given austempering temperature as shown in figure 2.14, the stage one reaction rate is controlled largely by the difference in the carbon content between the high carbon reacted austenite C^S_γ, and the original austenite content C^0_γ. This difference (ΔC, shown for a low austenitisation temperature, T^γ_1 in figure 2.14), is a function of austenitising temperature, as alloys austenitised at a higher temperature will have a higher C^0_γ. The thermodynamic driving force for the stage one reaction (ΔG_I) is proportional to $C^S_\gamma - C^0_\gamma$ or ΔC [55]. It can be seen in figure 2.14 that either alloying additions or austenitisation temperature variations that reduce C^0_γ effectively increase the chemical driving force for the stage one reaction. This in turn increases the rate of the stage one reaction. In addition, reducing the Si level or increasing the amount of Mn in the alloy increases C^0_γ, so that the rate of the stage 1 reaction decreases [55].

Therefore, large additions of Mn result in a large decrease in the driving force for the stage one reaction. This element also segregates strongly into the last liquid to solidify in the melt. The results of this can be detrimental for the mechanical properties of the alloy as the last liquid to solidify may have no driving force to transform and hence the austenite will remain unreacted. Because of the low carbon content of this austenite, it may transform to martensite on cooling to room temperature, hence the mechanical properties of the alloy will be poor [55].

Figure 2.14. Schematic free energy-composition diagram [55].
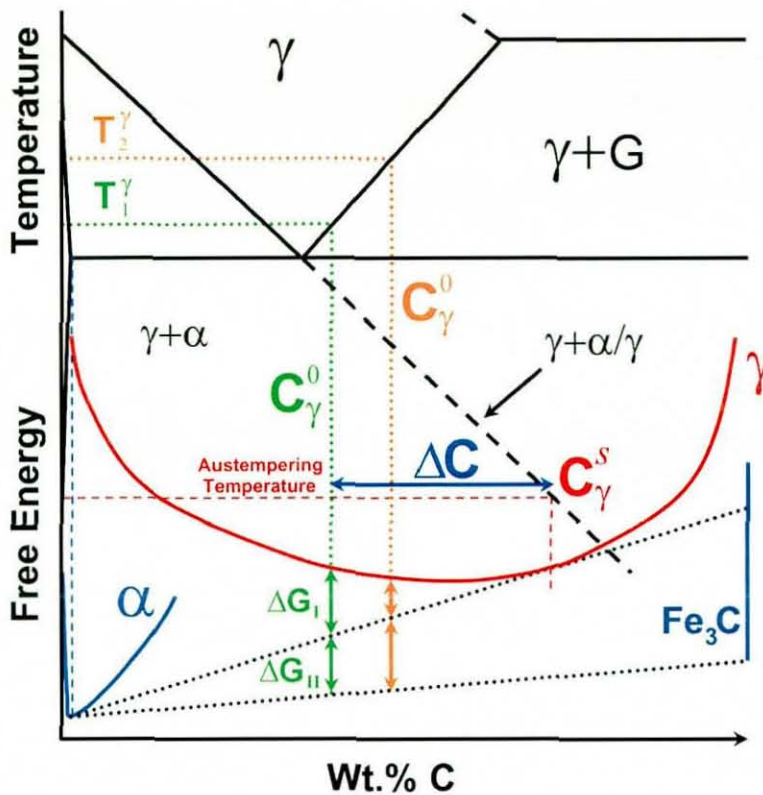
2.6.2 Stage 2

After stage one has ended stage two begins. During stage two the high carbon austenite decomposes to the equilibrium phases of ferrite and carbide. As with stage one, the rate of the decomposition reaction is dependent on the austempering temperature and the alloy composition. The stage 2 reaction is very rapid at high austempering temperatures [15]. Hence it can be seen that the amount of high carbon austenite increases to a maximum at the end of stage one and then decreases during stage two.

2.6.3 Processing window

The processing window can be seen in figure 2.13. It is the area on the diagram between stages 1 and 2 where the volume fractions of high carbon austenite

and bainitic ferrite are constant. The processing window defines the austempering time interval over which the austemperered ADI alloy satisfies ASTM standard A897: 1990 for ADI [56]. The start of the window has been defined as the time required for the unreacted austenite volume to decrease to 3%. The end of the processing window is defined as the austempering time at which the volume of reacted austenite has decreased to 90% of its maximum value [41].

Although austempering has been described as two different reactions, the stage two reaction can often start before the stage one reaction is complete as different areas of the microstructure undergo these reactions at different rates [15]. This effect is largest in ADI with high segregation levels, or in components with large cross sections. This overlap results in closure of the processing window. During the time interval of the processing window, the stable microstructure of the high carbon reacted austenite and bainitic ferrite results in the production of ADI alloys with optimum mechanical properties [2;15;22]. If a combination of severe microstructural segregation and rapid stage 1 austempering kinetics occur, the processing window may be closed for some alloys, hence optimum mechanical properties are not reached.

2.7 Mechanical Properties of ADI Alloys

The outstanding mechanical properties of ADI stem from the presence and continuity of the fcc austenite matrix [9]. The most important and unique characteristic of these materials is their excellent ductility and high strength. The mechanical properties of ADI are at optimum levels at the end of stage one of the austempering reaction [2;15;22]. For a given composition, the austenitisation temperature and time have some effect on mechanical properties, but the austempering temperature and time have the major effect [18]. At low austempering temperatures, lower bainitic ferrite is formed producing bainitic ferrite possibly with very fine carbides. These alloys have a high hardness (up to 480 HB), can be very strong with an ultimate tensile strength (UTS) ranging from 1200-1600 MPa, but only have limited ductility.

At high austempering temperatures, upper bainite is formed, which consists of a feathery carbide free bainitic ferrite distribute in high carbon austenite. These alloys have a lower hardness (280-320 HB), and an UTS ranging from 850-1050 MPa.

Their ductility values are considerably higher ranging from 5-16%. At intermediate austempering temperatures an intermediate microstructure between upper and lower bainitic ferrite exists. These alloys have an UTS ranging from 950-1250 MPa and a ductility of between 3-6%. The mechanical properties of some national standard ADI alloys are shown in table 2.3.

Table 2.3. National standards for ADI [10].

Grade	Minimum Yield Strength (MPa)	Minimum Tensile Strength (MPa)	Minimum Elongation (%)	Minimum Unnothched Charpy Value, (J)	Typical Brinell Hardness (HB)
Grades of ADI Proposed by BCIRA in 1986					
ADI 950/6	697	950	6		
ADI 1050/3	792	1050	3		
ADI 1200/1	947	1200	1		
Grades to ASTM Standard A897M-90 (metric)					
850/550/10	550	850	10	100	269-321
1050/700/7	700	1050	7	80	302-363
1200/850/4	850	1200	4	60	341-444
1400/1100/1	1100	1400	1	35	388-477
1600/1300/-	1300	1600	-	-	444-555
Grades to Japanese Standard JIS G 5503					
FDC 900A	600	900	8		-
FDC 1000A	700	100	5		-
FDC 1200A	900	1200	2		340
Grades to VDG Standard W52					
GGG-80B	500	800	6-15		250-310
GGG-90B	600	900	5-12		270-340
GGG-120B	950	1200	2-5		330-390
GGG-140B	1200	1400	1-2		43-47 HRC
GGG-150B	-	1500	-		45-51 HRC
Proposed SIS Grades of ADI (Sweden)					
	600	900	8		280-320
	1200	1400	1		45 HRC

Alloying additions can also affect the mechanical properties of ADI as shown by Moore, Rouns and Rundman [9]. They found that increasing the amount of manganese and molybdenum in an alloy reduced ductility. The formation of UAV is

thought to be responsible. Increasing the austenitisation temperature was also shown to have the same effect. The continuity of the austenite matrix through the microstructure is important for the mechanical properties of ADI as discussed previously. Ways in which this continuity can be broken are numerous in cast iron alloys and include shrinkage, slag inclusions and segregation of the alloying elements [9]. All of these defects are located predominately in the last solid to form so may form a continuous volume throughout the material. It is obvious that these effects will be detrimental to the mechanical properties of the alloy.

2.8 Chill-Cast Iron

The wear resistance of materials used for engine components such as gears or camshafts is an important property for such applications. The combination of excellent wear resistance and relatively straightforward manufacturing make chill-cast iron a viable material for these applications [57]. Upon cooling, as previously discussed, two modes of solidification exist for cast irons; the iron-graphite eutectic reaction or the iron-iron carbide reaction. The former gives grey iron structures, whilst the latter results in white iron formation [57]. These two reactions occur at different temperatures depending on the chemical composition. For example adding 2 wt.% Si to the iron increases the temperature difference between the two reactions, permitting a larger undercooling to be tolerated and hence more time for graphite nucleation and growth before white iron formation occurs [1]. Inoculants such as FeSi or a reduced cooling rate also promote graphite formation. A high carbon equivalent also encourages the growth of the graphite eutectic [1]. Carbide stabilising elements like chromium can have the opposite effect, raising the iron-iron carbide eutectic temperature, and hence making white iron formation more likely [57].

Chill-cast iron is produced by locally increasing the cooling rate of the solidifying alloy to very high rates by placing metal implants in the mould. This results in there being insufficient time for carbon diffusion towards graphite nucleation sites to take place, hence the liquid undercools below the iron-iron carbide eutectic temperature, forming white iron [57]. As solidification proceeds through the casting, the rate of cooling below the surface reduces at a rate depending on the thermal

properties of the solidified layer. If the casting is thick enough, it will slow down to less than that required too maintain undercooling below the white iron eutectic, and hence a transition to iron-graphite eutectic reaction occurs [57]. The resulting component will have hard wear resistant chilled surface areas close to the mould chill implants and ductile grey iron away from these areas. Hence, localised hardening of important component areas such as lobes on camshafts or teeth on gear wheels can be obtained.

Further improvements to chill-cast iron have also been made by performing austenitisation and austempering heat treatments on alloys of ADI composition. This material is known as chill-cast ADI. The graphite has a spheroidal morphology as a result of the ADI alloy composition, hence spheroidal graphite iron and not grey iron is produced on solidification. The chill implants in the mould have the same influence as with the grey iron, producing a hard wear resistant white iron chilled layer. However, the mechanical properties of the spheroidal graphite iron areas of the component are increased using the same two heat treatments as normal ADI alloys undergo. The austenitisation heat treatment temperature and time are selected in order that the carbides in the chilled surface layers are not dissolved into the austenite. Hence, the advantages of the hard wear resistant chilled surface remain in the alloy, whilst the mechanical properties of the spheroidal graphite iron areas of the component are improved as they are transformed to ADI by the austenitisation and austempering heat treatments. However due to the high hardness of these materials, machining of chilled components can be an extremely difficult process. The alloys are also very brittle and may crack on subsequent heat treatment.

2.9 Ausformed ADI

A mechanical deformation treatment performed before the austempering heat treatment has been found to improve the microstructure of some ADI alloys [55]. The process, known as ausforming is added to the conventional two stage heat treatment of ADI alloys. The mechanical deformation, which is performed after the specimen has been cooled to the austempering temperature results in dislocation formation in the materials. The resulting strain in the alloy produces an extra mechanical driving

force in addition to the chemical driving force and hence increases the rate of the stage one reaction [55].

The result of this faster transformation is a much finer microstructure. Furthermore, since the deformation takes place uniformly throughout the microstructure, the increased driving force for the transformation is expected to occur uniformly throughout the microstructure [31]. It can therefore help to offset the effects of segregation by increasing the driving force for transformation of segregated areas in ADI alloy microstructures. However, this effect has only been observed in specimens austempered at low austempering temperatures (288-375°C) [31,55]. As the austempering temperature is increased (425°C) the ausforming produces no increase in the stage 1 reaction rate [55]. The ductility, yield strength and tensile strength have all been shown to increase if the ausforming treatment is performed prior to the austempering heat treatment [31]. The combination of an increase in the strength and ductility of these alloys is thought to result from the greater uniformity of the austempered microstructure, which is a direct result of the ausforming process [31].

2.10 Summary

The different member materials of the cast iron family have been introduced. Attention has been paid to ductile irons and in particular the material known as austempered ductile iron (ADI), which is produced after a two stage austenitisation and austempering heat treatment. The solidification behaviour of ductile iron alloys has been discussed. The different phases that are found in ADI alloys, typically graphite nodules, austenite and bainitic ferrite, but also carbides, pearlite and martensite, have been examined in respects of their nucleation and growth, and morphology. The influence of the major alloying additions on the microstructure and their segregation behaviour was also highlighted. The transformation kinetics, temperatures and times of the austenitisation and austempering heat treatments have also been discussed, as well as their influence on the final alloy microstructure. Attention has also been drawn to the problems faced by alloy designers and heat treaters in combating the effect of alloying element segregation, which can slow transformation rates, resulting in alloys being produced with below optimum mechanical properties. Finally, two modifications to the production of ADI alloys have

been discussed. Chilled ADI can be used to produce alloys with extremely hard and wear resistant layers, whilst ausformed ADI alloys have been shown to possess more uniform and superior mechanical properties as a result of a deformation process prior to austempering.

3 MTDATA Introduction

and Database Testing

3.1 Introduction to Thermodynamic Modelling

Phase diagrams have been used for many years to help predict thermodynamic equilibria in systems and therefore improve the understanding of metallurgical problems. Recently, several computer software programs have been produced that make this task easier. Commercially available software packages have now been developed, which using critically assessed thermodynamic data, can predict the phase equilibria of multi-component systems given the system composition, temperature and pressure. One such package, known as MTDATA, is used extensively in this work [58,59]. The present chapter outlines what MTDATA is, describes how it functions and validates the accuracy of the databases it uses by comparing predictions to experimentally determined phase diagrams.

3.2 Thermodynamic Basis of MTDATA

MTDATA is a computer program that predicts the phases present at thermodynamic equilibria in multi-component systems. It is based upon critically assessed thermodynamic data and uses an exceptionally reliable Gibbs free energy minimisation algorithm to perform the calculations [60]. The function that decides whether a process is thermodynamically favoured is the Gibbs free energy change, ΔG, which at constant pressure and at a given temperature is:

$$\Delta G = \Delta H - T\Delta S \qquad [3.1]$$

ΔH and ΔS are the changes in enthalpy and entropy of the components in the system and T is the temperature (K). For a reaction to proceed, ΔG must be negative. Equation 3.1 represents the driving force for equilibrium in systems. A reaction will only proceed if the product(s) have a lower free energy than the reactants.

The Gibbs energy of all solution phases is defined by the following equation[61]:

$$G = G^0 + G_{MIX} + G^{XS} \qquad [3.2]$$

This simple equation is the fundamental relationship that MTDATA uses to minimise the free energy of a system and hence, calculate equilibrium in systems. G^0 is the contribution of the pure components of a phase to the Gibbs free energy of that phase. This is simply the Gibbs energy of the species in its stable state. For example, water is liquid at 298K, so at this temperature, G^0 will be the free energy of water. The second term represents the mixing contribution to the free energy of the phase. This term defines the entropy and enthalpy change on mixing of two or more species in the phase, but does not account for any interactions that may occur between the species. The last term G^{XS}, corresponds to the contribution to the free energy of the system from non-ideal interactions between components. In reality, attractive and repulsive interactions exist between atoms in phases, and this term accounts for these interactions. This term is also known as the excess Gibbs energy of mixing.

Equation 3.2 can be written in the more general form [61]:

$$G = \sum_i x_i G_i^0 + RT \sum_i x_i \ln x_i + \Delta G^{xs} \qquad [3.3]$$

where x_i is the mole fraction of component i, ΔG^{XS} is the excess Gibbs energy of mixing and R is the gas constant. To enable the thermodynamic modelling of multi-component systems, suitable expressions have been derived for the excess Gibbs energy for different types of solution phases. The model which is most applicable to the solution phases found in ADI alloys is the sublattice model [61]. The model is very versatile and can be used for intermetallics and alloy systems, where component interactions are quite large. A sublattice phase can be envisaged as being composed of interlocking sublattices on which various components can mix. One or more sublattices, with one or more types of atoms on each sublattice, may be used to describe a structure so that stoichiometric, non-stoichiometric and substitutional phases may all be described. For example in steels, one lattice can be used for substitutional elements such as Mn, whilst another can be used for interstitial atoms such as C. The sublattice model is the approach MTDATA uses to model the excess Gibbs energy of mixing for the alloys of interest in this work. However, for other types of system (e.g. slags or molten salts) different models will be used.

In ferromagnetic, anti-ferromagnetic and ferri-magnetic materials, there is competition between the different electron spin arrangements. Therefore, the enthalpy of certain metals and their associated alloys are lowered by specific forms

of spin polarisation. These effects have to be accounted for when the Gibbs free energy of a system is minimised. MTDATA uses a model proposed by Inden to perform this task, a detailed description of which can be found in Saunders [61].

Once the influence of magnetism has been accounted for, the minimisation of the Gibbs energy of the system can be started. MTDATA attempts to provide a true system equilibrium by considering the Gibbs energy of all the phases and minimising the total Gibbs energy of the system. Calculation of thermodynamic equilibrium in a system is performed in a series of steps. Firstly, the number of degrees of freedom of a system are reduced, by defining a series of constraints such as mass balance or the composition range in which each phase exists. Secondly, the Gibbs energy of the system is calculated using the appropriate model for the excess Gibbs energy and accounting for any influence of magnetism. An exceptionally reliable Gibbs energy minimisation algorithm known as 'multiphase stage 1' is used to perform the calculations [60]. Finally, an iterative technique is used to minimise the free energy of the system. The result is the prediction of equilibrium phases in a system with a defined composition, temperature and pressure.

3.3 Thermodynamic Databases

MTDATA databases are computer files that store the parameters needed to model the Gibbs energy of a phase as a function of composition, temperature and pressure. The accuracy of equilibrium predictions made by MTDATA depends greatly on the accuracy of the thermodynamic data that MTDATA uses. Due to this fact, a great deal of work has been performed to obtain good quality thermodynamic data. Sources of thermodynamic data used by MTDATA include both the National Physical Laboratory and the Scientific Group Thermodata Europe (SGTE) [60], which is a consortium of European centres engaged in the development of thermodynamic databanks for inorganic and metallurgical systems. Thermo-Calc Fe database (TCFE), which has been specifically produced for iron base systems is also used in this work [62]. Additionally, databases are available for many other types of system, including alloys, aqueous solutions and semi-conductors.

Thermodynamic data for the databases are typically obtained from well known binary and ternary systems, and sometimes from higher order systems. Experimental

measurements of thermodynamic quantities such as heat capacities and enthalpies of formation can be made on such simple systems. These critically assessed thermodynamic data for simpler subsystems are then used to model more complex multi-component systems. The thermodynamic data are usually held in databases using a polynomial function for the Gibbs energy. SGTE uses the following equation [61]:

$$G_{m[T]} - H_m^{SER} = a + bT + cT\ln(T) + \sum_{2}^{n} d_n T^n \qquad [3.4]$$

The left hand side of the equation represents the Gibbs energy relative to a standard reference element (SER). H_m^{SER} is the enthalpy of the element or substance in its reference state at 298K, whilst a, b, c and d_n are coefficients and n represents a set of integers typically 2, 3 and −1.

3.4 MTDATA Modules

MTDATA is divided into a number of modules which are accessed using a character based user interface (command line for DOS, Windows 3.1/9x/NT or UNIX), or by a graphical user interface (Windows 9x and NT only). All the modules can be accessed using the character based interface, but certain modules cannot be accessed using the graphical based interface. The function of some of the modules relevant to this work is briefly outlined below [63]:

- **ACCESS:** Defines systems and retrieves thermodynamic data from databases.
- **MULTIPHASE:** Performs phase equilibrium calculations, plotting and tabulating the results for multi-component systems.
- **APPLICATION:** Accesses built-in applications (e.g. Scheil and Isopleth) or applications made with users own code.

The multiphase module is used to perform equilibrium calculations and plot out the results (e.g. calculating the carbon content of austenite for a given temperature and alloy composition). The Access module is used to create thermodynamic databases specific to the alloys of interest. These databases are
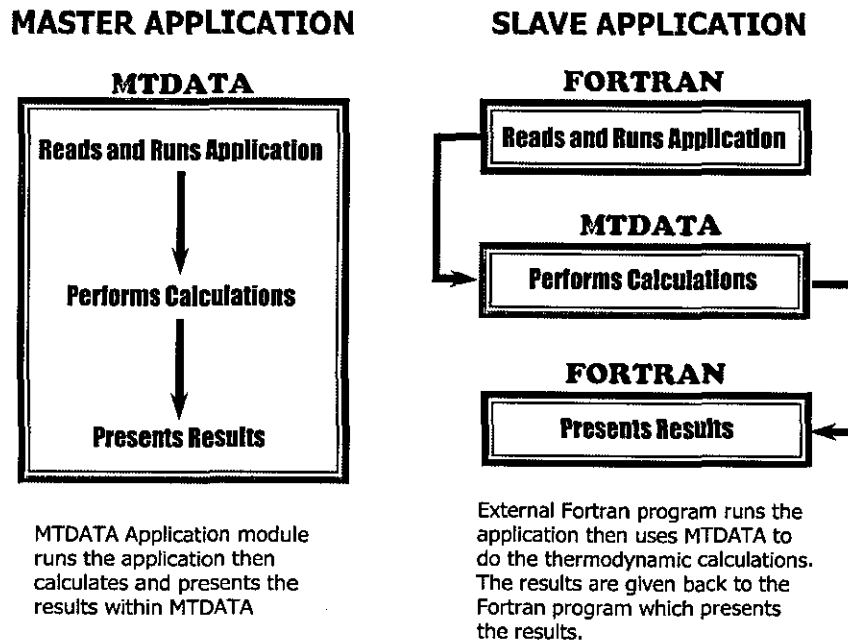
known as MPI files and are used to speed up thermodynamic calculations. For example, if an equilibrium calculation is performed on an alloy containing only Fe and C, a whole range of phases under certain conditions of temperature and pressure could be produced. The carbon for instance could form diamond if the temperature and pressure conditions resulted in this form of carbon being the most stable phase.

However, if users have a good knowledge of the systems they are modelling, they can create a specific database containing information only on the phases, temperature and pressure conditions of interest. Hence if the system of interest was a simple Fe-C alloy, always subjected to atmospheric pressure only, the phases (excluding carbides) that could be stable over the temperature range of 273-2073K are liquid, graphite, austenite and ferrite. By creating an MPI file just containing information on these phases and the elements Fe and C, calculation speed is vastly increased, since MTDATA will not have to calculate the free energy of irrelevant phases that are in the database such as diamond. Hence, MPI files that were tailored to the alloys of interest were used widely in the models in this work.

The Application module was also extensively used in this work. It can be used in one of two ways. Firstly, users can use the Application module to access in-built applications to perform certain calculations or routines. For example the 'Scheil.mac' application performs a solidification calculation based on the Scheil model, whilst the 'Isopleth.mac' routine calculates temperature-composition sections through multi-component, multiphase systems at a fixed pressure. Advanced users can also write their own in-built programs using Fortran that can be accessed through the Application module in MTDATA. Since they are run using a normal MTDATA session using MTDATA as master, these applications are known as **'Master Applications'**.

Alternatively, the Application module can be used in another way. Programs can again be written in Fortran, for use with MTDATA, but this time the program is not accessed through MTDATA. Instead, the program is linked to MTDATA in such a way that MTDATA performs the required thermodynamic calculations, before returning the results to the users program. The program therefore runs independently, using MTDATA as a slave to do the required calculations. Hence, these types of program are known as **'Slave Applications'**. The difference between the two types of Application is shown in figure 3.1.

Figure 3.1. A schematic diagram of the difference between 'Master Applications' and 'Slave Applications' used in MTDATA's Application Interface.

MASTER APPLICATION

MTDATA

Reads and Runs Application

Performs Calculations

Presents Results

MTDATA Application module runs the application then calculates and presents the results within MTDATA

SLAVE APPLICATION

FORTRAN

Reads and Runs Application

MTDATA

Performs Calculations

FORTRAN

Presents Results

External Fortran program runs the application then uses MTDATA to do the thermodynamic calculations. The results are given back to the Fortran program which presents the results.

A series of functions and subroutines have been created that command MTDATA to modify variables and perform certain tasks. These can be incorporated into Master and Slave Applications and can also be combined with normal Fortran commands to create independent programs. Some examples of these functions are shown below:

SET_TEMPERATURE ()	Sets the value of temperature (in K) to be used in MTDATA calculations.
MASS_IN_PHASE()	Returns the mass of a phase after a successful equilibrium calculation.
COMPUTE_EQUILIBRIUM()	Performs an equilibrium calculation for a system with fixed composition, temperature and pressure.

The advantage of Slave Applications over Master Applications is that the combination of Fortran and MTDATA allow very large and complex programs to be written without these calculations having to be performed individually in MTDATA, therefore saving time. Calculations can also be performed at much higher speed

using this method, hence, the time savings are further increased. This gives the programmer a very powerful tool for performing complex phase equilibrium calculations and furthermore, allowing the capability to link the program with kinetic code. Slave applications have been used for all the modelling in this work.

3.5 MTDATA Database Testing

As outlined in section 3.4 data files known as MPI files can be produced by MTDATA that are tailored to specific systems. Three thermodynamic databases (SGTE, TCFE and MTSol – Materials Thermochemistry Solutions Database) were available for use in this work. In the following section the results of a comparison of three identical MPI files (one from each database) to empirically obtained phase diagrams is shown. Each MPI file contained thermodynamic information on the elements Fe, C, Si, Mn, Mo, Ni, Mg, P, Cu and Cr and on the phases graphite, austenite, ferrite, cementite and liquid.

Figures 3.2 a, b, c, d, e, f, g, h and I compare the predictions made by the MPI files with the results of Hillard and Owens' high purity Fe-C-Si ternary alloys [64]. As can be seen from figure 3.2, the predicted phase boundaries are in good agreement with Hillard and Owens' values for both the eutectic and austenite liquidus values. However, agreement between the measured and predicted position of the graphite liquidus for all three alloys is less good. The predicted values are consistently greater than the measured values for all cases by approximately 30-100°C. Hillard and Owen used thermal analysis techniques to obtain their results. The samples were heated in a furnace to a maximum temperature of 1550°C and cooled at a controlled rate of around 4°C/min. A thermocouple placed inside the sample which measured the temperature, hence a cooling curve was obtained that could be used to identify phase changes in the alloys. The liquidus temperatures predicted by MTDATA are equilibrium values. Undercooling of the graphite could take place before solidification occurs, which is not accounted for by MTDATA and hence this could be the source of the discrepancy observed.

Further comparisons were made with experimental measurements made by Wieser for an Fe-C iron and an Fe-C-Si iron containing 2.0 wt.% Si. [65]. The results of these comparisons are shown in figure 3.3. Again, there is good agreement

between the eutectic and austenite liquidus for both alloys and all the databases. Comparisons between the measured graphite liquidus and predicted values do show a better agreement than with Hillard and Owens' results, especially for the iron that contained no Si (figures 3.3a, b and c). However, there is still some discrepancy regarding this region of the phase diagram, which is accounted for in the same way as previously.

It can be seen from the comparisons made in figures 3.2-3.3 that the three different databases gave almost identical predictions of the five phase diagrams which were used to compare them. The systems used for this comparison were relativity simple, containing up to 3 elements, compared with real ADI alloys which can contain over 10 different elements. In the following chapter phase boundary predictions are made for systems that contain more elements and also over a wider temperature range.

Figure 3.2. Comparison of MPI file predictions with the results of Hillard and Owen for 2.5, 3.5 and 5.2 wt.% Si ternary systems [64].
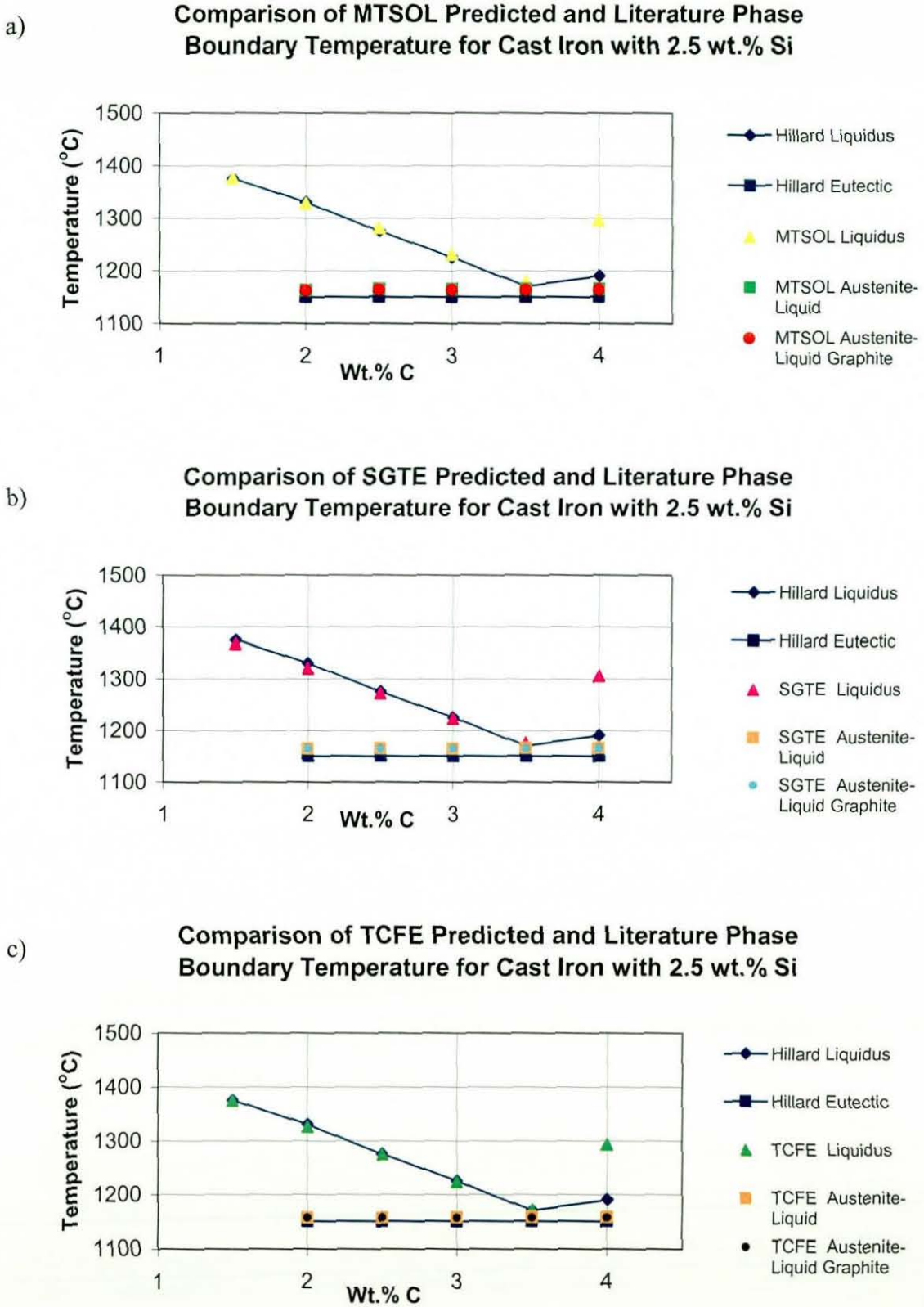
a)

Comparison of MTSOL Predicted and Literature Phase Boundary Temperature for Cast Iron with 2.5 wt.% Si

b)

Comparison of SGTE Predicted and Literature Phase Boundary Temperature for Cast Iron with 2.5 wt.% Si

c)

Comparison of TCFE Predicted and Literature Phase Boundary Temperature for Cast Iron with 2.5 wt.% Si

d)

Comparison of MTSOL Predicted and Literature Phase Boundary Temperature for Cast Iron with 3.5 wt.% Si

e)
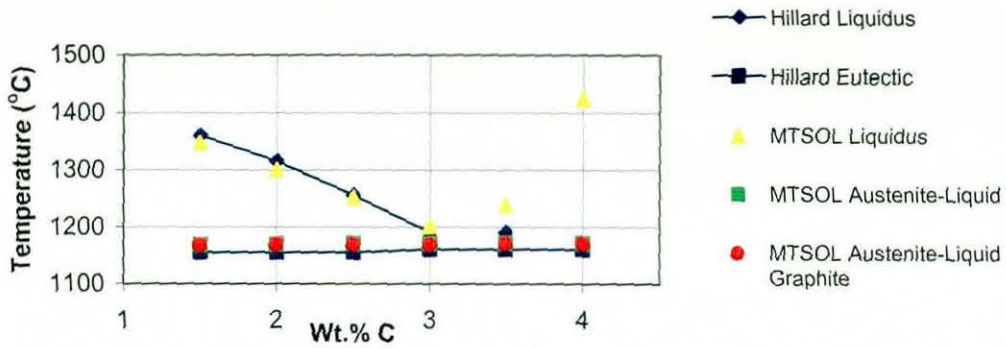
Comparison of SGTE Predicted and Literature Phase Boundary Temperature for Cast Iron with 3.5 wt.% Si

f)

Comparison of TCFE Predicted and Literature Phase Boundary Temperature for Cast Iron with 3.5 wt.% Si

g)

Comparison of MTSOL Predicted and Literature Phase Boundary Temperature for Cast Iron with 5.2 wt.% Si

Legend:
- ◆ Hillard Liquidus
- ■ Hillard Eutectic
- ▲ MTSOL Liquidus
- ■ MTSOL Austenite-Liquid
- ● MTSOL Austenite-Liquid Graphite

h)

Comparison of SGTE Predicted and Literature Phase Boundary Temperature for Cast Iron with 5.2 wt.% Si

Legend:
- ◆ Hillard Liquidus
- ■ Hillard Eutectic
- ▲ SGSOL Liquidus
- ■ SGSOL Austenite-Liquid
- ● SGSOL Austenite-Liquid Graphite

i)

Comparison of TCFE Predicted and Literature Phase Boundary Temperature for Cast Iron with 5.2 wt.% Si

Legend:
- ◆ Hillard Liquidus
- ■ Hillard Eutectic
- ▲ TCFE Liquidus
- ■ TCFE Austenite-Liquid
- ● TCFE Austenite-Liquid Graphite

Figure 3.3. Comparison of MPI file predictions with the results of Wieser [65] for a Fe-C iron and Fe-C-2.0 wt.% Si alloy.

a)

Comparison of MTSOL Predicted and Literature Phase Boundary Temperature for a Fe-C Iron

b)

Comparison of SGTE Predicted and Literature Phase Boundary Temperature for a Fe-C Iron

c)
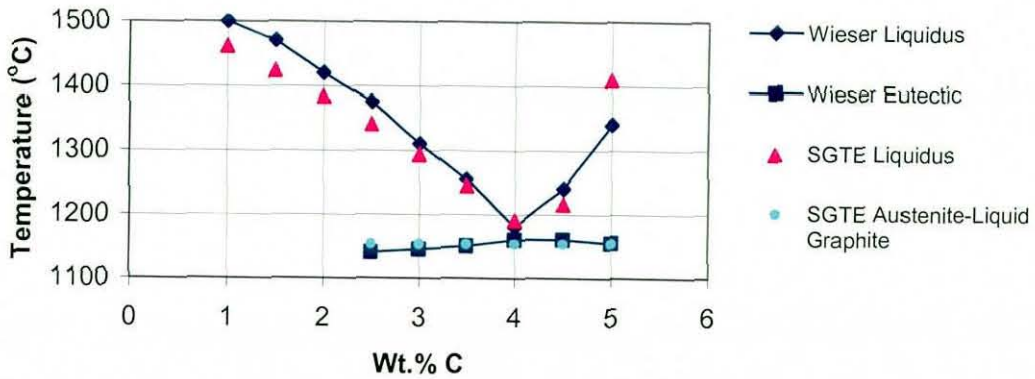
Comparison of TCFE Predicted and Literature Phase Boundary Temperature for Fe-C Iron
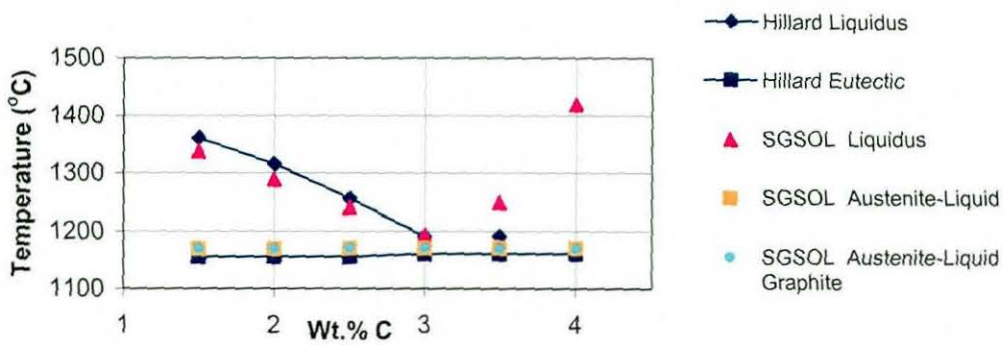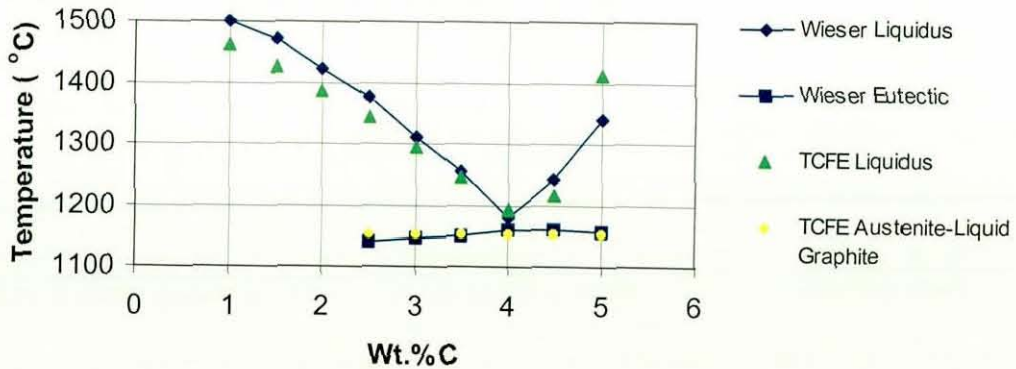
d)

Comparison of MTSOL Predicted and Literature Phase Boundary Temperature for Cast Iron with 2.0 wt.% Si
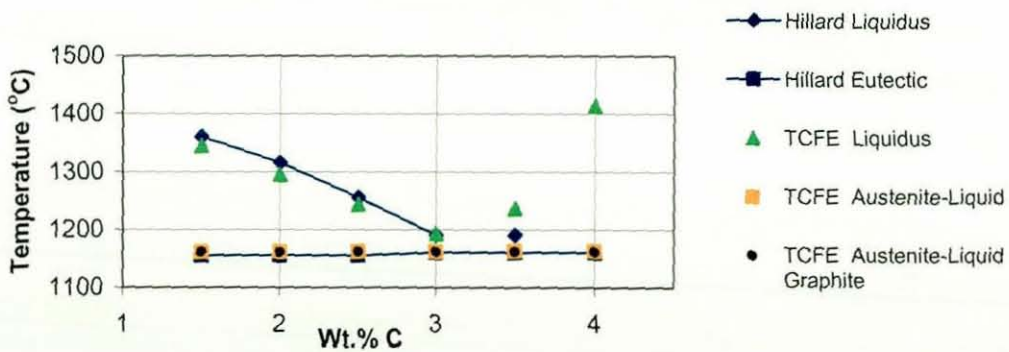

e)
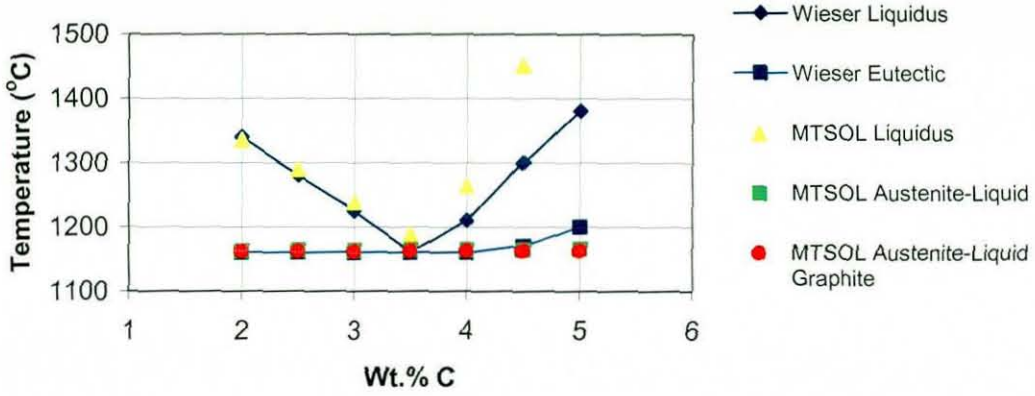
Comparison of SGTE Predicted and Literature Phase Boundary Temperature for Cast Iron with 2.0 wt.% Si
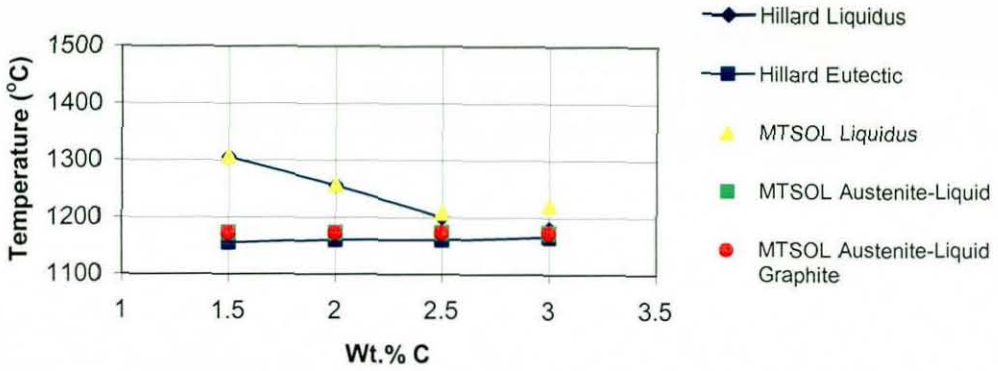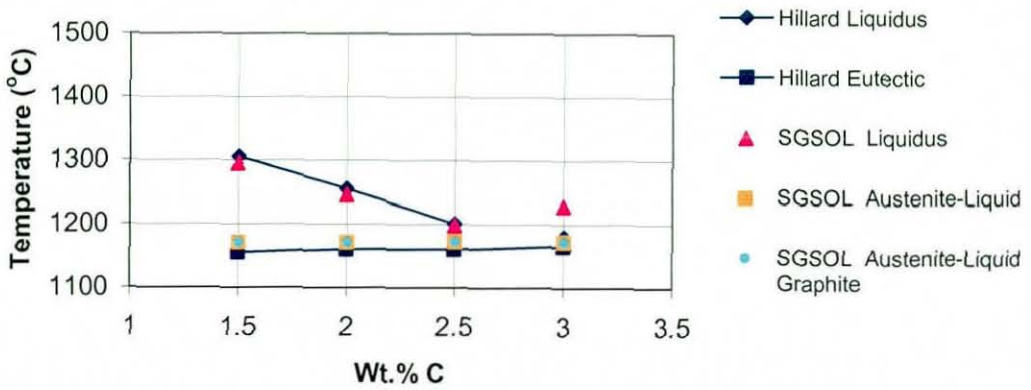

f)
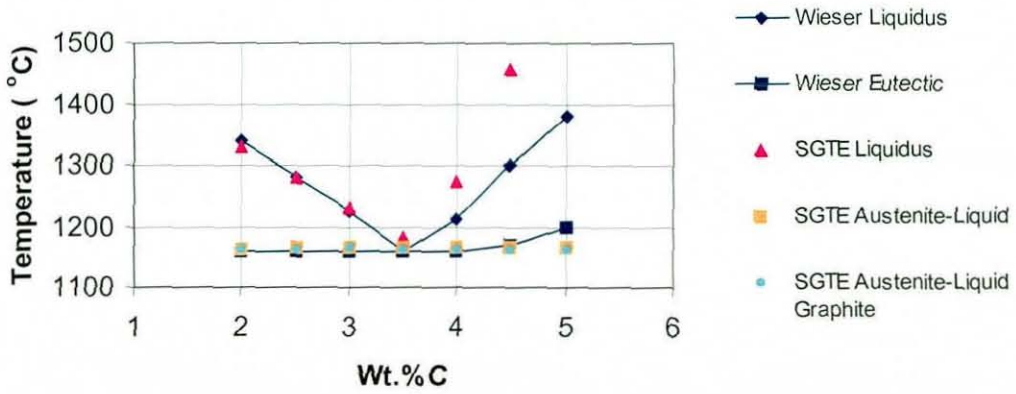
Comparison of TCFE Predicted and Literature Phase Boundary Temperature for Cast Iron with 2.0 wt.% Si
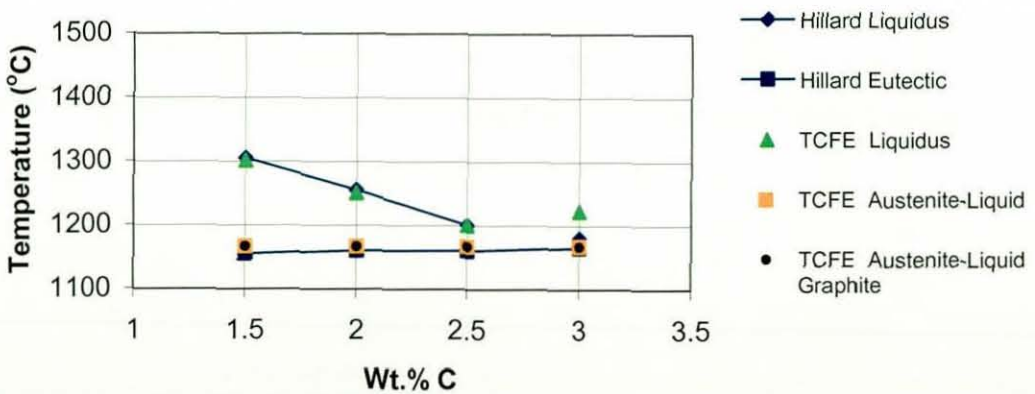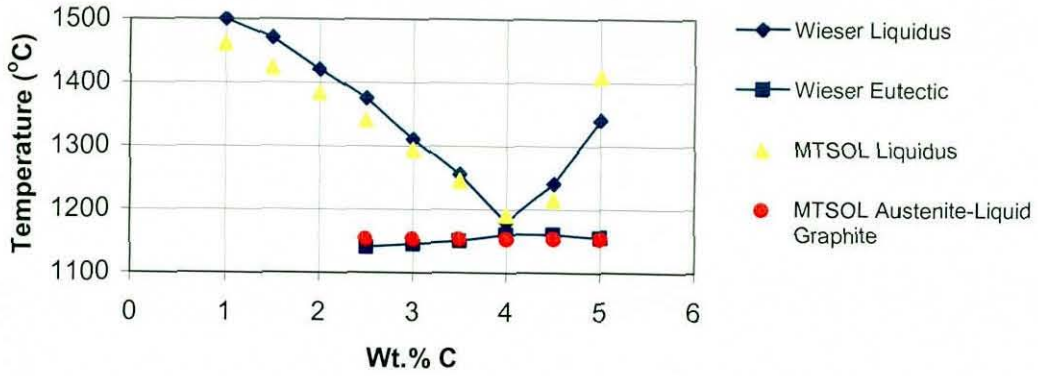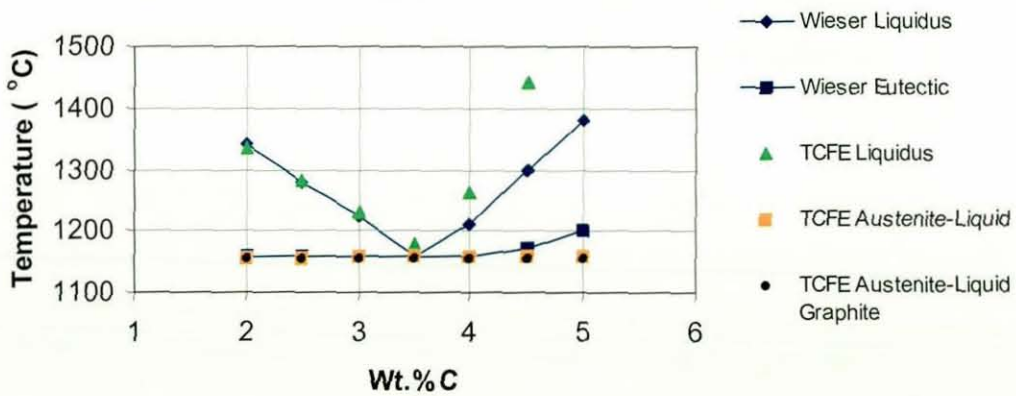
3.6 Summary

MTDATA, the free energy minimisation software package has been introduced and the fundamentals of how it calculates and minimises the free energy of multi-component systems have been discussed. Sources of thermodynamic data and how such data are obtained have also been highlighted. The main modules of MTDATA which are used in this work have been discussed. Most relevant to the current work is the Application Interface. The differences between master and slave applications and how Fortran can be used to construct more powerful and complex applications was discussed. Finally, empirically based phase boundary measurements were taken from five simple systems and compared to predictions made using three different thermodynamic databases. The comparison revealed no significant differences between the predictions made by the different databases. In general, good agreement was obtained between the predictions and the empirical results, and therefore these databases can be used with confidence for predictions in future work.

4 Modelling of Chill Tendency in Ductile Iron Alloys

4.1 Introduction

The use of metal inserts in casting moulds to increase the rate of solidification and hence promote carbide formation in cast iron alloys is a common practice. In the foundry industry, these inserts are known as 'chills'. Chills are placed in the mould in areas of a casting where an increase in hardness is required. Close to the chills, carbides are encouraged to form upon melt solidification. The increased volume fraction of carbides in matrix areas close to the chill results in a local hardness increase which is beneficial in applications that require high levels of resistance to wear, such as gears or camshafts. The mechanical properties of such a component can be usually improved by heat treatment. The purpose of this chapter is to develop a model that can predict how chemical composition will influence the extent of carbide formation in ductile iron alloys during solidification.

4.2 Microstructural Investigations

In this work, chill cast ductile iron camshafts were subjected to austenitisation and austempering heat treatments. The composition of the alloy discussed in this chapter is shown in table 4.1, along with a standard ADI alloy composition SG7. The object of the heat treatments was to increase the mechanical properties of the core of the camshafts by transforming the matrix into one typical of an ADI alloy, whilst retaining some carbides in the surface of the camshafts to increase the wear performance of the component. The resulting component should possess the excellent mechanical properties of ADI alloys through the core of the camshaft, whilst having improved wear resistance in the surface of the cams due to the presence of carbides, which remain in the component after heat treatment. However upon heat treatment, large surface cracks were found to develop in the material making them unsuitable for use as shown in figure 4.1. Several heat treatment variations were used in an attempt to overcome the problem with limited success [66;67]. Camshafts obtained from the manufacturers were sectioned and their microstructure was examined optically in an attempt to understand the problem.

Table 4.1. Composition of chill cast alloy and SG7 (all wt.%).

Alloy	Fe	C	Si	Mn	Mo	Mg	P	S	Cu	Cr	Sn
Chilled	Bal	3.71	1.38	0.25	0.44	0.03	0.03	0.01	0.98	0.02	0.05
SG7	Bal	3.66	2.52	0.16	0.00	0.04	0.04	0.01	0.51	0.00	0.00

Figure 4.1 Post austempering cracking in chilled machined ADI camshafts a) after washing and rinsing and b) after polishing and dye penetrant testing [68].

a)   b)
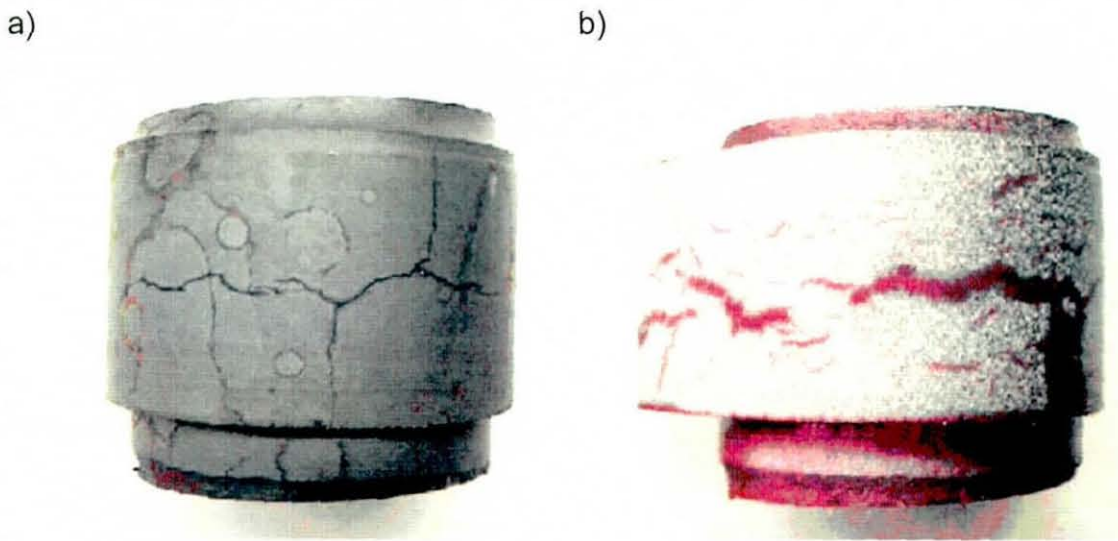
Figure 4.2. Optical micrographs before heat treatment of
a) the cam surface   b) the cam centre
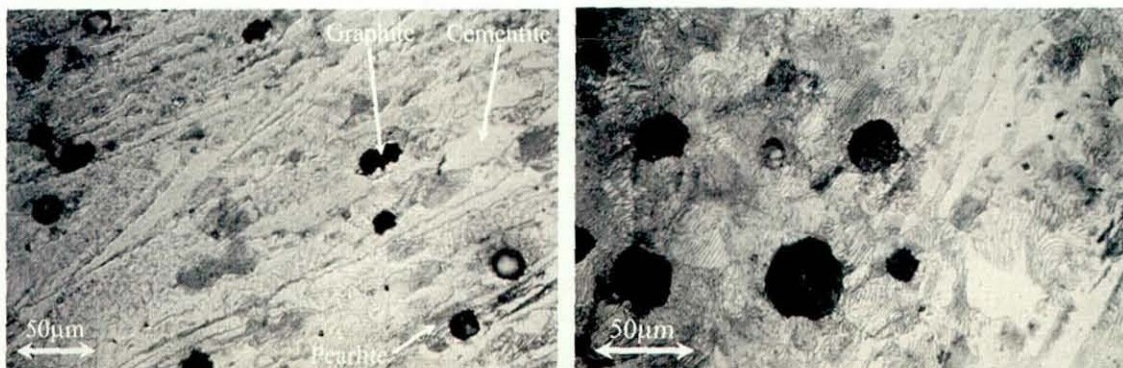
Subsequent metallurgical investigations revealed that carbides penetrated deep into the camshafts and were even found in the centre of the castings. Figure 4.2 shows optical micrographs of the cam surface and centre. The carbides (large

white needles) can easily be seen in both micrographs, although in a much greater quantity near the surface due to the increased cooling rate of the chill. The greater quantity of pearlite in the centre of the cam should also be noted along with the increase in the graphite nodule size. The pearlite is found in greater quantities in the centre due to the slower cooling rate during solidification. During solidification the large volume fractions of carbide that form due to the chill remain stable to room temperature, reducing the amount of matrix that is available to transform to pearlite whilst cooling through the eutectoid reaction. The larger nodules are again a result of the slower cooling rate, which allows them more time to grow than in the faster cooling surface material.

X-ray diffraction was used to positively identify the cementite in the material. Several problems were encountered during the use of this technique in identifying the phases present in the material. Firstly, the strong diffraction of the ferrite (110) plane masks the highest intensity cementite diffraction peaks (211), (102), (220), (031) and (112).

Figure 4.3. An X-ray diffraction trace for the chilled alloy.
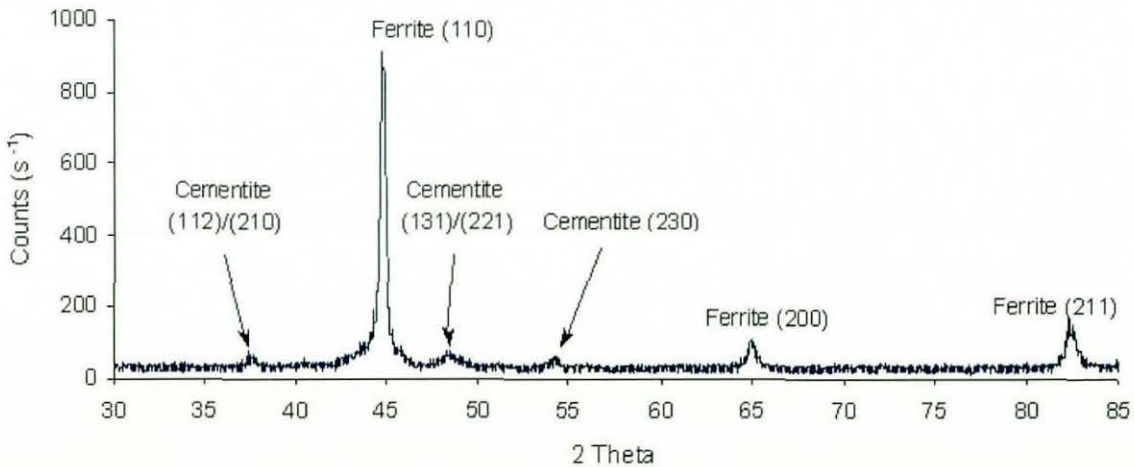
Secondly, since the carbides are produced with the aid of a chill, the material tends to solidify directionally. The directional solidification favours various planes in the material. The intensity of diffraction in crystals with texture is known to vary when compared to a crystal that has no texture [69]. Some diffraction planes are reinforced, whilst others do not diffract. The magnitude of these effects depend upon the degree of texture within each individual casting and therefore are not known in the current investigations.

The nature of the orthorhombic structure of cementite also produces a large quantity of diffraction planes. Over the angular range investigated there are over 50 different planes that cause diffraction of varying intensities [70]. The diffraction angles of some planes are also very close together. For example the (131) and (221) planes have diffraction angles of 24.28° and 24.50° respectively, and similar intensities. This makes identification of the exact diffraction plane in cementite difficult.

Finally, the radiation source used in the investigations was copper. Copper X-rays produce fluoresce radiation when incident upon iron, resulting in low intensity results being produced, which also makes identification of the material more difficult. This is discussed in more detail in section 10.2. Figure 4.3 shows an X-ray diffraction pattern obtained from a chilled sample. The peaks which identify the phases present in the material are shown in the figure. Some peaks show captions that quote two diffraction planes. This is a result of the close diffraction angles of various cementite planes, which made it impossible to identify the exact diffraction plane in these cases. Hence both of the possible diffraction planes are included in the figure.

Microhardness tests using a load of 50g were carried out on the carbide and pearlite phases in the microstructure. Thirty separate tests were performed in each phase and the results were averaged. The hardness of the cementite phase was found to be extremely high at around 940 HV, whilst the pearlite phase produced microhardness values of 309HV. All the measured values were within ±10% of their respective mean values.

Figures 4.4, and 4.5 show SEM pictures of the carbides and corresponding elemental maps. For each particular elemental map, brighter colours signify a higher concentration of that particular element in that region of the microstructure. The microscope used was a Leo 1530VP field emission gun SEM and the concentrations were measured using an EDAX Pegasus energy dispersive X-ray (EDX) analysis system, fitted with an ultra thin window. The ultra thin window facilitates the detection of carbon, although not quantitatively. The 'swiss cheese' appearance of the carbides in figure 4.4a arises because the image corresponds to a section through a number of dendrite arms. The segregation of Mo to larger carbides can be clearly seen in the Mo elemental map (figure 4.4b). The Si elemental map in figure 4.4c shows that this element strongly segregates away from the carbides no matter what their size.

Figure 4.4. A SEM image and corresponding elemental maps of chilled ductile iron.
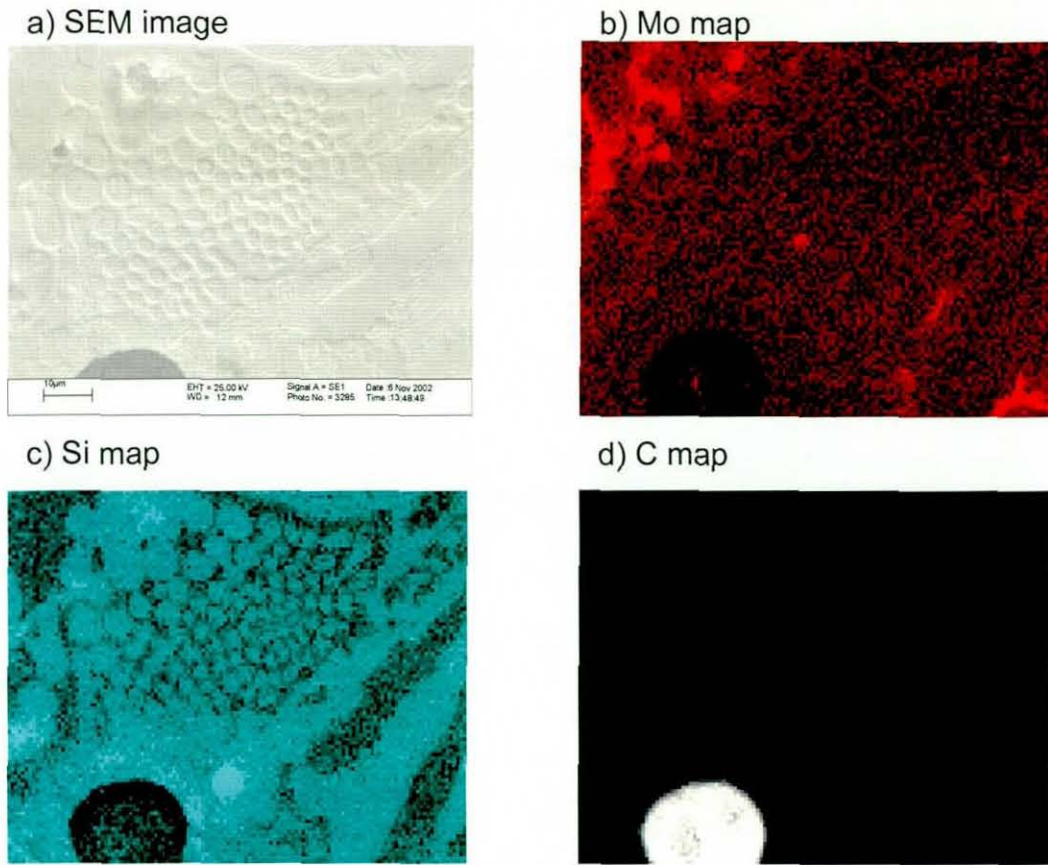
a) SEM image

b) Mo map

c) Si map

d) C map

Figure 4.5. A SEM image and corresponding elemental maps of chilled ductile iron.

a) SEM image

b) Mo map

c) Si map

d) Cu map
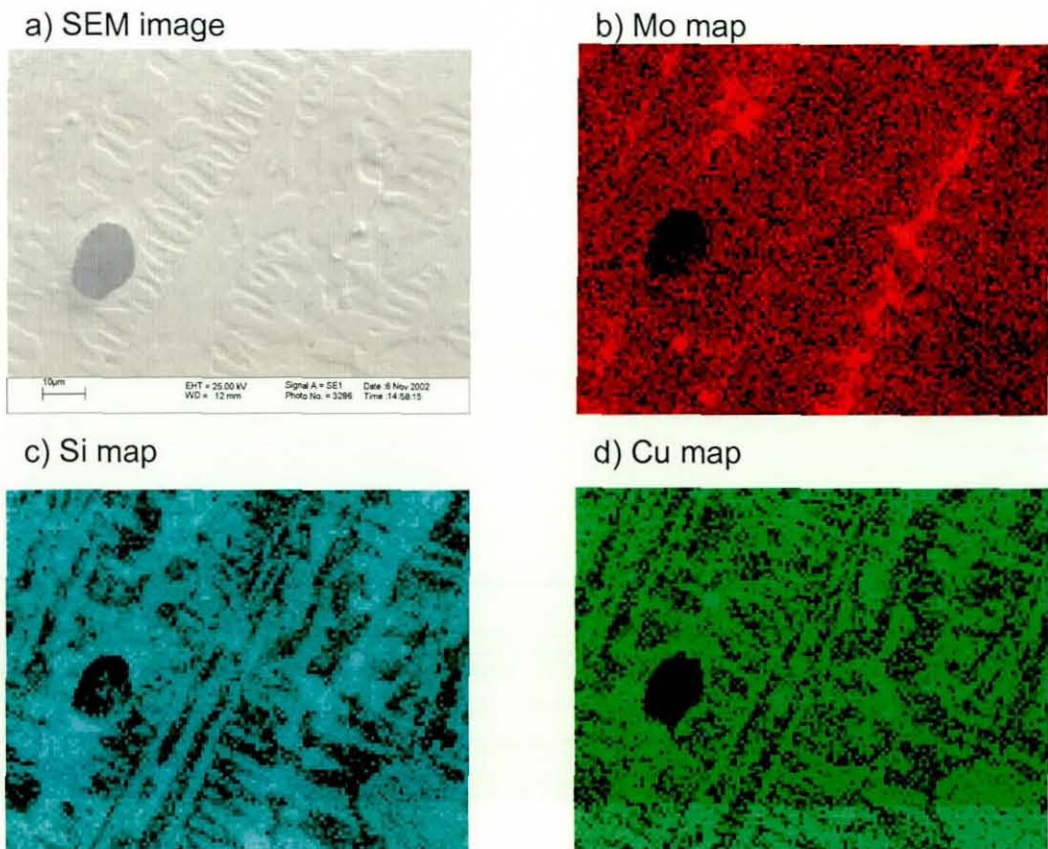
Si is also found in high quantities around the graphite nodule. Figure 4.4d also shows a map for the element C. C can be detected although not quantitatively analysed, and as would be expected the higher C concentrations are found in the graphite nodule.

Figure 4.5 shows another image of the same chilled ductile iron alloy. The dendrite arms in figure 4.5a can clearly be seen. Again, Mo is present in high quantities in the large carbides in the micrograph and Si in found in areas of the matrix where carbides are not present. Figure 4.5d shows an elemental map for Cu. Cu seems to follow the same segregation behaviour as Si, since it is found in larger quantities away form the carbides in the microstructure.

4.3 The Metallurgical Perspective of the Problem and Relevant Literature

The production of a successful model to predict the influence composition has on the chill tendency of these alloys requires a good understanding of the problem from a metallurgical perspective. The reason for the large carbide formation in these camshafts can be understood by looking at the phase diagram shown in figure 4.6. The black lines in the figure represent the equilibrium system of iron and graphite, whilst the blue lines represent the metastable system of iron and cementite.

Upon slow cooling from the melt in a hypoeutectic alloy of carbon content X (red line in figure 4.6), austenite dendrites would firstly nucleate and then grow from the liquid. Upon further cooling, the growth of austenite dendrites would continue. The eutectic temperature (1146°C) is then reached and the rest of solidification occurs as a graphite and austenite eutectic. However, this situation would only occur with a very slow cooling rate and where graphite nucleation is readily promoted. In reality, a faster cooling rate produces undercooling, and a substantial proportion of the alloy solidifies below the metastable eutectic temperature, and hence solidifies as austenite and Fe_3C (a two phase mixture known as ledeburite).

The magnitude of the undercooling is further increased by the influence of chills. As the solidification rate increases, a greater degree of undercooling occurs[71]. As with a normally cooled alloy, primary austenite dendrites are the first solid to form. However, due to the increased cooling rate induced by the chill, the austenite dendrites are much finer [4]. The effect of the chill on the solidification of the surface

layers of the alloy is to rapidly cool them well below the metastable γ-Fe$_3$C eutectic temperature (blue lines on the figure 4.6). There is little time for the equilibrium solidification of eutectic cells of austenite and graphite to occur. Hence, the majority of the alloy solidifies as eutectic cells of austenite and cementite. The cell count is much greater than that of an alloy cooled normally, due to the greater number of fine primary austenite dendrites that host the eutectic cells [4]. This is the behaviour observed in the camshaft shown in figure 4.1. Furthermore, if the chill is rapid enough, there will be no time for graphite formation to occur and hence alloys will solidify as white iron [71].

Figure 4.6. A schematic phase diagram for the Fe-C system.
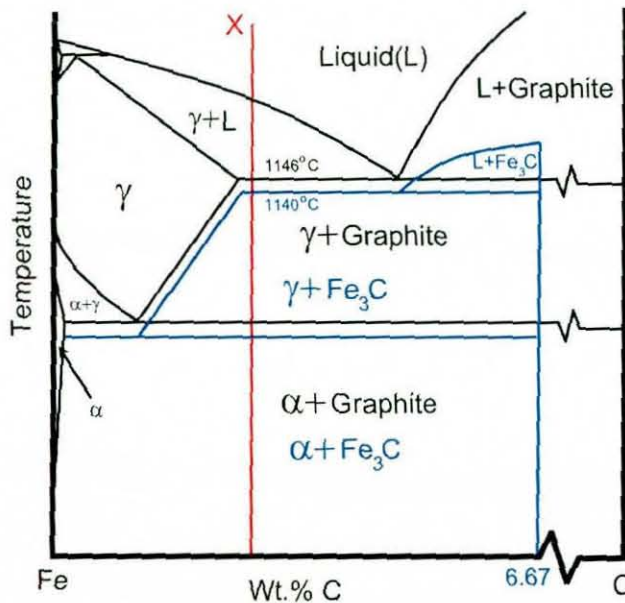
Relationships were found in literature that predict the solidification behaviour of grey cast iron alloys based on their compositions [2;72-74]. The solidification behaviour of a typical hypoeutectic cast iron is highlighted in the cooling curves in figure 4.7. The first solid to form in a hypoeutectic cast iron is austenite. The formation of austenite dendrites first occurs at the austenite liquidus temperature (TAL). As the austenite dendrites nucleate, latent heat evolves, hence the gradient of the cooling curve decreases. The growth of austenite continues until the temperature of eutectic solidification (TES). At the TES, graphite nucleation occurs in the carbon rich liquid between the dendrite arms. Eutectic solidification continues, as does the

cooling of the alloy. This is accompanied by an increased amount of latent heat evolution as increasing amounts of liquid solidify. Eventually, the large amount of latent heat arrests the cooling at the temperature of maximum eutectic undercooling (TEU). Eutectic cell growth becomes established, therefore the temperature rises to the eutectic recalescence temperature (TER). At the TER, steady state growth occurs as the latent heat evolved is balanced by the heat removed by cooling. As solidification nears completion, the temperature falls as less latent heat is liberated. Solidification is completed at the temperature TEE in figure 4.7 [2].

Figure 4.7. A schematic diagram of the solidification behaviour of cast irons.

TYPICAL CAST IRON   CHILLED CAST IRON

Not to scale   TAL = Temperature of Austenite Liquidus   TES = Temperature of Eutectic Solidification
TEU = Temperature of Eutectic Undercooling   TER = Eutectic Recalescence Temperature
TEE = End of Solidification
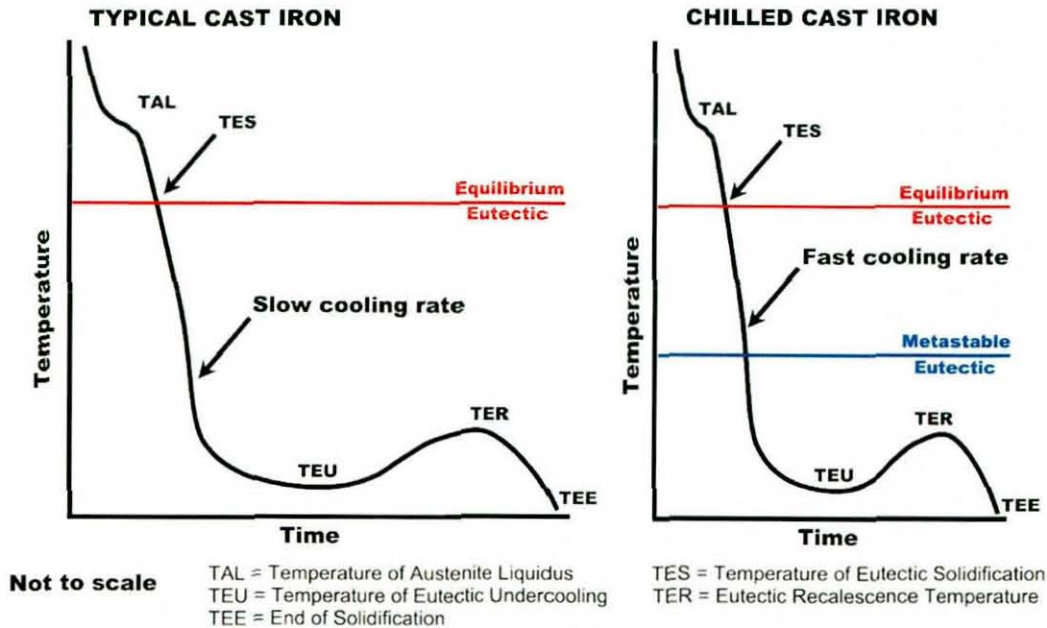
Figure 4.7 also shows the cooling curve for a cast iron solidified with the aid of a chill. As can be seen in the figure, the TEU and TER temperatures are well below the metastable eutectic temperature. The majority of solidification occurs after the TEU temperature, therefore a large proportion of this alloy would contain Fe_3C. This is thought to be occurring in the camshaft shown in figures 4.1.

Various empirical relationships exist in literature that predict the TAL, TEU and TER temperatures of grey cast irons. Carbon, silicon and phosphorous have been found to have the most influential behaviour on the TEU temperature, but other elements such as chromium can also have an effect [73]. Donald and Moore

proposed that the TEU temperature in °C can be given by the following relationship [75]:

$$TEU = 1140 - 9.8C - 12.1(Si + 2.45 P) \qquad [4.1]$$

where C, Si and P are the wt.% of those elements in the iron. This relationship is valid over a composition range of 3.05-3.76C, 0.61-2.88Si and 0.01-1.9P, all wt.%. Kubick, Javid and Bradley propose the following similar relationships for the TEU temperatures of inoculated (TEU_f) and uninoculated (TEU_b) melts, where TEU is in Fahrenheit [72]:

$$TEU_f = 2006 + 15.1C + 16.9Si - 89.9P \qquad [4.2]$$

$$TEU_b = 1958 + 23.6C + 28.3Si - 79.6P \qquad [4.3]$$

Table 4.2 shows the predicted TEU temperatures for a simple cast iron alloy containing 3C, 2Si and 0.01P (all wt.%). It can be seen in table 4.2 that the Donald and Moore [75] relationship predicts a much lower TEU temperature. In fact this temperature is lower than any literature observations taken from cooling curve experiments [72;74]. Therefore, it was thought that equations 4.2 and 4.3 were more accurate than equation 4.1. Another advantage of relationships 4.2 and 4.3 is that they are valid over a wider composition range than equation 4.1. Hence the relationships proposed in Kubick's papers were used in this work.

Table 4.2. Predicted TEU temperatures using various relationships.

Relationship	TEU Temperature (°C)
Donald and Moore [75]	1086
Kubick (inoculated) [72]	1140
Kubick (uninoculated) [72]	1135

ADI alloys commonly have addition of other elements such as Mn, Mo, Mg, Cu and Cr. These elements will have also some influence on the TEU temperature and yet are not accounted for in the relationships. The influence of most alloying elements is not thought to be large, since most of these elements do not have a potent chill tendency. However, Cr is known to increase the chill tendency strongly, and therefore

these relationships should be used with some caution in alloys containing this element [2].

Literature relationships do also exist for the TAL and TER temperatures [2;72-74]. However, the accuracy of the TER temperature predictions is much less than that for the TEU temperatures. This is primarily attributed to the variability associated with the inoculation practice [72]. Therefore these relationships were not used in the model. The temperature rise during recalescence is rarely more than 6°C, so therefore it was assumed that TEU is approximately equal to TER [72]. The TAL temperature can also be predicted using MTDATA (see section 3.5), therefore it was not thought necessary to use the TAL relationships found in literature. MTDATA can also predict these temperatures taking into account all the alloying elements that are present in the system, hence it is assumed to be more accurate.

4.4 Eutectic Temperature Model Basis and Development

The production of a successful model to predict the solidification behaviour of cast irons in respect to the phases present requires the knowledge of both the equilibrium and metastable eutectic temperatures, as well as the TEU temperature. The equilibrium and metastable temperatures can be calculated using MTDATA. Again, it takes into account interactions between all the alloying elements in the system and hence is thought to be more accurate than any relationships found in literature. Once the equilibrium and metastable eutectic temperatures are calculated using MTDATA and the TEU temperature is found using Kubick's empirical relationship [72], it can be determined whether or not the TEU temperature is above or below the metastable eutectic temperature. Hence the basis of a model that could predict the solidification behaviour of the cast iron was established. If the TEU temperature of an alloy was found to be below the metastable eutectic temperature, then that alloy would at least partly solidify below the metastable eutectic temperature and hence contain some carbide, and visa-versa.

Three MPI files (see section 3.4) were produced in MTDATA using three different thermodynamic databases, SGTE, MTSol and TCFE. The MPI files contained thermodynamic data on the elements Fe, C, Si, Mn, Mo, Mg, P, Cu and Cr

and the phases liquid, graphite, austenite, ferrite and cementite. These phases were chosen because it is known they exist in cast iron alloys.

A suitable Fortran program was then written as an MTDATA Slave Application. It performed calculations of the equilibrium and metastable eutectic temperatures, and the TEU temperature. The operation of the program is highlighted schematically in figure 4.8. As can be seen in the figure, the chemical composition is input into the model. Cementite is then classified 'absent' from the system and the temperature is set to 1800°C. The system temperature is reduced in steps of 1°C and equilibrium calculations are performed at each temperature until a new phase is found to be present in the system. This is the liquidus temperature. The model records the value of the liquidus temperature and the continuous reduction in temperature starts again until another new phase is found to be stable in the system. This is the metastable eutectic temperature. Again the equilibrium eutectic temperature is recorded by the model. Cementite is then classed to be 'present' in the system and graphite 'absent', and the process is repeated again. Finally, the TEU temperature is calculated by the model using the Kubick's relationship and the results are compared.

A series of theoretical alloy compositions were run through the model and the predictions made by the different databases were compared. Figure 4.9 shows model predictions of (a) the equilibrium and (b) the metastable eutectic temperatures, made using the MTSol database, against the corresponding model predictions made by the SGTE and TCFE databases. As can be seen in figure 4.9a all the predictions using the three databases for the equilibrium eutectic temperature were within ±10°C of each other.

Figure 4.9b shows the corresponding results for the metastable eutectic temperature. Again excellent agreement is observed (within ±10°C) for all databases, except for a pair points which are not in agreement with the rest. The MTSol prediction for this composition is approximately 30°C higher than the corresponding predictions made using the SGTE and TCFE databases. The composition of this data point was well within the compositional limits of the databases, hence this cannot account for the error. Each element of this data point had its mass value independently changed by a small amount (0.001 wt.%) and the composition was again run through the model to determine if one particular element was responsible for the error. All of the slight composition changes produced results within ±10°C of

the other predictions made by the other databases. Hence the source of the error could not be determined. As a result the MTSol database was thought to be unreliable and was therefore not used in the remainder of this work.

Figure 4.8. Schematic diagram of eutectic temperature model.
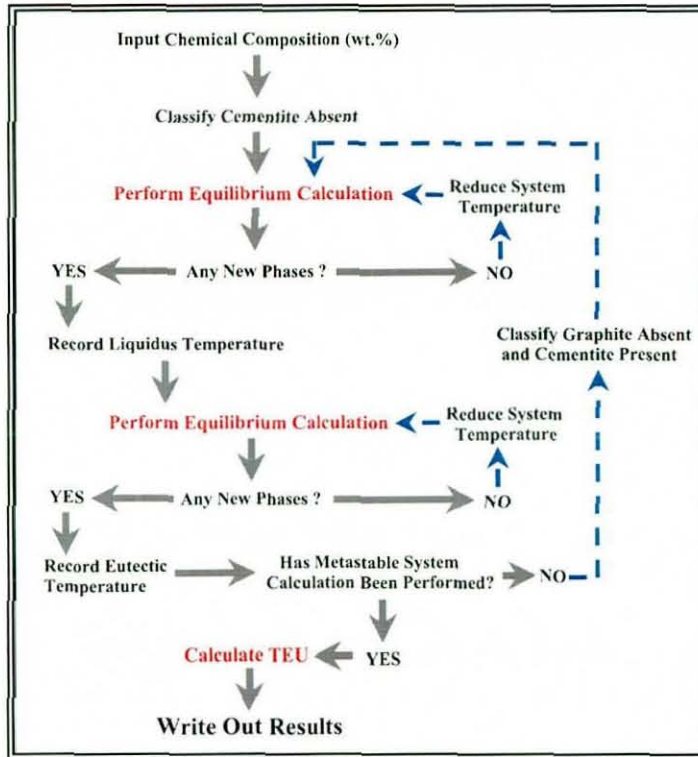
The accuracy of the TEU relationship was also tested for a range of different cast iron compositions and types as shown in figure 4.10. The dotted lines represent the general trends shown by the different types of cast iron. Values of the TEU were found in literature for different types of cast iron and then equation 4.2 was used to predict the TEU values. As can be seen in figure 4.10, there is a good correlation between the predicted and literature values for the grey irons. The ductile iron TEU temperatures appear to be around 5-10°C below those that the model predicts. This observation supports the need for the adjustment of equation 4.2 to account for the behaviour of ductile irons. However, it should also be noted that the equation 4.2 does not take into account the rate of cooling or the presence of any chills used in the casting process, which would clearly influence the actual TEU temperature of each alloy, which cast an error of uncertainty in the results.

Figure 4.9. Comparison of a) equilibrium and b) metastable eutectic temperature predictions made using the MTSol, SGTE and TCFE databases.

a)   b)
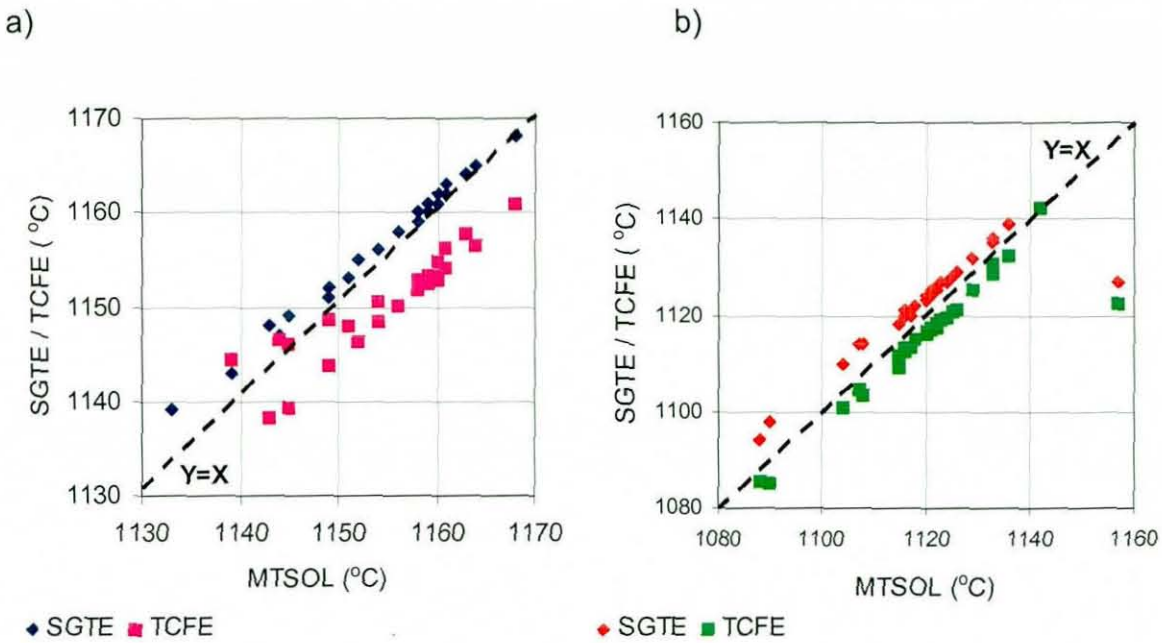
When equation 4.2 is used to predict the TEU behaviour of white cast iron, as shown in figure 4.10, the predicted TEU temperatures are above the TEU temperatures observed experimentally. This is a consequence of the low level of inoculation and/or fast cooling rate given to these alloys as graphite is an unwanted phase. Hence a large undercooling is needed before graphite will form in these alloys. This is reflected in the difference between the predicted TEU and literature TEU values for these alloys, since equation 4.2 does not account for inoculation.

Figure 4.10. Comparison of literature and predicted TEU values for grey iron [76], ductile iron [77] and white iron [78].
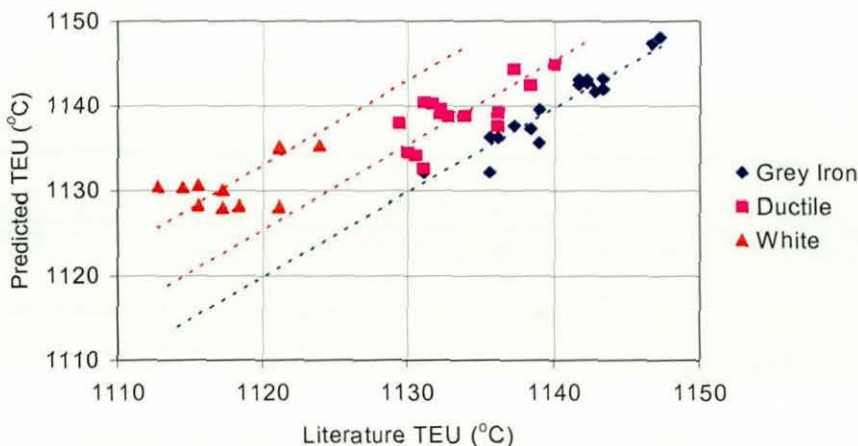
4.5 Comparison of Model with High Temperature Differential Thermal Analysis Results

Differential thermal analysis (DTA) was performed on the chilled ductile iron in order to compare the measured and predicted liquidus, eutectic and eutectoid temperatures with measured results. DTA is a technique commonly used in materials research to detect transformation and transition temperatures in metal and polymer systems [79]. A small cylindrical sample and an inert reference material, which shows no thermal activity over the temperature range of interest are exposed to the same heating regime [80]. Reactions are detected in the sample during heating or cooling, by measuring the temperature difference between the reference and sample using a thermocouple [79;81]. When the sample undergoes a reaction the temperature difference between the sample and reference changes, identifying the temperature and type of reaction. The sample will either absorb (endothermic) or release heat (exothermic) [80]. If a constant heating rate is used the temperature difference can be plotted against temperature. Such a plot for the chilled ductile iron specimen is shown in figure 4.11, where the austenite formation and liquid formation reaction peaks can be clearly identified.

Figures 4.11 a, b, c and d also show the equilibrium and metastable phase boundary temperatures as predicted by the model using the SGTE and TCFE databases. On heating of the sample, the first peak encountered occurs at around 750°C, corresponding to the austenite formation reaction and is endothermic. Two peaks can be identified, the first much smaller than the second. On closer examination when in comparison with phase boundaries predicted by TCFE (Figs 4.11 b and d), the smaller first peak seems to correspond to a reaction in the equilibrium system, whilst the second peak in better agreement with the metastable phase boundaries. Although the material is chilled and contains large amounts of Fe_3C, graphite is also present in the system. It therefore seems reasonable that the two peaks could indeed represent the austenite formation reaction, which in some areas of the matrix corresponds to the equilibrium reaction, whilst in other areas the metastable reaction. This distinction cannot be made using the SGTE database as both the equilibrium and metastable austenite formation reactions are shown to occur over a similar temperature range.

Figure 4.11. A DTA trace of a chilled ductile iron specimen compared to predictions of phase boundary temperatures by the eutectic temperature model.

a)

Equilibrium Phase Boundary Predictions
(SGTE)

b)

Equilibrium Phase Boundary Predictions
(TCFE)

c)

Metastable Phase Boundary Predictions
(SGTE)

d)

Metastable Phase Boundary Predictions
(TCFE)
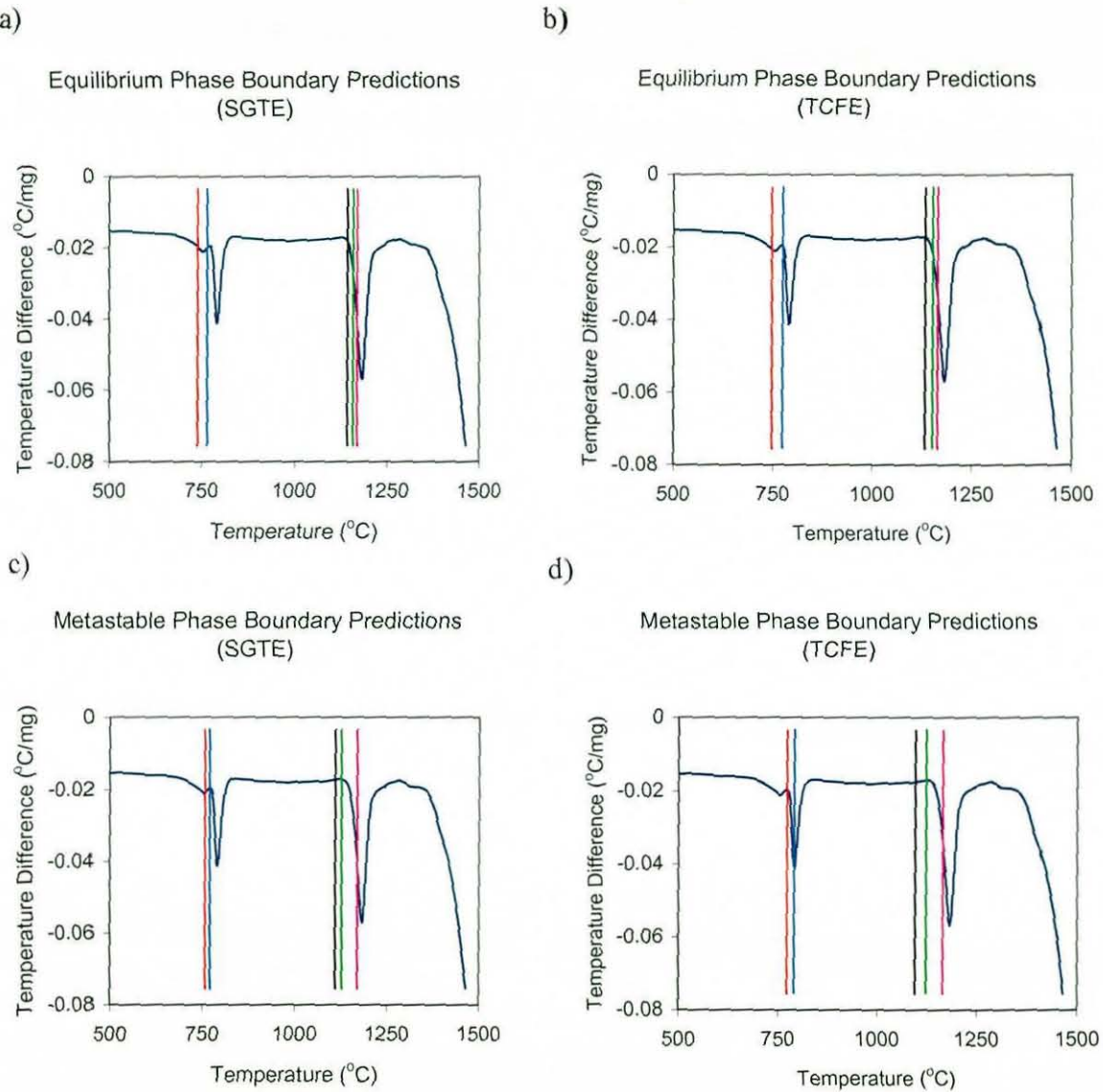
Phase changes predicted to occur on cooling:
(A = graphite in equilibrium system and Fe_3C in metastable system)

———— $L \rightarrow L + \gamma$ ———— $L + \gamma \rightarrow L + \gamma + A$ ———— $L + \gamma + A \rightarrow \gamma + A$
———— $\gamma + A \rightarrow \alpha + \gamma + A$ ———— $\alpha + \gamma + A \rightarrow \alpha + A$
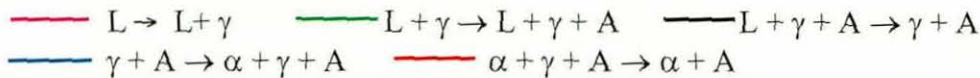
As the temperature increases further the liquid formation is encountered as the sample progressive melts. The best agreement between the predicted phase boundaries and the DTA endothermic peak, which represents the liquid formation and melting of the alloy, coincides with the equilibrium phase boundary predictions for both databases. This could be due to the slow heating rate of the sample, which may result in the dissolution of the Fe_3C phase as the temperature slowly rises, removing the

phase from the system. The SGTE database seems to produce a more accurate prediction of these phase boundaries, which are the most critical for the eutectic temperature model, since they determine whether graphite or cementite form during the eutectic transformation.

4.6 Comparison of Model with Magmasoft Predictions

Figure 4.12 shows a Magmasoft prediction of the cooling curves of the chilled material at different distances below the surface of the cam lobe. Magmasoft is simulation software that is widely used in the casting industry to predict microstructure, thermal stresses and other properties of castings [82]. The geometry of the cam lobe in the simulation was identical to those investigated in this work. The liquidus temperature and the equilibrium and metastable eutectic temperatures are also shown in figure 4.12 as predicted by the SGTE database.

Figure 4.12. A Magmasoft prediction of cooling curves at different distances below the surface of the chilled cam lobe (courtesy of Federal Mogul).
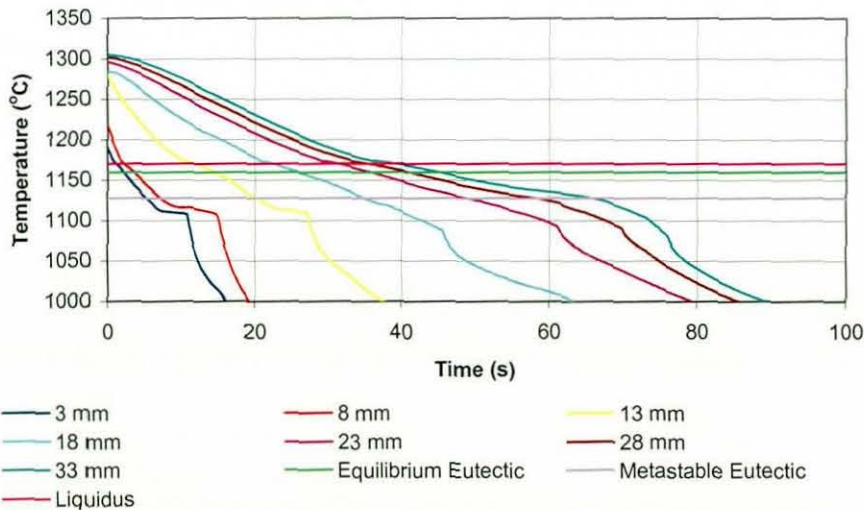
As can be seen on the cooling curves, the cooling rate decreases with distance below the surface of the chilled camshaft lobe. Stages of solidification can also be identified on the cooling curves as discussed previously in section 4.3 and highlighted in figure 4.7. A slight decrease in the rate of cooling is observed in all the

curves at the liquidus temperature as the liquid metal starts to solidify (TAL). The TEU and TER temperatures of the cooling curves that are 3, 8 and 13 mm below the chill surface are shown to be below the metastable eutectic temperature, characterised by a sharp thermal arrest. This indicates that most of the material in these areas will solidify with the metastable eutectic reaction, hence large quantities of Fe_3C will be produced in these matrix areas. Towards the centre of the cam lobe, the cooling rate slows and solidification occurs at a slower rate, over a range of temperatures, hence no sharp arrest of the cooling rate is observed in these curves. The material found towards the centre of the cam lobe is therefore expected to solidify by a mixture of the two eutectic reactions. This is exactly the microstructure that is found in the cam lobe in reality (see figure 4.2), with large quantities of white iron found in the surface layer of the cam lobe, whilst towards the centre, more graphite nodules are encountered, although some carbides are still found to be present.

Figure 4.13 shows another Magmasoft prediction of the cooling curves for a chilled cam lobe, but this time the alloy used is SG7, which is a standard ADI alloy, the composition of which is shown in table 4.1. This alloy has not been designed to promote chill, therefore it contains higher levels of Si to suppress carbide formation and promote the graphite eutectic reaction.

Figure 4.13. A Magmasoft prediction of cooling curves at different distances below the surface of a chilled SG7 cam lobe (courtesy of Federal Mogul Technology).
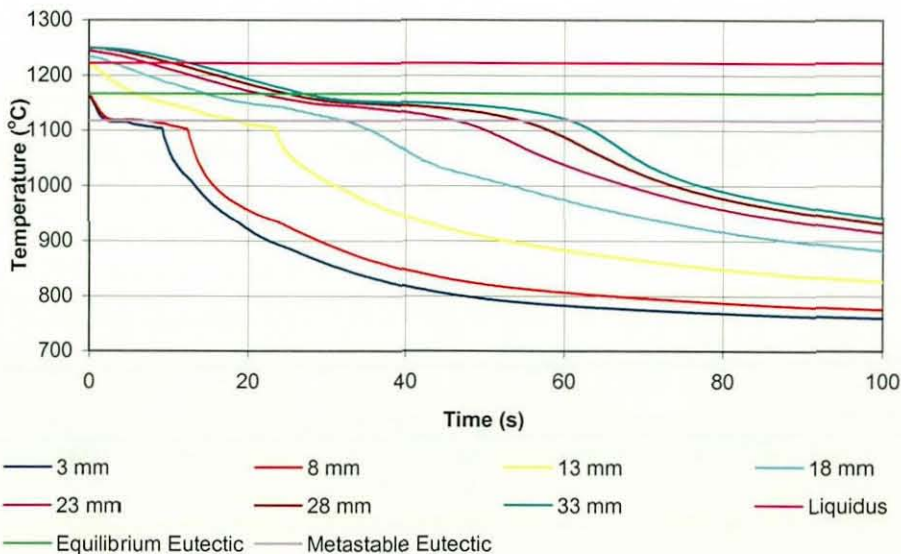
Again on figure 4.13 SGTE database predictions of the liquidus and metastable and eutectic temperatures are shown. The thermal arrest that occurs at the TER temperature only occurs below the metastable eutectic temperature (as predicted by SGTE) in the material 3 mm below the surface of the cam lobe. This is in contrast to the cooling curve for the chilled alloy composition, where the three regions closest to the surface all had their TER thermal arrest below the metastable eutectic temperature. Therefore this alloy would be expected to contain much less cementite in its microstructure than the chilled alloy. Hence it can be seen that composition can have an important influence on the chill tendency of these materials.

4.7 Influence of Alloy Composition on Model Predictions

It is well known that various alloying elements influence the equilibrium and metastable eutectic temperatures in different ways in cast iron alloys [2]. Some of these effects are summarised in figure 4.14. The magnitude of these effects varies from element to element. Silicon and chromium both have a potent effect. For example, silicon greatly suppresses the metastable eutectic temperature whilst chromium has the opposite effect.

Figure 4.14. The influence of alloying additions on the eutectic temperatures of cast iron alloys.
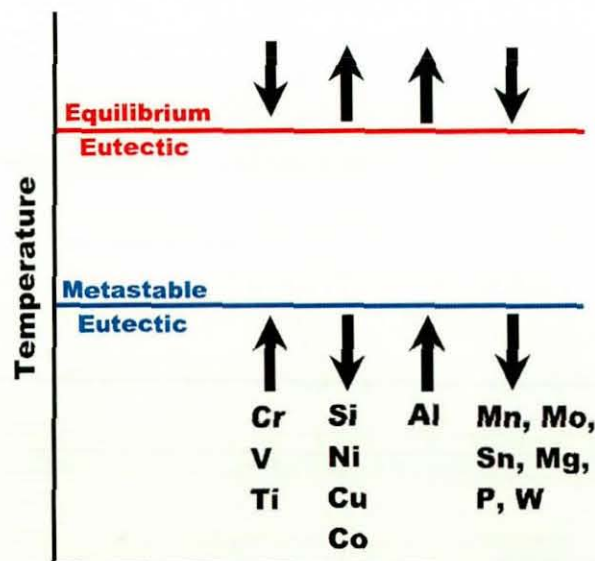
The influence of these alloying elements was further investigated using the eutectic temperature model. The composition of a typical cast iron alloy (3C, 2Si all wt.%) was input into the eutectic temperature model, with Fe making up the balance. Then, the quantity of each element was varied in turn to assess the influence of that particular element on the equilibrium and metastable eutectic temperatures and on the TEU temperature. Since the TEU calculation (equation 4.2) only accounts for the influence of C, Si and P, the other elements had no effect. The results of the calculations for the influence of C, Si, Cr, P and Mo are shown below. In the figures, TEUI represents the relationship for an inoculated iron (equation 4.2), whilst TEUB represents the relationship for an uninoculated iron (equation 4.3). The orange line represents the estimated behaviour of ductile iron, since the relationships for the TEU temperatures used in this work are based on grey irons. No relationships for the TEU temperatures of ductile irons could be found in literature. However, some empirical information was found, which indicated that the TEU temperatures for ductile irons were 10-20°C below those of grey iron [76]. The orange line represents this observation on figures 4.15-4.19 below (e.g. TEUI minus 10°C).

Figure 4.15. The influence of carbon on the eutectic temperatures and TEU.

◆ Equilibrium Eutectic ■ Metastable Eutectic ▲ TEUI ● TEUB × TEU Modified
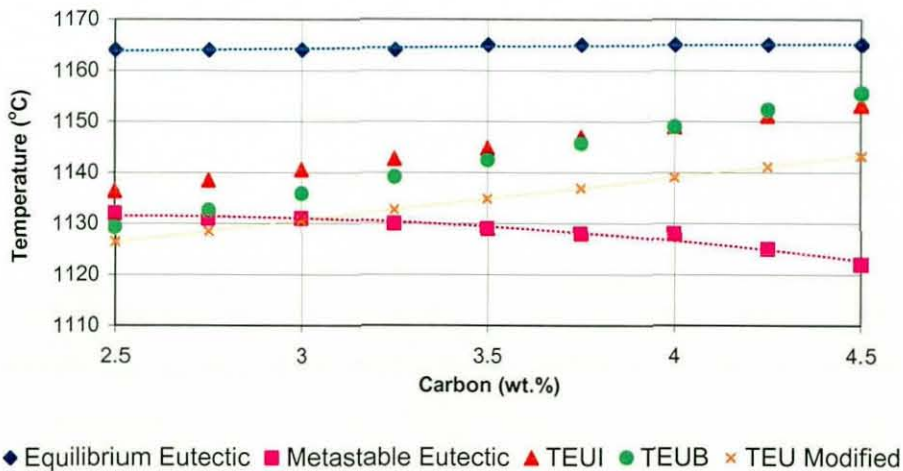
Some elements such as Cu and Mg, which are not displayed here, had less of an influence on the eutectic and TEU temperatures. The potent influence of elements like Si and Cr can clearly be seen in figures 4.16 and 4.17. Silicon increases the equilibrium eutectic temperature whilst suppressing the metastable eutectic.

Chromium has the opposite effect, hence it brings the two eutectic temperatures closer together.

Figure 4.16. The influence of silicon on the eutectic temperatures and TEU.

◆ Equilibrium Eutectic ■ Metastable Eutectic ▲ TEUI ● TEUB ✕ TEU Modified
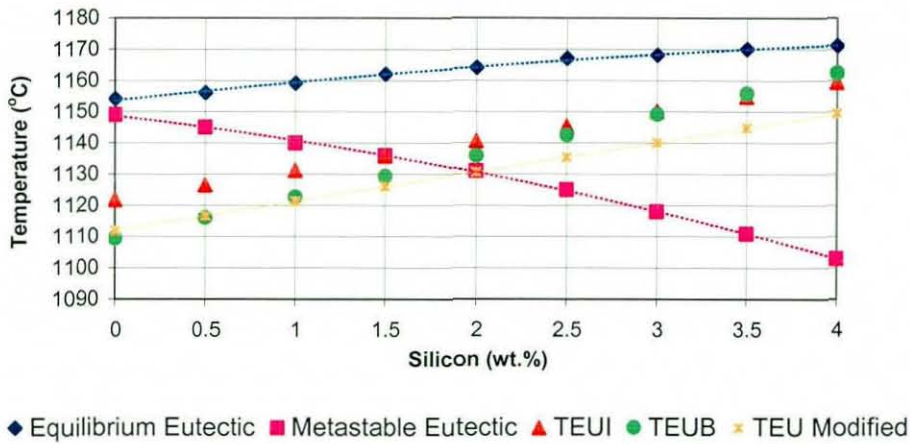
Figure 4.17. The influence of chromium on the eutectic temperatures and TEU.

◆ Equilibrium Eutectic ■ Metastable Eutectic ▲ TEUI ● TEUB ✕ TEU Modified
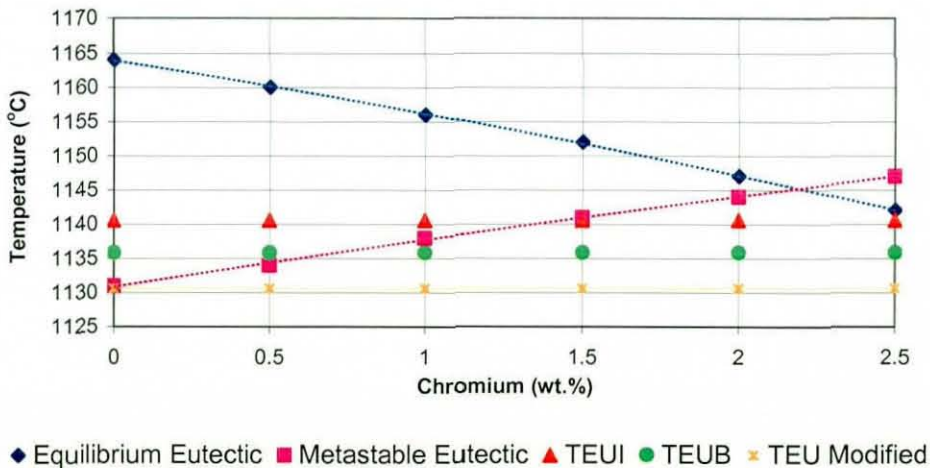
The behaviour of phosphorous also shows the potent influence of this element. However in practice, phosphorous is seldom present in any cast iron relevant to this research in quantities greater than 0.02 wt.%, and was only shown because it is one of the parameters in the TEU relationships. Other elements such as molybdenum reduce both the equilibrium and metastable eutectic temperatures. Carbon slightly raises the equilibrium eutectic temperature, whilst reducing the

metastable eutectic temperature. The trends shown in figures 4.15-4.19 are in agreement with those found in literature [2], which are shown in figure 4.14. It can be seen that such an approach can be used to investigate how additions of various alloying additions influence the eutectic temperatures and hence the chill tendency of ductile irons.

Figure 4.18. The influence of phosphorous on the eutectic temperatures and TEU.

◆ Equilibrium Eutectic ■ Metastable Eutectic ▲ TEUI ● TEUB × TEU Modified
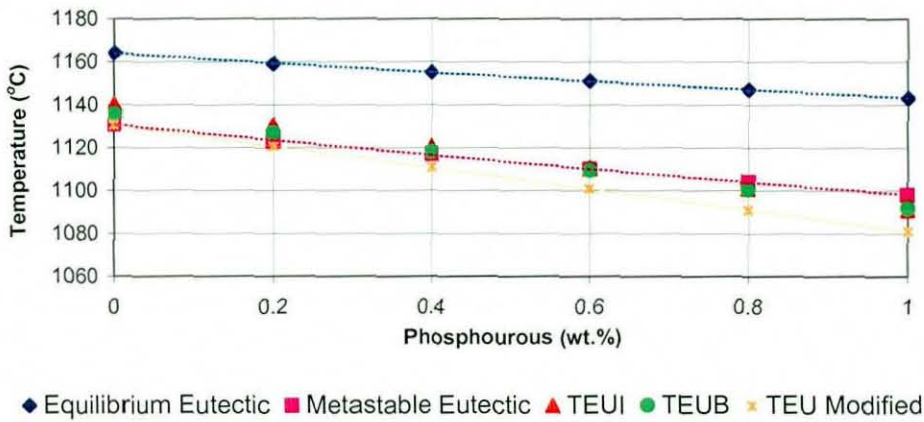
Figure 4.19. The influence of molybdenum on the eutectic temperatures and TEU.

◆ Equilibrium Eutectic ■ Metastable Eutectic ▲ TEUI ● TEUB × TEU Modified
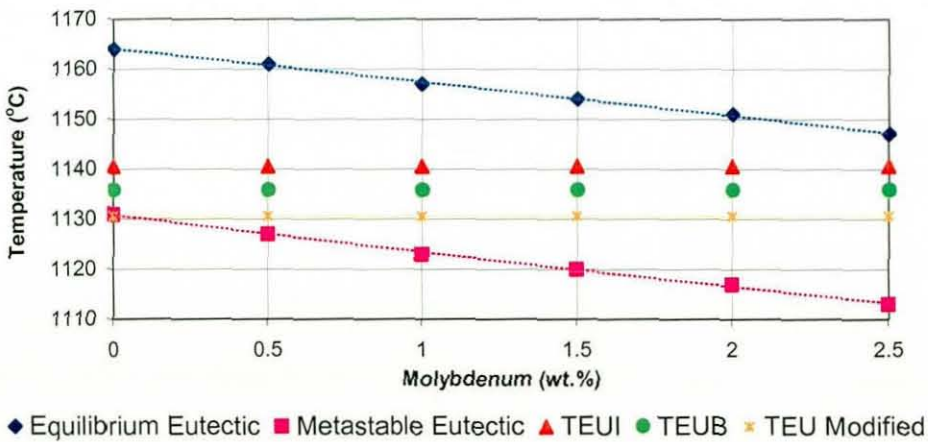
The influence of 1 wt.% of each element on the equilibrium and metastable eutectic temperatures of this alloy are summarised in table 4.3. It can be seen from the table that all the elements except C, Si and Cu reduce the metastable eutectic temperature. Cr is the only element of interest that increases the metastable eutectic

temperature. The table also shows whether additions of the elements diverge or converge the eutectic temperatures. Mn and Cr are the only elements that converge the eutectic temperatures. Mo additions neither diverge or converge the eutectic temperatures. An important issue to raise at this point is that although table 4.3 shows the general influence of single alloying additions, the influence of a combination of several alloying elements was not found to be cumulative.

Although this model is useful in comparing the chill tendency of different ductile iron compositions there are other parameters that it does not account for which have a large effect on chill tendency. The difference in cooling rate across casting sections, the material the chill is made from and its size and geometry as well as edge effects in the castings are some factors which all have an influence on the chill depth obtained in a casting. These parameters go beyond the scope of the current research project, so are discussed no further here. However, if a component is produced to a fixed geometry under identical casting conditions, the eutectic temperature model can be used as a useful tool to predict chill depth in the component of interest.

Table 4.3. Influence of 1 wt.% of alloying element on the equilibrium and metastable eutectic temperatures.

Element	Influence on Equilibrium Eutectic (°C) per 1 wt.% Addition	Influence on Equilibrium Metastable (°C) per 1 wt.% Addition	Converges or Diverges the Eutectic Temperatures as Element Quantity is Increased
C	+ 0.50	- 5.00	Diverges
Si	+ 4.25	- 11.50	Diverges
Mn	- 4.80	- 3.44	Converges
Mo	- 6.80	- 6.80	Neither
Mg	- 9.00	- 19.6	Diverges
P	- 21.00	- 32.6	Diverges
Cu	+ 2.00	- 3.84	Diverges
Cr	- 8.80	+ 6.40	Converges
Ni	0.00	- 4.80	Diverges

4.7 Summary

The phases present in the microstructure of a chilled ductile iron camshaft have been identified as graphite, pearlite and cementite. The cementite was shown to have an extremely high hardness, which due to its brittle nature and large volume fraction in the surface layers of the casting, resulted in the component cracking upon heat treatment. The theory behind the formation of this microstructure was introduced. Particular attention was drawn to the influence cooling rate variations, either naturally occurring across a component or artificially induced with the aid of a chill, had on the change of microstructure across the casting.

A model was developed that predicted the equilibrium and metastable eutectic temperatures and also the temperature at which the majority of solidification would occur, which for reasons of practicality was equated to the temperature of eutectic undercooling (TEU temperature). Hence, if the TEU temperature was found to be below the metastable eutectic temperature, quantities of cementite would be expected to form in the sample upon solidification. It was also demonstrated that good agreement was observed between measured and predicted eutectic temperatures for a number of different alloys.

A differential thermal analysis (DTA) experiment was performed on the chilled ductile iron sample and good agreement was obtained between the experimentally observed austenite formation and liquid fomation temperatures and the corresponding model predictions using the SGTE database. The potential of the model to be combined with cooling curve data (produced either experimentally or using Magmasoft), to predict the difference in microstructure across a component was also demonstrated. Finally the influence individual alloying elements have on the equilibrium and metastable eutectic temperatures was estimated, highlighting the potential of the model to be useful in new alloy development.

5 Microstructural and Mechanical Properties Model – Previous Work[†]

5.1 Modelling the Microstructure of ADI Alloys

5.1.1 Microstructural model introduction

A model that predicts the microstructure of ADI alloys has been developed during a recent research project at Loughborough University [20]. The chemical composition, austenitisation and austempering temperatures are the inputs into the model. The model then calculates the microstructure that would be produced after a specific heat treatment for the given alloy at the end of stage one of the austempering heat treatment. This is when the optimum mechanical properties are observed in the alloy, since the volume fractions of high carbon retained austenite and bainitic ferrite are a maximum [2;15;22]. Versions of the model also allow for both the austenitising and austempering heat treatment times to be entered, enabling the model to account for the kinetics of the various transformations. A schematic diagram of the modelling process is shown in figure 5.1.

The following sections of this chapter discuss in more detail the various stages of the microstructure model. This is followed by a section highlighting how the phase volume fraction predictions, have been used to predict the yield strength of ADI alloys. In chapter 6, the model is analysed in more detail, against a wide range of literature data and the results are critically assessed. Chapters 7 and 8 of this thesis discuss modifications to the microstructural model that have been performed as part of this work in order to improve the model predictions.

5.1.2 Modelling of austenite carbon content and graphite volume fraction

As can be seen in figure 5.1, the alloy composition in wt.%, the austenitisation temperature (°C) and austempering temperature (°C), are input into the model. This information, in conjunction with a commercially available Gibb's free energy minimisation package, MTDATA, and the SGTE thermodynamic database, were used to make equilibrium predictions of the graphite volume fraction and austenite carbon content as a result of the austenitising heat treatment. The austenitisation time of ADI alloys is generally long enough to expect equilibrium conditions to be

achieved in the microstructure, especially with respect to the fast diffusing carbon, and therefore the austenite carbon content could be expected to be close to the calculated equilibrium value. MTDATA predictions of the austenite carbon content have also been shown to be in good agreement with measured values for long austenitisation time (2 hours) [20].

Figure 5.1. Schematic diagram of the microstructural modelling process produced as part of a previous work [20].
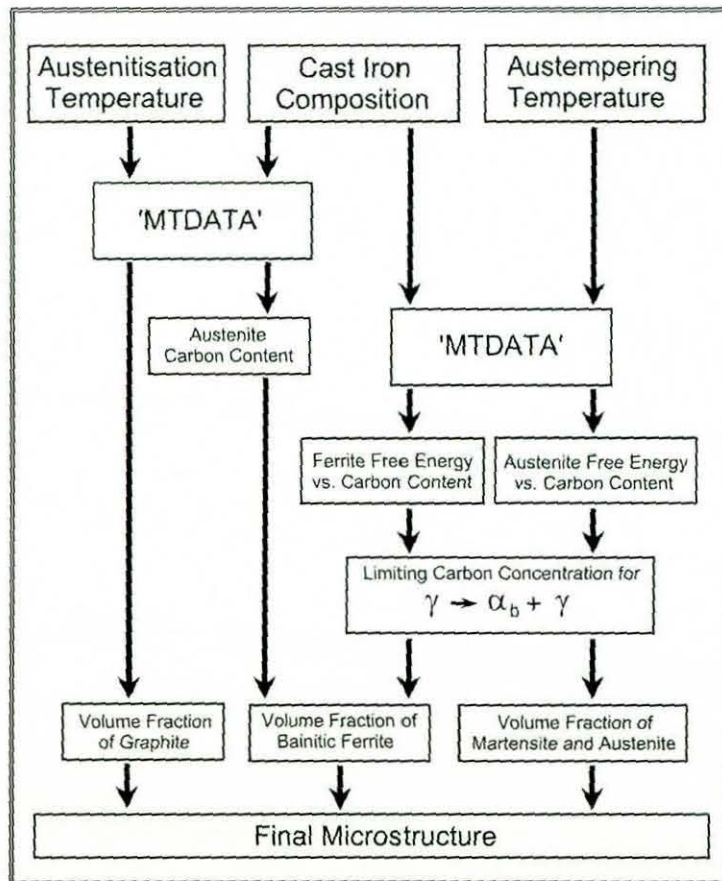
Accommodation of short (non equilibrium) austenitisation times was also included in the model, using both an equation proposed in literature and a complete diffusion couple model to solve the diffusion equation for the austenite/graphite equilibria [20;49]. The shorter austenitisation times were based on the following empirically based equation, which used data from Darwish and Elliott [49]:

$$C^0_\gamma = A \ln(t) + B \qquad [5.1]$$

where C^0_γ is the austenite carbon content at the end of austenitisation for a time of t minutes, and A and B are coefficients dependent on the austenitisation temperature[20]. Hence, a full range of ADI austenitisation times could be used to produce an accurate austenite carbon content prediction at the end of the austenitisation heat treatment.

It was assumed that the volume fraction of graphite predicted using this method remained constant after austenitisation through the subsequent quench to the austempering temperature, the austempering heat treatment itself and the final quench to room temperature after completion of austempering. There are studies on ADI alloys which support this assumption [22;83]. MTDATA can only predict thermodynamic equilibrium in systems, and therefore the volume fraction of bainitic ferrite cannot be predicted using this software package.

5.1.3 Bainitic ferrite volume fraction prediction

Five components are used in the model to predict the volume fraction of bainitic ferrite. They are the austenite carbon content, C^0_γ, equilibrium values of which were obtained using MTDATA (previous section), the austempering temperature, the limiting austenite carbon content, X_{T0}, the carbon content of saturated ferrite, X_α, and the alloy composition. It was assumed that C^0_γ does not change on quenching from the austenitisation temperature to the austempering temperature, due to the high cooling rate between the two heat treatment temperatures. Investigations on ADI alloys have supported the assumption that the matrix carbon content of ADI remains constant on quenching from the austenitisation temperature to the austempering temperature [22;83]. The experiments showed that for high austempering temperatures (where little or no carbide is present in the bainitic ferrite), measurements of the austenite carbon content after austenitisation are equal to the amount of carbon present in the matrix during austempering.

The formation of carbides was also neglected in the model. This assumption is valid for most ADI alloys, due to the high Si content which results in carbide formation

being suppressed [2,27]. At lower austempering temperatures, carbide formation may occur during austempering [24;29;30]. However, the carbide volume fraction remains small and hence was neglected in the calculations.

During austempering the austenite transforms to bainitic ferrite. Excess carbon is then partitioned from the bainitic ferrite into the surrounding austenite, increasing its carbon content. This reaction ceases when the carbon content in the austenite becomes too great and the diffusionless transformation to bainitic ferrite becomes thermodynamically impossible. This value is the limiting austenite carbon content, X_{T0}.

Figure 5.2. Calculation of bainitic ferrite volume fraction [20].

Divide mass fractions by densites to obtain volume fractions
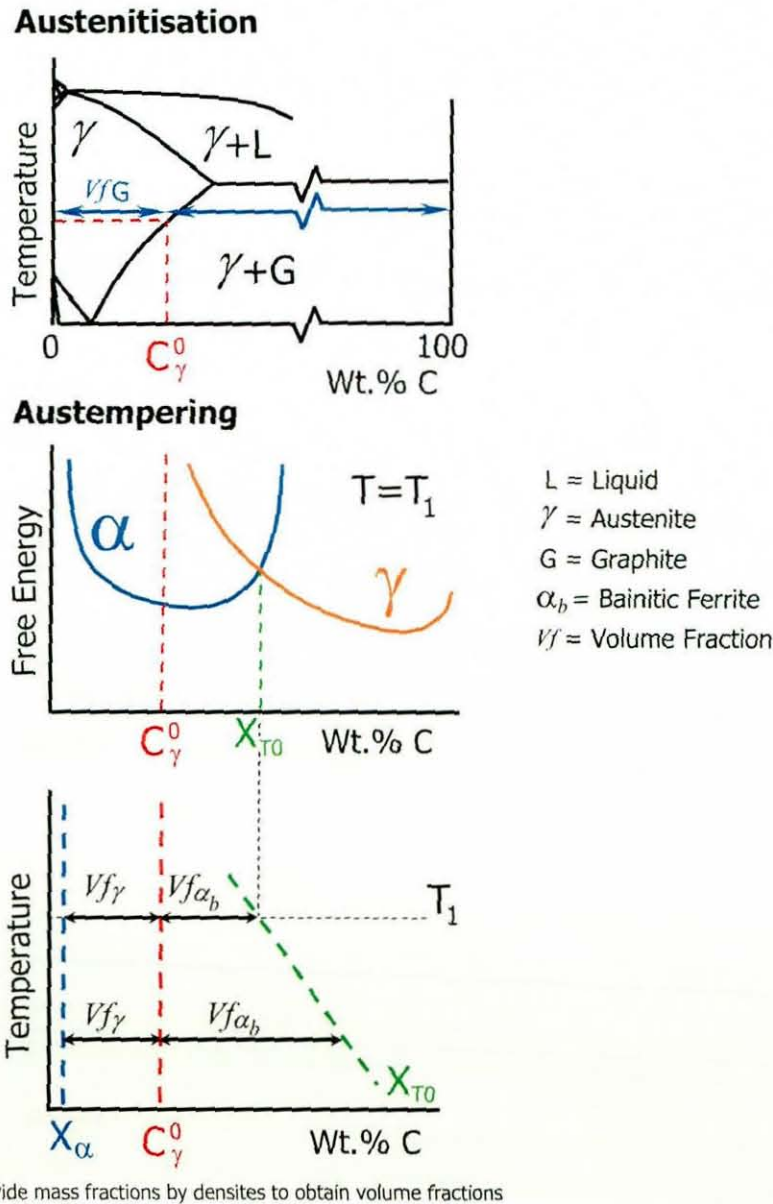
X_{T0} was calculated using MTDATA and X_{α} was calculated at the austempering temperature using an empirical expression [20]. The austempering temperature and alloy composition were used in conjunction with MTDATA to obtain the limiting austenite carbon content from the Gibb's free energy curves as shown in the austempering section of figure 5.2. X_{T0} represents the carbon concentration for which the Gibb's free energies of the austenite and ferrite phases become equal. From figure 5.2 it can be seen that the volume fraction of carbide free bainitic ferrite, $Vf\alpha_b$, can be simply calculated using the lever rule:

$$Vf\alpha_b = \frac{X_{T0} - C_{\gamma}^0}{X_{T0} - X_{\alpha}} \qquad [5.2]$$

where C_{γ}^0 is the initial austenite carbon content (following austenitisation), and X_{α} is the maximum carbon content of saturated ferrite at the austempering temperature. The value of the limiting austenite carbon content, X_{T0}, decreases with increasing temperature as shown in the diagram (figure 5.2), hence greater volume fractions of bainitic ferrite are predicted at lower austempering temperatures.

Figure 5.3 shows a comparison between the predicted bainitic ferrite volume fraction measurements made using the model and X-ray and dilatometry measurements of the volume fraction of bainitic ferrite for some ADI samples [20]. The predictions made by the model showed excellent agreement with the dilatometry results. However, comparison of the predicted results with those determined from X-ray diffraction measurements of the volume fraction of austenite, which was stable at room temperature, were not as good. A consistent discrepancy in the volume fraction results of approximately 30% volume fraction of bainitic ferrite was observed. This was also the case when predictions were compared to magnetic measurements of the volume fraction of bainitic ferrite in a steel reported by Le Houillier *et al* which are also shown in figure 5.3 [84].

Since the X-ray and magnetic measurements showed good agreement, it was suggested that the discrepancy in the results were not due to errors in the measured values [20]. Moreover, since excellent agreement was obtained between the initial austenite carbon content measurements, C_{γ}^0 and predictions, this source of error was eliminated [20]. However, as shown in figure 5.3 the predicted results do fall on a

straight line parallel to the ideal y=x relationship, suggesting the calculation of the volume fraction of bainite was not flawed. This conclusion lead to the experimental development of a new hypothetical limiting austenite carbon content, X_{T*}, which it was thought would produce better results between predictions and X-ray diffraction measurements:

$$X_{T*} = X_{T0} - 7.1 \times 10^{-3} \, T_\alpha + 3.65 \qquad [5.3]$$

where T_α is the austempering temperature (°C). Recalculation of the volume fraction of bainitic ferrite using X_{T*} produced predictions of bainitic ferrite in better agreement with the X-ray diffraction and magnetic measurements than X_{T0}. The predictions made by the model using X_{T*} as the limiting austenite carbon content are compared to a wide range of literature data in figure 5.4.

Figure 5.3 Measured and predicted volume fraction of bainitic ferrite for different alloys and various heat treatments [20].
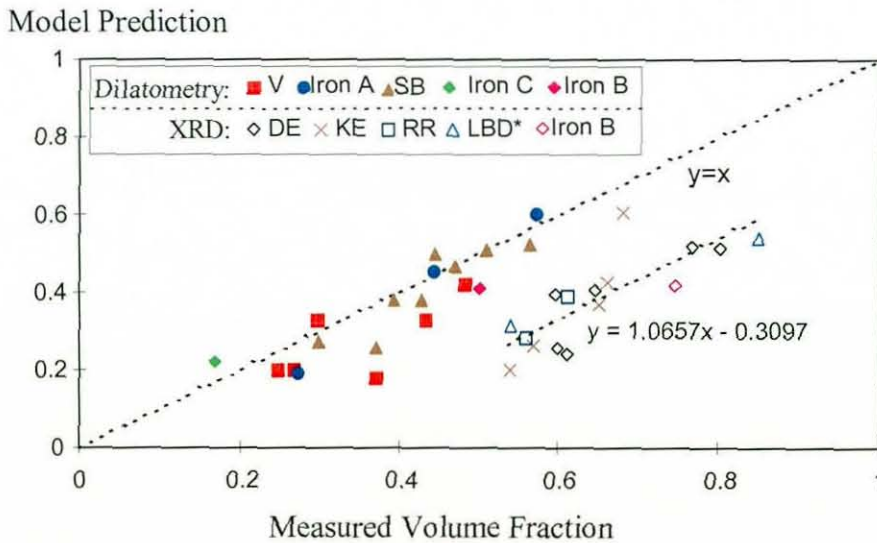
The predictions show good agreement with dilatometry (solid symbols). When compared with results deduced from XRD measurements (open symbols) the ideal relationship (y=x) is not obtained, however predictions do lie on a single line. The predictions for the LBD* steel are magnetic measurements [84]. Figure reproduced form [20].

5.1.4 Volume fractions of austenite and martensite

Once the volume fractions of bainitic ferrite and graphite are known, the amount of austenite present in the microstructure at the end of austempering but before cooling to room temperature can be calculated. The austenite furthest away from the graphite nodules may not have received enough carbon to have a martensite start temperature above room temperature and hence may transform to martensite on cooling to room temperature. The martensite start temperature was calculated for the alloys using the relationship proposed by Andrews [85], where the austenite carbon content was taken to be X_{T0} or X_{T*} depending on the model version:

$$M_s = 539 - 423(\ X_{T*} \text{ or } X_{T0}\ ) - 30.4Mn - 17.7Ni - 12.1Cr - 7.5Mo \quad [5.4]$$

where M_s is the martensite start temperature (°C) and Mn, Ni, Cr and Mo are the concentrations in wt.% of the respective elements in the alloy. Equation 5.4 was then used in the following relationship to establish the proportion of the austenite phase that transforms to martensite on cooling to room temperature:

$$1 - Vf_m = \exp(-0.011(M_s - T_Q)) \qquad [5.5]$$

where Vf_m is the volume fraction of martensite and T_Q is the temperature (°C) to which the casting is cooled [20].

The previous sections have described how the microstructural model calculates the microstructure of the ADI alloys given their composition and heat treatment parameters. The separate sections of the model, including subroutine calls to perform Gibb's energy minimisation's using the Application interface within MTDATA, were compiled into a single Fortran computer program that was used as a starting point in the current work. This model however does not take into account any segregation that occurs in the microstructure or the kinetics of the austempering reaction.

Data from over 200 different ADI alloys were taken from literature and this was used to validate the accuracy of the model [11;14;15;17;22;23;32;39;41;44;49;52-54;86-95]. Figure 5.4 compares the predictions for the volume fraction of austenite made by the model

to those obtained from literature. As can be seen in figure 5.4, in general good agreement is obtained between the model predictions and the literature values. These results will be discussed in more detail in chapter 6.

Figure 5.4. Comparison of model prediction of the volume fraction of austenite in ADI alloys with those taken from literature, using X_{T*} as the limiting austenite C content*.
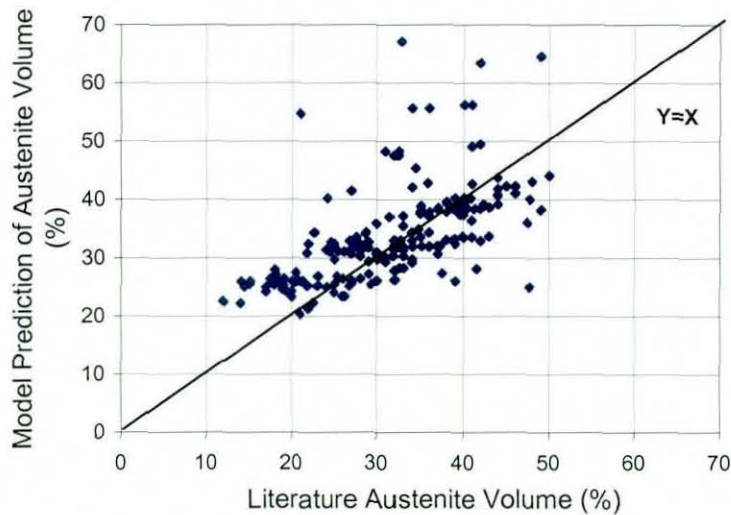
*The literature values are obtained using X-ray diffraction and therefore do not consider the presence of graphite in the sample. The volume faction of graphite in ADI alloys in generally small (<0.1) and therefore should not greatly influence the model predictions. Nevertheless, the predictions shown above were made by normalising the model predictions to account for the absence of graphite volume fraction measurements in the experimental results, therefore producing a like with like comparison.

5.2 Modelling of Mechanical Properties of ADI Alloys

The microstructural model outlined in section 5.1 has also been used as a basis for the prediction of simple mechanical properties of ADI alloys, such as yield strength and hardness [96]. As previously stated, the model predicts the microstructure of ADI alloys at the end of stage one of the austempering heat treatment, given their composition and heat treatment temperatures. This information

is then used as the basis of the strength prediction of the ADI alloy. In a simple law of mixtures approach, the strength of each phase is calculated and then multiplied by its volume fraction (as predicted by the microstructural model) and then summed to produce the strength prediction for the alloy [96]. The process of calculating the strength of each phase in the microstructure will now be examined in more detail.

5.2.1 Calculation of the yield strength of the bainitic ferrite phase

The mechanical properties of mixed microstructures of bainite and martensite have been investigated by several authors [16,97], and were used as the basis for the calculation of the strength of the bainitic ferrite phase in the ADI alloys. These works tackle the problem by considering the strength of a number of intrinsic elements that contribute to the overall strength of the steel. These intrinsic elements were then adapted by using ADI relevant parameters to predict the strength of the ADI alloys. Bhadeshia [16] considers the following components for the yield strength of a steel:

- The strength of pure annealed iron, which is equal to 219 MPa [16] and will be the same for ADI alloys, for which the majority element is iron.
- The alloy solid solution strengthening, information on which can be found in published experimental data [98]. ADI alloys typically contain more alloying elements than steels, but the same theory was used in these instances as applicable to steels.
- The interstitial carbon strengthening, σ_{ssc}, which can be predicted using solid solution theory from the following formula, where the strength is in MPa

$$\sigma_{ssc} = 1722.5 \times X_\alpha^{0.5} \qquad [5.6]$$

and the concentration of carbon, X_α is expressed in wt.% [16]. Only a small amount of carbon can be dissolved into bainitic ferrite, so for both steels and ADI alloys, X_α is assumed to be 0.02 wt.%C [16].
- The strengthening due to lath size, σ_g, which is found using the following formula:

$$\sigma_g = 115 \ (L)^{-1} \qquad [5.7]$$

where σ_g is in MPa and L is a mean linear intercept of bainitic ferrite plates measured at random sections on random orientations [16]. L is approximately twice the plate thickness, t_α. This is not based on the Hall-Petch relationship, but another relation due to Langford and Cohen [99], because at sub micron grain sizes the mechanisms of yielding are different, involving the initiation of the dislocations at the sources in grain boundaries [33]. For ADI alloys, plate thickness varies as a function of austempering temperature, so the following empirical relationship based on TEM observations, was derived to predict the magnitude of t_α in μm as a function of austempering temperature, T_α which is measured in degrees Celsius[96]:

$$t_\alpha = 0.004 \times (T_\alpha + 273.15) - 1.09 \qquad [5.8]$$

- The strengthening due to dislocations. When martensite or bainite form at high temperatures, the shape change due to the shear transformation causes plastic deformation, and hence the accumulation of dislocations in the parent and product phases. The extent of the plasticity depends on the yield strength and hence on temperature [16]. It has been suggested that the dislocation density, ρ_d, can be represented empirically as a function of temperature alone for the temperature range 570-920K [16]:

$$\log_{10}\{\rho_d\} = 9.2840 + \frac{6880.73}{(T_\alpha + 273.15)} - \frac{1780360}{(T_\alpha + 273.15)^2} \qquad [5.9]$$

where ρ_d has units of m^{-2}. The strengthening of bainite, σ_p (MPa) due to the dislocations is given by:

$$\sigma_p = 0.38 \ \mu b \ (\rho_d)^{0.5} \cong 7.34 \times 10^{-6} \ (\rho_d)^{0.5} \qquad [5.10]$$

where μ is the shear modulus and b is the magnitude of the Burgers vector [16]. This is the same relationship that was used to predict the strength contribution of dislocations to the bainitic ferrite phase in ADI alloys [98]. The individual strength

components calculated using this methodology were summed to predict the strength of the bainitic ferrite phase in ADI alloys [98].

5.2.2 Calculation of the martensite phase strength

The strength of any martensite present in the alloys was calculated using an identical method as that of bainitic ferrite (see section 5.2.1), the only differences being that the C content in solid solution in the martensite is higher and the martensite plate size is smaller than that of bainitic ferrite. The strength due to solid solution carbon in martensite, σ_{ssc} can be estimated using the following expression, where the strength is in MPa [97]:

$$\sigma_{SSC} = 1171.3 \times X_{T0}^{1/3} \qquad [5.11]$$

Equation 5.7 was again be used to estimate the strengthening due to the martensite plate size, however, for simplicity the martensite plate size was assumed to be half that of bainitic ferrite.

5.2.3 Calculation of the austenite phase strength

The yield strength of the austenite phase in ADI alloys can also be simulated from a model found in literature. The empirical model taken from a paper by Singh and Bhadeshia calculates the strength of austenite in steels based on the transformation temperature and the composition of the steel as follows [100]:

$$\sigma_y = (1 - 0.26 \times 10^{-2} \, T_r + 0.47 \times 10^{-5} \, T_r^2 - 0.326 \times 10^{-8} \, T_r^3) \times 15.4 \, (4.4 + 23 \, w_c$$
$$+ 1.3 \, w_{Si} + 0.24 \, w_{Cr} + 0.94 \, w_{Mo} + 32 \, w_{Ni}) * \qquad [5.12]$$

* The equation was modified from the one found in the reference by the addition of the second bracket that was apparently missing from the equation. Hence, a correct strength value was produced once the error was corrected.

where $T_r = T_\alpha - 25$, and T_α is the transformation temperature (°C) and w represents the concentration of the element identified by the subscript in wt.%. The yield strength of the austenite is given in units of MPa. This was the method used to predict the strength of the austenite phase in ADI alloys [96].

5.2.4 Graphite phase strength

Microhardness measurements were performed to predict the strength of the graphite phase in the ADI alloys. A strength value of 120 MPa was then used for the strength prediction method [96].

5.2.5 Results of yield strength predictions

Once the strength of the individual phases in the microstructure were calculated, a simple law of mixtures approach was used to estimate the yield strength of the alloys. The results of these predictions are shown in figure 5.5. Again, reasonable agreement is obtained between the measured and predicted alloy yield strengths. The discrepancies between the predictions and measured values are also analysed in more detail in Chapter 6.

Figure 5.5. Predicted yield strength of alloys in database using law of mixtures approach.
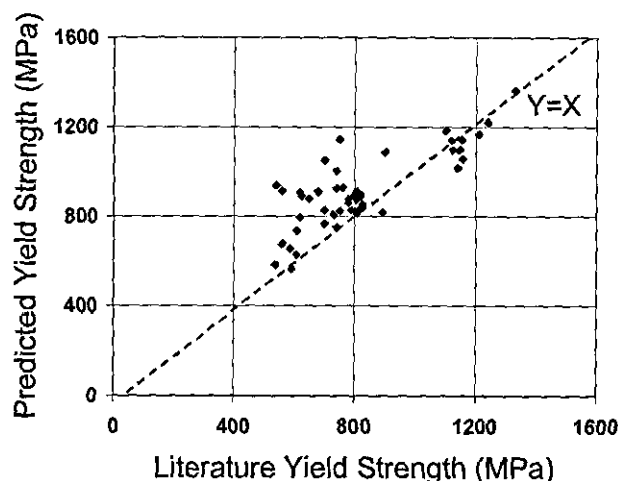
5.3 Summary

A microstructural model, produced as part of a previous work [20], which is capable of predicting the microstructure and mechanical properties of ADI alloys, has been introduced and it's theoretical basis has been discussed. The results of predictions made by the model have been compared to corresponding literature data for a wide range of alloys. In general good agreement has been obtained between predicted and reported microstructural and mechanical property data.

6 Microstructural and Mechanical Properties Model Analysis

6.1 Introduction

Chapter 5 introduced the microstructure and mechanical properties model for ADI alloys, which was the starting point for this work. It also demonstrated the accuracy of predictions made by the model, by means of comparing estimates of microstructural volume fractions and yield strength values made by the model to measurements on actual alloy systems. This chapter analyses the predictions made by the model in greater detail, and highlights the reason for errors made by the model, when it is used to predict the microstructure in certain types of ADI alloys.

6.2 Model Testing Using Published Data

Extensive testing of the microstructure model was performed using published data taken from literature [11;14;15;17;22;23;32;39;41;44;49;52-54;86-95]. A database containing information such as alloy composition, heat treatment times and temperatures, phase volume fraction and mechanical property measurements taken after completion of stage 1 of austempering was created. The completed database contained information from over 200 different alloys. The model version using the modified limiting austenite C content, X_{T*}, (see section 5.1.3) was run for each alloy in the database and the measured and predicted volume fractions of austenite at the end of stage 1 of austempering were compared. The results of the microstructural model predictions are presented in figure 6.1.

As can be seen in figure 6.1 reasonable agreement is observed between the measured and predicted volume fractions for each specimen. The austempering temperature of each point in figure 6.1 is also highlighted. It is interesting to note the clusters of points that occur for each particular austempering temperature. The significance of these clusters is discussed in section 6.3. As would be expected, alloys austempered at lower temperatures are generally predicted to contain lower volumes of austenite in their microstructures and vice versa. This is due to the increase in the limiting austenite carbon content X_{T0} as the transformation temperature is reduced as shown in figure 5.2. A greater volume fraction of bainitic ferrite has to be produced at lower transformation temperatures before the austenite

carbon content is enriched enough to reach X_{T0}, which signifies the end of stage 1 of austempering.

Figure 6.1. Microstructure predictions for alloys in the database as a function of austempering temperature (°C).

Comparison of Literature and Austenite Volume Fractions For Different Austempering Temperatures
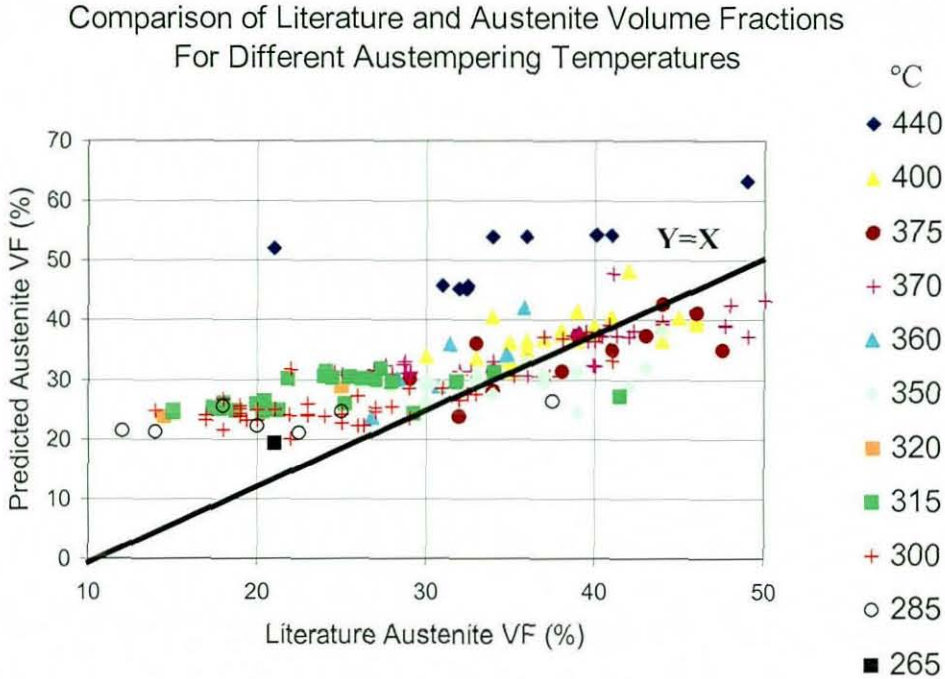
6.3 Microstructure Model Analysis

Analysis of the clusters of points from the same austempering temperature shown in figure 6.1 was performed. The average X_{T0} value for each austempering temperature data group was calculated from the individual X_{T0} values of each data group. So for example at 300°C the average X_{T0} value was calculated from all the individual X_{T0} values of the alloys that were austempered at 300°C. This process was repeated at each austempering temperature.

A series of constants ranging in size from 0.8 to 2.0, increasing in size by 0.1 were then added to the average X_{T0} values previously found at the different austempering temperatures. The volume fraction of austenite was then calculated using the new X_{T0} + constant parameters, with the aid of equation 5.2. These data were then plotted separately for each austempering temperature against the corresponding literature measurement of the austenite volume. This is shown in

figure 6.2 for the data at 440°C. The constant that when added to the average X_{T0} value produced the best fit between the predicted and measured austenite volumes was then selected and added to the average X_{T0} value to produce a new austenite carbon content known as X_{Fit} (i.e $X_{Fit} = X_{T0} + A$, where A is a constant specific to the austempering temperature). Figure 6.2 shows how the X_{Fit} parameter was calculated for the data points at 440°C. As can be seen in the figure, the best agreement between the literature and model values occurs when $X_{Fit} = X_{T0} + 1.2$ in this case. The process was then repeated for each austempering temperature.

Figure 6.2. An example of how the X_{Fit} parameter was calculated at 440°C.
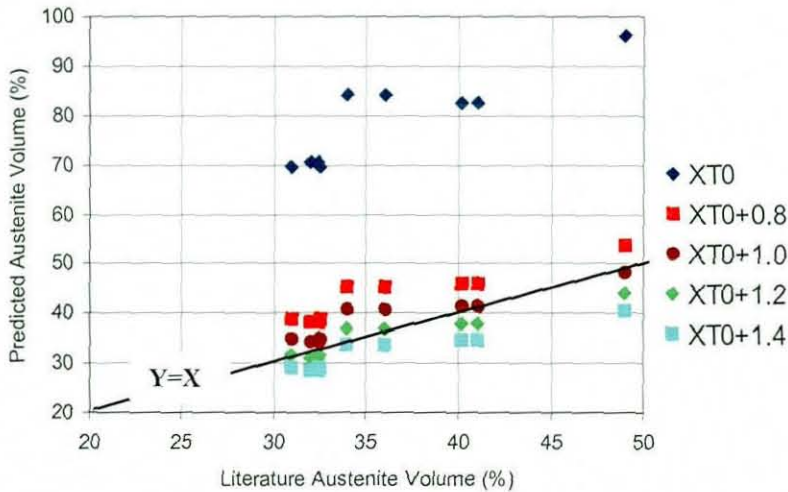
X_{T^*} was replaced with the new austenite carbon content X_{Fit} in the lever rule calculation (see equation 5.2). When used in the lever rule calculation $X_{Fit,}$ provides the best match between the predicted and measured austenite volume fractions. The X_{Fit} values are plotted against austempering temperature in figure 6.3. Although X_{Fit} produces the best trend between the literature results and model predictions it lacks any physical justification and is used in this work only as an aid to help demonstrate weaknesses in the model predictions. A polynomial expression was then fitted to X_{Fit} as a function of austempering temperature to highlight the trend of the X_{Fit} data. Figure 6.3 shows the tendency observed along with the average and range of X_{T0} and X_{T^*} values for the data at each austempering temperature.

As can be seen in figure 6.3 the polynomial expression shows good agreement with X_{T^*}, which is the austenite carbon content used in the original version

of the microstructural model, except at the highest austempering temperature of 440°C and lower austempering temperatures (less than 300°C). At high austempering temperatures the austenite carbon content predicted by the polynomial expression is shown to increase. This contradicts the trend expected from theory. As the austempering temperature increases the transformation to bainitic ferrite ultimately decreases to zero, since the austenite can only transform to bainitic ferrite if its carbon content is less than the value X_{T0} [101]. The limiting austenite carbon content X_{T0} is also shown in figure 6.3. As would be expected it reduces with increasing austempering temperature, which is contradictory to the trend highlighted by the polynomial expression at austempering temperatures above 400°C.

Figure 6.3. Polynomial expression for the austenite carbon content as a function of austempering temperature.
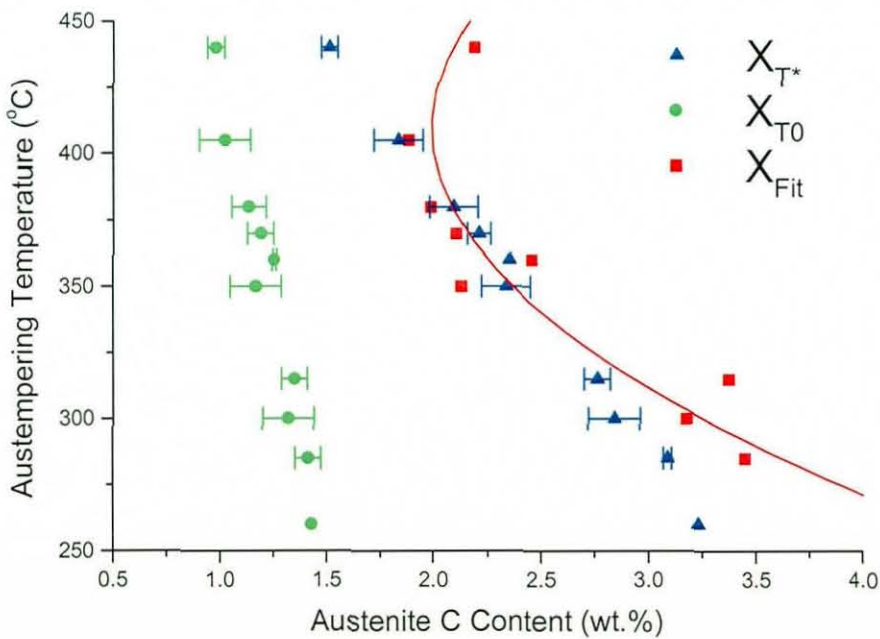
The data for the alloys austempered at 440°C comes from different sources, so experimental error in these measurements is unlikely to be the cause of the inaccuracy [11;15;49;86]. In fact, it is thought the trend observed arises due to the closure of the processing window during austempering at this high temperature.
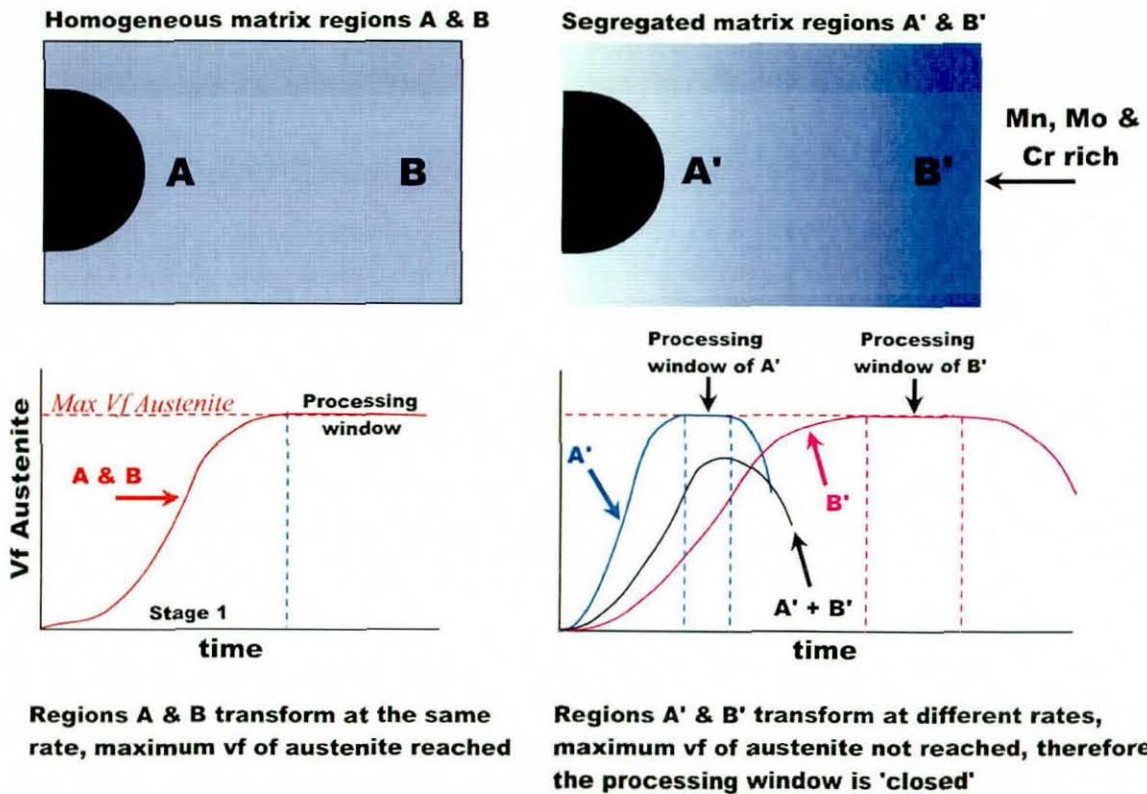
Normally in ADI alloys the stage 1 austempering reaction proceeds at a reasonably uniform rate throughout the alloy. However, austempering progresses at

a fast rate in ADI alloys at high temperatures. Stage 1 of the austempering process can be completed in as little as 15 minutes in ADI alloys austempered at 440°C [15]. Problems can be encountered in ADI alloys when a segregated alloy is subjected to such a high temperature austempering heat treatment. Due to segregation of alloying elements in the castings, the local transformation rates differ. Si segregates strongly to the graphite nodules [2;32;102]. Since this element is a strong ferrite stabiliser, the driving force for ferrite formation in these areas of the microstructure is increased, leading to a fast transformation rate during austempering [32;48;103]. Mn and Mo however segregated between the graphite nodules [24;48;102]. These elements tend to slow the transformation rate in these matrix areas [2;41;48]. Therefore at high austempering temperatures, due to the faster transformation rate in the Si rich matrix regions, the stage 1 austempering reaction is completed quickly followed after a short time by the commencement of the stage 2 reaction. Meanwhile, the areas of the matrix rich Mn and Mo, which transform at a slower rate, have only just started the stage 1 austempering reaction [23;32]. Hence the maximum volume fraction of austenite in not reached, as part of the austenite breaks down into the stage 2 transformation products of ferrite and carbides. In these alloys, the processing window is said to be closed [15]. A closer look at the sources of the 440°C data revealed that the processing window was closed for all the alloys in question [11;15].

Figure 6.4 shows a schematic diagram of this problem, where microstructure regions A′ and B′ transform at different rates. It can be seen in the diagram that this results in the maximum volume fraction of austenite not being reached in the alloy, even though the local maximums in regions A′ and B′ are reached. Crucially, the maximum austenite volume fractions are reached at different austempering times in the regions A′ and B′. The resulting alloy will display inferior mechanical properties because of the lower volume fraction of austenite present in its microstructure.

At lower austempering temperatures, the austempering process and the processing window generally cover greater time periods. Although different regions of the matrix still transformation at different rates, the entire matrix of the alloy is usually found to be present at the same time within the processing window, due to the increased time period that the processing window spans. Hence these alloys reach their maximum potential regarding their mechanical properties.

Figure 6.4. A schematic diagram of the closure of the processing window in ADI alloys.

Regions A & B transform at the same rate, maximum vf of austenite reached

Regions A' & B' transform at different rates, maximum vf of austenite not reached, therefore the processing window is 'closed'

The microstructure model assumes that the maximum volume fraction of austenite is always reached. In ADI alloys at high transformation temperatures this may not be the case, due to the combination of a fast transformation rate and segregation effects, hence the model predictions do not accurately match with the experimental results. This is demonstrated by the trend in figure 6.1. The literature measurements of the austenite volume fraction are below their maximum values, due to the onset of the stage 2 reaction in some matrix regions. When fitted with the model predictions, this results in an over prediction of the volume fractions of bainitic ferrite due to the matching of the experimental and literature austenite volume fractions. Hence the X_{Fit} parameter increases at the high austempering temperatures. If the microstructure transformed to bainitic ferrite at a uniform rate then the model predictions would be much more accurate at these high austempering temperatures. However, as demonstrated by the literature results, this is not the case in these alloys. At lower austempering temperatures the stage 1 transformations can take several hours to reach completion and any difference in local transformation kinetics

is not significant due to the increased time of transformation, so the model predictions are much more accurate.

At lower austempering temperatures the microstructure model predictions made using X_{T*} seem to under predict the volume fraction of bainitic ferrite in comparison with the polynomial expression. This difference increases as the austempering temperature decreases. Due to the high content of Si found in ADI alloys carbide precipitation is largely inhibited during transformation, especially at higher austempering temperature [32,83]. However, at lower austempering temperatures carbides such as θ, η and ε have all been observed in ADI alloys[39;40;43;44]. The microstructure model assumes that no carbide formation occurs during any stage of the alloy heat treatment. However, the formation of cementite or other carbides could lead to the formation of more bainitic ferrite since some of the carbon that should enrich the austenite after it is partitioned from the bainitic ferrite will reside in carbides and not the austenite matrix. More bainitic ferrite formation will therefore occur before the austenite is enriched enough in carbon for the formation of bainitic ferrite to cease [16]. Hence the formation of carbides could lead to the model under predicting the volume fraction of bainitic ferrite at lower austempering temperatures as shown in figure 6.3.

It has been shown that the amount of supersaturated carbon trapped in bainitic ferrite plates increases as the austempering temperature reduces in an ADI alloy and austempered spheroidal graphite cast steels [21,83]. This supports the hypothesis that the amount of carbide precipitated in bainitic ferrite increases as the austempering temperature reduces. An increase in the amount of carbide present in bainitic ferrite as the austempering temperature reduces also matches the trend observed in figure 6.3, where the difference between the model predictions and the polynomial expression increase, as the austempering temperature reduces.

A similar argument could also be applied to a situation where carbon diffuses out of the matrix and into the graphite nodules during austempering instead of enriching the austenite. However, the under prediction of the austenite volume fraction by the model increases with a decrease in temperature. So if this were the case, the rate of carbon diffusion to the graphite nodules would have to increase with a reduction in temperature. Hence it can be seen that this hypothesis goes against the first law of diffusion.

6.4 Summary

Microstructural predictions for ADI alloys made by a model, (which was produced in previous work), have been analysed in some detail, as part of this work. The results of predictions made by the model have been compared to corresponding literature data for a wide range of alloys. In general good agreement has been obtained between predicted and reported microstructural and mechanical property data. Anomalies in predictions made by the model have also been investigated. For high austempering regimes, errors in model predictions have been linked to the segregation of alloying elements, which slows the local transformation rate. At lower austempering temperatures, it has been shown that model inaccuracies could be related to the precipitation of carbides, which is not accounted for in the current model.

7 Accounting for Segregation in the Microstructure Model

7.1 Introduction

Segregation of alloying elements that occurs in ADI alloys is known to slow down the austempering rate in segregated matrix areas, therefore making commercial heat treatments more difficult to perform [2;22;23;32;38]. Thus, the development of a model that can predict the magnitude of alloying element segregation in ductile iron alloys would be beneficial to industry. This chapter begins by introducing the Scheil approach as a method of predicting the segregation behaviour of alloying elements in ADI alloys. It then describes how the Scheil approach has been combined with the microstructure model to enable the segregation of alloying elements which occurs in castings, to be accounted for by the model. The predictions made by the model are then compared to experimentally obtained segregation profiles.

7.2 Scheil Approach Introduction

Segregation of alloying elements can lead to differing rates of transformation during the austempering of ADI alloys, as discussed in the previous chapter. It is therefore necessary to incorporate the effect of segregation of alloying elements into the microstructure model. In order to do this, a Scheil type approach was taken.

The Scheil approach considers the one-dimensional freezing of an alloy. It assumes that diffusion of solute does not occur in the solid, and that in the liquid diffusion is rapid and complete [104]. The first assumption requires that the composition of the freezing solid varies continuously as the solidification front advances and that the solid retains this composition variation after the front has passed. Its composition is always uniform, since there is complete diffusion in the liquid, although this uniform composition changes as solidification progresses [104]. A typical example of an alloy that can be modelled using the Scheil approach is shown in figure 7.1a. This phase diagram has been idealised by assuming the solidus and liquidus lines are straight. X_S and X_L are the mole fractions of solute in the solid and liquid respectively. The partition coefficient k can be defined as $k = X_S/X_L$ [105].

Figure 7.1. Schematic description of Scheil solidification in an alloy.
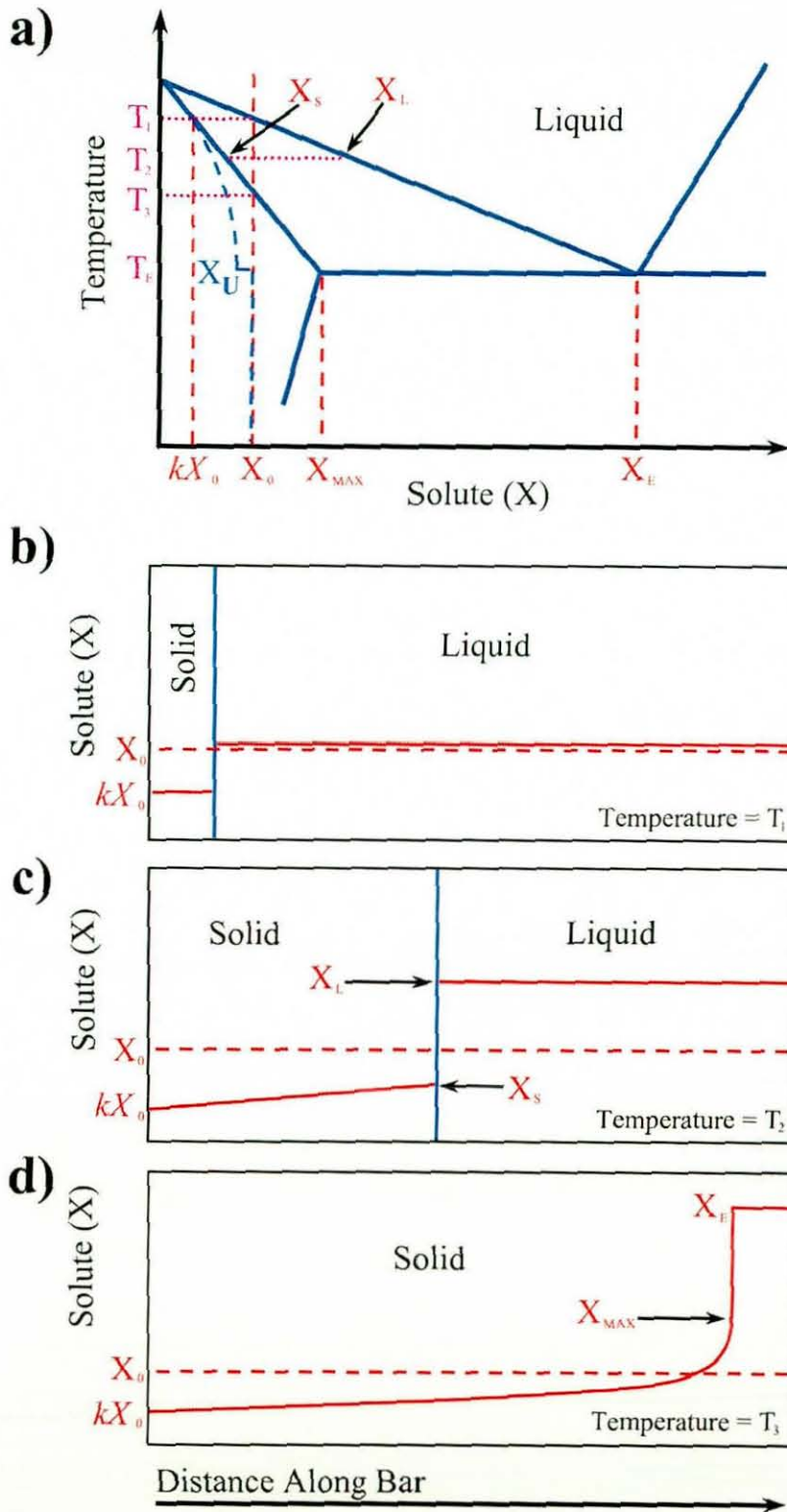
Consider a planar solid/liquid interface moving along an alloy bar. During equilibrium solidification, an alloy of composition X_0 in figure 7.1a begins solidification at temperature T_1. The solid that forms initially has a composition kX_0. As the alloy cools further, more solid forms. If the cooling rate is slow enough, the alloy will solidify homogeneously, with the composition of the solid and liquid following the solidus and liquidus lines in figure 7.1a. Since solidification is one dimensional, conservation of solute is required (ignoring the difference between molar volume of the two phases). At T_3, the last liquid will have a composition X_0/k and the bar will have a composition X_0 along its entire length [105].

Using the Scheil approach, the first solid will again form at temperature T_1, and at this stage contains kX_0 moles of solute. Because $kX_0 < X_0$, the first solid will contain less solute than the liquid from which it forms and hence solute is rejected into the liquid and raises its concentration above X_0 (see figure 7.1b). The temperature of the liquid has to decrease before further solidification can occur and the next solid layer will be slightly richer in solute than the first one. This process continues and therefore the liquid becomes richer in solute, as the temperature of solidification decreases, as shown in figure 7.1c.

The composition of the solid and liquid in contact with each other at this stage can be given by the equilibrium phase diagram. However, there is no diffusion in the solid, and therefore the separate solid layers retain their original composition. Hence the mean composition X_U is always lower than the composition at the solid/liquid interface (see dashed line in figure 7.1a). The lever rule can be used to calculate the relative amounts of solid and liquid at a given interface temperature, using X_U and X_L. Hence the liquid can become richer in solute than X_0/k and it may even reach the eutectic composition, X_E. A fully solidified bar will have a solute composition as shown in figure 7.1d [105].

The variation of X_S along the bar can be obtained by equating the solute rejected into liquid when a small amount of solid forms to the resulting increase in the solute levels in the liquid. Ignoring the molar volume differences:

$$(X_L - X_S)df_S = (1 - f_S)dX_L \qquad [7.1]$$

where f_s represents the weight fraction of solid material in the bar. Integrating equation 7.1 using the conditions that occur at the start of freezing, namely $f_s = 0$ and $X_S = kX_0$ results in equation 7.2:

$$X_S = kX_0 (1 - f_s)^{(k-1)} \qquad [7.2]$$

and

$$X_L = X_0 (1 - f_s)^{(k-1)} \qquad [7.3]$$

Equations 7.2 and 7.3 are known as the Scheil equations [105]. The extent of segregation calculated by the Scheil process is usually more than encountered during solidification, due to solid state diffusion [104], i.e. it represents the worst case scenario. In real alloys segregation of alloying elements is likely to be somewhere between that predicted by the Scheil approach and equilibrium. Section 7.3 describes how this approach was used in combination with the microstructure model to account for the segregation of alloying elements when making volume fraction predictions.

7.3 Segregated Microstructure Model Development

Section 2.1.7 highlighted three different models of the solidification process, which can be used for ADI alloys. In this work, the uninodular model was used as a basis to represent the segregation pattern that occurs upon solidification in ADI alloys. Although this method is not thought to represent as accurately as possible the reality in real alloy systems, its simplicity enables it to be easily incorporated into modelling processes, and hence it was used in this work.

The uninodular model assumes the first phase to nucleate is graphite. The graphite nodules then act as nucleation centres for the remaining liquid to solidify. The remaining liquid solidifies firstly on the graphite nodules and then growth of the solid continues out from the graphite nodules, which are therefore at the centre of the growth. The alloy therefore solidifies as a series of 'cells', each starting from a graphite nodule. As solidification progresses, segregation of the alloying elements in the liquid occurs. The worst segregation is found at the boundary between two 'cells' (halfway between two nodules). Therefore, when the Scheil approach is being used

in conjunction with the uninodular methodology to model segregation in ADI alloys, it represents the range of segregation that occurs between two graphite nodules. A slave computer program (see section 3.4) was written in Fortran, that in conjunction with MTDATA, simulated Scheil solidification of ADI alloys. This process is outlined schematically in figure 7.2.

Figure 7.2. Schematic diagram of the solidification model.

SEGREGATION MODELLING

```
                    ┌──────────────────────┐
                    │  Input Composition   │
                    └──────────────────────┘
                               │
                    ┌──────────────────────────────┐
                    │ Calculate Liquidus Temperature │
                    └──────────────────────────────┘
                               │
             ┌───────────────────────┐
             │   MTDATA Computes      │◄──────────────┐
             │   Equilibrium          │               │
             └───────────────────────┘               │
                               │                      │
             ┌───────────────────────┐      ┌──────────────────┐
             │   Record Mass and      │      │  Reduce System   │
             │   Composition of       │      │  Temperature     │
             │   Solid Shell Formed   │      └──────────────────┘
             └───────────────────────┘               ▲
                               │                      │
             ┌───────────────────────┐               │
             │   Deduct Shell Mass    │               │
             │   From System Mass     │               │
             └───────────────────────┘               │
                               │                      │
             ┌───────────────────┐                    │
             │   Is Liquid        │                    │
             │   Mass Greater     │────────► YES ──────┘
             │   Than 0.5%?       │
             └───────────────────┘
                               │
                              NO  ────►  ┌──────────────────┐
                                         │ Remaining Liquid │
                                         │ Assumed Solid    │
                                         └──────────────────┘
                                                  │
                    ┌────────────────────────────────────┐
                    │ Cumulatively Sum Shell Masses to    │
                    │ Produce Ten Shells of Equal Mass    │
                    └────────────────────────────────────┘
                                                  │
                    ┌────────────────────────────────────┐
                    │ Solidification Modelling Completed  │
                    └────────────────────────────────────┘
```

A thermodynamic data file (MPI file, see section 3.4) was created for an ADI alloy using the SGTE thermodynamic database. Ten elements (Fe, C, Si, Mn, Mo, Ni, Mg, P, Cu, Cr) were allowed in the MPI file. Only the phases liquid, graphite, austenite, ferrite and cementite were classified as 'normal'. The alloy composition was input into the model and the temperature was reduced from 1600°C until the first phase boundary was detected (the liquidus). An equilibrium calculation was then performed and the stable phases and their compositions were reported and

recorded. The stable phases that formed at each temperature step were considered as one shell of solid. Their composition was deducted from the system mass. If the mass of liquid remaining in the system was less than 0.5% of the original system mass then it was assumed that the remaining liquid solidified. If not, then the system temperature was reduced and a new equilibrium calculation was performed.

This process continued until less than 0.5% of the original system mass remained in the system as liquid. The program then terminated and wrote out the phases present and the composition of each shell. The phases present were typically austenite and graphite. Carbide formation was unlikely to occur since the program terminates before the remaining liquid composition is segregated enough for this to take place.

Once solidification was completed, ten shells (number chosen arbitrarily) of equal mass were produced by cumulatively summing the smaller shells, starting with the shell that solidified first and commencing through to the last shell that solidified. Since the Scheil model steps in temperature, the shells did not have equal masses. However, ten shells of equal mass could be produced, because the step in temperature was small, therefore many thousands of shells were predicted to form during the Scheil stage of the modelling process. At the point when the masses of the shells were summed any carbon in the system was ignored. Hence, if at the start of the Scheil simulation the system mass was 100 kg and the alloy originally contained 3.5 wt.% C, then each of the ten shells has a mass of 9.65 kg or 9.65 wt.% of the original system mass. Due to the segregation behaviour of many of the alloying elements present, the first shell (which represented the first material to solidify) had a substantially different composition from the last shell (which represents the last material that solidified). The substitutional element composition of each of the shells was then assumed to be fixed and therefore would not change on any subsequent heat treatment.

At this point, each shell was given an even quantity of the carbon in the system. Hence in the current example, each shell was allocated 0.35 kg or 0.35 wt.% of the carbon in the system. Therefore, each shell now had a mass of 10 kg or 10 wt.% of the original system mass. Since carbon is an interstitial element, it was assumed that it could reach equilibrium within the confines of each shell, due to its high diffusivity in an iron crystal. A real ADI alloy, after solidification, would be cooled to room temperature before being austenitised and austempered. However, since the

composition of the substitutional elements in each shell was assumed not to change on any subsequent heat treatment, the cooling of the alloy to room temperature was ignored. This is justified, because carbon was the only element permitted to diffuse in the material. Any changes that occurred to each shell on cooling (for example pearlite formation) would be eliminated during the austenitisation heat treatment, as the matrix transformed back to its original state of austenite and graphite.

The austenitisation heat treatment is now simulated individually for each of the shells, in the same manner as the original microstructure model (see section 5.1.2). Since the austenitisation heat treatments in commercial alloys last for time periods of greater than two hours, it is assumed the equilibrium austenite carbon content will be reached in each shell. Alternatively, equation 5.1 can be used with each shell to incorporate shorter austenitisation times.

Following the simulation of the austenitisation heat treatment, the graphite in each shell was relocated to form a single nodule (see figure 7.3). Although graphite was predicted to be present in all of the shells this is not the case and it was all relocated to form one nodule. This does not influence the segregation profile of the alloy because only the graphite phase was 'moved'. The distribution of graphite amongst the shells was an artefact of the Scheil type simulation, produced by the assumption that there was zero (carbon) diffusivity in the solid. Therefore, the carbon was unable to diffuse through the austenite to the graphite nodules.

In reality, the segregation profile predicted by the model is equivalent to that which is found in a ductile iron microstructure starting from one graphite nodule and finishing in-between two nodules, which is why the graphite was relocated. Hence, a uninodular simulation was produced where shells, centred around a single graphite nodule, represent the whole of the cast iron. This prediction was clearly not the true microstructure, but each individual shell represented the sum of all the material in the casting with that composition, and since solidification was determined by composition, the outer shell corresponded to the last areas to solidify. Nodule count does not affect this type of simulation, because if for example the nodule count was reduced, each shell would represent the sum of a smaller number of larger volumes for a given composition.

Figure 7.3. Schematic diagram illustrating the redistribution of graphite, the modelled microstructure and the segregated microstructure in an alloy.
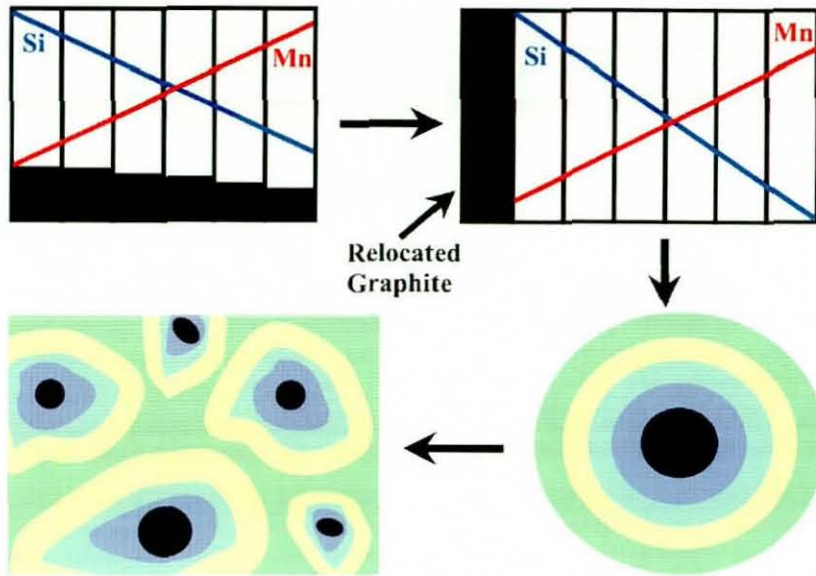
The graphite was relocated to form ONE nodule, but the segregation profile remained unchanged. The modelled segregation profile around one nodule was then assumed to simulate the segregation profiles around all the nodules in the alloy.

Since each nodule acted as a nucleating point for a 'cell', it was assumed that this simulated segregation profile would be applicable to all the nodules throughout the material (i.e. it was considered to be the average segregation profile around an average nodule, and was therefore applicable throughout the whole alloy). The relocation of graphite and a schematic diagram of the segregation profile in a ductile iron are presented in figure 7.3.

Following the relocation of the graphite, it was assumed, as in the original microstructural model, that no change occurred to the graphite on subsequent cooling or heat treatment. The shells were then cooled to the austempering temperature and the austempering heat treatment was simulated for each shell as discussed previously in sections 5.1.3 and 5.1.4. Hence the volume fractions of the phases in each of the shells were predicted. The shell mechanical properties were then calculated using the method outlined in section 5.2. Finally, the volume fraction and mechanical property values were summed to produce volume fraction and mechanical property predictions for the whole alloy. Some of the predictions made by the segregated microstructure model are shown in the following section.

7.4 Segregated Microstructure Model Results

7.4.1 Comparison of measured and predicted segregation profiles

Quantitative line scan measurements in ductile iron alloys are typically used to measure the segregation profiles between two graphite nodules, as demonstrated in section 2.9. However, these line scans represent a one dimensional view of segregation behaviour, and hence are prone to fluctuations which arise due to the three dimensional nature of the segregation process. Therefore, quantitative assessment of segregation model predictions by comparison with line scan profiles has been shown to be difficult [6]. Hence in this work, segregation profiles were obtained in a different manner, resulting in a thorough appraisal of the true extent of alloying element segregation in the alloys.

Due to the limited number of alloys available, raw material was cast into sand moulds in the foundry in the Manufacturing Engineering Department at Loughborough University, to enable the analysis of more iron compositions. The casting process proved extremely difficult due to the small volumes of material being produced. Charges had a typical mass of only 4-8 kg due to the small capacity of the furnace crucible. The alloys were all inoculated with a combination of Fe-Si-Mg, Ni-Mg and ZI80, which is a commercial ductile iron inoculant. The inoculation however, required careful experimentation. Grey iron was produced on several occasions before the correct level of inoculation (40g Fe-Si-Mg, 50g Ni-Mg and 30g ZI80 per 4kg charge) was found to produce ductile cast iron.

Difficulties were also encountered when adding carbon to the melts. Carbon being an element with a low atomic mass tended to float towards the surface of the melt before it was dissolved into the liquid iron. Some of the carbon therefore was not dissolved into the melt, as it become encrusted with molten slag that floated on top of the melt. This lead to lower C concentrations in the alloys than anticipated [2]. Hence it can be seen that for such small charges, the margin for error is very small in the production of ductile iron castings of the correct composition and inoculation level.

To produce the sand moulds, sand was mixed with a 2% sodium silicate binder and then compacted into the moulds, which were then flushed with CO_2 gas. This removed the moisture from the sand moulds, causing them to set. The castings

were then poured into the sand mould, and the moulds were buried in a sand pit and left to cool for 12 hours.

Four castings of differing composition were eventually produced. Three castings were ductile irons and one was a mixture of ductile and grey. Samples for optical microscopy were cut from the castings. They were then mounted and polished to reveal their structures. The microstructures were typical of ductile iron alloys containing mainly ferrite and pearlite. Some alloy carbides rich in Mn and Mg were present in all the castings, and are highlighted in the micrographs shown in figure 7.4. Due to the high Cu concentrations a small number of Cu rich particles were also observed in alloys 3, 4 and 6. Energy dispersive X-ray (EDX) analysis of these particles showed they had a typical composition of 70 Cu, 25 Fe and 5 Ni (all wt.%). The compositions of these alloys (named alloys 3-6 respectively) are listed in table 7.1. Etching of these alloys to reveal their microstructures proved difficult since the high Si concentrations they possessed slowed the etching rate. Hence the microstructures have a very dark appearance, due to the increased etching time that was needed to reveal their structures.

Table 7.1. Composition of alloys (all wt.%).

| Alloy	Fe	C	Si	Mn	Mo	Mg	P	S	Cu	Cr	Ni
1	Balance	3.3	2.06	0.44	0.0	0.050	0.029	0.06	0.38	0.05	0.01
2	Balance	3.45	1.62	0.45	0.0	0.043	0.032	0.05	0.50	0.04	0.01
3*	Balance	2.30	5.77	1.29	0.04	0.29	0.018	0.001	2.39	0.09	2.44
4*	Balance	2.24	4.64	1.07	0.04	0.31	0.015	0.010	2.90	0.06	2.59
5	Balance	2.58	3.32	0.54	0.04	0.25	0.009	0.008	0.77	0.03	1.62
6*†	Balance	2.77	4.26	0.63	0.04	0.13	0.012	0.008	1.20	1.08	2.23

* Samples for validation of the segregation model, not for ADI production.

† This alloy contained some graphite with a flake type morphology.

The as cast microstructures of alloys 1 and 2, which were produced in a commercial foundry, are also included in figure 7.4 for comparison purposes. These two alloys were received from the foundry in the form of camshafts. No alloy carbides were found in the microstructures of these two alloys. They also have higher nodules

counts than alloys 3-6. This is because alloys 1 and 2 were commercially cast in large volumes and hence inoculation of these alloys was more effective and easier to control than alloys 3-6.

Figure 7.4. Optical micrographs of Alloys 1-6, highlighting carbides present.
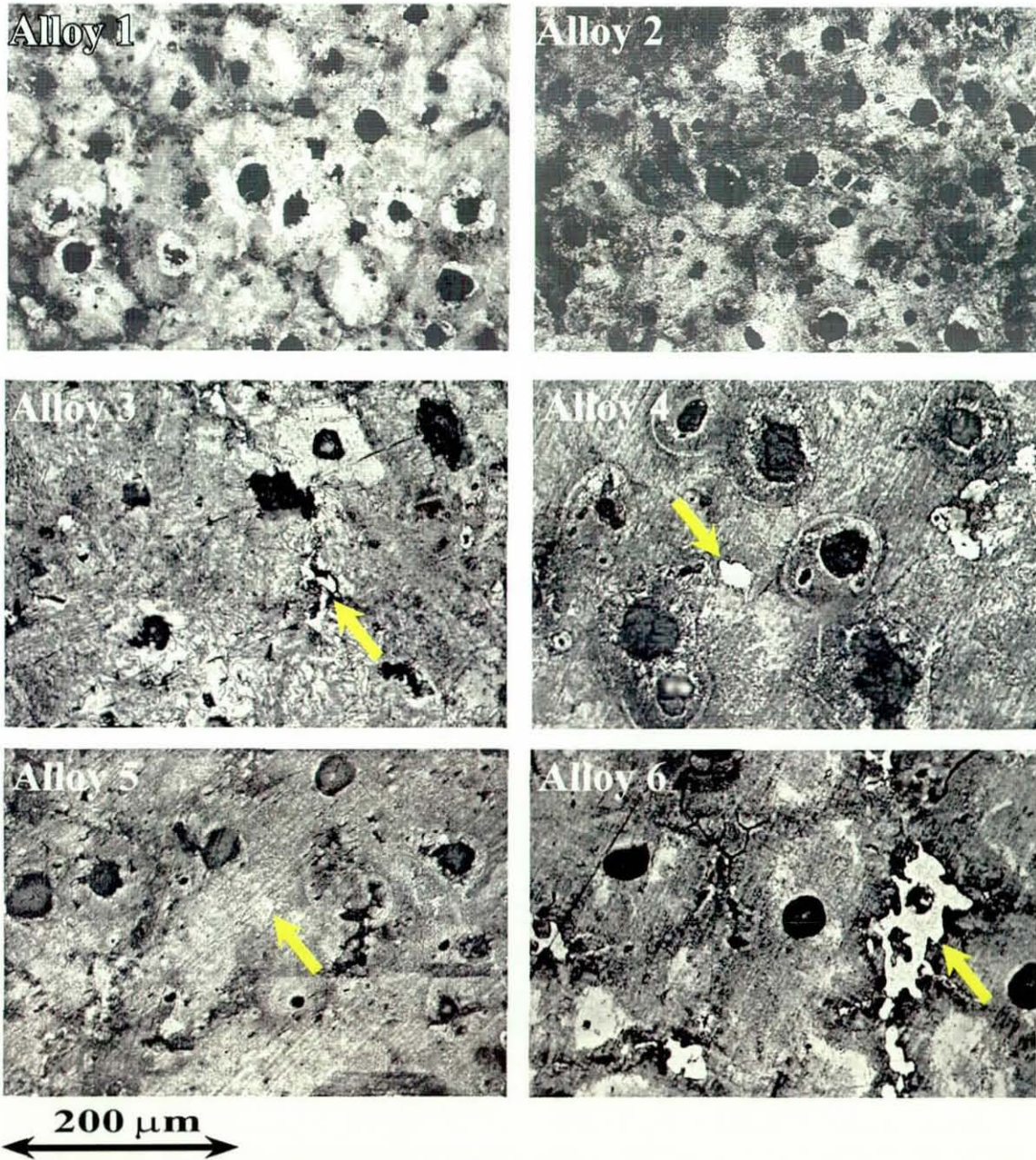
Scanning electron microscopy (SEM) analyses were performed on as cast specimens using a Leo 1530VP field emission gun SEM. At each point in a grid incorporating over one thousand points (see figure 7.5), the concentrations of the major alloying elements such as C, Si, Mo, Mn and Cu were measured using an

EDAX Pegasus energy dispersive X-ray (EDX) analysis system with an ultra thin window detector. The ultra thin window of the EDX system allows the concentration of carbon to be detected in the alloys. However, since C is a very light element, the concentration measurement is not particularly quantitative because of uncertainties in the mass absorption coefficients of light elements [106]. Although generally very accurate concentration measurements can be made using this system some error could be present in the results due to the influence of background noise especially when for small concentration measurements or when overlapping of energy spectra occurs. A typical grid is shown in figure 7.5, where the large matrix area incorporated in the analysis can be clearly seen. The information obtained was used in a statistical analysis of the segregation profile found in the alloys, using a methodology proposed by Hayrynen *et al.* [107]. The method used allows the overall segregation pattern to be obtained by using the large amount of experimental data to signify the range of concentrations found during solidification. Hence, if 90% of the Si points measured have a concentration less than 2.0 wt.% the Si concentration at a solid fraction of 0.9 is defined as 2.0 wt.%. If the concentration of C measured at a point was greater than 3.0 wt.% the point was discarded from the analysis, because it was assumed to be a graphite nodule.

Figure 7.5. A grid of points showing how element concentration was typically measured using EDX analysis.
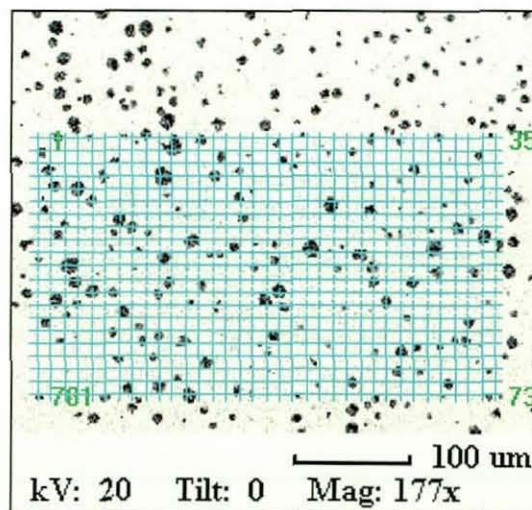
Data for each element are sorted by the nature of the segregation behaviour of the element. For example in ADI alloys, Si is known to segregate to the first liquid to solidify, hence is found in greater quantities close to graphite nodules, whilst Mn and Mo display the opposite behaviour [2,23]. Hence the Si data (starting from the graphite nodule), were sorted in a descending order, whilst the data for Mn and Mo were sorted in the opposite manner. Therefore the highest concentrations of Si were assumed to represent areas of the matrix next to the graphite nodule, whilst the lowest concentrations signify the last to freeze areas between two graphite nodules. Although the unique composition of each point is not maintained, a thorough appraisal of the composition range is obtained from the vast number of concentration measurements (over one thousand in each alloy). A comparison of the Scheil segregation model profiles produced for different ductile iron alloys (compositions listed in table 7.1) are compared with the segregation profiles obtained using the described method in figures 7.6 - 7.9.

As can be seen from figure 7.6, reasonable agreement is obtained between the predicted and measured segregation profiles for both alloy 1 and 2 using this method for all the alloying elements concerned. In figures 7.6 - 7.10, shell 1 represents material adjacent to a graphite nodule (first to solidify), whilst shell 10 represents material halfway between two nodules (last to solidify). As expected, figure 7.6 shows Si and Cu are predicted to segregate to the first solid to form by the model, whilst Mn is predicted to segregate to the last liquid to solidify in both alloys. The segregation profiles predicted using the model were also used as a basis for predicting the influence of segregation on the local microstructure as described in sections 7.4.2 and 7.4.3.

Alloys 3 and 4 contained much higher concentrations of Si, Cu and Ni than would be found in commercial ADI alloys. However, these alloys are useful for verifying the generic applicability of the segregation model. It was interesting to note in these alloys that the predicted segregation profile for Si was different than those of alloys 1 and 2, which contained much lower concentrations of this element. In alloy 3 (which has the highest Si concentration of all the alloys), the predicted segregation behaviour is the opposite of alloys 1 and 2, since the Si concentration is shown to increase with distance from the graphite nodule. Hence the highest concentrations were predicted to be present in the last liquid to solidify. Alloy 4 shows transitional type behaviour since the highest Si concentrations were predicted in shells 6-9 which

represent material that solidified after the halfway point of solidification, but not at the very end. The experimental concentration measurements for alloys 3 and 4 are compared to the Scheil model predictions in figures 7.7 and 7.8 respectively.

Figure 7.6. Comparison of Scheil model segregation prediction with experimentally obtained results for alloys a) 1 and b) 2.

a)

b)
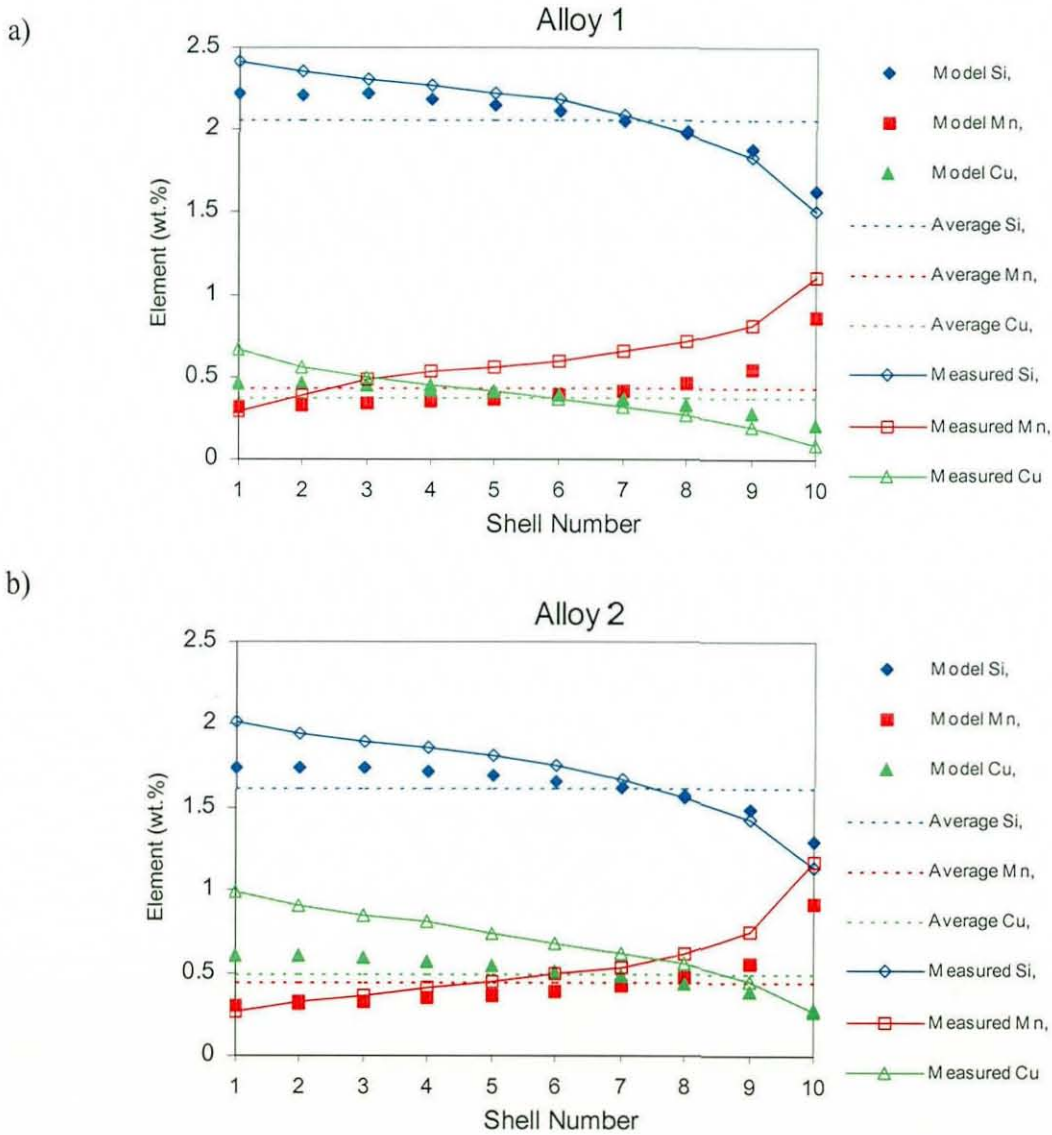
The apparently strange segregation behaviour of Si has been observed experimentally elsewhere in cast iron alloys, and is referred to as reverse microsegregation [2,108]. Reverse microsegregation occurs when the concentration of Si becomes so high that it interacts with carbon in the system, changing its nature to become a carbide stabilising element [2,109]. This process commences at a Si

concentration of approximately 4-5 wt.% [2,109]. The concentrations of Si in alloys 3 and 4 as seen in table 7.1 are much higher than those of normal ADI alloys, which typically contain 2.0-3.5 wt.% Si. Hence, this explanation seems plausible for alloys 3 and 4.

The predicted increase in Si concentrations with distance from the nodule raised another issue regarding the validation of model predictions using the experimentally obtained data. For alloys 1 and 2 the empirically obtained segregation data were sorted via known elemental behaviour. However, this method could not be applied to Si in alloys 3 and 4 due to the irregular behaviour of the segregation of this element. Therefore for these alloys, the Si was sorted by using Mn as a basis. Mn still segregates to the last shells to solidify in these alloys, and so the concentrations of Si were linked to the corresponding Mn concentrations (from the same EDX concentration measurement point), and the Mn concentrations were sorted in the usual way based on their known segregation behaviour. The remaining elements were also sorted by their known segregation behaviour and are presented in figures 7.7a and 7.8a. Figures 7.7b and 7.8b show all the measurement points for Si. The black lines on the figures 7.7b and 7.8b represent the moving average value of 50 individual points, highlighting the general trend observed.

It can be seen in figures 7.7b and 7.8b that in the later shells a slight increase in average Si concentration does occur, although the overall profile does seem to be reasonably uniform. In both cases near shell 10 the concentration of Si reduces. This is probably due to carbides which may be close to these microstructural areas which contain the highest Mn concentrations in the alloys.

Figures 7.7a and 7.8a show that good agreement was observed between the measured and predicted segregation profiles. The measured Mn profile follows the trend of the model results exactly. The small difference between the measured and predicted composition profiles is most likely an artefact of the inclusion of C in the measured concentration analysis. As previously mentioned, C can be detected using the SEM, but cannot be quantitatively analysed accurately [106]. However, C had to be included in the experimental analysis of the concentration points in the grid, because measurement points that were on top of graphite nodules had to be removed from the experimental results. Therefore, the quantitative analysis of C in the measured results could have a knock on effect by slightly over or under estimating the concentration of other elements in the alloy. It was suspected in this work that the

quantitative analysis of C resulted in slight greater and smaller measurements of Mn and Si concentrations respectively in all the alloys.

Figure 7.7. Comparison of Scheil model segregation prediction with experimentally obtained results for alloy 3.

a)

b)
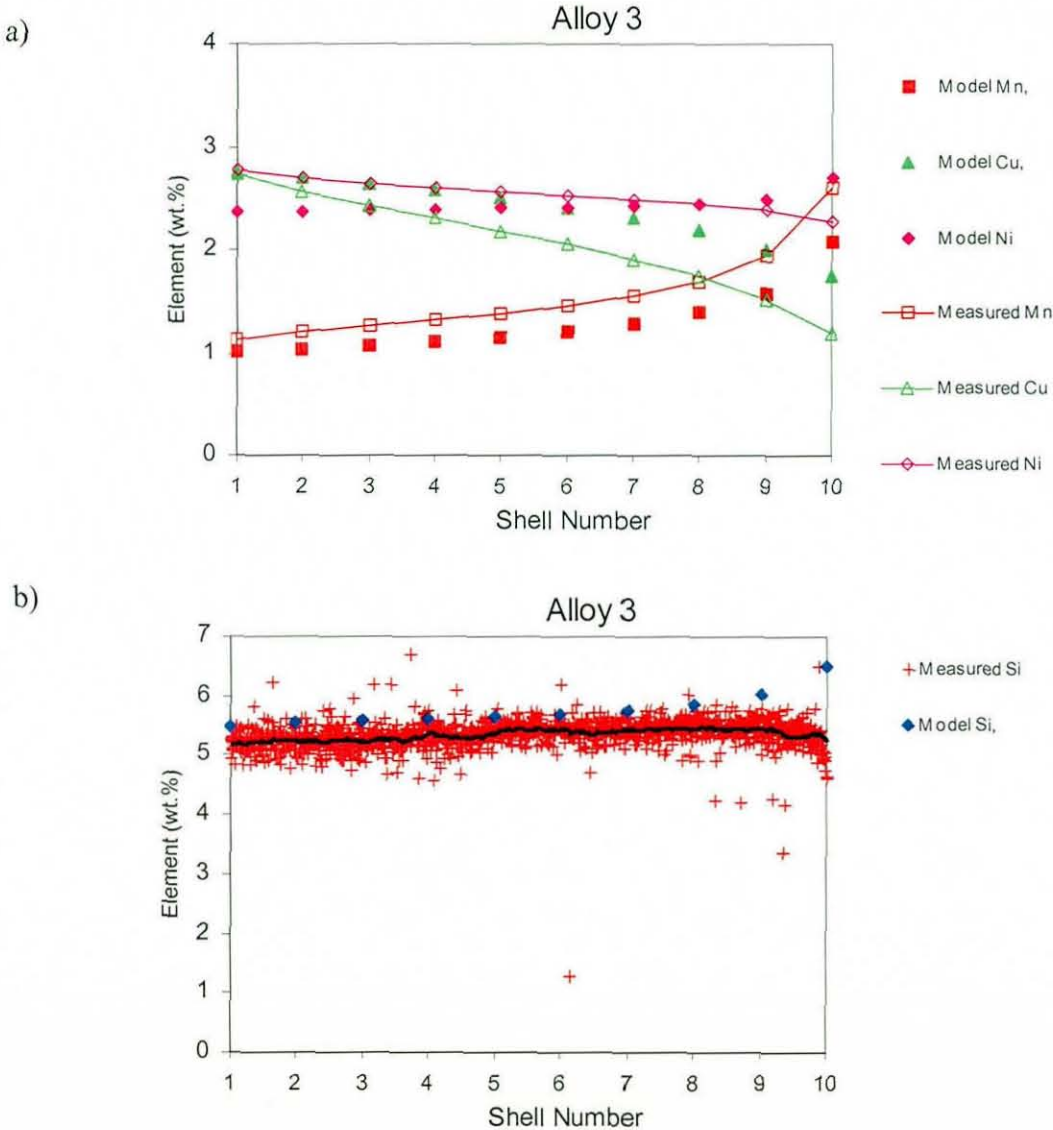
The measured concentration of Cu is lower than that predicted by the model in figures 7.7a and 7.8a. This is a consequence of the presence of some Cu rich particles, which were observed in both alloys as previously mentioned. The presence of these particles results in less Cu being present in the matrix, and is not predicted by the model, therefore lower Cu concentrations are measured in the microstructure. However, the trend predicted by the model is the same for the measured

concentration profiles in both alloys. Alloys 1 and 2 did not contain these Cu-rich particles, therefore as shown in figure 7.6, the predicted Cu concentration profiles are more accurate.

Figure 7.8. Comparison of Scheil model segregation prediction with experimentally obtained results for alloy 4.

a)

b)
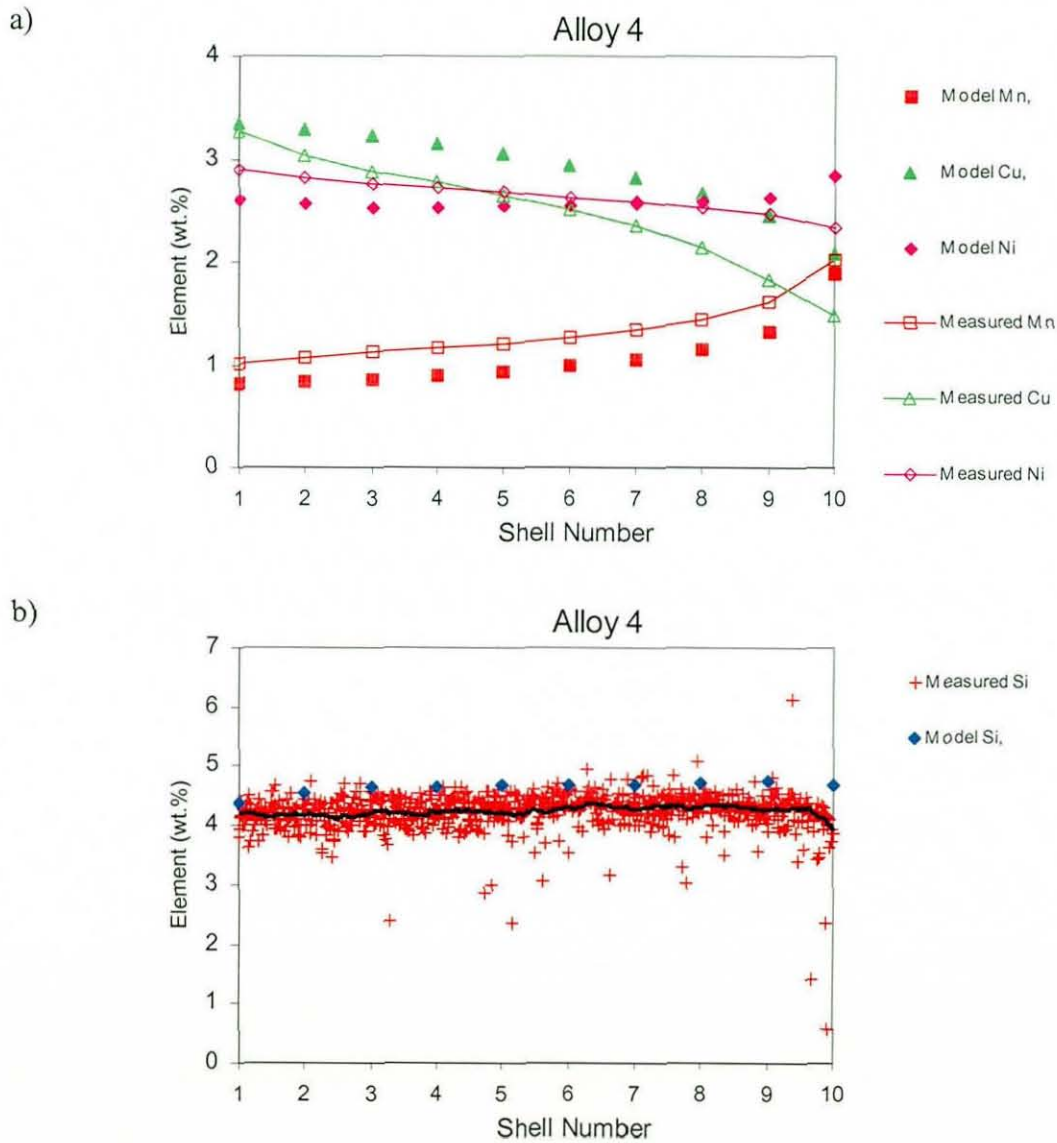
Ni is predicted to have an almost neutral segregation by the model. Theoretically it should be found in higher concentrations close to graphite nodules, although it does not tend to segregate strongly [2;107]. The concentration of Ni is predicted to increase slightly in the last shell of both alloys 3 and 4, in a mirror image profile of the predicted Si concentrations. Therefore, it its thought that the inverse

segregation of Si could influence the segregation of Ni in the predictions.

Figure 7.9 shows the model predictions and experimental results for alloy 5. Due to the medium concentration of Si in this alloy, the experimental results were sorted by their expected segregation behaviour as with alloys 1 and 2. There is a good match between the predictions and experimental results for Si, although in the first few shells the Si concentration is predicted by the model to rise slightly. This alloy contained a borderline concentration of Si between the high concentrations in alloys 3 and 4 and those typically found in ADI alloys. Therefore the slight rise in Si concentration could be accounted for by a mixed type behaviour. The Mn and Cu experimental results also show the same trend as predicted by the model, and the agreement between the model and experimental measurements is good. The Ni displays similar behaviour as in alloys 3 and 4.

Figure 7.9. Comparison of Scheil model segregation prediction with experimentally obtained results for alloy 5.
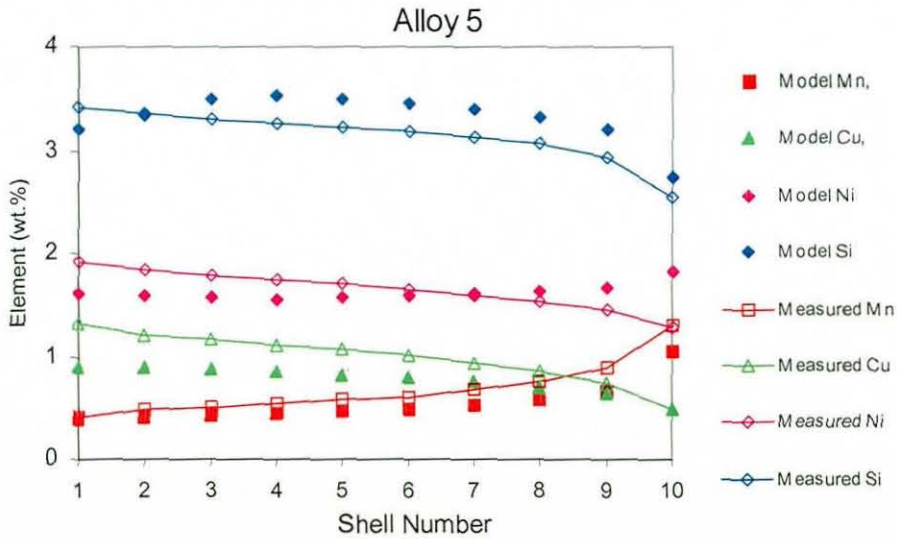

Figure 7.10 shows the results for alloy 6. Again as with alloy 5, there is good agreement between the trend of the model predictions and experimental results for Si. The quantitative analysis of C as explained earlier in this section could account for the slightly lower measured Si concentrations. The experimental concentrations of Ni and Mn follow their expected trends and are in good agreement with model predictions. The concentrations of the measured Cu profile are slightly lower than the

model predictions. As with alloys 3 and 4, this alloy contained some Cu rich particles which deplete Cu from the matrix and therefore accounts for these differences. Alloy 6 also contained a significant concentration of Cr. Cr is a strong carbide stabilising element and is found to segregate to the last solid to freeze region [2]. The model predicts this behaviour, but the measured concentration of Cr in shell 10 is lower than that predicted by the model. This is thought to be a consequence of the use of the Scheil approach as described in section 7.2, since it predicts the worst type segregation behaviour.

Figure 7.10. Comparison of Scheil model segregation prediction with experimentally obtained results for alloy 6.
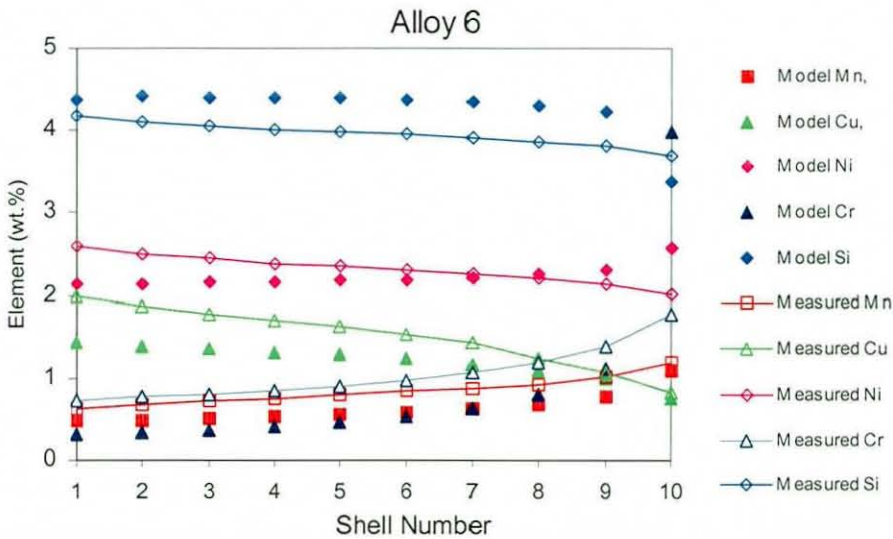
The results presented in figures 7.6-7.10 show that the segregation model predictions display good agreement with compositions typically encounter in ADI alloys. The results of the model predictions also suggest that the segregation model can be used with some confidence when the alloying element concentrations are greater than those typically observed in ADI alloys.

7.4.2 Modelling of the austenitisation heat treatment

Due to the different compositions of the ten shells, during austenitisation the equilibrium between the austenite carbon content and the graphite nodules changes

for each shell. This is demonstrated in this section using alloy 1 as an example. The local equilibrium austenite carbon content for the ten shells after austenitisation at 950°C is shown in figure 7.11 for alloy 1, the composition of which is listed in table 7.1. As can be seen in figure 7.11, the austenite carbon content is found to increase in the last areas of the microstructure to solidify. This is a direct consequence of the segregation behaviour of the alloying elements. Si is a graphite stabilising element and is found in lower quantities in the last liquid to freeze. Hence less graphite (therefore more carbon in the austenite) is predicted to form in the last shells.

Figure 7.11. Austenite carbon content C^0_γ predictions for the ten shells of alloy 1 after austenitisation at 950°C.
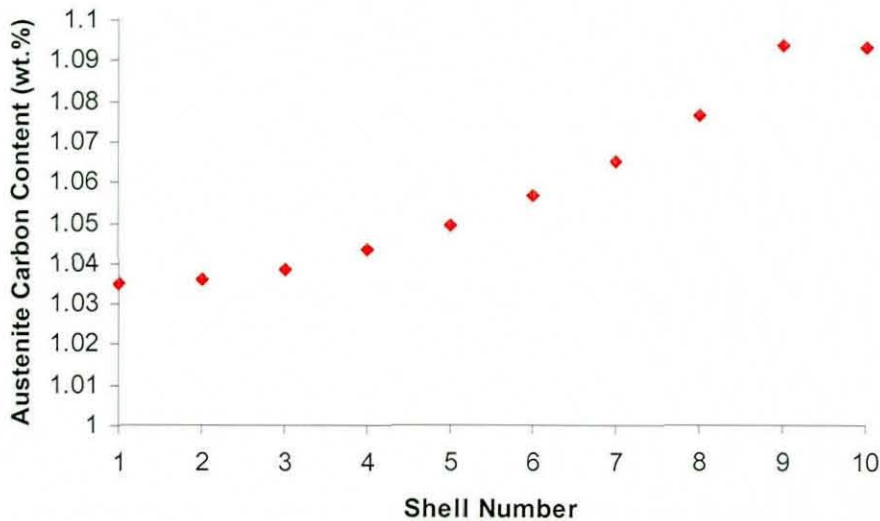
The strong influence of P can also be seen in figure 7.11. Although the alloy only contains a small quantity of this element (0.029wt.%), the model predicts that it segregates potently to the last liquid to solidify. In fact over 80% of the P in the alloy is predicted to solidify in the last shell. Since P is a potent graphitizing element, some extra carbon in the last shell is tied up in graphite [2]. This accounts for the reduction in the austenite carbon content of the last shell, and also demonstrates the powerful influence small additions of some elements can have on phase equilibrium. Fe_3P particles have been identified in ADI alloy remote from graphite nodules [20;110]. Hence this provides support for the hypothesis that P concentrations could be high in the last liquid to freeze.

The austenite carbon content has an important influence on the reaction kinetics of the austempering process as highlighted in section 2.6.1. Therefore the differences demonstrated in the local austenite carbon content as a result of segregation have an important influence on the subsequent transformation kinetics during the austempering process.

7.4.3 Modelling stage 1 of the austempering heat treatment

The final stage of the segregated microstructure model is the prediction of the microstructure volume fractions that occur in the alloys at the end of stage 1 of the austempering heat treatment. This is again demonstrated using alloy 1 as an example in this section. The results of the local phase volume fractions calculated using the X_{T*} version of the model are shown in figure 7.12, for alloy 1 after austenitisation at 950°C and austempering at 320°C. Although in the figure graphite is predicted to occur in each shell it has been relocated as in figure 7.3, and is just shown in each shell for completeness. As can be seen in figure 7.12, the local changes in composition do have some influence on the local phase volume fractions. This is due to changes in the magnitude of the microstructure model parameters X_{T0} as shown in figures 7.13 and X_0 as seen in figure 7.11. X_{T0} and C^0_γ are predicted to decrease and increase respectively with distance from the graphite nodule. The volume fraction of bainitic ferrite is found to decrease with distance from the graphite nodule, whilst the volume fraction of austenite increases due to the combined influence the magnitude of X_{T0} and C^0_γ have on the lever rule calculation (see section 5.1.3). After examination of the segregation profile for alloy 1 in figure 7.8, this would be expected. Silicon has a strong influence on the stability of ferrite and since it is found in large quantities close to the nodules (shell 1), more bainitic ferrite is found there [2;32]. No martensite is predicted to occur in any of the shells in alloy 1. This is not surprising, since careful selection of alloy composition and heat treatment temperatures and time will prevent martensite formation in ADI alloys. Indeed, martensite is an unwanted phase, since it embrittles ADI alloys, especially if it forms a continuous path in the matrix of the alloy [15].

Table 7.2 compares the average volume fractions calculated by the normal

microstructure model, which does not account for segregation, with the segregated microstructure model. As can be seen, there is very little difference in the predictions between the two models, although the model which accounts for segregation predicts a slightly higher volume fraction of bainitic ferrite in the sample.

**Figure 7.12.** Local phase volume fraction predictions for alloy 1 after austenitisation at 950°C and austempering at 320°C.
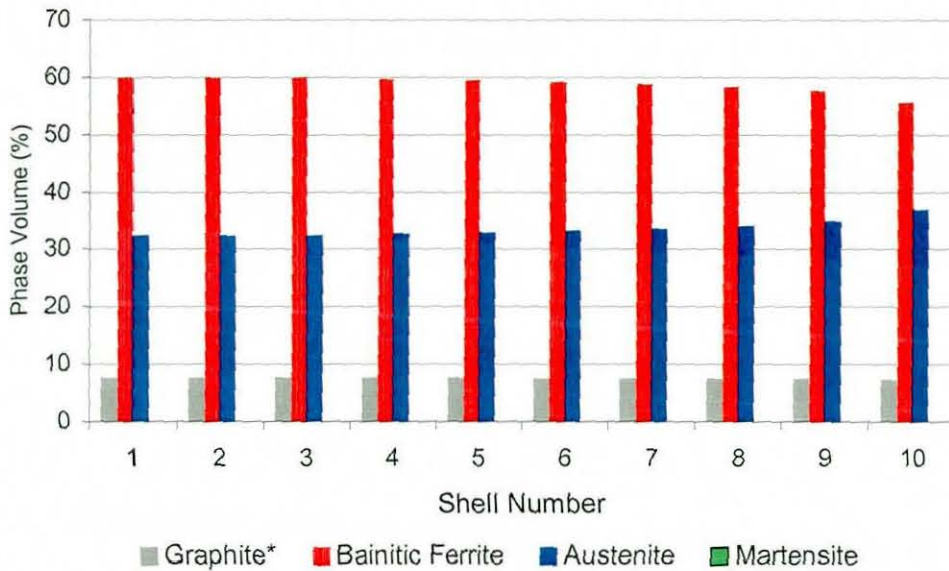
* Graphite phase was relocated after austenitisation and is shown in each shell only for completeness.

Table 7.2. Comparison of microstructure model predictions with and without accounting for segregation, for alloy 1 after 950°C austenitisation ad 320°C austempering.

Model	Vf Bainitic Ferrite	Vf Austenite	Vf Graphite	Vf Martensite
Normal	0.578	0.346	0.076	0.000
Segregation	0.589	0.335	0.076	0.000

Finally, as with the microstructure model, the phase volume fractions are used in a law of mixtures approach as a basis to predict the simple mechanical properties of the alloys. Along with the phase volume fractions, the mechanical property predictions for each shell are then averaged, producing calculations of the phase volume fractions and mechanical property values for the whole alloy.

Figure 7.13. Limiting *austenite carbon content* X_{T0}, predictions for the ten shells of alloy 1 after austenitisation at 950°C and austempering at 320°C.
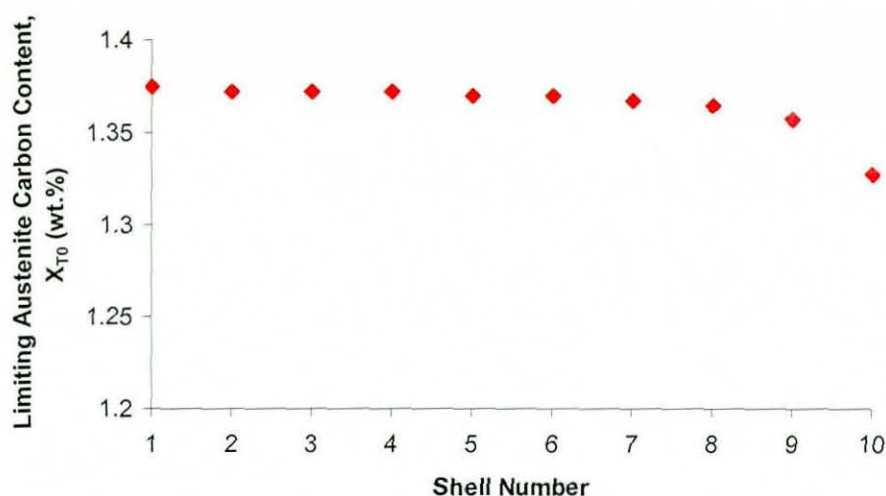
7.5 Summary

This chapter has shown how the segregation of alloying elements predicted using the Scheil approach, in conjunction with MTDATA, can be used as a basis for modelling the microstructure of ADI alloys. A slave application was written, that in conjunction with MTDATA, predicted the segregation of alloying elements that occurred upon solidification around an average graphite nodule. Experimental data were obtained, which thoroughly measured the total extent of alloying element segregation in six different cast iron alloys. These data were used to validate the model predictions. Excellent agreement was obtained for alloys 1 and 2, which have compositions typical of commercial alloys and therefore are of key interest to this work. Very good agreement was also obtained for another four alloys, and reasons for discrepancies between the model predictions and experimental results were given. The final sections of the chapter showed how the segregation of alloying elements predicted by the model influenced key microstructure model parameters for alloy 1. Hence, the influence segregation of alloying elements has on local microstructure can be accounted for by using the model discussed in this chapter. Chapter 8 extends the segregation model further by showing how it can be used as a basis to predict local microstructure transformation times for the stage 1 austempering reaction in ADI alloys.

8 Modelling of Local Austempering Transformation Kinetics and M_S Prediction Improvements

8.1 Introduction

The previous chapter showed how the Scheil approach can be used to predict the segregation behaviour of alloying elements in ADI alloys. It also highlighted the changes in the local microstructure predictions made by the model as a result of segregation. This chapter takes this concept further by showing how the same methodology can be used as the basis for predictions of the local transformation kinetics of the stage 1 austempering reaction. Finally, a new method of predicting the martensite start temperature of each microstructure shell is demonstrated.

8.2 Modelling of Stage 1 Austempering Kinetics

8.2.1 Introduction

Section 7.3 discussed the development of a new model that predicted the local microstructure of ADI alloys, taking into account the influence of alloying element segregation. Differences in local transformation kinetics during the austempering process produce difficulties in the industrial production of ADI alloys. Hence a model which could account for the influence alloying element segregation has on the local transformation kinetics of stage 1 of the austempering process would be beneficial to ADI producers. The kinetics of stage 1 of the austempering process have been previously predicted for ADI alloys, by adapting a model developed for steels [20]. The same methodology was used in this case, although MTDATA was incorporated into the model to accurately calculate the necessary thermodynamic parameters for all elements.

8.2.2 Kinetic modelling basis

The kinetics of the austempering process were modelled using a methodology originally developed for steels by Bhadeshia [111], and subsequently modified by Rees and Bhadeshia [112;113], and Chester and Bhadeshia [114]. The underlying ideas in the

model and changes made to make it applicable to predicting the kinetics of stage one of the austempering process for alloyed ductile cast irons are outlined in the following section.

The model gives a time, t, for a given normalised volume fraction, ξ, of bainite to be formed, where ξ is given by the actual volume fraction of bainite, v, divided by the maximum volume fraction of bainite, Ω. The increase in the normalised volume fraction, $d\xi$, in a time, dt, is given by [112]:

$$\Omega d\xi = (1-\xi)uI\ dt \qquad [8.1]$$

where u is the volume of a bainitic subunit and I is the nucleation rate of ferrite per unit volume, which is a function of the temperature and the maximum free energy available for the nucleation of ferrite, ΔG_{max}. It is assumed that carbon partitions into the austenite during bainitic ferrite nucleation [111;112]. ΔG_{max} is in turn a function of alloy composition and the volume fraction of ferrite, since carbon enrichment of the untransformed austenite during austempering will lower the size of the free energy change as the volume fraction of ferrite increases [112].

Both Widmänstatten ferrite and bainitic ferrite originate from the same nucleus, so nucleation is taken into account from the point where Widmänstatten ferrite formation becomes possible, below the Widmänstatten ferrite start temperature, W_s [114]. This enables the definition of a universal nucleation function of temperature, G_N, which is applicable to all steels [112]. In a steel, nucleation first becomes possible below W_s, at the point when ΔG_{max} exceeds G_N. Hence, G_N represents the minimum free energy change needed for nucleation of ferrite at W_s, by a displacive mechanism [112].

If the nucleation rate of ferrite per unit volume, I, at W_s is constant for all steels and to ensure the activation energy for nucleation is directly proportional to ΔG_{max}, I can be given by the following formula [112]:

$$I = K_1 \exp\left(-\frac{K_2}{RT} - \frac{K_2 \Delta G_{max}}{rRT}\right) \qquad [8.2]$$

where K_1, K_2 and r are empirical constants, T is the temperature (°C) and R is the gas constant.

As the bainitic reaction proceeds, ΔG_{max} reduces due to the carbon build up in the austenite surrounding the bainitic ferrite plates. For growth to continue, the driving force for transformation without a change in composition of the ferrite nucleus, $\Delta G^{\gamma \to \alpha}$, must be greater than the stored energy of ferrite ($\Delta G^{\gamma \to \alpha} > -400$ Jmol^{-1}), whilst the condition for nucleation must also be satisfied ($\Delta G_{max} > G_N$). Both conditions need to be met in order for bainite formation to occur [112]. During the transformation as the austenite becomes enriched in carbon, the size of both $\Delta G^{\gamma \to \alpha}$ and ΔG_{max} will reduce and the reaction will cease when either criterion is no longer met. The free energy for nucleation was assumed to vary linearly with the extent of the reaction between its initial value ΔG^0_{max}, and its final value when the reaction ends, G_N hence:

$$\Delta G_{max} = \Delta G^0_{max} - \xi \left(\Delta G^0_{max} - G_N \right) \qquad [8.3]$$

Equation 8.3 assumes the reaction terminates due to failure of the nucleation criterion, but the model also includes the growth criterion when the reaction ceases when the volume fraction of bainite equals Ω.

Alloys that have a higher carbon content partition more carbon into the area surrounding the newly formed bainitic ferrite plates during transformation. This carbon build up results in a temporary reduction in the local driving force for transformation and slows further nucleation on the previously formed plates (autocatalysis) [112]. Hence the autocatalysis factor, β, is dependent on the overall carbon concentration of the alloy:

$$\beta = \lambda_1(1 - \lambda_2 x) \qquad [8.4]$$

where λ_1 and λ_2 are empirical constants and x is the mean carbon content of the alloy in mole fraction, or in the case of ADI alloys the carbon content at the end of austenitisation, C^0_γ.

The autocatalysis factor was further modified to account for the high carbon contents encounter in ADI alloys, as proposed by James [20]. Equation 8.4 becomes negative at carbon contents greater than 0.72 wt.%C. This value is readily exceeded

in ADI alloys, resulting in the model requiring the log of a negative number. Therefore it was replaced with a modified relationship, which is positive for all carbon contents:

$$\beta_m = \lambda_1/\exp(2 \lambda_2 x) \qquad [8.5]$$

The nucleation rate due to the austenite grain boundaries was assumed to be proportional to the surface area of the austenite grains per unit volume, due to the number of suitable sites for nucleation being directly proportional to the grain boundary area [112]. The following expression was used to relate the constant K_1, which is used in the nucleation rate expression (equation 8.2), to the austenite grain size:

$$K_1 = (LK'_1)^{-1} \qquad [8.6]$$

where L is the mean linear intercept of a series of random lines with austenite grain boundaries and K'_1 is an empirical constant.

K_1 was modified by James to produce a better agreement between the predicted austempering kinetics and his own experimental results for ADI alloys [20]. He empirically reduced the size of K_1 from 34.456 to 13.0 (making nucleation theoretically more difficult in ADI alloys), producing a better fit between his experimental data for ADI alloys with the model.

The K_1 term influences the ease of bainitic ferrite nucleation. If K_1 is large, nucleation is easier. He proposed no theoretical reason for this change. However, in ADI alloys, bainitic ferrite is observed to nucleate and grow mainly from the graphite nodules or the graphite matrix interface as shown in figure 8.1.

Although not attempted in the current work, it should be theoretically possible to devise a relationship for the K_1 term incorporating nodule count, since in alloys with a high nodule count (and therefore nodule surface area), bainitic ferrite nucleation should be easier due to the increase in the available nucleation sites. The increase in the rate of bainitic ferrite nucleation should be proportional to the graphite nodule surface area, hence nodule count and size information could be included in a relationship to account for the different mechanism of bainitic ferrite nucleation.

Figure 8.1. A dark field micrograph of alloy 1 (composition listed in table 7.1) after austenitisation for 90 minutes at 950°C and austempering at 320°C for 10 minutes. Bainitic ferrite plates (white) can be identified near graphite nodules in a matrix of martensite and austenite.
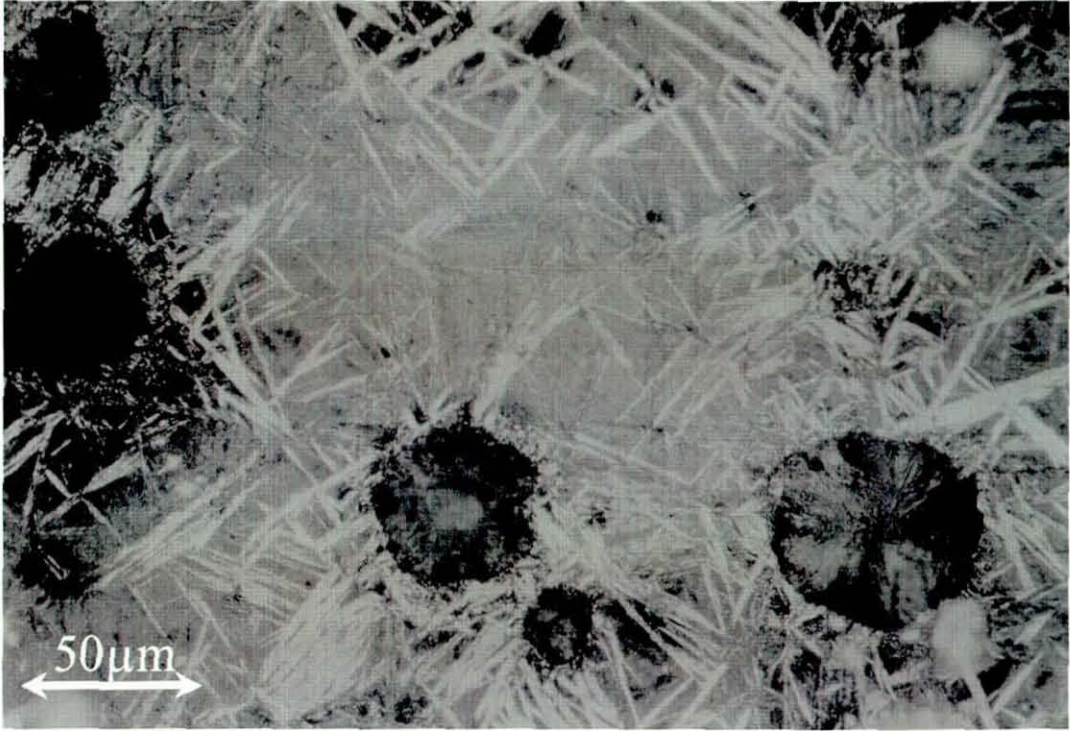
The influence of the volume of bainitic subunits, u, has also been accounted for in a later work, by varying the subunit size with temperature, using the following linear relationship [114],

$$u_w = 0.001077T - 0.2681 \qquad [8.7]$$

where u_w is the subunit width and T is the isothermal transformation temperature (°C). A minimum value for u_w of 0.05μm was used, and the subunit thickness, u_t, was assumed to be 10μm. The subunit volume is then calculated, converted into mm³, and then incorporated into the constant K'_1/u.

Substitution of the nucleation rate into equation 8.1 yields a differential equation, the solution of which is described in detail by Chester [115]. The final relationship is as follows:

$$t = \frac{e^{C}}{A(B+1)} \left\{ \begin{array}{l} e^{E}\left(\ln|1 + B\xi| + f(-(E+D\xi)) - f(-E)\right) \\ -e^{-D}\left(\ln(1-\xi) + f(D(1-\xi)) - f(D)\right) \end{array} \right\} \qquad [8.8]$$

where $\qquad A = \dfrac{uK_1}{\theta}, \qquad B = \beta\theta, \qquad C = \dfrac{K_2}{RT}\left(1 + \dfrac{\Delta G_{max}^{0}}{r}\right),$

$D \approx \dfrac{K_2\left(\Delta G_{max}^{0} - G_N\right)}{rRT}, \qquad E = \dfrac{D}{B} \qquad and \qquad f(x) = \dfrac{x}{1\times 1!} + \dfrac{x^2}{2\times 2!} + \dfrac{x^3}{3\times 3!} + ...$

8.2.3 Calculating the thermodynamic parameters in the model using MTDATA

The Fortran code to compute the bainitic ferrite reaction kinetics for stage one of the austempering reaction was combined with the segregated microstructure model (section 7.3). The program was linked with MTDATA, and simulated the individual reaction kinetics for each of the ten shells produced by the Scheil segregation model. In each shell, the austenite and ferrite free energy curves were calculated by MTDATA as a function of carbon content. They were used to determine the local maximum free energy change associated with the formation of a mole of ferrite nuclei, ΔG_{max}. A simplification of this parameter was also calculated, where the free energy change for the formation of a mole of ferrite nuclei is assumed to occur with no change in composition ($\Delta G^{\gamma \to \alpha}$). Hence, the influence on the transformation thermodynamics of all of the alloying elements present in the alloy could be accounted for by using MTDATA. A schematic diagram showing how the parallel tangent construction is used to calculate ΔG_{max} and $\Delta G^{\gamma \to \alpha}$ is shown in figure 8.2. Due to the nature of the ferrite free energy curves produced using MTDATA, the minimum free energy of ferrite is always found to coincide with a carbon content of zero wt.%C. Therefore ΔG_{max} and ΔG_2 in figure 8.2 are always equal.

Figure 8.2. A schematic diagram showing the use of parallel tangent construction to find ΔG_{max}, adapted from [26].
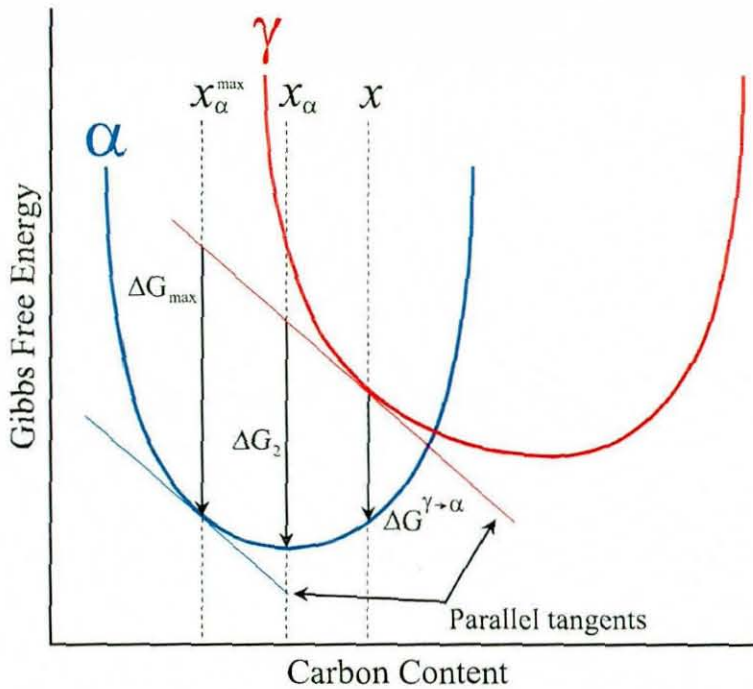
$\Delta G^{\gamma \to \alpha}$ No composition change in nucleus
ΔG_2 Parallel tangents method, nucleus composition X_α
ΔG_{max} Maximum possible free energy change, nucleus composition X_α^{max}

Figure 8.3 shows the free energy curves calculated by the program for shell 1 of alloy 2 after austenitisation at 950°C, for an austempering temperature of 320°C (*composition shown in table 7.1*). The ferrite curve clearly shows that the ferrite has a minimum free energy when the carbon content of the alloy is zero. This behaviour was observed in a wide range of ferrite free energy curves which were investigated. The curves cross at the point where the austenite has the critical carbon content X_{T0}, as outlined in section 5.1.3.

Figure 8.3. The free energy curves of ferrite and austenite for shell 1 of alloy 2 after austenitisation at 950°C, for an austempering temperature of 320°C.
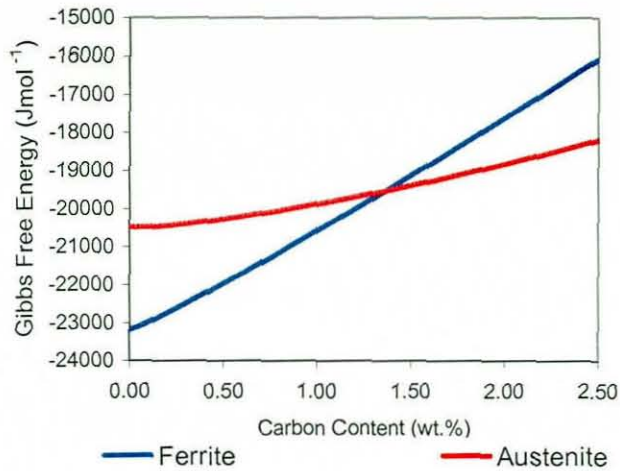
8.2.4 Testing of the austempering kinetics model

Dilatometry measurement data were obtained from two sources for comparison with the kinetic model; experiments performed by Vassileva [116] and data obtained from the Materials Algorithms Project website (MAP site) [117]. The compositions of the two alloys are listed in table 8.1.

Table 8.1. Composition of alloys (all wt.%).

Alloy	Fe	C	Si	Mn	Mo	Mg	P	S	Cu	Cr	Ni
Vassileva[116]	Balance	4.2	2.9	0.28	0.045	0.04	0.04	0.01	0.0	0.0	0.0
MAP [117]	Balance	3.55	2.51	0.549	0.152	0.042	0.015	0.012	0.311	0.0	0.0

For comparison purposes, the model was run using four different driving force calculations and the results were compared to the dilatometry data. The first driving force used in the model was $\Delta G^{\gamma \to \alpha}$, then $\Delta G^{\gamma \to \alpha}$ was recalculated to incorporate the stored energy of bainitic ferrite, by adding 400 Jmol^{-1} to the ferrite free energy curve, $\Delta G^{\gamma \to \alpha*}$ [26]. The next driving force used was ΔG_{max}, and finally ΔG_{max}, again recalculated to incorporate the stored energy of bainitic ferrite, ΔG^{*}_{max}. The calculations were also performed assuming a fixed alloy composition, hence the

segregation effects as discussed in chapter 7 were not accounted for in the comparisons at this stage.

Figures 8.4 a, b and c show the results of the model predictions against the dilatometry data of Vassileva [116]. For all the heat treatment regimes shown in figure 8.4 the best agreement between the dilatometry transformation time and the model results is when the calculated free energy change is ΔG^*_{max}. When $\Delta G^{\gamma \to \alpha}$ is used as the driving force, the model predicts a much greater transformation time than when ΔG_{max} is used. Since the magnitude of $\Delta G^{\gamma \to \alpha}$ is much lower than that of ΔG_{max}, a longer transformation time prediction should be expected.

As can be seen in the figures 8.4 a, b and c the maximum volume fraction of bainitic ferrite measured by dilatometry does not agree well with the model predictions. This was expected, due to reasons outlined in section 5.1.3, where it was shown that dilatometry results were not in good agreement with the model predictions regarding the volume fraction of bainitic ferrite. Nevertheless, good agreement was observed between the model predictions and calculations of the volume fraction of bainitic ferrite using X-ray diffraction and magnetic measurements. However, figure 8.4 shows that the time for the transformation can still be compared to the model results. All the kinetic model predictions are for stage 1 of the austempering process. Stage 1 is completed when the bainite reaction has ceased in ADI alloys and is characterised in the dilatometry results as the point on the curve where the volume fraction of bainitic ferrite reaches its maximum. This point can therefore be compared to the model results as demonstrated in figure 8.5 where the volume fraction predictions made by the X_{T^*} model version, have been matched to the dilatometry results. This was done by simply multiplying all of the model data by the result of the division of the maximum volume fraction of austenite measured by the dilatometry and the maximum volume fraction of austenite measured by the model. As can be seen in figure 8.5, excellent agreement is obtained between the dilatometry results and model predictions, using ΔG^*_{max}, when the results of the model are matched to the dilatometry volume fractions. This demonstrates that although the volume fraction predictions do not agree with the dilatometry results, the kinetic predictions are accurate for these alloys. Hence, ΔG^*_{max} was the driving force used in all the subsequent kinetic model predictions of the stage 1 austempering transformation.

Figure 8.4. Comparison of kinetic model predictions with the experimental data of Vassileva: a) 950/300°C, b) 950/350°C and c) 950/400°C [116].
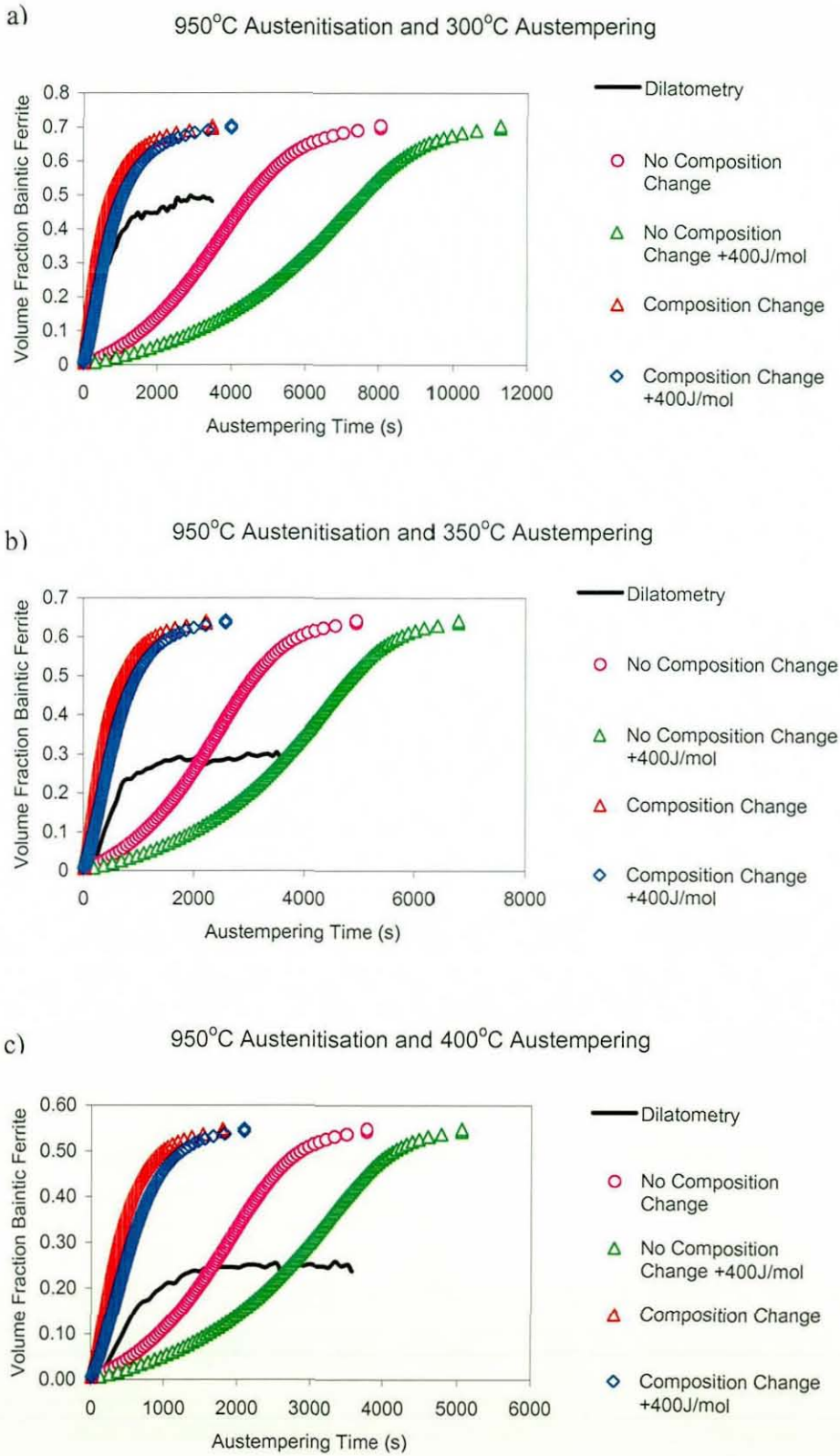

a) 950°C Austenitisation and 300°C Austempering

b) 950°C Austenitisation and 350°C Austempering

c) 950°C Austenitisation and 400°C Austempering

Figure 8.6 compares the results of the model predictions using ΔG^*_{max} as the free energy change, against the MAP dilatometry data for an ADI alloy of composition listed in table 8.1 [117]. Again as seen in figure 8.6 the dilatometry volume fractions do not agree well with the model predictions. However, the transformation times predicted by the model for all heat treatment conditions are in good agreement with the dilatometry results. Therefore it can be seen that good agreement is achieved between model predictions of transformation kinetics and dilatometry transformation time results.

Figure 8.5. Comparison of kinetic model predictions with the dilatometry data of Vassileva [116] when model volume fractions are matched to the dilatometry results.
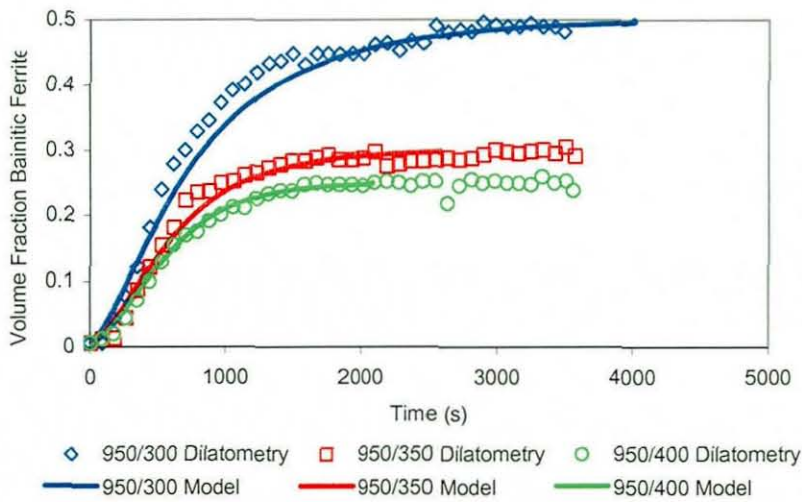
Figure 8.6. Comparison of kinetic model predictions with the experimental data obtained from MAP [117].
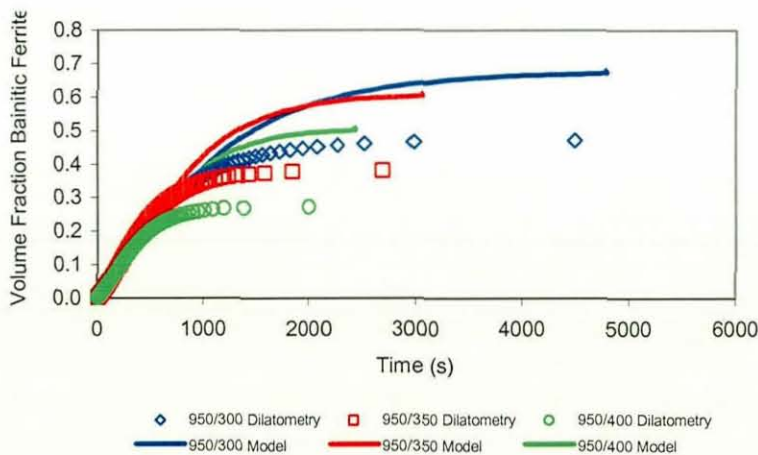
8.2.5 Comparison between local austempering kinetics model and image analysis measurements on alloys 1 and 2

Section 8.2.4 showed that good agreement was obtained between kinetic predictions of stage one of the austempering heat treatment and experimental results of the microstructure model for a fixed alloy composition. The following section shows the results of the kinetic predictions when they are incorporated into the segregated microstructure model as discussed in part 8.2.3. Hence the influence of alloying element segregation as described in chapter 7 can be included in the microstructure model kinetic predictions. These predictions are then compared to experimental results.

The compositions of alloy 1 and 2 are listed in table 7.1. Alloy 1 contained more Si, but slightly less Cu than alloy 2. Specimens with dimensions of 20×10×10 mm were cut from castings for heat treatment. Both materials were austenitised in a nitrogen environment in an electrically heated furnace at a temperature of 950°C for a time of 90 minutes. The samples were then immediately placed in an austempering nitrate-nitride salt bath at a temperature of 320°C for times ranging from 1-240 minutes. Image analysis was performed on all the samples to measure the volume fractions of the untransformed austenite volume (UAV), the retained austenite (RA), bainitic ferrite and graphite, using the ASTM standard method [118]. This involved superimposing a transparent plastic test grid over the image. The phase under each grid point was identified and recorded, then divided by the total number of points, yielding a percentage value for each phase. The process was repeated on randomly selected images from each sample, enabling the volume fractions of the phases to be calculated to an accuracy of ± 10%.

The segregation that occurred in the casting was calculated using the segregated microstructure model. The results of these predictions and comparisons with experimental results have been presented in section 7.4.1, where in both alloys Mn was found in higher concentrations in the last liquid to solidify, whilst Si displayed the opposite behaviour. The influence that segregation has on local austenite carbon content after austenitisation and local microstructure after stage one of austempering have been presented in parts 7.4.2 and 7.4.3 respectively. The local transformation kinetics were then calculated for both alloys. The prediction of the segregation

profiles enabled stage one driving force predictions to be made as a function of distance from the nodules in the alloys.

Figure 8.7 shows the influence segregation has on ΔG^*_{max} (see section 8.2.3) for alloys 1 and 2 as a function of distance from the graphite nodule. In figure 8.7 shells 1 and 10 represent material next to and in between graphite nodules respectively. The driving forces for both specimens are seen to reduce as the distance from the nodule increases. The severity of this reduction increases with distance from the graphite nodule especially in the last region to solidify, which is where Mn segregation is predicted to be most severe. Mn is known to slow the austempering reaction, hence the reduced driving force found in these regions is consistent with that expected [37].

Alloy 2 is predicted to have lower driving forces than alloy 1 for the stage 1 transformation. This is a result of the composition difference between the two alloys. Si, which is found in lower quantities in alloy 2, is a ferrite promoting element. Therefore, it is expected that an alloy containing more of this element would possess a greater driving force to transform to ferrite, as observed in figure 8.7. Indeed Mallia *et al.* found that higher Si contents increased the stage 1 driving force in ADI alloys[32]. Although the quantity of Si is predicted to reduce with distance from the graphite nodule, the difference between the Si concentration in the two alloys remains approximately equal in all the shells. Hence, the driving force difference between the two alloys does not change significantly across the shells.

Figure 8.7. Variation in calculated stage 1 driving force with distance from the graphite nodule.
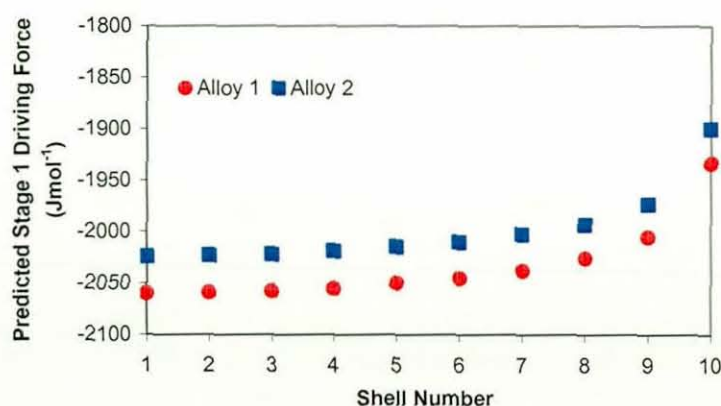
The effect of the reduction in the driving force on the time needed to complete stage 1 of austempering can be seen in Figure 8.8. The time needed to complete stage 1 of austempering is predicted to be 20 minutes longer in the shell furthest from the nodule compared to the shell closest to the nodule for both alloys. This is a direct consequence of the reduced driving force in the last shell, which stems from its high Mn content. As would be expected due to the lower Si content, alloy 2 takes a greater time to complete its transformation than alloy 1 for all shells.

Figure 8.8. Variation in predicted stage 1 transformation time with distance from the graphite nodule.
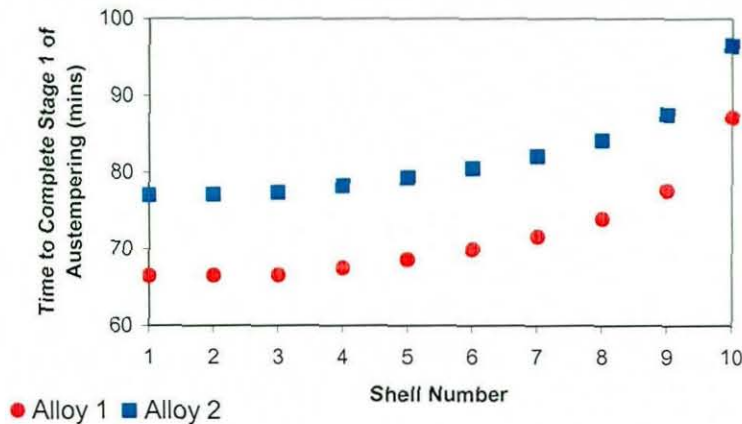
Figures 8.9 and 8.10 compare the predicted reaction kinetics for the first (closest to the nodule) and last (furthest from the nodule) shells of alloys 1 and 2 respectively with the measured volume fractions of bainitic ferrite. The end of the lines in the figures represent the completion of stage 1 of austempering. The untransformed austenite volume (UAV), is the austenite that has not been significantly enriched with C to be retained on cooling to room temperature. For both materials it was found to fall below 3% after 90 minutes of austempering which signifies the end of the stage 1 reaction in accordance with the ASTM A897M 1990 standard[56]. In both alloys, the time needed for completion of the stage 1 reaction is in good agreement with the 90 minute value corresponding to the UAV volume fraction falling below 3%. The predictions of the how the volume fraction of bainitic ferrite changes with austempering time are also in reasonable agreement with the corresponding measured volume fractions of bainitic ferrite, although for both alloys

the model seems to under estimate the volume fraction of bainitic ferrite. As can be seen in both figures, the shell which is first to solidify, is predicted to complete stage 1 in a shorter time period than the last shell, as discussed previously.

Figure 8.9. Measured and predicted transformation kinetics for alloy 1.
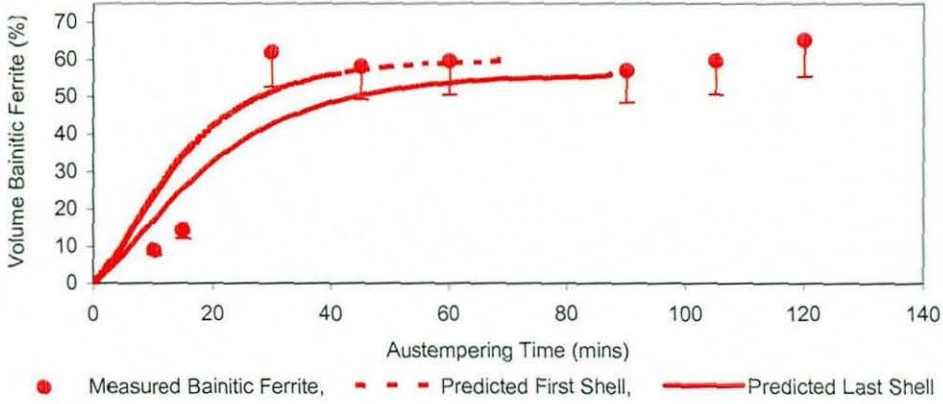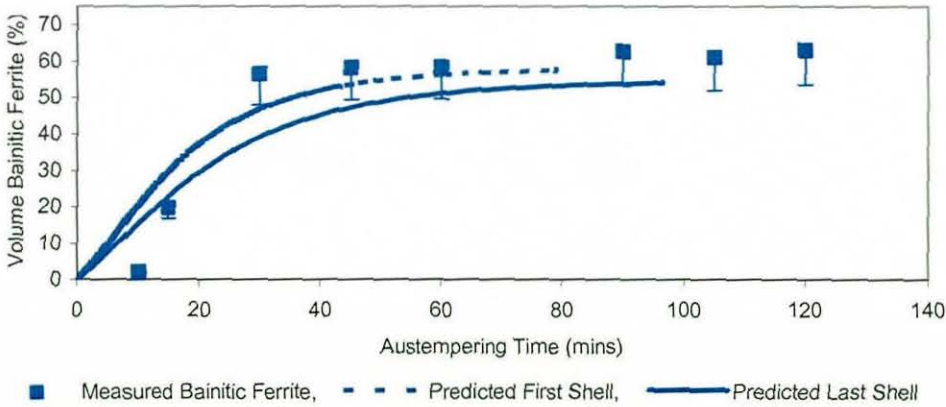

**Figure 8.10.** Measured and predicted transformation kinetics for alloy 2.

Error bars of minus 15% are included in the figures 8.9 and 8.10. Image analysis of the ADI microstructures tends to over estimate the volume fraction of bainitic ferrite since thin films of austenite trapped between bainitic ferrite plates cannot be resolved easily using optical microscopy [84]. Therefore the values for the volume fraction of bainitic ferrite shown in figures 8.9 and 8.10 are expected to be an overestimation. This is reflected in the size and nature of the error bars. Figure 8.11

shows a SEM image of the thin films of austenite sandwiched between bainitic ferrite plates in alloy 1 after austempering for 30 minutes. These thin films of austenite cannot readily be identified using optical microscopy. For comparison, larger regions of austenite that can be observed optically are also highlighted.

Image analysis was performed on SEM images of alloy 1 after austempering for 30 minutes, using the ASTM standard method [118]. The average volume fraction of bainitic ferrite measured was 53%, whilst the corresponding image analysis results from optical micrographs showed a bainitic ferrite volume fraction of 62%. This 9% difference between the two measurements is within the ~15% error bar limit. These observations confirm the need for the use of the error bars in figures 8.9 and 8.10, when comparing optical image analysis results with the model predictions.

Figure 8.11. A SEM image of thin films of austenite sandwiched between bainitic ferrite plates in alloy 1 after austempering for 30 minutes.
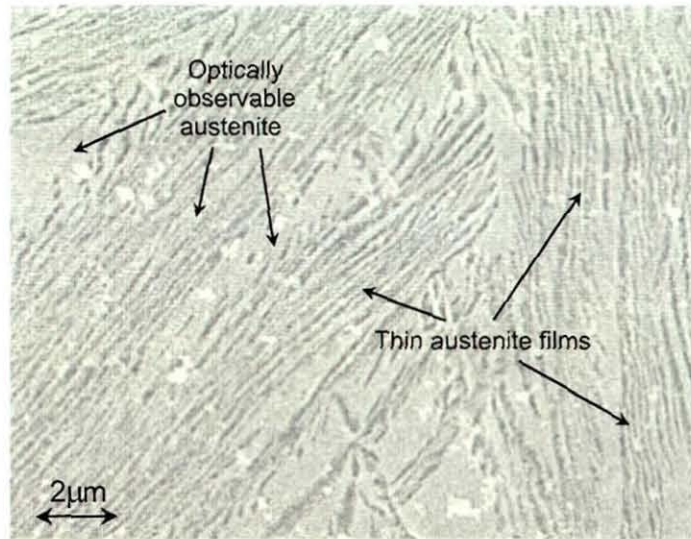
The kinetic predictions produced by the model are in agreement with observations in commercial alloys, where matrix areas that contain higher concentrations of alloying elements due to segregation effects, are known to transform at a slower rate during austempering [2;31;32;38;55]. This problem is of important commercial value to ADI producers since these effects can result in the optimum mechanical properties of ADI alloys not being reached [2;15]. However, it is impossible to obtain accurate experimental measurements to confirm the individual transformation rate of material representative of each of the ten shells in the model,

since all the experimental methods used to monitor the austempering process measure bulk, not local, material properties. In spite of this, the applicability of the model is still valid since it is founded on the well established principle that segregation influences local austempering kinetics in ADI alloys [15;23].

Figure 8.12 shows how the microstructure of alloy 1 changed as a function of time through the austempering heat treatment. The changes in microstructure can be related to the formation of bainitic ferrite with changes in austempering time as predicted in the kinetic model in figure 8.9. Figure 8.12 show that the bainitic ferrite plates have started to form after 5 minutes of austempering. The majority of the matrix is martensite, since the metastable austenite was not enriched enough with C to prevent martensite formation on quenching to room temperature. As austempering time increases, so does the volume fraction of bainitic ferrite in the microstructure. After 20 minutes of austempering, some areas of martensite can still be seen in the sample because some of the austenite has still not been enriched enough with C to prevent its formation on quenching to room temperature.

The micrograph after 60 minutes shows that some microstructural regions are slow to transform to bainitic ferrite. It is interesting to note that most of these slow transforming regions are far from the graphite nodules. However, the regions close to the nodule have completed the stage 1 austempering reaction, as predicted by the kinetic model in figure 8.9. After 75 minutes of austempering the untransformed austenite volume is much lower as the stage 1 transformation nears completion. Little difference can be observed in the microstructures shown after austempering for 90, 105 and 120 minutes. This is because as predicted by the kinetic model (see figure 8.9) the stage 1 transformation has completed and the volume fraction of bainitic ferrite and retained high C austenite remain stable in the microstructure through the processing window.

Figure 8.12. Optical micrographs showing the influence of austempering time on the microstructure of alloy 1 after austenitisation at 950°C and austempering at 320°C.
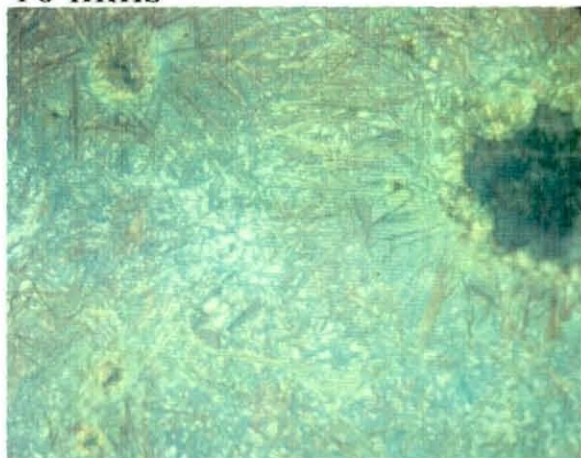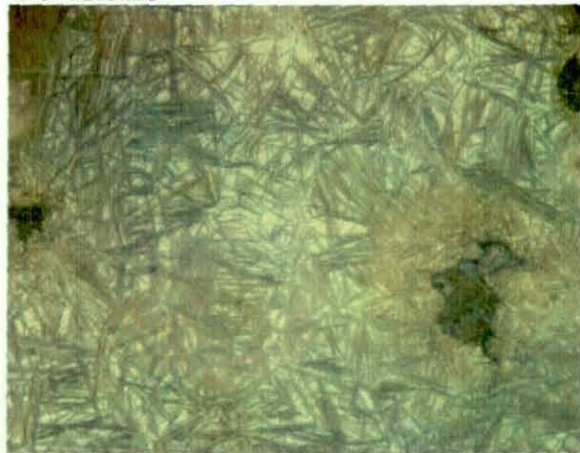
1 min
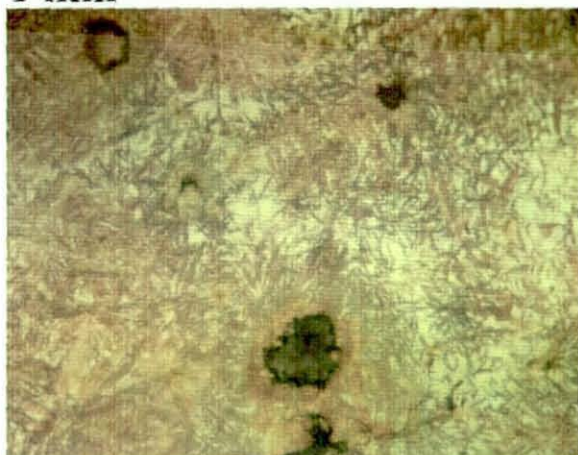
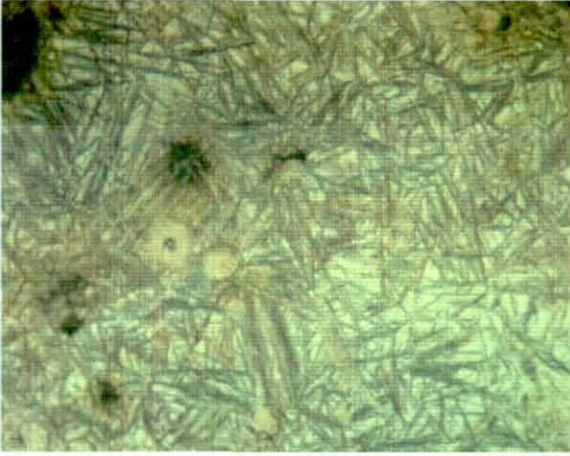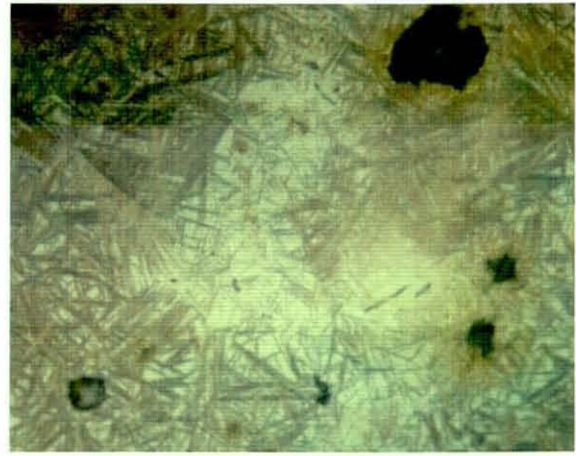5 mins

10 mins

15 mins

20 mins

30 mins

60 μm
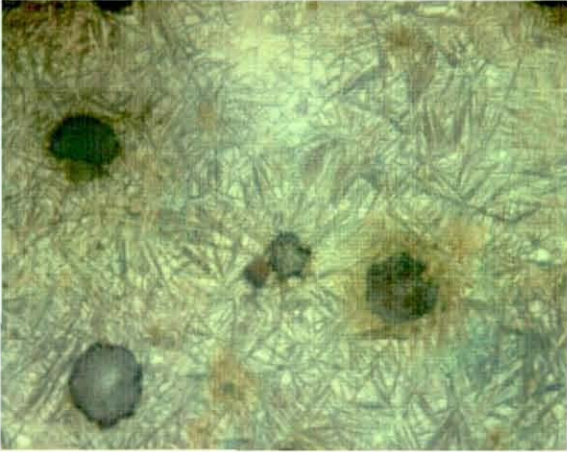←———→
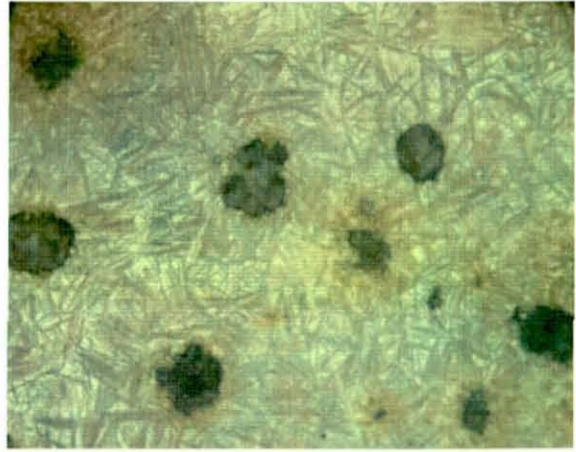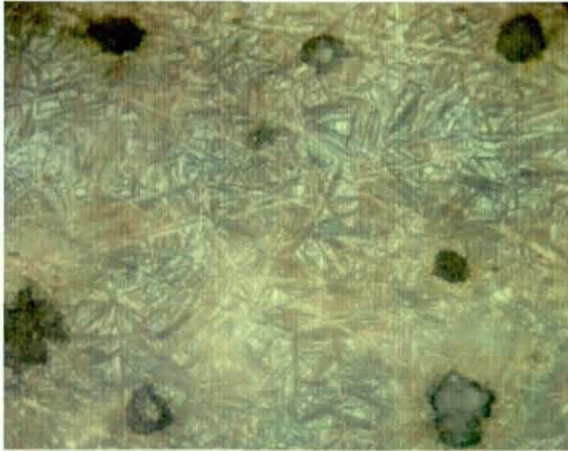
Figure 8.12. Continued.

45 mins

60 mins

75 mins

90 mins

105 mins

120 mins

60 μm

8.2.6 Comparison between local austempering kinetics model and X-ray diffraction measurements obtained from literature

A wide range of literature measurements regarding the transformation kinetics of austempered ductile iron alloys are available in literature [15;22;24;32;49;90]. Most of these works use X-ray diffraction to monitor the austempering transformation kinetics. The data in one such work by Darwish and Elliott [15] are compared to the kinetic predictions of the segregated microstructure model in this section. The compositions of the two alloys in question are listed in table 8.2. Figures 8.13 and 8.14 show the predicted 10 shell segregation profile for the major alloying elements in the two alloys. As expected, in both figures Si and Cu are predicted to segregate towards the graphite nodule and hence are found in higher concentrations in shell 1, and the Ni in figure 8.13 shows an almost neutral segregation profile.

Table 8.2. Composition of Darwish and Elliott alloys (all wt.%) [15].

Alloy	Fe	C	Si	Mn	Mo	Mg	P	S	Cu	Cr	Ni
Cu iron	Balance	3.8	2.77	0.037	0.0	0.034	0.03	0.02	0.33	0.02	0.07
Cu-Ni iron	Balance	3.60	2.80	0.016	0.0	0.04	0.01	0.01	0.90	0.06	1.02

Figure 8.13. Model prediction of the segregation of major alloying elements in the Cu iron.
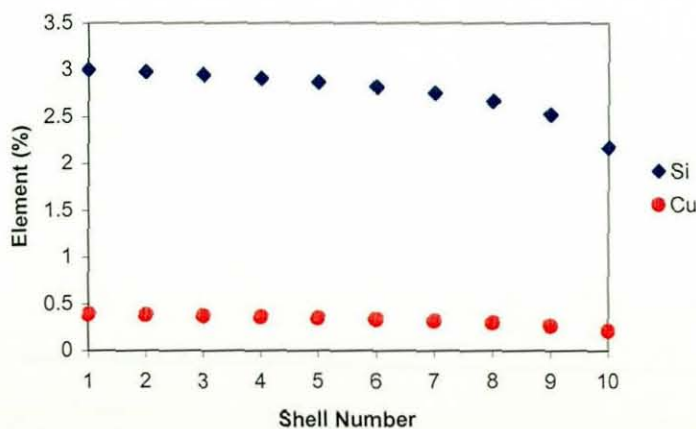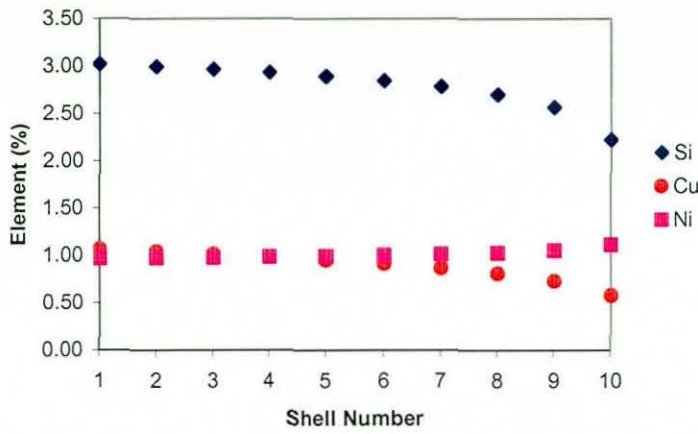
Figure 8.14. Model prediction of the segregation of major alloying elements in the Cu-Ni iron.


Darwish and Elliott austenitised the alloys at 900°C and austempering was performed at 300, 370 and 440°C in both alloys for times ranging from 1-1440 minutes [15]. The retained austenite volume, austenite C content and untransformed austenite volume (UAV) as a function of austempering time were recorded using X-ray diffraction measurements on quenched samples [15]. A comparison of the ΔG^*_{max} values calculated by the model as a function of shell number is shown in figure 8.15 for the alloys that were austempered at 300°C.

Figure 8.15. Variation in calculated stage 1 driving force with distance from the graphite nodule for Cu and Cu-Ni alloys austempered at 300°C.
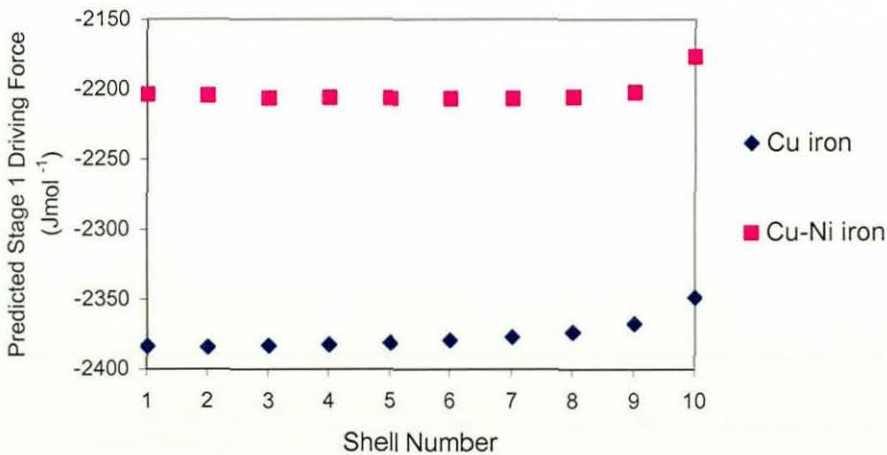
As can be seen in figure 8.15, the ΔG^*_{max} values are greater for the Cu iron than for the Cu-Ni iron. Ni and Cu are both known to stabilise the austenite phase field in steels [33;119]. Therefore, it was thought that the influence these elements have on the free energy of the austenite phase resulted in the driving force being smaller in this alloy. The concentration of Ni in the Cu-Ni iron listed in table 8.2 was halved and the model was rerun with the new composition to demonstrate this effect. The free energy curves for the austenite and ferrite phases for shell 1 of the Cu-Ni alloy are shown in figure 8.16, where they are compared to the corresponding free energy curves when the Ni concentration was halved. As can be seen in the figure, halving the Ni concentration had little influence on the free energy of ferrite, but a significant reduction in the austenite free energy occurs, which is in agreement with the austenite stabilising characteristic of Ni. Hence it can be seen that a high Ni content will lead to a reduction in ΔG^*_{max}.

Figure 8.15. The influence of Ni concentration on the free energy of ferrite and austenite in shell 1 of the Cu-Ni iron.
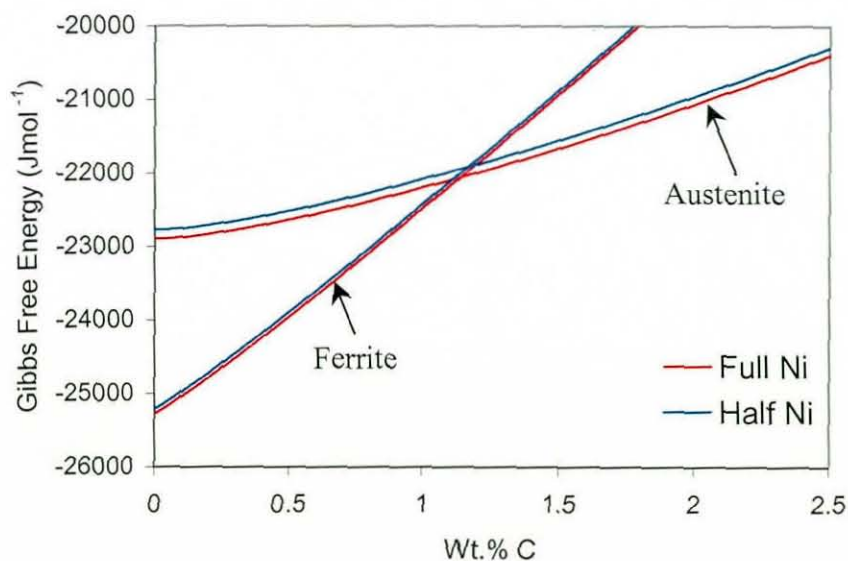
The process was repeated, but this time the Cu concentration was halved. Figure 8.16 shows the influence Cu concentration has on the austenite and ferrite free energies in the Cu-Ni iron. As can be seen in the figure, the behaviour is not that which was expected, as an increase in Cu concentration does not lower the austenite

free energy. However, the free energy of the ferrite phase is seen to increase with concentration of Cu. Therefore, although Cu has little direct influence of on the free energy of austenite it does seem to reduce the stability of the ferrite phase and therefore indirectly increase the stability of austenite. This would also help explain the observations in figure 8.15 where ΔG^{*}_{max} is smaller in the Cu-Ni alloy.
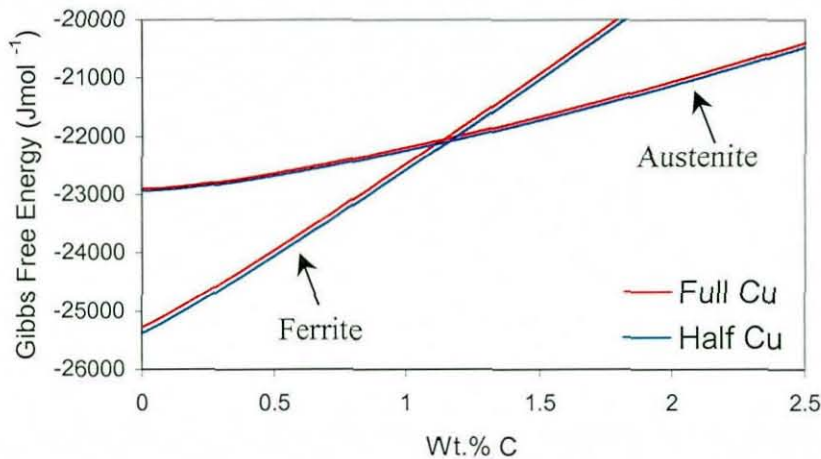
Figure 8.16. The influence of Cu concentration on the free energy of ferrite and austenite in shell 1 of the Cu-Ni iron.


Figures 8.17 and 8.18 compare the predictions of the stage 1 transformation kinetics for the bainitic ferrite phase made by the model for the Cu and Cu-Ni irons respectively, to the retained austenite and UAV experimental measurements of Darwish and Elliott [15]. The end of stage 1 of austempering is signified by the point where the UAV value falls below 3% according to the ASTM standard [56]. This point generally coincides with the transformation time were the volume fraction of retained austenite becomes constant. In all the figures, the transformation time needed to complete stage 1 of austempering is in good agreement with these experimental measurements. It can also be seen that the accuracy of the phase volume predictions made by the model is in good agreement with the retained austenite measurements for all the heat treatments except where the alloys were austempered at the highest temperature of 440°C. The 440°C measurements do not agree with the model predictions because as previously discussed in section 6.3, the processing window is closed for these alloys, therefore the maximum volume of bainitic ferrite is not reached.

Figure 8.17. Comparison of kinetic model predictions for the volume of bainitic ferrite with experimental results of Darwish and Elliott for a Cu iron [15].

a) Austenitised at 900°C, austempered at 300°C
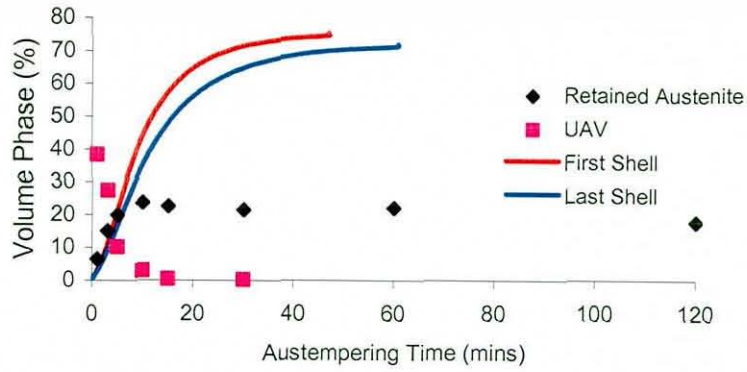
b) Austenitised at 900°C, austempered at 370°C
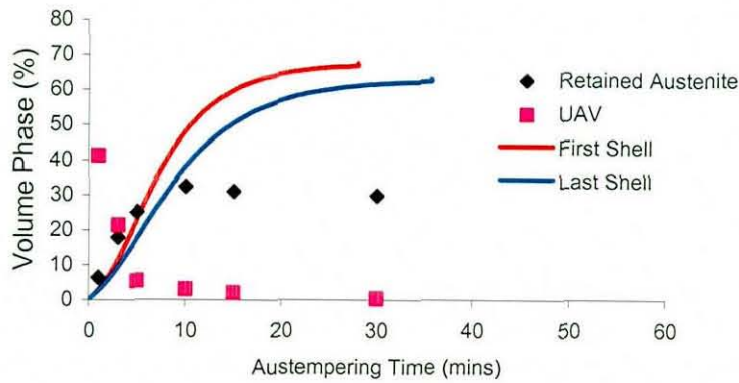
c) Austenitised at 900°C, austempered at 440°C

Figure 8.18. Comparison of kinetic model predictions for the volume of bainitic ferrite with experimental results of Darwish and Elliott for a Cu-Ni iron [15].

a) Austenitised at 900°C, austempered at 300°C

b) Austenitised at 900°C, austempered at 370°C
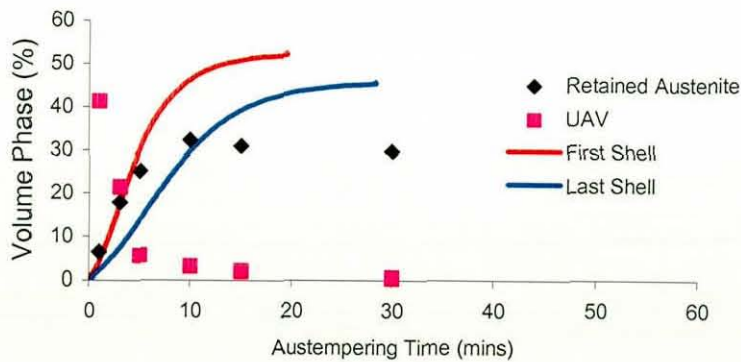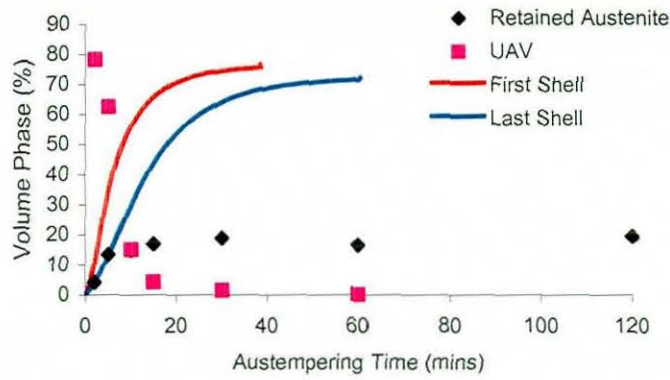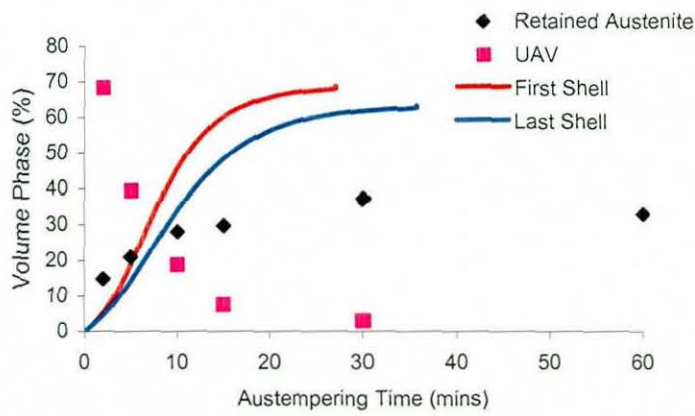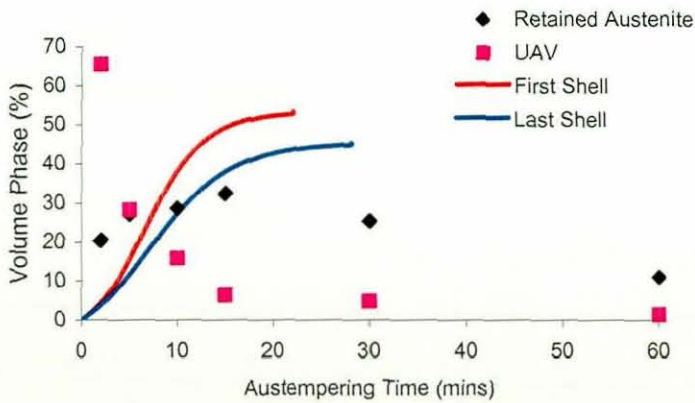

c) Austenitised at 900°C, austempered at 440°C

Although the Cu and Cu-Ni irons were only austenitised at 900°C, table 8.4 shows how the average ΔG^*_{max} from the 10 shells was predicted to change as a function of heat treatment for the Cu irons. The austenitisation heat treatment plays an important role in the kinetics of the austempering process. Higher austenitisation temperatures generally produce higher austenite C contents, and therefore reduce the driving force for the transformation to bainitic ferrite during austempering as shown in figure 2.14 [2;49;55]. Table 8.4 shows the important influence of austenitisation temperature is accounted for by the model calculations. For a fixed austempering temperature, as the austenitisation temperature reduces, ΔG^*_{max} is seen to increase, which is the behaviour expected [2;49;55]. However, table 8.4 also shows that the calculated influence of the austenitisation temperature is much less potent than that of the austempering temperature. As the austempering temperature increases, ΔG^*_{max} significantly reduces. This is in agreement with the theoretically expected behaviour which states that as the austempering temperature increases the transformation to bainitic ferrite ultimately decreases to zero, since the austenite can only transform to bainitic ferrite if its carbon content is less than the value X_{T0} [26;101]. Therefore it can be seen that the transformation kinetics model is capable of accounting for the important influence of austenitisation and austempering temperature when calculating ΔG^*_{max} values for ADI alloys.

Table 8.4. Comparison of calculated ΔG^*_{max} values for different heat treatments in the Cu iron.

Heat Treatment Details Austenitisation/Austempering (°C)	1000/ 300	950/ 300	900/ 300	900/ 370	900/ 440
Average ΔG^*_{max} (Jmol^{-1})	-2260	-2320	-2376	-1807	-1272

8.3 Improvement of Martensite Start Temperature Prediction

As shown in section 5.1.4, in the original model version the relationship proposed by Andrews [85] was used to calculate the martensite start temperature (M_S) of the austenite in ADI alloy microstructures. One drawback of using this relationship

is that it only accounts for the influence of the elements C, Ni, Mo, Mn and Cr. ADI alloys contain significant quantities of other elements such as Si and Cu that are not accounted for by the relationship and hence could influence the M_S temperature.

A thermodynamic approach exists which states that martensite formation occurs when the driving force for the austenite to martensite transformation reaches a critical value at the M_S temperature [120;121], hence:

$$\Delta G^{\gamma \to \alpha'} \{M_S\} = \Delta G_C^{\gamma \to \alpha'} \qquad [8.9]$$

where $\Delta G^{\gamma \to \alpha'} \{T\}$ is the free energy change of austenite to martensite of the same chemical composition at a temperature T and $\Delta G_C^{\gamma \to \alpha'}$ is the critical driving force needed to trigger martensite formation. This term accounts for the Zener ordering of carbon atoms and hence differs from the transformation of austenite to ferrite of the same chemical composition, $\Delta G^{\gamma \to \alpha}$. The Zener ordering energy term is related to changes in crystal symmetry from bcc to bct, which may occur due to ordering of carbon atoms in the ferrite [122;123].

Ghosh and Olson proposed a method of calculating the critical driving force, $\Delta G_C^{\gamma \to \alpha'}$, for a wide range of steels [85;124]. This approach was modified by Cool and Bhadeshia, producing a better agreement between experimental results and M_S temperature predictions for a series of steels [125]. As part of this work an MTDATA slave application was written that calculated for comparison purposes, $\Delta G_C^{\gamma \to \alpha'}$ using both methods and the driving force for the austenite to ferrite transformation, $\Delta G^{\gamma \to \alpha}$, as a function of alloy composition and temperature. The Zener ordering energy, G_Z, was also calculated as in reference 126 by the program and combined with $\Delta G^{\gamma \to \alpha}$, producing $\Delta G^{\gamma \to \alpha'}$ values over a temperature range of 1000-1K in steps of one K, as shown in equation 8.10:

$$\Delta G^{\gamma \to \alpha'} = \Delta G^{\gamma \to \alpha} + G_Z \qquad [8.10]$$

The program then independently found the temperature where the conditions of equation 8.9 were met for both of the $\Delta G_C^{\gamma \to \alpha'}$ values (i.e. the M_S temperatures). The slave application therefore was independently able to predict the M_S temperature of ADI alloys accounting for all of the alloying elements in the system.

M_S temperature data for a large number of steels and ductile iron alloys were found in the literature and compared with the model predictions [125;127;128]. It was found that the critical driving force, which was calculated in the program using the Cool method, produced the best fit with the literature results. The predictions using the Cool critical driving force are shown in figure 8.19 along with the M_S predictions using the Andrews relationship, which was used by the original microstructure model. As can be seen in the figure, the agreement between the model predictions and experimental measurements of the M_S temperature is good. In particular, excellent agreement is observed between the ductile iron literature M_S temperatures values and the model predictions. A better agreement is also observed between the experimental and predicted M_S temperatures using the Cool critical driving force method, than with the predictions made using the Andrews equation. Therefore the model based on the Cool critical driving force method for calculating the M_S temperature of ADI alloys was incorporated into all versions of the microstructure model, replacing the Andrews relationship.

Figure 8.19. Comparison of predicted M_S temperatures with experimental measurements for a range of steels and ductile iron alloys.

◆ Steels (Cool) ■ Irons (Cool) ○ Steels (Andrews) □ Irons (Andrews)
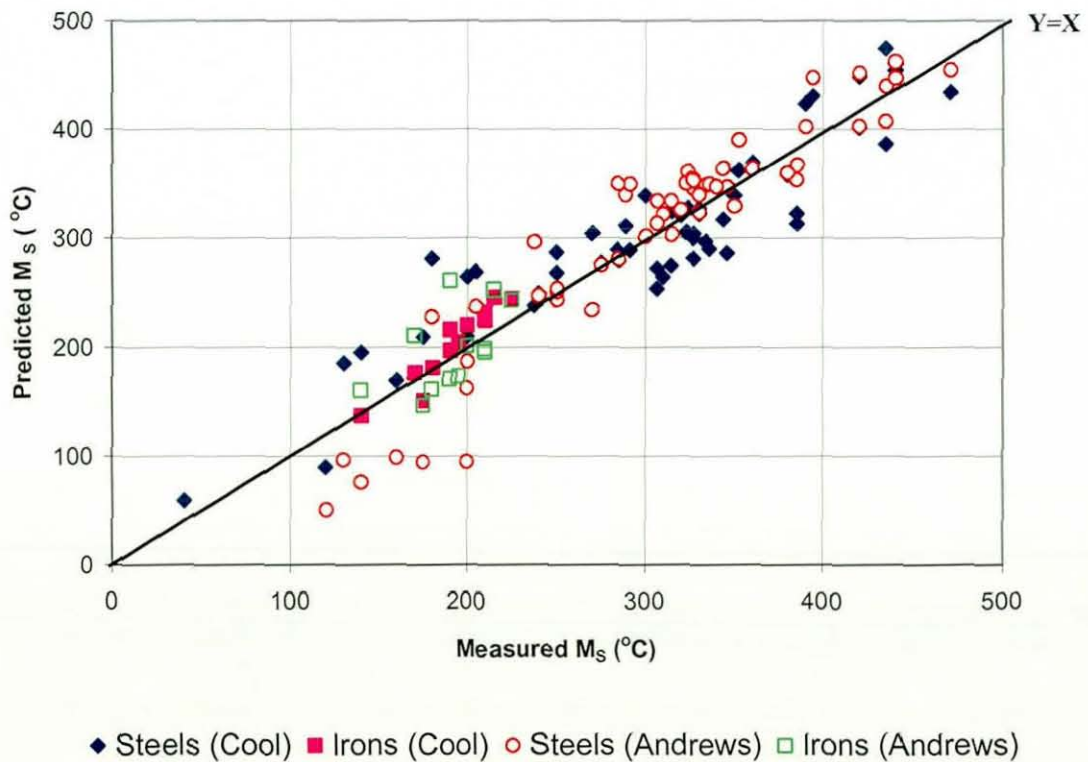
8.4 Summary

A method of predicting the kinetics of stage one of the austempering process in ADI alloys has been introduced. MTDATA was used to calculate the driving force for the austempering transformation in the model. Experimental data taken during the austempering of ADI alloys have been used to validate the accuracy of the kinetic predictions. Good agreement was observed between the predications and experimental data over a wide range of austempering temperatures.

The kinetic predictions were then incorporated into a model described in chapter 7 which predicted alloying element segregation in ductile iron alloys. This enabled predictions of local alloy transformation kinetics to be made. Although the variations predicted to occur during austempering are difficult to measure experimentally, the predictions are in agreement with what is generally observed and theoretically expected in ADI alloys. It was also demonstrated that the kinetic predictions made by the model were capable of accounting for the important influence of austenitisation and austempering temperatures on the rate of transformation in ADI alloys. Finally, a new method based on thermodynamics, which accounts for all the alloying elements present in ADI alloys has been used to estimate the martensite start temperature. This method was shown to be an improvement over the original empirically based relationship.

The accumulation of the various modelling processes discussed in chapters 5, 7 and 8 enabled a new model to be produced for ADI alloys. The new model makes use of MTDATA throughout the modelling process, to calculate the necessary thermodynamic parameters, therefore maintaining its generic applicability to all ADI alloys. The main improvements of the new model are that it accounts for segregation and calculates local transformation kinetics in ADI alloys, and therefore attempts to address issues that are of concern to alloy producers.

9 Introduction to High Temperature X-ray Diffraction and Preliminary Investigations

9.1 Introduction

High temperature diffraction X-ray was developed as an experimental method in the early 1920's. Since then it has developed into a technique which is useful to measure the lattice parameter of iron and steels as a function of temperature and hence is a useful tool for monitoring phase transformations. In more recent times experiments have been performed to investigate phase stability, oxidation and texture in iron based alloys. The early literature is briefly reviewed and then this chapter details the development of the high temperature X-ray diffraction technique at Loughborough University. A large amount of preliminary work was performed over a period of over 18 months, which yielded little useful experimental data, but nevertheless was crucial for the establishment of a reliable experimental platform, which could be built upon for subsequent experiments described in Chapter 10.

9.2 The Principle of X-ray Diffraction

X-ray diffraction is a useful technique for obtaining information about the crystal structure and properties of a material. This technique utilises the fact that if a beam of incident X-rays, which has a wavelength of the same order of magnitude as the atomic spacing of the crystal, strikes the material, the X-rays are scattered in all directions [1;129]. The majority of radiation scattered from one atom is cancelled out by the radiation scattered from other atoms. However, X-rays that collide with certain crystallographic planes at a specific angle are reinforced. This concept is known as X-ray diffraction and is shown schematically in figure 9.1. The beam of X-rays is reinforced when conditions satisfy equation 9.1 which is known as Bragg's law [1;69;129]:

$$Sin\ \theta = n\lambda\ /\ 2d_{hkl} \qquad [9.1]$$

where θ is half the angle between the incident beam and the diffracted beam which is also known as the Bragg angle, λ is the wavelength of the incident X-rays, n is the order of diffraction and d_{hkl} is the spacing between the planes that cause

reinforcement of the scattered radiation. Samples are generally prepared in the form of a powder, hence some planes are always orientated at the correct angle to satisfy Bragg's law [1;69]. A type of moving detector known as a diffractometer records the angles where diffraction occurs producing a characteristic diffraction pattern for the crystal. Since the wavelength of the incident radiation is known, the inter planar spacings (d-spacings) of the diffracting planes can be calculated. This information can then be compared to a reference library leading to the identification of the material [1;69].

Figure 9.1. Schematic diagram of X-ray diffraction, showing a) destructive and b) reinforcing interactions between the crystal and the incident X-rays. Reproduced from [1].
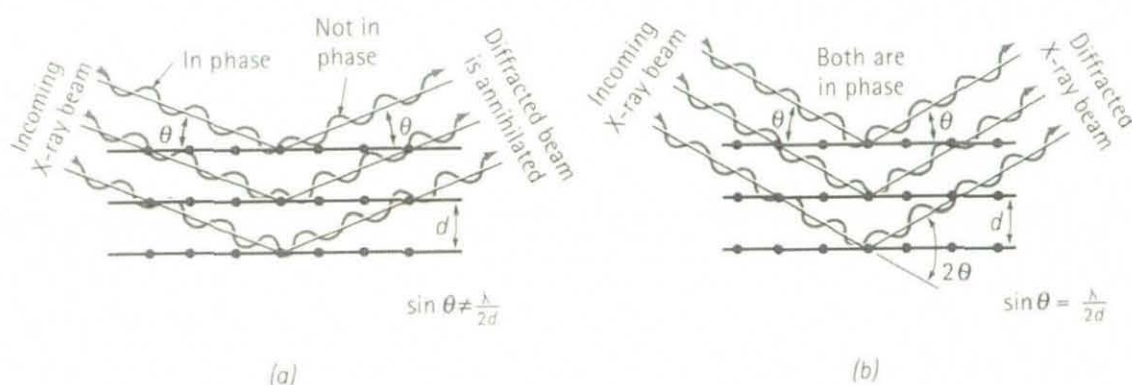
9.3 A Brief History of High Temperature X-ray Diffraction of Iron

Laue in 1912 was the first to demonstrate that Roentgen rays as they were known at that time, or X-rays as they are known today, caused interference phenomena whilst passing through a crystalline system [130]. Later that year W.H. Bragg and his son W.L. Bragg developed a method which had greater practical significance by investigating the behaviour of Roentgen rays reflecting against crystal surfaces. This in 1912, lead W.L. Bragg to formulate a relationship between the angle which X-rays were reflected and their wavelength which today is known as the Bragg law [131]. For their efforts Laue in 1914 and then W.H. and W.L. Bragg in 1915 won the Nobel prize in physics. Room temperature Roentgen investigation of crystalline

structures then developed rapidly and by the early 1920's the first high temperature investigations were being undertaken.

In 1921, Westgren was the first to prove that the α/γ transformation in iron was associated with the change from a body centred cubic to a face centred cubic structure, and that β iron did not exist [132]. Many authors at the time thought that iron had three crystallographic variations. α iron existed from ambient temperature to 768°C, where a transition in structure was thought to occur as a result of the change in the magnetic properties of iron that took place above 768°C. This iron variant was known as β iron and was thought to be stable until 880°C, where the transformation to γ iron occurred. Westgren's discovery conclusively proved otherwise and hence is still regarded as the most far reaching success of early high temperature X-ray research.

Becker was the first to successfully use high temperature X-ray techniques to measure the thermal expansion coefficient of iron [133]. Many authors were now developing their own high temperature cameras which are too numerous to mention here, however a number have been reviewed by Goldschmidt [134]. By the 1950's high temperature X-ray diffraction was an established technique for the measurement of the thermal expansion of crystals and was also used widely in the observation of phase transformations and hence the establishment and refinement of phase diagrams.

By 1955 the thermal expansion of iron had been successfully calibrated by Basinski *et al.* [135], whose results were later confirmed by Goldschmidt [136]. Previously, measurements on iron had shown greatly divergent results concerning both lattice parameter and Ae$_3$ temperature as shown in figure 9.2. These errors were probably due to the accuracy of temperature measurement and stability in early works.

High temperature X-ray studies were now being utilised in an increasing number of applications. The establishment of pure iron data provided a foundation for comparison with new research into steels. The advantage of the high temperature X-ray technique is that in multi-phase materials the expansion of each phase can be monitored individually, which is impossible using bulk dilatometry [137]. Tool steels are one such material. The individual expansions of the austenite, ferrite and M_6C carbide were measured as a function of temperature in an 18W, 4Cr and 1V (all

wt.%) tool steel [137]. Heat resistant steels used in the power generating industries were another example where high temperature X-ray analysis proved useful. The simulation of practical conditions that the materials are subjected during X-ray investigations helped in a number of problems encountered in the industry. Phase transformations could be monitored as a function of temperature and time, the solution and precipitation of secondary phases could be observed and the development and relief of internal strains could be studied [137]. The study of high temperature oxidation was another use of high temperature X-ray diffraction which was utilised during this period [138].

Figure 9.2. Early measurements of the iron lattice parameter as a function of temperature [136].
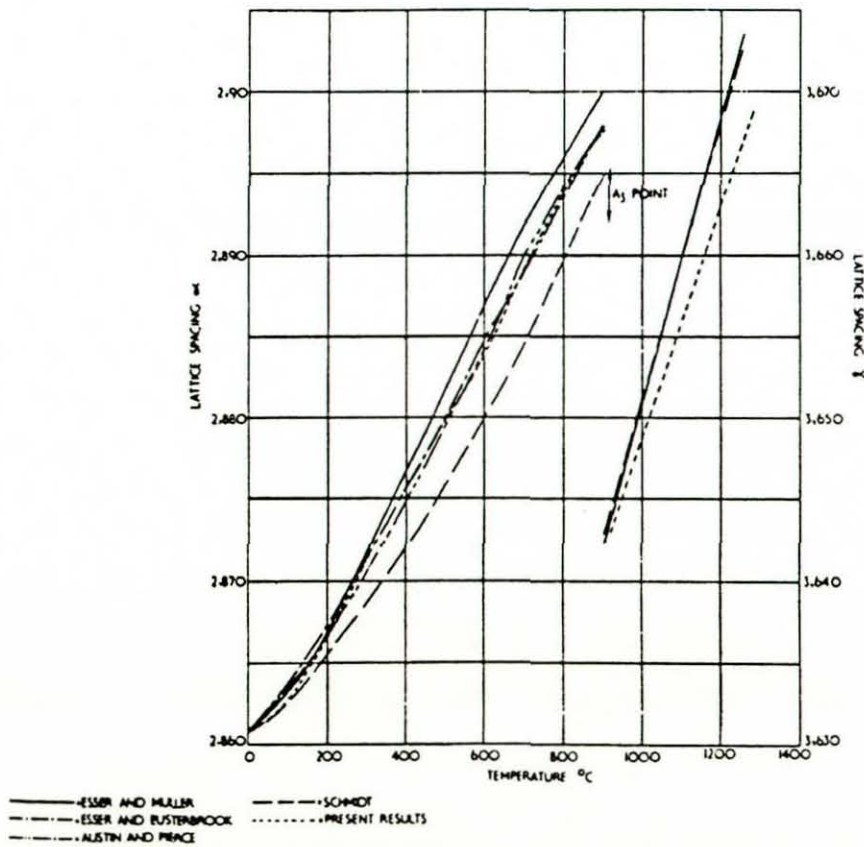
In 1970, Ridley and Stuart published the results of a high temperature X-ray diffraction study on a range of steels [139]. They determined the lattice parameter of austenite as a function of carbon concentration and temperature. This was the first

published study on this subject since the early work of Esser and Müller in 1933 [140]. Recent references to high temperature X-ray studies on materials have been largely focused on oxidation studies [141;142] and investigations performed on ceramic materials [143;144]. Indeed preliminary searches for published studies on iron based alloys between the years 1980-2000 have yielded no results. However, interest in high temperature X-ray diffraction of steels has been rekindled recently following a study regarding texture development during the austenite-ferrite transformation in low carbon steels [145].

9.4 Experimental Technique, Development and Preliminary Experiments

The high temperature X-ray experiments in this work were performed using a newly purchased Bruker AXS X-ray diffractometer as shown in figure 9.3, which had a copper X-ray tube (wavelength, λ_{Cu} = 1.54 Å), 40 kV and 40 mA. The specimen was placed on a platinum heating band, the temperature of which was adjusted by resistance heating. A thermocouple welded to the underside the heating band controlled the temperature of the band. Heat was then assumed to be transferred to the specimen by conduction between the touching surfaces of the polished specimen and heating band. The specimen and heating band were sealed inside a vacuum chamber for the duration of the test, hence the investigations could be performed under vacuum conditions or in the presence of an inert gas or another controlled atmosphere, which is particularly important for experiments on steel and cast iron alloys. Figure 9.4 shows a close up photograph of the inside of the vacuum chamber. The platinum heating band, ductile iron specimen and the position of the two thermocouples are highlighted in figure 9.4.

Before any successful high temperature X-ray investigations were performed a number of problems had to be overcome with the X-ray machine, because it had not been used previously for any high temperature X-ray work. It should be noted that some of these problems were substantial and took a significant amount of time and effort to solve.

The specimens were required to be in the form of thin flat, parallel sided plates. Flat plates of material with a uniform thickness no greater than 2 mm had to be prepared. The ductile iron material was supplied in the form of camshaft castings.

The shaft sections between the cams were first cut out of the camshaft using a metallurgical saw. This produced cylindrical sections of raw material approximately 25 mm in diameter. These were sliced into thin discs roughly 2.5 mm in thickness which were subsequently ground down to less than 2 mm in thickness. The discs were ground using with progressively finer silicon carbide papers to 1200 grit, before being given a final polish on a 6 μm diamond impregnated polishing cloth. The polishing process was repeated on both sides of the disc.

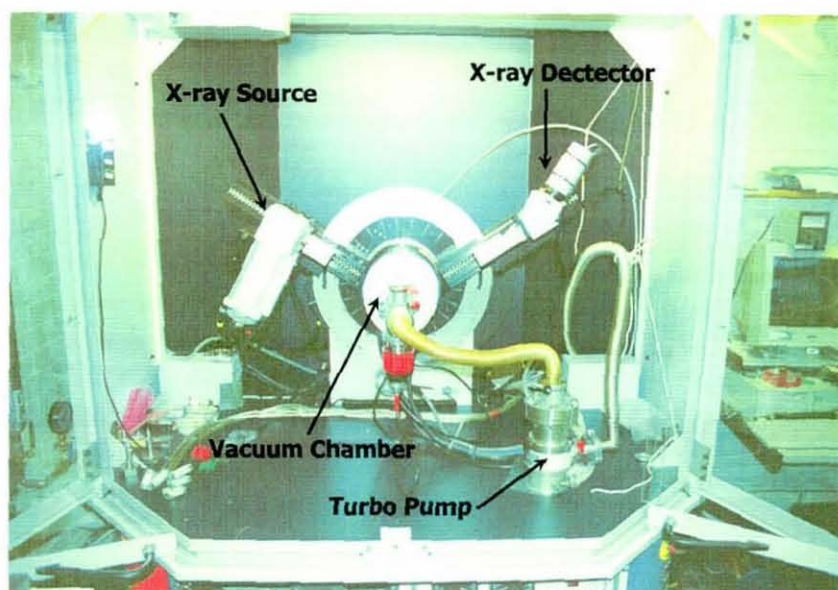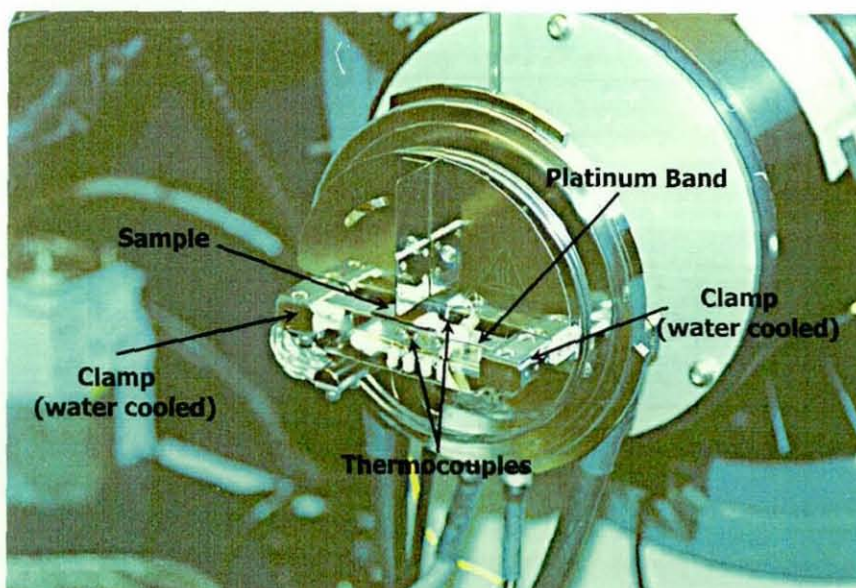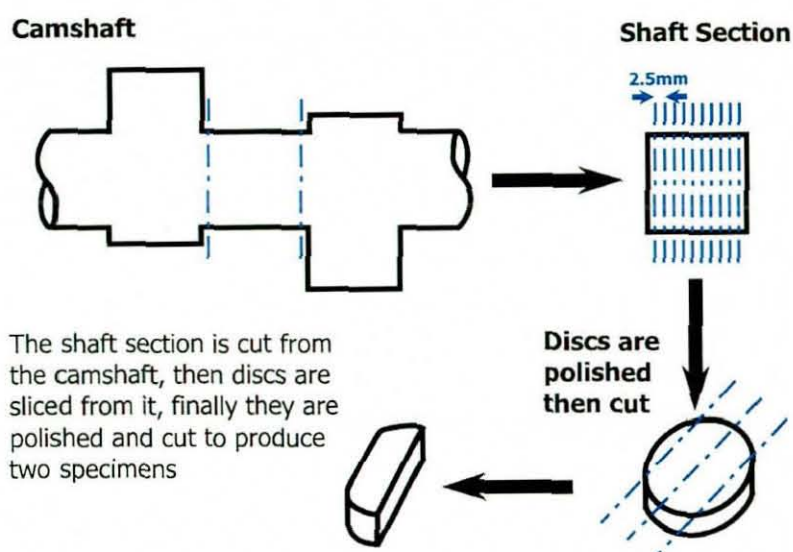**Figure 9.3** Bruker AXS high temperature X-ray diffractometer.

Figure 9.4. Internal view of vacuum chamber.

The thickness of the discs were then measured in several places to ensure they had a thickness less than 2mm which was uniform across the disc. Only discs with a thickness within ±0.025mm were used for experimental purposes. The discs were then cut in half and had their edges trimmed to produce two specimens. A schematic diagram of the specimen preparation is shown in figure 9.5. Specimens of alloys 1 and 2 (compositions listed in table 7.1) were prepared in this way.

Figure 9.5. Schematic diagram of specimen cutting and preparation.

Camshaft

Shaft Section

2.5mm

The shaft section is cut from the camshaft, then discs are sliced from it, finally they are polished and cut to produce two specimens

Discs are polished then cut

The aim of the experiments was to perform austenitisation heat treatments on the ductile iron specimens and monitor the change in austenite lattice parameter as a function of time at austenitisation temperatures of 900, 950 and 1000°C. The tests were performed under vacuum conditions in order to prevent oxidation of the specimens. The specimen was initially heated to 900°C and then intensity data were collected between the angular range of 48-52° which corresponded with the austenite (200) peak. This peak was selected because it is the most intense austenite diffraction peak that is not in the vicinity of any of the ferrite peaks in the system. The angular step size was 0.02° and the dwell time at each step was 1 second. The scan was then repeated a further nineteen times. Total data collection time was just over two hours. However, during the test no austenite peak was detected as would have

been expected. Indeed observation of the sample and the heating band through the furnace window during the test revealed that the heating band glowed bright orange during the experiment whilst the sample remained dark in colour. Hence, the sample had clearly not reached the temperature of the heating band. Although the specimen had been polished 'flat' it seemed most probable that there was not enough physical contact between the heating band and the specimen to raise its temperature to that which was required during the test.

In order to test this hypothesis pure iron powder was placed on the heating element and the test was repeated. It was hoped that the fine particles of iron powder would transform to austenite during heating, since due to their small size they would certainly be in contact with the heating element. Testing the powder would also eliminate the possibility of the ductile iron specimen buckling on heating, hence not being in contact with the heating band. However, no austenite peak was detected during this test. Examination of the powder on its removal from the vacuum chamber revealed that the powder had been oxidised. Although the test had been performed under vacuum conditions, oxidation of the iron particles still took place, possibly because of their very large surface area.

To overcome the oxidation problem the test was repeated in a helium environment. The chamber was evacuated and then flooded with He gas. This was repeated three times to eliminate as much oxygen from the system as possible. The test was then repeated on the iron powder. As the temperature of the band increased to 900°C, the powder glowed with a similar orange to that of the heating band. The (200) austenite peak was also detected as the sample transformed to austenite. After a few minutes of collecting data, the chamber was evacuated and immediately the iron powder ceased to glow orange and appeared black in colour as in the previous test, even though the platinum heating band still glowed orange. This confirmed the hypothesis that under vacuum conditions, insufficient amounts of heat were being transferred to the specimen, hence the specimen was not reaching the desired temperature.

The role of the He as the inert gas was also crucial. Firstly, it prevented oxidation of the iron powder and secondly, it has a much higher thermal conductivity than other suitable gases as shown in table 9.1. As can be seen from the table, the thermal conductivity of He gas is the same order of magnitude as water, and is one order of magnitude greater than O_2, CO_2, Ar and N_2 gases. A schematic diagram

showing the difference He gas had on the specimen heating can be seen in figure 9.6.

Table 9.1. Thermal conductivities of some substances at 300K [146].

Substance	He	O_2	CO_2	Ar	N_2	H_2O	Fe
k ($Wm^{-1}K^{-1}$)	0.150	0.0267	0.0166	0.0177	0.0260	0.614	80.0

Figure 9.6. Schematic diagram showing the influence of He gas on the specimen temperature.
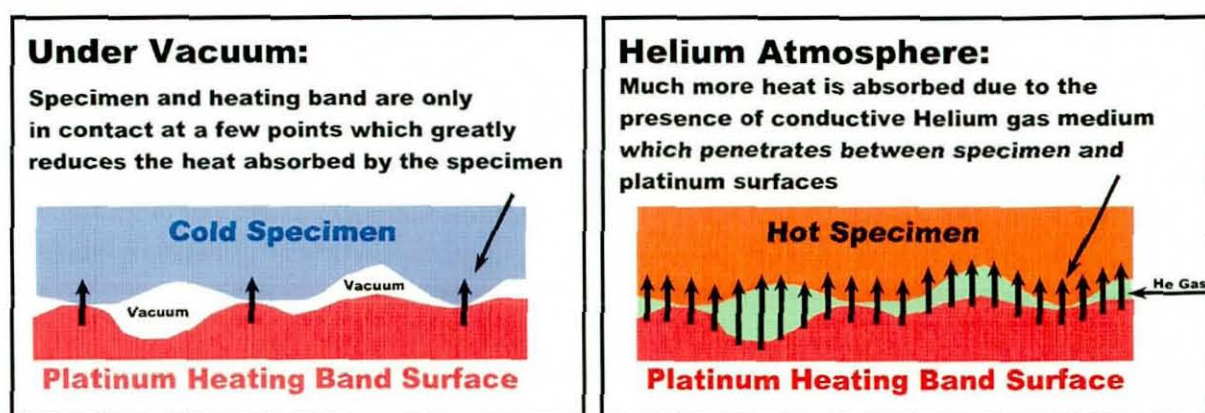
To verify whether the temperature of the specimen had reached that of the heating band, a test was performed with pure iron. When pure iron is heated and reaches a temperature of 910°C it undergoes a phase transformation from body centred cubic (bcc) to a face centred cubic (fcc) crystal structure. This information can be used as a useful temperature calibration tool. The thermal expansion of pure iron can also be used for calibration purposes since it is well documented as a function of temperature. A high purity iron (minimum 99.9985% Fe) specimen plate 20 mm × 10 mm × 1 mm was heated in a He environment as in the previous experiment and then held at a set temperature for 5 minutes. The diffractometer then collected data from the ferrite (200) peak and the austenite (200) peaks. The temperature was subsequently raised at a rate of 10°Cs⁻¹ and the test was repeated. The results of the experiment are tabulated in table 9.2.

Table 9.2. Pure iron specimen results.

Temperature (°C)	Ferrite (200) Peak Detected?	Austenite (200) Peak Detected?
200	Yes	
300	Yes	
400	Yes	
500	Yes	
600	Yes	
800	Yes	
890	Yes	No
900	Yes	No
910	Yes	No
920	Yes	No
930	Yes	No
940	Yes	No
950	Yes	No
1000	No	Yes
1050	No	Yes

As can be seen from table 9.2, the first austenite peak in the pure iron specimen was detected when the heating band had reached a temperature of 1000°C. The test was repeated, this time using 10°C temperature steps between the 950-1000°C range. Austenite was detected then at 970°C, suggesting that the temperature of the sample was 50-60°C below that of the heating band. Hence even when using conductive He gas to increase the amount of heat absorbed by the specimen, the specimen was still not reaching the desired temperature.

A range of experimental modifications were initiated to overcome this problem. Firstly, copper paste was used as an intermediary, to try and improve the conduction of heat between the sample and heating element. Although the paste claimed to be suitable for use at temperatures of up to 1100°C, it tended to dry out and crumble during experiments and provide to be ineffective. The sample was also mechanically clamped onto the heating element. Again however, this proved to be ineffective.

Finally, it was decided the only remaining solution was to replace the heating

element with the sample itself. A mild steel sheet with a thickness of 1 mm, was used to see if the platinum heating band could be replaced by one of a different material. A strip with the same dimensions (10 x 1 x 101 mm) as the heating element was cut from the steel sheet. A Pt - Pt 10 wt.% Rh thermocouple was spot welded onto the sample and connected to the temperature control unit of the X-ray diffractometer, and the sample was fixed in position. The sample was heated to 1000°C and the austenite (200) peak was detected in the sample, showing that the heating band could be replaced by one of a Fe based alloy and still reach the temperatures of interest for the current work.

Replacing the platinum heating band with the specimen had several advantages and disadvantages. The advantages were that the specimen temperature could be accurately measured and controlled because the thermocouple was welded directly onto the sample. Importantly, using this method it was also possible to run the experiments under vacuum conditions, hence oxidation of the sample was controllable. However, the samples were very difficult to machine from the raw material, which was in the form of camshafts, and connecting the thermocouples to the temperature control unit was an extremely difficult and delicate operation.

Experiments continued on the steel strip sample to measure the maximum rate at which a sample could be cooled. The temperature and heating (or cooling) rate of the sample is controlled by the balance of heat input into the sample via resistance heating to that removed from the sample via conductive cooling. Water is continuously circulated through the clamps which hold each end of the sample in place to perform the cooling operation. The clamps are shown in figure 9.4. Unfortunately, the current that heats the sample cannot just be turned off by the temperature control unit, allowing the sample to cool as fast as possible to the temperature of interest. A specific cooling rate has to be programmed into the temperature control unit of the X-ray diffractometer, and a small current always has to be passing through (heating) the sample. If the cooling rate input into temperature control unit cannot be maintained in the sample, the control unit crashes and the experiment ends. These experiments determined that in the mild steel strip sample, a cooling rate of 2.5°Cs^{-1} could be maintained from 1000°C until 300°C with the temperature control system remaining stable and within its operating limits.

A room temperature X-ray diffraction scan was also performed on each of the

alloys listed in table 7.1, in their as cast condition. Specimens for the experiments were cut from the castings and polished using progressively finer silicon carbide papers to 1200 grit, before being given a final polish on a 6 μm diamond impregnated polishing cloth. Since these alloys were all produced by casting the molten iron into sand moulds, the possibility existed that some texture (preferred crystal orientation) developed in the samples during the solidification process. The results of the high temperature X-ray diffraction experiments could be misleading if any of the alloys had preferred crystallographic orientation [69]. Therefore, these experiments were performed to investigate this possibility. Figure 9.7 shows the results of the room temperature X-ray experiment on alloy 6, which is typical of the results obtained for the other 5 alloys. The magnitude of the ferrite diffraction peaks is in agreement with those stated in the powder diffraction file where the ferrite (110) peak has the highest intensity and the ferrite (200) and (211) peaks have intensities of 20% and 30% respectively of the ferrite (110) peak [70]. Hence, no texture was detected in any of the castings.

Figure 9.7. Room temperature X-ray diffraction pattern of alloy 6.
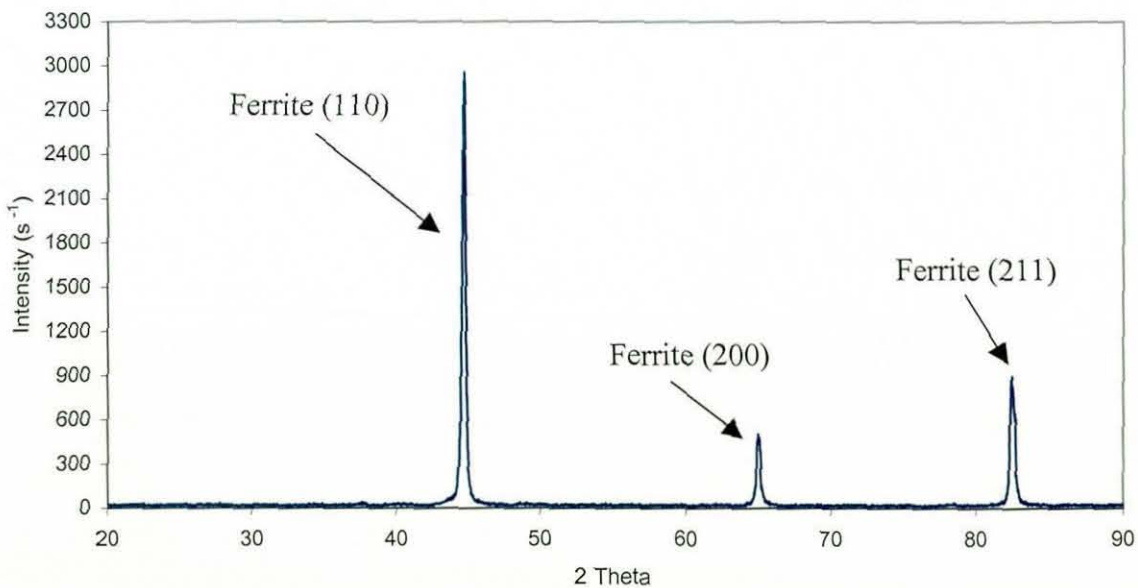
9.5 Summary

This chapter has demonstrated the principles behind the X-ray diffraction technique. High temperature X-ray diffraction was also introduced, and some of the

preliminary work which was performed before accurate work was possible on actual ductile iron samples has been highlighted. Attention was drawn to some problems which had to be solved before accurate scientific experiments could be carried out, including accurate measurement and control of the sample temperature. It was also shown that no texture was present in the as cast samples, which were to be used in subsequent high temperature X-ray diffraction experiments. This process has allowed the possibility of undertaking high temperature X-ray diffraction measurements on ductile iron samples, which are discussed in the following chapter.

10 High Temperature X-ray Diffraction Measurements

10.1 Introduction

This chapter presents and discusses the results of high temperature X-ray diffraction work on ductile iron alloy samples. Issues concerning the use of Cu as the X-ray source on Fe samples are highlighted in the first section. Some calculations which were performed to determine the magnitude of the X-ray beam that was in contact with the sample are then presented. Next, it is demonstrated how the volume fraction of austenite and ferrite in austempered ductile iron samples can be calculated from peak intensity data taken at elevated temperatures. The results of the high temperature experiments performed in this work are then presented, and subsequently compared to corresponding room temperature X-ray measurements in the final section of this chapter.

10.2 The Interaction of X-rays from a Cu Source with Fe

When an X-ray beam is incident upon a material, three interactions can occur between the incident beam and the material. Firstly, some of the incident beam will pass into, and be absorbed by, the material. Secondly, some of the incident beam can be scattered, and finally, fluorescence radiation may also be produced by the material [69;129]. The scattering of X-rays by the material and in particular the discovery that scattering of X-rays at particular angles is reinforced according to Bragg's Law led to the development of the X-ray diffraction technique [1;69]. X-ray fluorescence is also important for this work. If the incident beam of X-rays has an energy more than the critical excitation energy for electrons in a given atomic shell, it can knock electrons out of their shells. The ejected electrons are known as photoelectrons and the emitted characteristic radiation is known as fluorescent radiation. X-ray fluorescence results in a large proportion of the energy of the incident beam having its energy converted into fluorescent radiation [69;129]. Therefore the amount of incident beam which is diffracted is reduced, leading to lower intensity measurements in X-ray diffraction experiments [69].

One atom which interacts with Cu radiation producing large quantities of fluorescent radiation is Fe. This leads to a reduction in X-ray diffraction intensity data

of around 80% compared to a Cr X-ray source [69]. At room temperature this is not normally a problem, since longer dwell times can be used during X-ray diffraction experiments to increase the intensity of the results. However, at high temperatures when kinetic measurements (as in this work) are the aim of the experiments, fast collection of data is of major importance, so dwell time cannot be increased. An increase in temperature also results in an increase in the level of thermal vibration of the atoms in crystal. Correspondingly, there is a subsequent fall in the intensity of diffraction data acquired.

In the early stages of the high temperature X-ray diffraction experiments in this work, the intensity of data obtained in experiments proved to be too low. Although diffraction peaks could be detected, it was decided that an increase in the intensity of the measurements would be beneficial. This increased intensity was obtained by using wider slit sizes at the X-ray source and detector. Typically in X-ray diffraction a 1 mm wide slit is placed at the X-ray source. At the detector, 2 slits are used. The first again has a 1 mm width and the final slit has a 0.2 mm width. Both the 1 mm wide slits in the source and detector were replaced by slits with a 2 mm width. It was thought that any detrimental effects the larger slit widths produced, such as broader peaks and greater noise, could be tolerated for the improvement in the intensity of data.

Figure 10.1 shows two room temperature diffraction patterns for a (110) ferrite peak in alloy 3, using the original and modified slit configurations. A dwell time of 1 second and a step size of 0.02° was used in both experiments. As can be seen in the figure, using the larger slit sizes substantially increases the intensity data. Importantly however, the maximum intensity of both diffraction peaks corresponds with the same diffraction angle. More noise, as would be expected, is observed in the pattern produced with the large slit configuration. The peak produced using the modified slit arrangement is also slightly wider. This comparison demonstrates that wider slits could be used without a great loss in experimental data quality, but was beneficial in terms of the intensity of the diffraction peaks. Therefore, the large slit configuration was used in all the high temperature X-ray diffraction experiments presented in this work.

Figure 10.1. Two room temperature diffraction patterns for a (110) ferrite peak using the original and modified slit configurations.
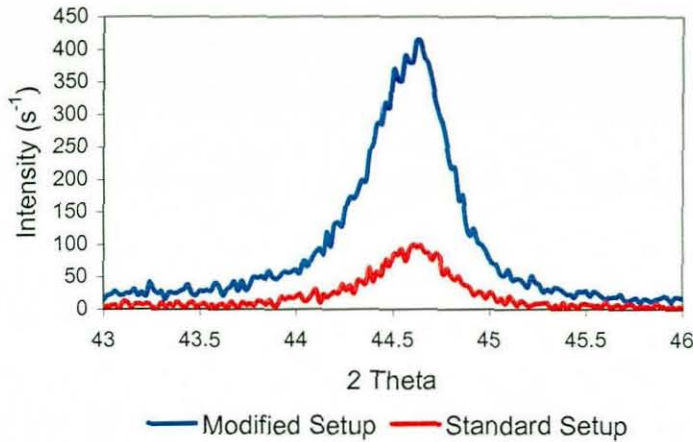

10.3 Calculation of the Sample Area Exposed to the Incident X-ray Beam

Due to the resistance method used to heat the samples during experiments, only a limited length of the sample was subjected to a uniform temperature during the experiments. The method used to measure this length is detailed in section 10.8.3. The results of the calculated spread of the incident beam for different incident angles are shown in table 10.1. Three measurements were required to perform the calculations. They were the slit width at the source (2 mm), the distance between the slit and the source (120 mm) and the distance from the source to the sample (300 mm). It was assumed the source of the X-rays was from a single point. Relatively simple trigonometrical calculations were then performed to calculate how much the incident X-ray beam spreads before it hits the sample. Figure 10.2 is a schematic diagram of a sample and incident X-ray beam, showing the meaning of lengths ab and bc listed in table 10.1. ac is the total length of the sample exposed to the incident X-ray beam. Comparing the results of these calculations with the measurement given in section 10.8.3 could then be used to demonstrate whether or not, at the angles of interest, the whole of the incident X-ray beam was irradiating a section of the sample with a uniform temperature.

Table 10.1. Calculations of the spread of the incident X-ray beam on the sample surface for different incident angles.

Incident Angle (θ^o)	ab (mm)	bc (mm)	ac (mm)
5	26.28	31.85	58.13
10	13.79	15.17	28.96
20	7.17	7.51	14.68
30	4.95	5.09	10.04
40	3.87	3.94	7.81
50	3.25	3.30	6.55
60	2.88	2.91	5.79
70	2.66	2.68	5.34
80	2.54	2.55	5.09
90	2.51	2.51	5.02

Figure 10.2. A schematic diagram showing the spread of the incident X-ray beam, were ac is the total length of samples exposed to incident radiation.
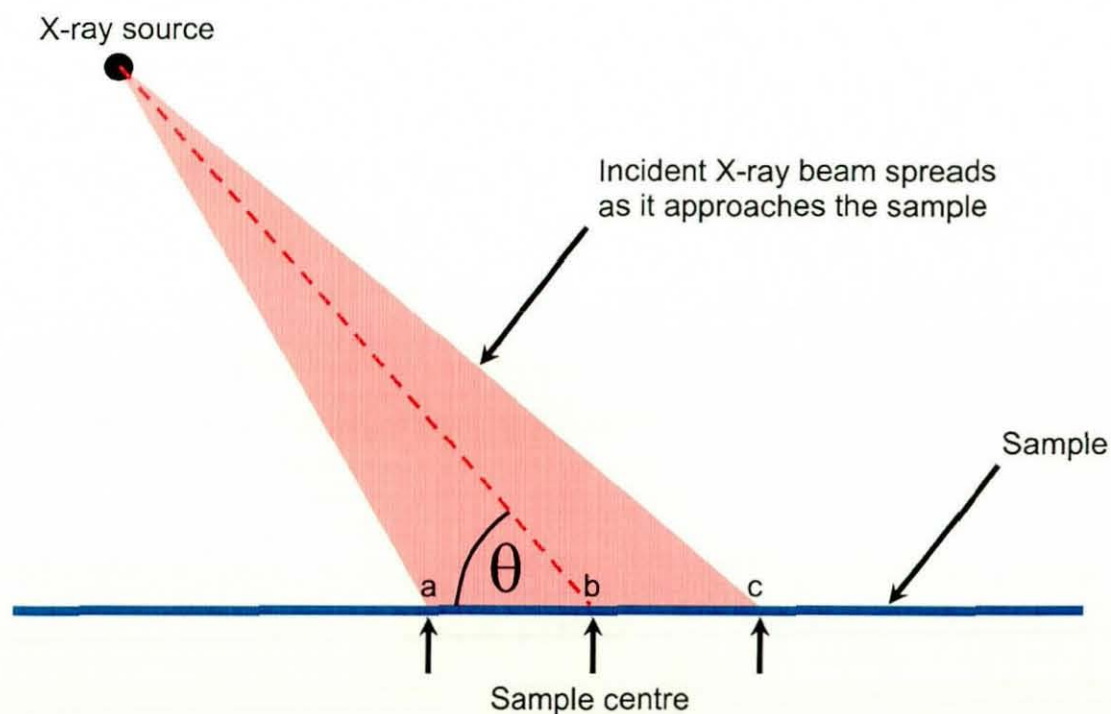
10.4 Calculation of the Volume Fractions of Austenite and Ferrite from Peak Intensity Data

The direct comparison method was used to estimate the volume fractions of austenite and ferrite in some austempered ductile iron samples [69]. The method utilises X-ray intensity data from single or multiple pairs of austenite and ferrite peaks. The methodology is outlined in the following section. The volume fraction of austenite Vf_γ was calculated using the following relationship:

$$Vf_\gamma = \frac{I_\gamma / R_\gamma}{\left(I_\gamma / R_\gamma\right) + \left(I_\alpha / R_\alpha\right)} \quad [10.1]$$

where I_γ and I_α are the integrated intensities of the austenite and ferrite peaks respectively, and R, which is calculated separately for each austenite and ferrite peak, is given by:

$$R = \left(\frac{1}{V^2}\right)\left[|F|^2 P\left(\frac{1 + \cos^2 2\theta}{\sin^2 \theta \cos \theta}\right)\right]\left(e^{-2M}\right) \quad [10.2]$$

where V is the volume of a unit cell of austenite or ferrite ($Å^3$), F is the structure factor, P is the multiplicity factor, θ is the Bragg angle and e^{-2M} is the temperature factor. The structure factor is in turn a function of the scattering factor f, which as its name suggests, accounts for how the electrons in atoms scatter the incident X-rays. For body centred cubic (bcc) crystals [69],

$$F = 2f \quad when \ h+k+l \ is \ even \quad [10.3]$$

$$F = 0 \quad when \ h+k+l \ is \ odd \quad [10.4]$$

For face centred cubic (fcc) crystals [69],

$$F = 4f \quad when \ h, \ k \ and \ l \ are \ unmixed \quad [10.5]$$

$$F = 0 \quad when \ h, \ k \ and \ l \ are \ mixed \quad [10.6]$$

Unmixed integers are either all odd or all even. The scattering factor has to be adjusted from its initial value *f* as calculated above because iron atoms are not independent of the wavelength of the scattered Cu radiation [69]. The correction factor Δf, has a value of approximately −1.25 for Cu X-rays incident on Fe atoms. The corrected scattering factor f_C, can then be calculated from equation 10.7 and substituted for the scattering factor *f* in equations 10.3 and 10.5 to calculate the structure factor.

$$f_C = f + \Delta f \qquad [10.7]$$

The multiplicity factor P accounts for the proportion of planes in a crystal contributing to same reflection, and is defined as the number of different planes in a form having the same spacing [69]. Parallel planes with different Miller indices are counted separately as individual planes. Values of P were obtained from tabulated data for both fcc and bcc crystals [69].

The temperature factor, e^{-2M} is of particular importance for this work since experiments were performed above ambient temperature. It describes as a function of temperature the influence thermal vibration has on the atoms. As the temperature of a crystal rises so does the amplitude of atomic vibrations about their mean positions in the lattice [69]. The increased atomic vibration has three dominant effects. Firstly, expansion of the unit cell occurs causing a shift in d-spacings, resulting in the diffraction lines moving to smaller angles. This effect can be used to measure the thermal expansion of crystals. Secondly, the intensity of diffraction lines decreases, because the increased vibrations of the atoms in the crystal have the effect of smearing the lattice planes. Reinforcement of the scattered radiation according to Braggs law requires the path difference between waves scattered by adjacent planes to be a whole number of wavelengths [1]. Therefore it can be seen that the increase in the vibration of atoms in these planes with an increase in temperature is not conducive to obtaining diffraction of the incident X-rays. This also causes the intensity of background scattering to increase, which is the third effect. The parameter M is calculated as follows:

$$M = \frac{1.15 \times 10^4 T}{A\Theta^2}\left[\phi(c)+\frac{x}{4}\right]\left(\frac{\sin\theta}{\lambda}\right)^2 \qquad [10.8]$$

where T is the absolute temperature, A is the atomic mass of Fe, Θ is the Debye characteristic temperature of Fe (430K), c is equal to Θ/T, λ is the wavelength of the X-rays (1.54 Å in this case) and θ is the diffraction angle. $\phi(c)$ values are obtained from tabulated data [69].

Once R has been calculated for both the austenite and ferrite peaks it was used in equation 10.1 to produce an estimate of the volume fraction of austenite, Vf_γ. The volume fraction of bainitic ferrite Vf_α, in ADI alloys was then simply given by equation 10.9:

$$Vf_\alpha = 1 - Vf_\gamma \qquad [10.9]$$

10.5 Production of High Temperature X-ray Diffraction Samples

Section 9.4 mentioned the difficulties encountered in machining samples for high temperature X-ray work from the raw material, which was in the form of camshafts. In fact only two samples could be produced from the Alloy 1 camshaft, the composition of which is listed in table 7.1. Therefore additional raw material was cast in the foundry in the Manufacturing Engineering Department at Loughborough University, to enable the production of more samples. This process has been discussed previously in section 7.4.1.

Blocks with dimensions of 105 x 100 x 10 mm were machined from the casting. Plates 1 mm thick, 105 mm long and 10 mm wide were then cut from the blocks using a spark erosion machine, to produce specimens suitable for high temperature X-ray diffraction work. Eight samples were cut from alloys 3, 4 and 5 and four for alloy 6 in addition to the two samples machined from the camshafts of alloy 1. The samples were polished on each side using 1200 grit silicon carbide paper, before being given a final polish on a 6 μm diamond impregnated cloth, before use in experiments to remove any oxide film that had built up.

10.6 Measuring Phase Boundaries Using High Temperature X-ray Diffraction

The first set of high temperature experiments were performed on Alloys 3, 4 and 6. These alloys, unlike alloy 5 contained higher concentrations of Si than would be used for ADI production. Therefore in these samples, only measurements of the phases boundaries were attempted. These specimens were also used to further tailor cooling rate configurations (see section 9.4), therefore reducing the need to perform such work on the valuable alloy 1 and 5 samples, which were to be used for phase transformation studies in ADI alloys.

10.6.1 Experiments on alloy 3

Alloy 3, the composition of which is shown in table 7.1, was the first sample to be tested. Some difficulties were encountered in the use of these specimens, so no useful experimental data was obtained, since the samples contained a fault running along their lengths causing many to break during polishing or during the experiments. Another sample slipped from the sample clamps during testing as it was heated, resulting in it sagging at higher temperature. This sample (3a) can be seen in figure 10.3 along with two other samples 3b and 3c. It should be noted that sample 3a was used as a sacrificial sample (after it buckled) to help establish the maximum rate at which the specimens could be cooled. Hence it was subjected to repeated heating and cooling cycles. During these trials, precious time on the X-ray diffractometer was not wasted waiting for the vacuum to reach adequate levels to limit oxidation. Hence it can be seen alloy 3a has a substantial oxide film, which is not observed on the other two samples. Some results were obtained for alloy 3b, but the temperature measurement was not thought to be reliable since after the experiment had ended the thermocouple did not appear to be firmly attached to be sample.

A room temperature scan of sample 3b after it was heated is shown in figure 10.4. As can be seen in the figure, quite a complex diffraction profile is displayed due in part to the oxides present on the sample, which can be seen visually in figure 10.3. Note in figure 10.4 that the maximum intensity of some of the larger peaks is not

shown, so that the smaller intensity peaks can be highlighted in the profile. The diffraction peaks which could be identified in the figure show that ferrite and magnesium silicate $Mg(SiO_3)$ were identified in the sample. Some of the smaller peaks could not be identified. Typically, the accurate identification of a substance in the sample requires the diffraction peaks in the experiment to be matched with the three highest intensity diffractions obtained from reference samples. These are listed in the Power Diffraction Index [70]. However, peaks sometimes overlap, making it difficult to identify all the substances when a number exist in a sample, as is the case in figure 10.4.

**Figure 10.3.** Experimental samples 3a, 3b and 3c.
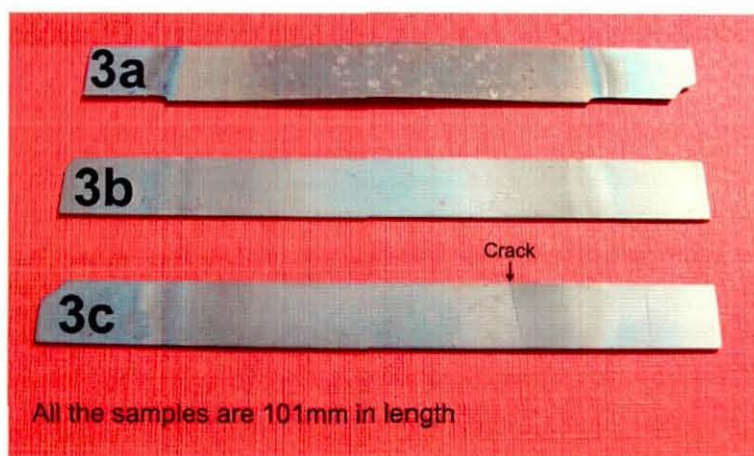
The presence of oxides on the samples shows that some oxidation of the samples had occurred. The experiments were typically started when the vacuum was equal to 3.0×10^{-3} mbar. In order to achieve this pressure, both the turbo and rotary vacuum pumps were operated for approximately 1 hour. Leaving the pumps working for several hours more did not result in a significant fall in vacuum pressure. The pressure was however observed to rise as the temperature of the sample increased as the start of the experiments. A large increase in vacuum pressure occurred at approximately 110°C, so a preheat for 5 minutes at 120°C was used on all subsequent samples before heating to experimental temperatures in order to try and limit the effect of oxidation.

It is interesting to note the intensity of the oxide diffraction peaks in figure 10.4 relative to those of ferrite. The maximum diffraction intensity of the magnesium

silicate was twice that of the largest ferrite peak, even though only a slight oxide film was present on the sample. The low intensity of the ferrite diffraction data has been explained previously in section 10.2.

**Figure 10.4.** A room temperature X-ray diffraction profile of alloy 3b after it was heated.
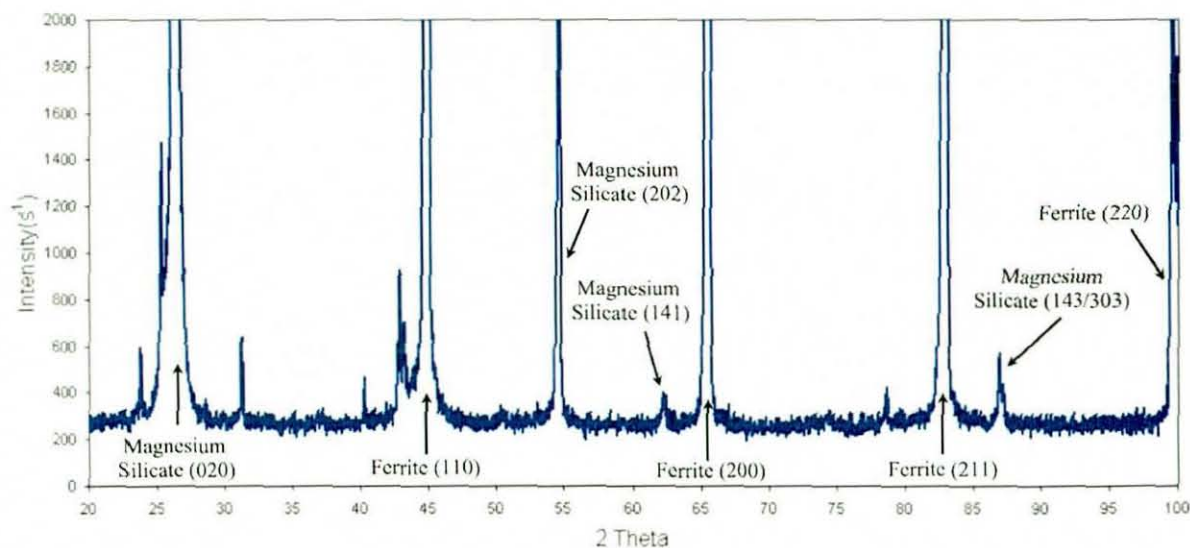
10.6.2 Experiments on alloy 4

Figure 10.5 shows some of the alloy 4 samples after they were tested. The composition of the alloy 4 samples is listed in table 7.1. The 120°C preheat seems to have had little influence on the level of oxide present on the samples. It was thought that the thermocouple fell off alloy 4b during the experiment, resulting in the sample melting. As in section 10.6.1, the experiments performed on this set of samples were aimed at observing the phase changes that occurred upon heating and cooling in the alloys. Some useful experimental data were obtained and improvements were also made to the experimental technique during these experiments.

The first experiment was performed on sample 4a. It was heated to a temperature of 740°C at a rate of 10°Cs^{-1} and held isothermally for 10 minutes. Scans were then performed between 49-50.5° and 80.8-82.3° to try and measure the intensity of the austenite (200) and ferrite (211) peaks respectively. A dwell time of 2

seconds and a step size of 0.02° were used during the experiment. The temperature was then raised by 20°C intervals, the sample was held for 2 minutes and the scans were repeated. The final measurement was taken at 1060°C. Some of the austenite and ferrite scans are shown in figures 10.6 and 10.7. These results suggest that austenite phase forms in the sample between 760°C and 780°C, whilst the ferrite phase is removed from the sample at temperatures above 900°C. As would be expected the intensity of the austenite peaks increases with temperature as greater quantities of austenite are present in the sample as the temperature rises. The opposite is the case for ferrite. Another peak is also observed in figure 10.6 at a slightly lower angle than the austenite (200) peak, which is probably attributed to an oxide.

Figure 10.5. Experimental samples 4a, 4b, 4c and 4d.
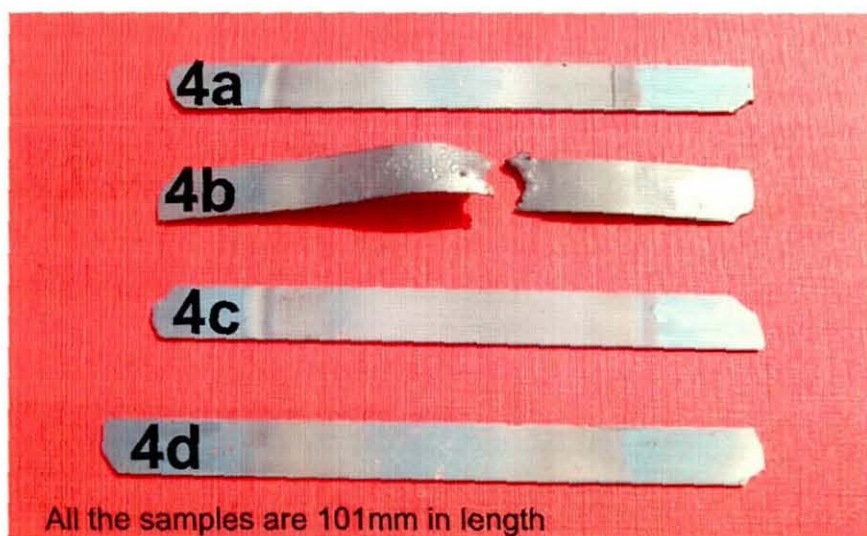
These experiments were repeated to ensure reproducibility, which was confirmed. For specimen 4e, a similar experiment was performed starting at a temperature of 720°C, but the holding time was increased from 2 minutes to 30 minutes to allow more time for equilibrium to be reached in the samples. The temperature steps were also reduced in size from 20°C to 5°C and the experiments were performed up to a maximum temperature of 900°C. After the scan at 900°C was completed, the temperature of the sample was reduced by 5°C, held for 30 minutes and the scan was repeated. The temperature was again incrementally reduced until the final measurements were taken at 720°C.

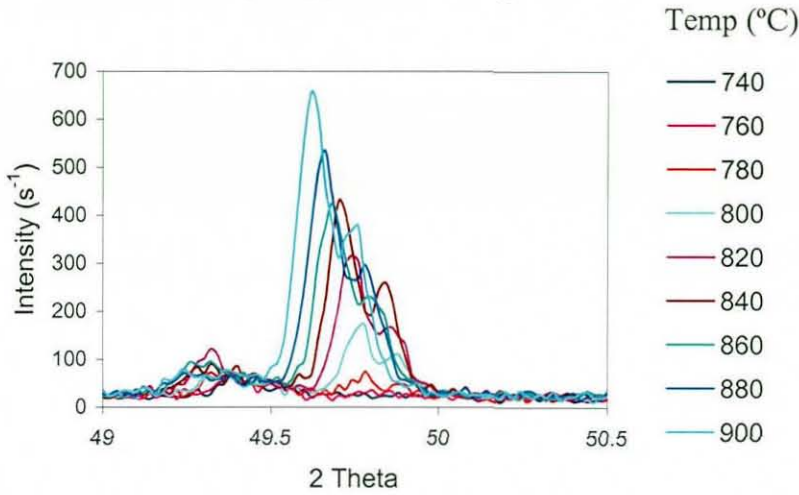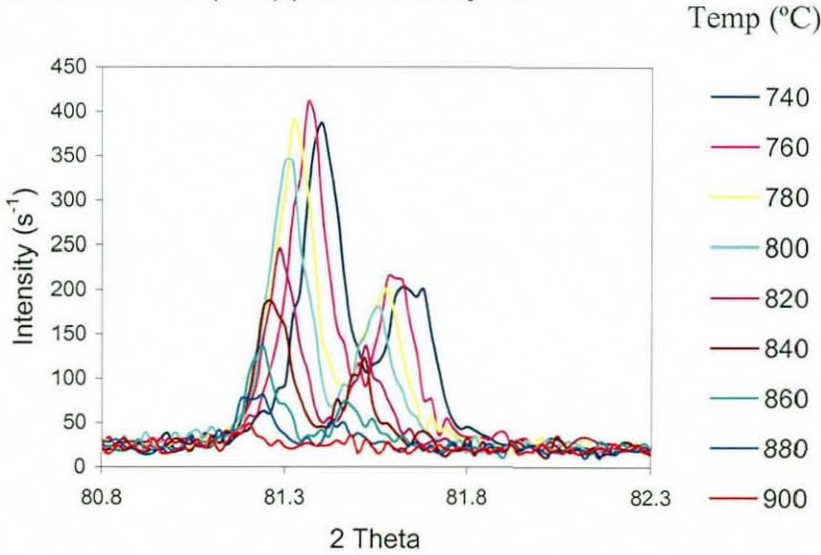**Figure 10.6.** Scans of austenite (200) peaks in alloy 4a.

Figure 10.7. Scans of ferrite (211) peaks in alloy 4a.

As can be seen in figure 10.8, some interesting results were obtained. Firstly, the small peak thought to be from an oxide, is again observed at a slightly lower angle than the austenite (200) peak. This peak is easily confused with the austenite peak as it occurs around the same diffraction angle, especially when austenite just starts to form in the sample. Importantly, austenite is first observed in the sample at a temperature of 805°C. In the previous experiments austenite was observed to be present in the sample between 760°C and 780°C. The difference in these results could be explained by the thickening of an oxide film. The longer delay times for which this sample was exposed at elevated temperatures would have favoured the

formation of a thicker oxide layer. This thicker oxide layer could mask the presence of low quantities of austenite in the sample.

**Figure 10.8.** Scans of austenite (200) peaks in alloy 4e.
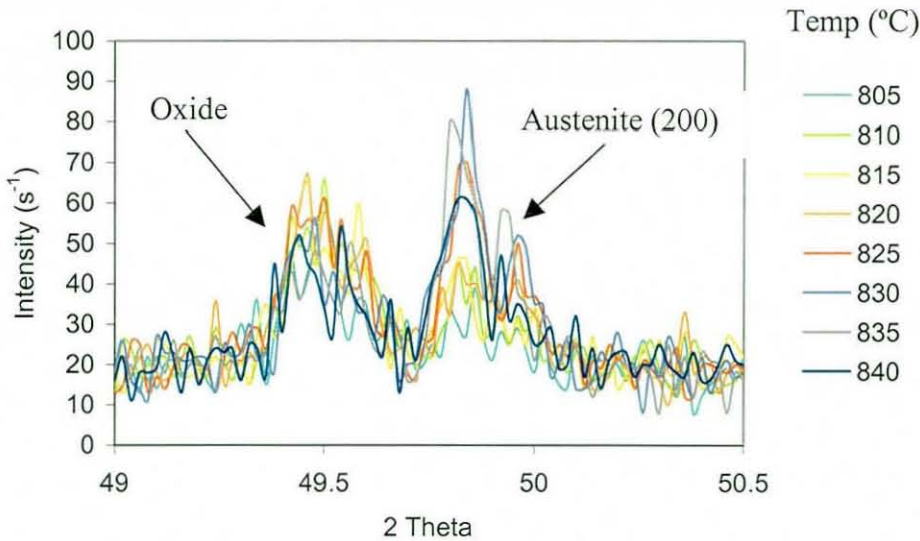
Good reproducibility was obtained between the heating and cooling results regarding the measurement of lattice parameters. The intensity measurements were not in as good agreement from corresponding heating and cooling temperatures, as shown in figure 10.9. On heating sample 4e, the intensity of the diffraction from the ferrite planes is seen to decrease. This is expected, since the volume fraction of the ferrite phase is also decreasing with increasing temperature, therefore a smaller number of ferrite crystals exist in the sample to contribute to diffraction. On cooling, the intensity is observed to increase as expected. However, the overall intensity of diffraction from the ferrite planes on cooling tends to be lower than that observed on heating. Once more, this observation could be explained by the formation of an oxide film, which thickens with experimental time. At a temperature below 750°C the intensity results on cooling become similar to those on heating. It is known in steels, that different oxide films can form at different temperatures [147-149]. The formation of a new type of oxide film below 750°C could explain this observation. Hence from the experimental observations on sample 4e, it can be seen that oxidation of the samples may have an important influence on the results obtained from the experiments.

Figure 10.9. Intensity of ferrite (211) diffractions as a function of temperature in sample 4e.
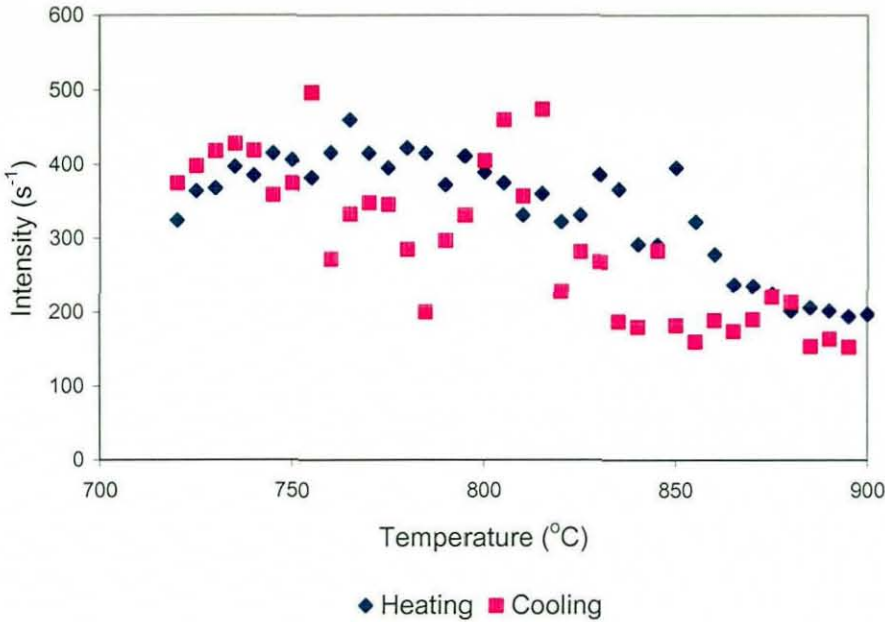

In order to try and combat the influence of oxidation, the angular range used in the experiments was changed to a single scan from 41.9-45.4°, for the experiments on sample 4f. This angular range incorporated the austenite (111) and ferrite (110) peaks. These peaks were selected because they produced the highest diffraction intensities in the respective phases, and therefore the intensity of both the austenite and ferrite peaks should increase as a result of this change. However, there was a possibility that the peaks could overlap, producing results that were much more difficult to interpret. The holding time before taking measurements was also reduced to 5 minutes for this sample to help minimise oxidation. In addition to the 120°C preheat performed on the samples, a second preheat was performed at 500°C for 10 seconds, again in an effort to reduce the levels of oxidation on the samples. A dwell time of 2 seconds and a step size of 0.02° was used during the experiment.

Figure 10.10 shows some of the results for specimen 4f. The increase in the intensity of the austenite peaks can immediately be seen. As previously mentioned, ferrite was not present in sample 4a above a temperature of 900°C (see figure 10.7). These observations were also recorded in repeat experiments, but in figure 10.10, small ferrite peaks are observed in the sample up to a temperature of 930°C, contradicting the previous observations. Once more, this discrepancy can be

explained by the presence of an oxide film. In sample 4a, the oxide film could have prevented the detection of small quantities of ferrite in the sample at these high temperatures. The ferrite (110) planes which were observed in specimen 4f, produce a much higher intensity ferrite peak than the (211) planes which were observed in previous experiments. Hence ferrite was detected at higher temperatures in sample 4f.

Figure 10.10. Scans of austenite (111) and Ferrite (110) peaks in alloy 4e.
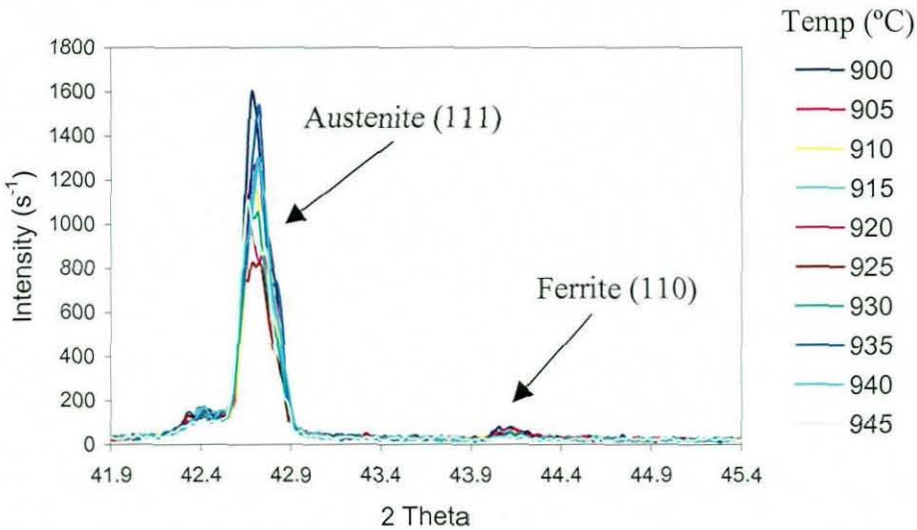
These observations do cast some doubt on the accuracy of the results. It has been stated that in mixed microstructures, X-ray diffraction can be used to readily detect constituent phases with a volume percent as low as 0.003% [150]. However, in these samples with the added complication of the presence of an oxide film that reduced the amount of incident X-rays that contact the sample bulk, it has to be assumed that the smallest detectable volume fraction was larger than 0.003%.

Figure 10.10 also shows that no overlap of the austenite (111) and ferrite (110) peaks occurred in the experiment, even at lower temperatures for which results are not shown. Therefore, the new angular range was used in all future experiments. Figure 10.11 shows that good reproducibility was obtained in the lattice parameter measurements on samples 4e and 4f. The small discrepancy between the two measurements is probably due to a slight height difference between the two samples.

Figure 10.11. A comparison of the ferrite lattice parameters measured in sample 4e and 4f.
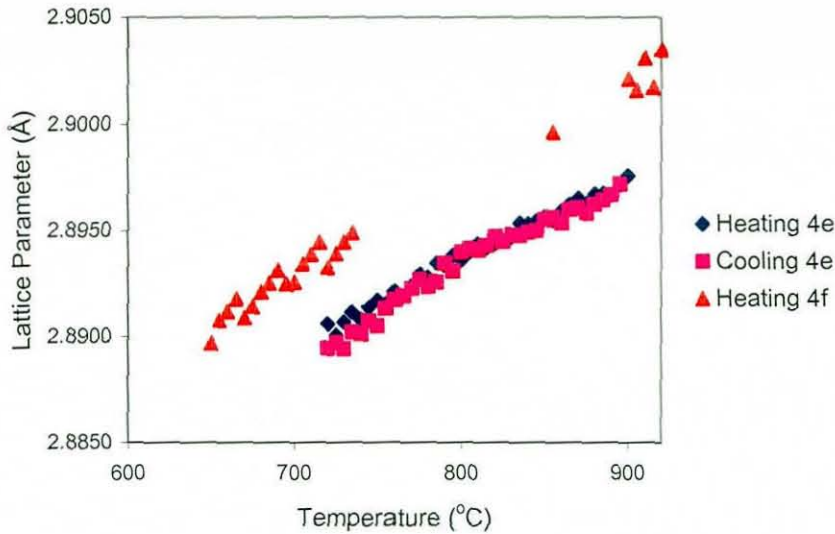

Figure 10.12 shows a room temperature scan on sample 4e, which was performed after the heating and cooling experiments. As can be seen in the diffraction pattern, several oxide peaks are visible. Iron manganese oxide $((FeO)_{0.198}$ $(MnO)_{0.802})$ was identified in the sample. Some magnesium silicate was also identified in the sample, as found on alloy 3. As can be seen, some other peaks were observed, which could not be positively identified due to the great number of peaks present in the diffraction pattern. However, a possibility exists that some iron manganese silicate $(FeMn(SiO_4))$ was present in the sample, which seems plausible given the nature of the other two oxides which were identified. It is interesting to note that none of the oxides typically associated with steels such as wüstite (FeO), hematite (Fe_2O_3) or magnetite (Fe_3O_4) [147;149] were present in samples 3 and 4. This is a consequence of the high Si concentrations of these alloys. A class of high temperature resistant cast iron alloys known as Silals exists, which rely on the Si based oxide films that form on their surfaces for their corrosion resistance at high temperatures [2;151]. Alloys 3 and 4 have similar Si concentrations to Silals, therefore the formation of Si based oxides on the sample surfaces is not surprising.

Figure 10.12. A room temperature X-ray diffraction pattern for specimen 4e.
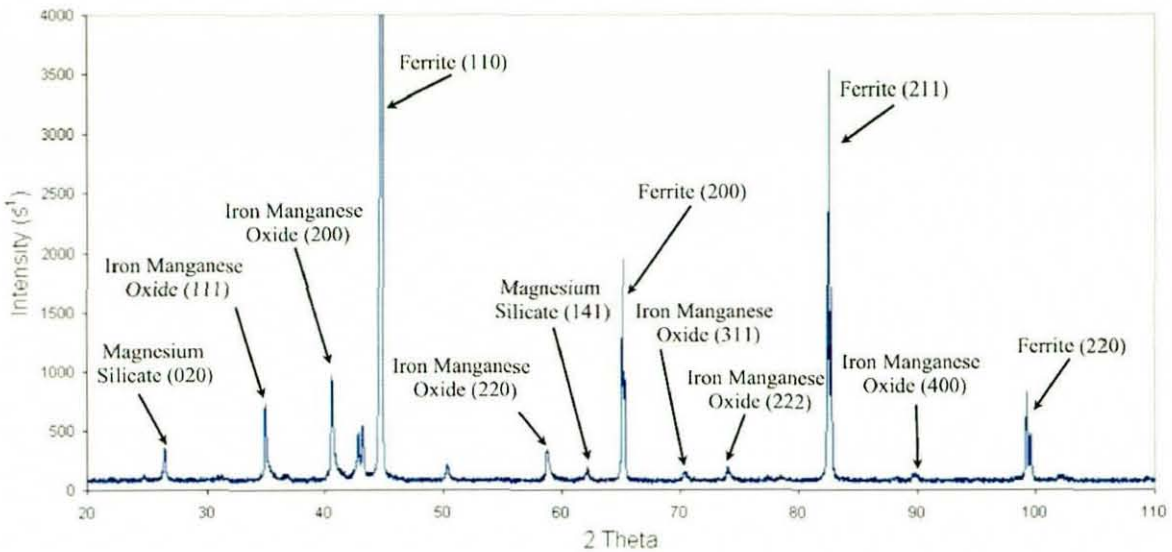
10.6.3 Experiments on alloy 6

The final phase boundary search experiments were performed on alloy 6. A similar experiment was performed to those on samples 4e and 4f. After the 120°C and 500°C preheats, the sample was heated to 650°C at a rate of 10°Cs⁻¹, held isothermally for 25 minutes, then a single scan from 41.9-45.4° was performed with a dwell time of 4 seconds and a step size of 0.02°, which incorporated the austenite (111) and ferrite (110) peaks. The dwell time was increased to 4 seconds so smaller quantities of phases present in the microstructure could be detected. The temperature then was raised by 5°C and the process was repeated. The final scan was performed at 950°C. The results are shown in figures 10.13 and 10.14. Figure 10.13 shows that austenite was first detected in the sample at 785°C, whilst figure 10.14 demonstrates that no ferrite was detected in sample 6a above 880°C. An oxide peak is again present in figure 10.13 to the left of the austenite (111) diffraction peak. The appearance of the oxide present on the sample differed from those observed on samples 3 and 4. As can be seen in figure 10.15, the oxide film has a white appearance. The composition of alloy 6 is listed in table 7.1, where it can be seen this alloy contains less Mg than alloys 3 and 4. Therefore, it was expected that some SiO_2 oxide was present in the sample. A room temperature X-ray diffraction pattern

of sample 6a confirmed that SiO_2 was present on the sample. As with the results from the previous two alloys, since an oxide film was present on the sample, some doubt remains in the accuracy of the experimental results, which were not therefore used for detailed experimental studies.

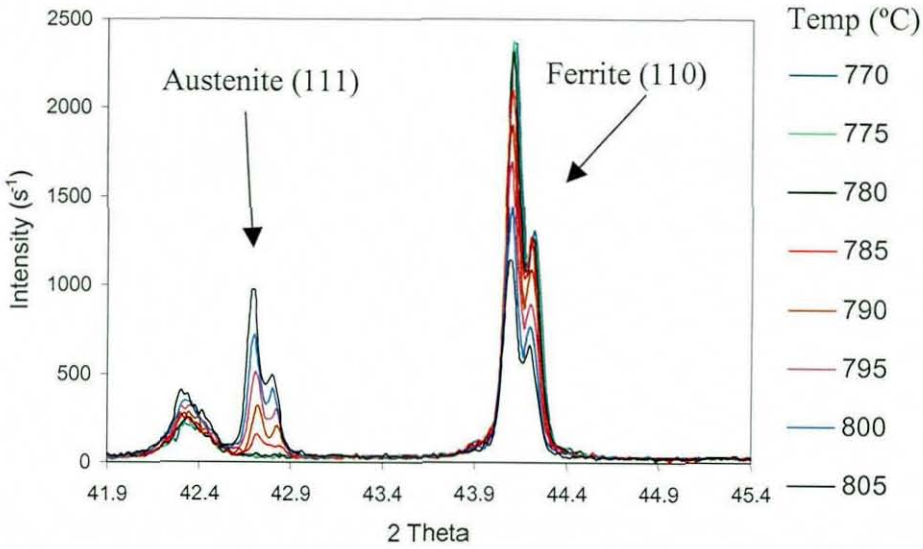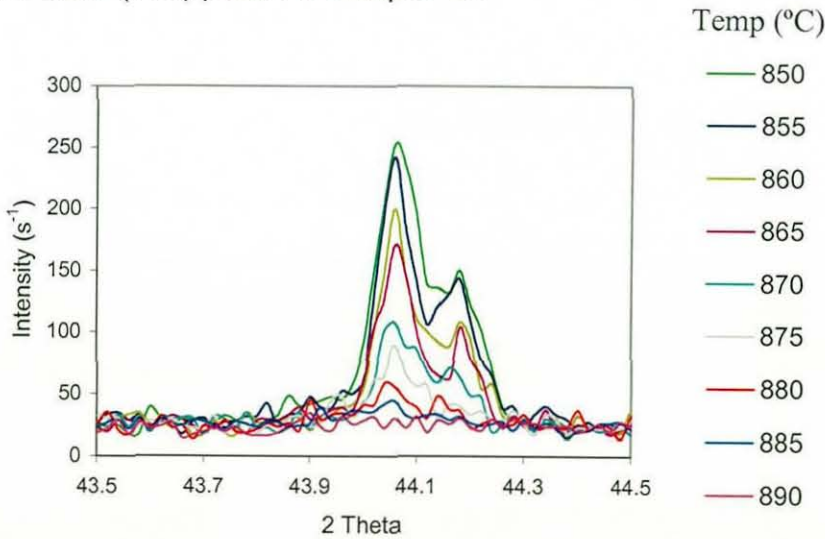**Figure 10.13.** Austenite (111) and ferrite (110) peaks in sample 6a.

Figure 10.14. Ferrite (110) peaks in sample 6a.

The experiments performed on alloys 3, 4 and 6 in section 10.6 have shown that the presence of oxide films can mask the presence of small volume fractions of phases present in the samples. However, oxide films present on the samples have

no influence on the measurement of the lattice parameter of the phases present in their microstructures, which is of importance for the experiments performed in section 10.7 and 10.8.

Figure 10.15. Oxide film on surface of sample 6a.

10.7 High Temperature X-ray Diffraction of Austempered Ductile Iron Alloys During Austenitisation

10.7.1 Introduction

Austenitisation experiments were performed on samples produced from alloys 1 and 5. This section presents the results of the high temperature experiments and shows how the austenite C content can be calculated from the X-ray diffraction data. These values are then compared to MTDATA predictions of the austenite C content. Samples were heated to the austenitisation temperature at a rate of $10^{\circ}Cs^{-1}$, where they were held isothermally. To reduce the time taken during these kinetic measurements, scans with a 2 second dwell time from $41.9-45.0^{\circ}$ were then performed which incorporated the austenite (111) and ferrite (110) peaks. The scans were repeated every 10 minutes for a total austenitisation time of over 1 hour. Since the measurements were taken only from a single peak some error will be present in these results, which is expected to bee no greater than $\pm 5\%$. The same can said for all X-ray experiments performed in this work.

10.7.2 Austenitisation of alloy 1

Only two samples were available from alloy 1, and therefore they had to be

reused after experiments to obtain enough experimental data. To limit the extent of any decarburisation or oxidation that may occur on the samples, they were left for a period of 16 hours in the vacuum chamber after the preheats had been performed in order to lower the vacuum pressure as much as possible before the experiments started. A very low pressure of 8.0×10^{-5} mbar was obtained by the prolonged evacuation process. This is a substantial improvement to the vacuum pressure obtained in previous experiments and was thought simply to be a result of two weeks of previous use of the vacuum system from working on the other samples. After one austenitisation experiment was completed, the sample was cooled to ambient at a rate of $0.5°Cs^{-1}$ and the next austenitisation experiment was started. A slow cooling rate was selected to avoid martensite formation in the samples on cooling.

Figure 10.16 shows how the austenite lattice parameter changed as a function of time for samples of alloy 1, which were austenitised at different temperatures. As can be seen in the figure, the austenite lattice parameter increases with temperature. This is expected since at higher austenitisation temperatures, more carbon is soluble in the austenite matrix [12;22;49], which causes the lattice parameter to increase. This is also combined with the thermal expansion of the austenite as the temperature rises.

In most experiments, the austenite lattice parameter was found to be almost constant with time during austenitisation. This suggests the carbon reaches its maximum solubility in austenite extremely quickly. However, it must be remembered that the time given in figure 10.16 is the time at which the scan commenced in the samples. This is the same for all the results in section 10.7. Each scan took a total of 310 seconds to complete, so approximately 60 seconds will have passed at the austenitisation temperature before the austenite (111) diffraction was measured. This could also explain why no ferrite was detected in any of the samples, since approximately 180 seconds at the austenitisation temperature passed before the ferrite (110) diffraction was determined. The samples are just 1 mm thick, so a uniform temperature was expected to be reached extremely quickly in the samples.

The experiments which were performed at 900°C show that the austenite lattice parameter increases slightly during the early stages of austenitisation before the saturation level is reached. Diffusion is slower at lower temperatures [1], so it could be possible in these samples that saturation of the austenite with C takes slightly longer in at 900°C. Good reproducibility was obtained during the experiments.

This is best demonstrated by the measurements taken at 950°C, which were taken from the same sample. Four separate experiments were performed at this temperature with very little difference in the experimental results. This observation suggests that little decarburisation of the samples took place due to the repeated austenitisation experiments. However, it is difficult to prove conclusively because if some decarburisation did take place in the samples it would also be difficult to detect because the C lost during the process could also be rapidly replaced at these high temperatures. There is also an almost infinite supply of C in the sample to replace any C lost during decarburisation because of the presence of the graphite nodules. Little oxidation was observed on the surface of the alloy 1 samples, even after the repeated heating cycles they were subjected to, which is probably a consequence of the very low vacuum pressure under which the experiments were performed.

Figure 10.16. Austenite lattice parameter as a function of time during the austenitisation of alloy 1.
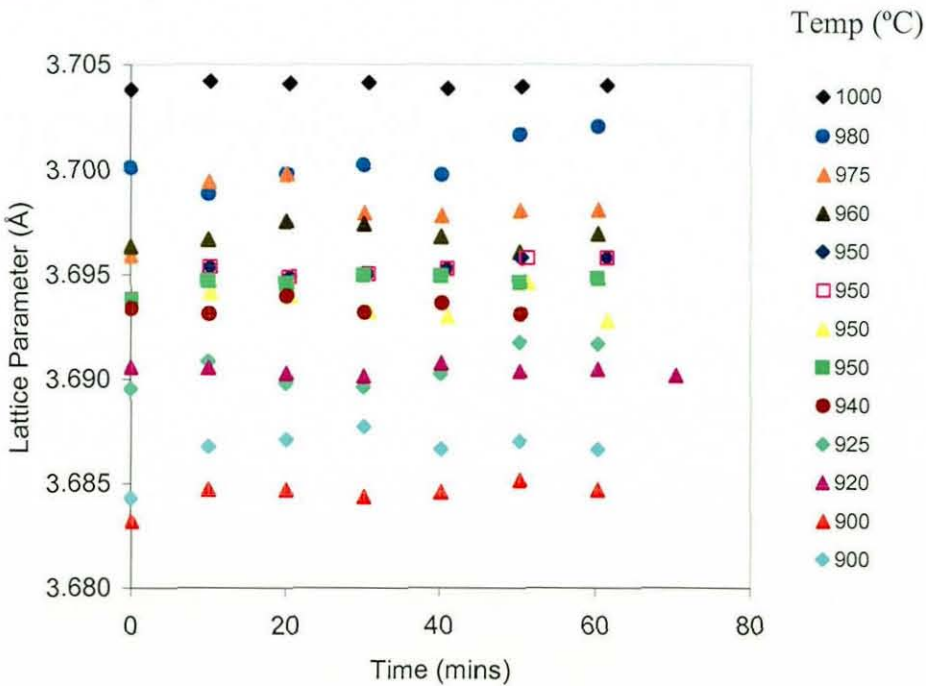
The linear thermal expansion coefficient of austenite, α_γ, is related to the austenite lattice parameter by the following relationship [152;153]:

$$a_\gamma = a_{0\gamma} \left[1 + \alpha_\gamma \times (T - 298) \right] \qquad [10.10]$$

where a_γ is the austenite lattice parameter at the absolute temperature T, and $a_{0\gamma}$ is the lattice parameter of austenite at 298K. Equation 10.10 was rearranged, making $a_{0\gamma}$ the subject of the formula. This expression was then used to calculate the room temperature lattice parameter of austenite from the high temperature X-ray diffraction measurement of the austenite lattice parameter. The actual experimental value of the austenite lattice parameter used in the calculations was the average of all the measurements at a given austenitisation temperature since they were approximately constant with time. Two different austenite thermal expansion coefficients were found in literature. One was from experiments on pressure vessel steels (Fe, 0.12-0.56C, 0.84Mn, 2.86-3.06Cr, 0.86-1.48Mo, 0.14Ni all wt.%) [152] and the other from investigations of a low carbon steel (Fe-0.18C-1.8Si-1.5Mn all wt.%) [153]. A third thermal expansion coefficient was calculated by the current author from experimental data taken from pure iron which is shown in figure 10.17. The relationship used to find the α_γ from this data was equation 10.11 [1]:

$$\alpha_{Exp} = \Delta a \div a_0 \Delta T \qquad [10.11]$$

where α_{Exp} is the linear coefficient of thermal expansion Δa is the change in lattice parameter over a temperature range ΔT and a_0 is the initial lattice parameter. In all cases, the expansion of austenite was assumed to be linear over the temperatures of interest. The different thermal expansion coefficients are shown in table 10.2.

Figure 10.17. Data used in the calculation of the austenite linear thermal expansion coefficient by the present author. [136]
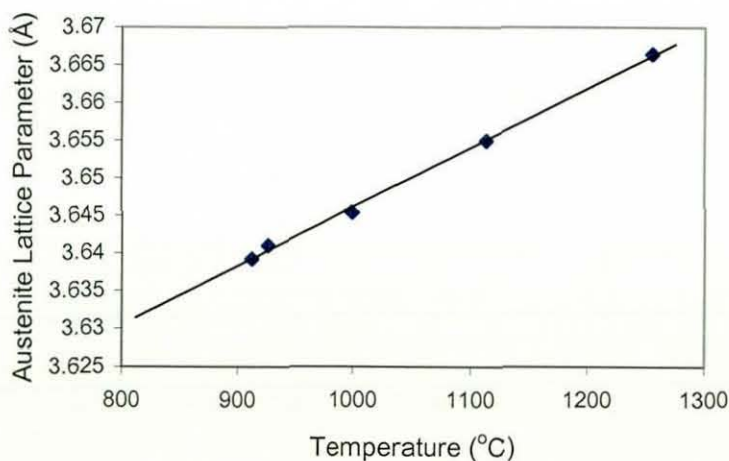
Table 10.2. The thermal expansion coefficients of austenite used in this work.

Calculated by present author	Choi *et al.* [153]	Bhadeshia *et al.* [152]
2.18×10^{-5} K^{-1}	2.41×10^{-5} K^{-1}	2.03×10^{-5} K^{-1}

Roberts and Wever have both produced relationships (see equations 10.12 and 10.13) which can be used at room temperature to estimate the carbon content of austenite in steel, from a knowledge of its lattice parameter [150;154]. The calculated room temperature lattice parameters from equation 10.10 were input into equations 10.12 and 10.13, producing estimates of the C content of the austenite,

$$a_m = 3.555 + 0.044x_\gamma \qquad [10.12]$$

$$a_m = 3.580 + 0.031x_\gamma \qquad [10.13]$$

where a_m is the measured room temperature austenite lattice parameter (Å) and x_γ is the C content of the austenite in wt.%.

Since the alloys used in this work typically contain high concentrations of alloying elements, a third method was also used to estimate the austenite carbon content, which accounted for the influence substitution alloying elements have on the austenite lattice parameter. Dyson and Holmes used linear regression analysis in their investigations on the effect of alloying elements on the austenite lattice parameter of a wide range of steels, producing the following relationship for the ambient austenite lattice parameter [155]:

$$a_{DH} = 3.5780 + 0.0330x_\gamma + 0.00095 \text{ Mn} - 0.0002 \text{ Ni} + 0.0006Cr + 0.0220N + 0.0056Al -$$
$$0.0004Co + 0.0015Cu + 0.0031Mo + 0.0051Nb + 0.0039Ti + 0.0018V + 0.0018W$$
$$[10.14]$$

where a_{DH} is the austenite lattice parameter (Å), and the alloying element concentrations are input into equation 10.14 in wt.%. Terms to account for the influence of two important elements in ADI alloys, Mg and Si are not included in this relationship. It is known however that Si concentrations have a negligible influence

on the austenite lattice parameter, hence there is no term in equation 10.14 to account for its effect [155]. Mg has a similar atomic radius to Al [1], therefore the concentration of Mg was accounted for in an identical fashion to Al in equation 10.14. The influence of P and S was neglected since their concentrations are generally found to be very low in ADI alloys.

The room temperature austenite lattice parameters as previously discussed were calculated from high temperature measurements using the three different thermal expansion coefficients and equation 10.10. These values were then individually substituted for a_{DH} and equation 10.14 was rearranged to produce equation 10.15 enabling the calculation of the austenite carbon content:

$$x_\gamma = (a_{DH} - 3.5780 - 0.00095 \text{ Mn} + 0.0002 \text{ Ni} - 0.0006\text{Cr} - 0.0220\text{N} - 0.0056\text{Al} + 0.0004\text{Co}$$
$$- 0.0015\text{Cu} - 0.0031\text{Mo} - 0.0051\text{Nb} - 0.0039\text{Ti} - 0.0018\text{V} - 0.0018\text{W}) / 0.033$$

[10.15]

The process was repeated for each austenitisation temperature. If multiple measurements had been performed at a specific austenitisation temperature (e.g. 900°C), then the average lattice parameter from all the measurements was used in the calculation. Therefore, at each austenitisation temperature, the austenite carbon content was estimated in three different ways (using equations 10.12, 10.13 and 10.15), for each of the thermal expansion coefficient values listed in table 10.2, producing a total of nine different austenite carbon content predictions. The results of these predictions are shown in figures 10.18-10.20, where they are also compared to MTDATA predictions of the equilibrium austenite carbon content during austenitisation.

Figures 10.18-10.20, show that as expected, the austenite C content is found to increase with austenitisation temperature. In all but two cases, the austenite carbon content calculated using the various methods is found to be much higher than the MTDATA predictions. The best agreement between MTDATA and the calculated austenite C content occurs when equation 10.10 is combined with the thermal expansion coefficient proposed by Choi *et al.* [153] and the austenite carbon content is calculated via equation 10.15 [155].

Figure 10.18. Calculated austenite carbon contents for alloy 1 using the thermal expansion coefficient estimated by the current author.

Figure 10.19. Calculated austenite carbon contents for alloy 1 using the thermal expansion coefficient from Bhadeshia *et al.* [152].
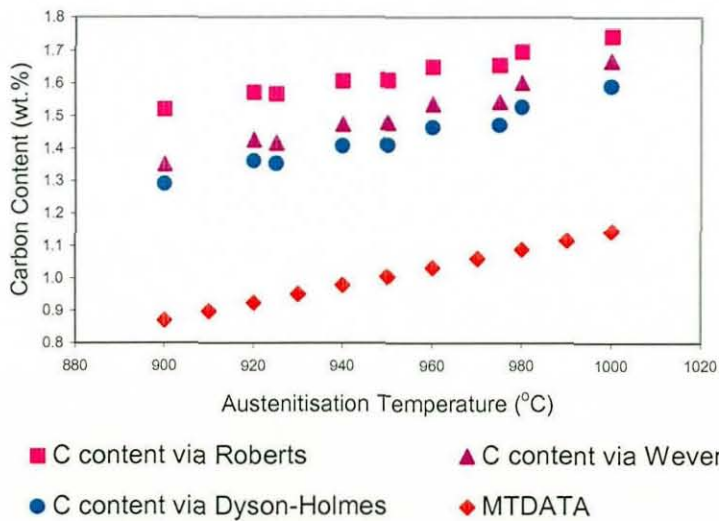
The Dyson and Holmes method (equation 10.15) does account for the influence of substitutional elements on the austenite lattice parameter, so in these highly alloyed samples it is logical that this method produces the best fit in comparison to the other methods which do not directly account for the influence of alloying additions. The composition of the alloy used by Choi *et al.* is also the closest match to that of alloy 1 since it contains similar concentrations of Si and Mn [153]. It

has been shown that good agreement exists between MTDATA predictions of the austenite C content and experimental measurements obtained using X-ray diffraction in quenched samples [20]. The MTDATA predictions are in best agreement with the calculated austenite C content when the Choi *et al.* thermal expansion coefficient is used in combination with the Dyson and Holmes relationship. Therefore, the calculations made using the Choi *et al.* coefficient of thermal expansion and the Dyson and Holmes relationship to calculate the austenite C content were thought to be the most reliable. The variation in these results also demonstrate the strong influence the thermal expansion coefficient and/or the assumption that it remains linear on cooling from the austenitisation temperature to room temperature have on the calculated austenite C contents.
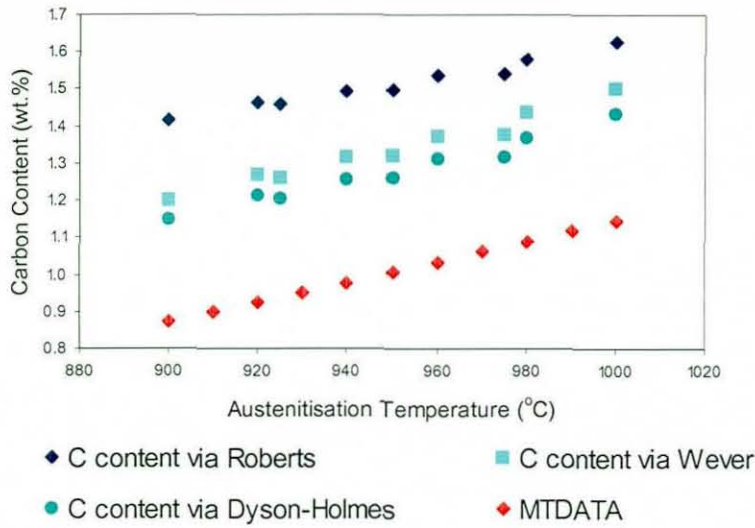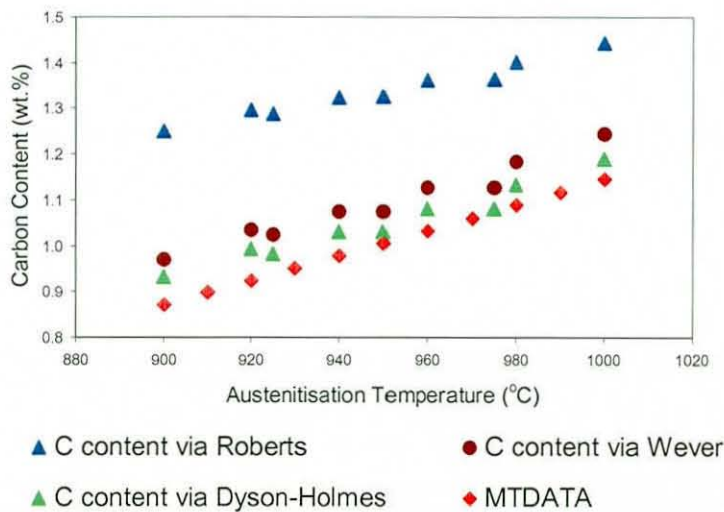
Figure 10.20. Calculated austenite carbon contents for alloy 1 using the thermal expansion coefficient from Choi *et al.* [153].

10.7.3 Austenitisation of alloy 5

For the alloy 5 specimens, austenitisation experiments were performed at 900°C and 1000°C. Six specimens were austenitised in total, three at each temperature. All the experiments were performed on different samples. For four of the samples, austenitisation experiments were performed using an identical experimental procedure as the alloy 1 specimens. However, for one sample at 900°C

and one at 1000°C, a scan was performed from 10-110°, with a 1 second dwell time and a 0.02° step size. These scans took 83 minutes to complete. The aim of these experiments was to determine if an oxide film was present on the samples during austenitisation.

The variation in austenite lattice parameter with austenitisation time is shown in figure 10.21. As can be seen in the figure, as with the alloy 1 samples, there is little change in the austenite C content with austenitisation time, suggesting the *equilibrium austenite C content is reached quickly in these samples*. Both sets of measurements also agree excellently with each other, demonstrating good experimental reproducibility in the different samples.

Figure 10.21. Austenite lattice parameter as a function of time during the austenitisation of alloy 5.
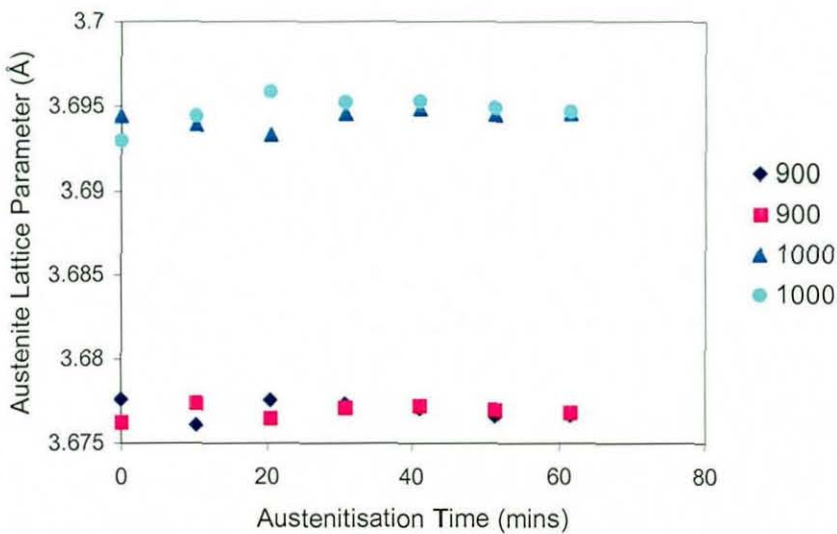
Figure 10.22 shows the austenitisation scan from 10-110° in sample 5e. As can be seen in the figure, only one small oxide peak was detected in the sample. It was identified as being magnesium silicate as was observed on samples 3 and 4. The intensity of the oxide peak is much lower than the ones observed in alloys 3 and 4. This is probably due to two main factors. Firstly, the X-ray diffraction patterns of samples 3b and 4e (see figures 10.4 and 10.12 respectively) were obtained after the samples had been exposed to high temperatures for much longer time periods, therefore it seems obvious that the oxide film in these samples will be thicker

resulting in higher intensity diffraction peaks. Secondly, by the time these experiments were being performed, experiments had been ongoing for a period of over two weeks. Over this time period a steady decrease in the vacuum pressure obtained during the experiments had been observed. Pressures of just 2.0×10^{-4} mbar were now obtainable during these experiments after 30 minutes of vacuum pump operation, which is over one order of magnitude lower than the pressures obtainable in earlier experiments for a similar pumping time. This undoubtedly also helped reduced the level of oxidation of the samples.

Figure 10.22. X-ray diffraction pattern of sample 5e during austenitisation at 900°C.
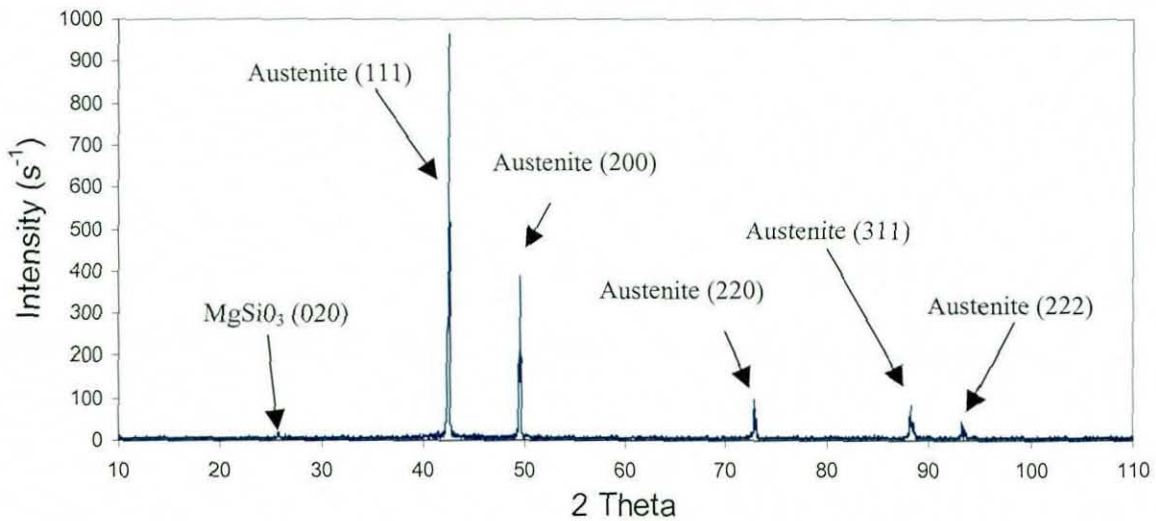
The best agreement between the austenite C content predicted by MTDATA and those calculated using the methods outlined in section 10.7.2, was again obtained when the Choi *et al.* thermal expansion coefficient [153] was used in conjunction with the Dyson and Holmes relationship [155] to predict the C content of the austenite. This agrees with the results of alloy 1 and is probably the best approximation as mentioned previously. The results for alloy 5 are shown in figure 10.23.

Figure 10.23. Calculated austenite carbon contents using the thermal expansion coefficient from Choi *et al.* in alloy 5 [153].
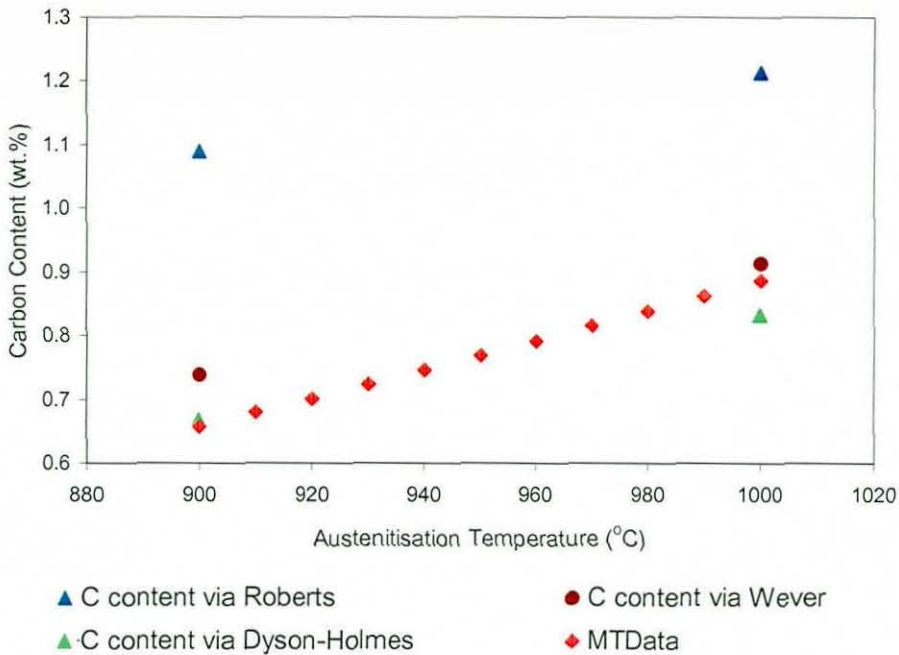
10.8 High Temperature X-ray Diffraction of Austempered Ductile Iron Alloys During Austempering

10.8.1 Introduction

After austenitisation for one hour at either 900 or 1000°C, specimens were cooled at as fast a rate as possible to the austempering temperature. The cooling rate had been optimised during previous experiments on alloys 3, 4 and 6. Cooling rates of 10°Cs^{-1}, 5°Cs^{-1} and 2.5°Cs^{-1} were obtainable from 1000 to 600°C, 600 to 400°C and 400 to 300°C, respectively. Samples were austempered at three different temperatures, 400, 350 and 300°C. During austempering, scans were made continuously of the austenite (111) and ferrite (110) peaks for 1 hour, then every 15 minutes for the next 3-6 hours from 41.9-45°. A step size of 0.02° and a dwell time of 2 seconds were used for all the scans. 120°C and 500°C preheats were used to help limit the oxidation of the samples before the initial austenitisation experiments were

performed. The vacuum pressure after the preheats was allowed to fall below 2.0×10^{-4} mbar before the experiments were started to again help minimise oxidation.

10.8.2 Austempering of alloy 1

Figure 10.24 shows the results of the first scan in alloy 1a which was performed immediately after the sample reached the austempering temperature of 400°C. The sample was austenitised at 900°C for 1 hour prior to austempering. As can be seen in the scan, no austenite (111) peak is visible in the X-ray diffraction pattern. At the start of austempering, the sample should be almost 100% metastable austenite, therefore no ferrite peak should be detected in the X-ray diffraction pattern, only the austenite (111) peak should be visible. As shown in figure 10.24, this is not the case. It took at total time of 70 seconds to reach the austempering temperature from the austenitisation temperature. It was suspected that this cooling rate was not fast enough to prevent pearlite formation on cooling to the austempering temperature in this alloy.

Figure 10.24. The first austempering scan in sample 1a at 400°C, showing a single ferrite (110) peak but no austenite (111) peak.
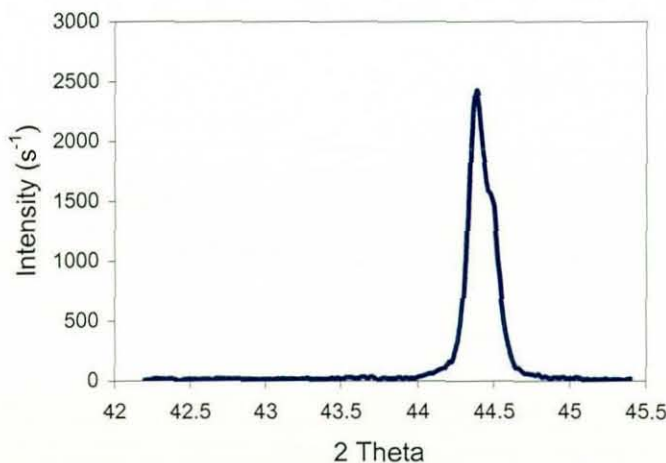
The composition of alloy 1 is listed in table 7.1. It is known that all alloying additions except Co tend to delay the reconstructive and displace transformations in steels [26;33]. It is thought that alloy 1 does not possess high enough concentrations of

alloying additions to prevent pearlite formation at this cooling rate. An ADI alloy would be quenched in a salt bath to the austempering temperature, resulting in a much faster cooling rate than was obtainable in the X-ray diffractometer. The time temperature transformation (TTT) diagram for alloy 1 was computed using a freely available software program, and is shown in figure 10.25 [156]. The carbon content input into the program was 0.87 wt.% C, which was calculated by MTDATA for alloy 1 as the C content after austenitisation. As can be seen in the figure, the maximum cooling rate produced in the sample should not come close to the reconstructive transformation curve in figure 10.25. This suggests that pearlite formation does not occur in this alloy when it is cooled at this rate. However, this program was developed for steels and hence the C content of these alloys is much greater than encountered in steels, so the predicted TTT diagram may not be reliable.

Figure 10.25. A calculated TTT diagram for alloy 1 [156].
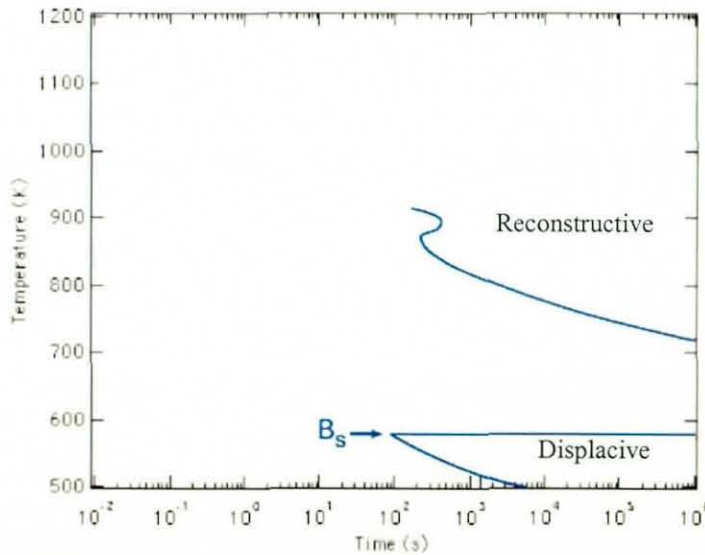
The sample was cooled to room temperature and polished so its microstructure could be observed. As suspected the microstructure consisted of pearlite and ferrite surrounding graphite nodules as shown in figure 10.26. No martensite was found in the sample, which could have formed when metastable austenite is cooled to room temperature. Again, this is more evidence to suggest that the cooling rate the sample was subjected to was not sufficiently fast enough to prevent pearlite formation on cooling. The tests were repeated on another sample

made from alloy 1, and again similar results were obtained. It was therefore concluded that it was not possible to produce ADI samples from alloy 1 in the high temperature X-ray diffractometer, due to the limited cooling rate imposed on the sample by the temperature control unit (see section 9.4).

Figure 10.26. Optical micrograph of sample 1a.
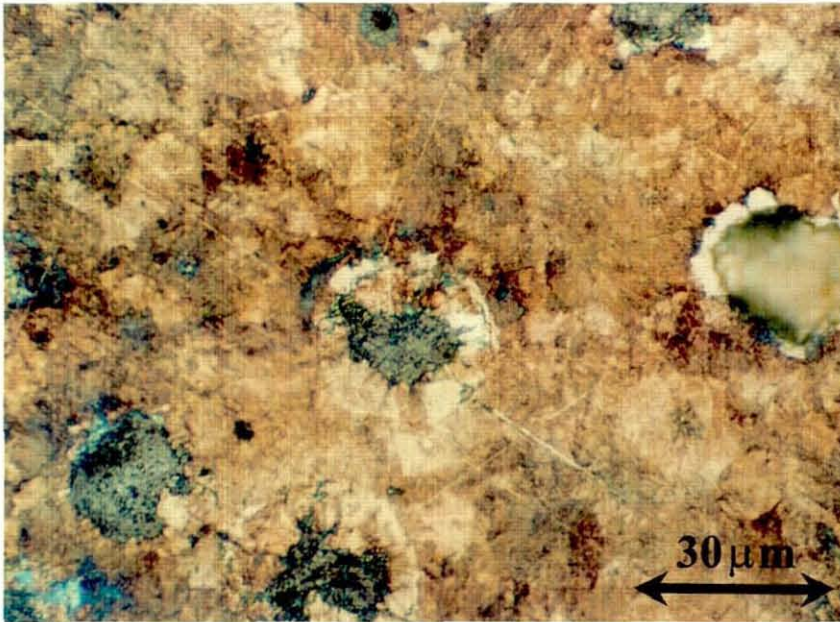
10.8.2 Austempering of alloy 5

The composition of alloy 5 is listed in table 7.1. As can be seen in the table, alloy 5 contains higher concentrations of Si, Cu, Ni and Mn than alloy 1. These elements delay the reconstructive and displacive transformations in steels [26;33]. Therefore it was more likely that the austenite could be cooled to the austempering temperature without pearlite formation occurring in these samples, therefore an ADI type microstructure could be produced.

The first sample was austenitised at 900°C for one hour and then austempered at 400°C. Figure 10.27 shows all the scans that were obtained during austempering. The austenite (111) and ferrite (110) diffraction peaks did not overlap in the scan. Austenite (111) peaks were detected in the sample. As austempering time increased, the magnitude of the austenite peaks is seen to fall, before reaching an almost constant value, whilst the intensity of the ferrite peaks increases before

becoming relatively constant. This suggests the quantity of austenite in the sample reduces as austempering time increases until a constant value is reached, whilst the quantity of ferrite increases before it becomes constant. This observation is consistent with the mechanism of the formation of bainitic ferrite in ADI alloys. During stage 1 of austempering, bainitic ferrite plates nucleate and grow, consuming the metastable austenite [21]. The bainitic ferrite also rejects carbon into the surrounding austenite enriching it with C. This process continues until the C content of the austenite reaches a critical concentration (the limiting austenite C content X_{T0}), where there it no longer has a driving force to transform to bainitic ferrite [21;157]. Hence some austenite is retained in the sample at the end of stage 1 of austempering. This austenite remains stable for a limited time period known as the processing window, before it slowly breaks down into a mixture of ferrite and carbide during stage 2 of austempering [15,22].

Figure 10.27. High temperature X-ray diffraction scans of sample 5c during austempering at 400°C.
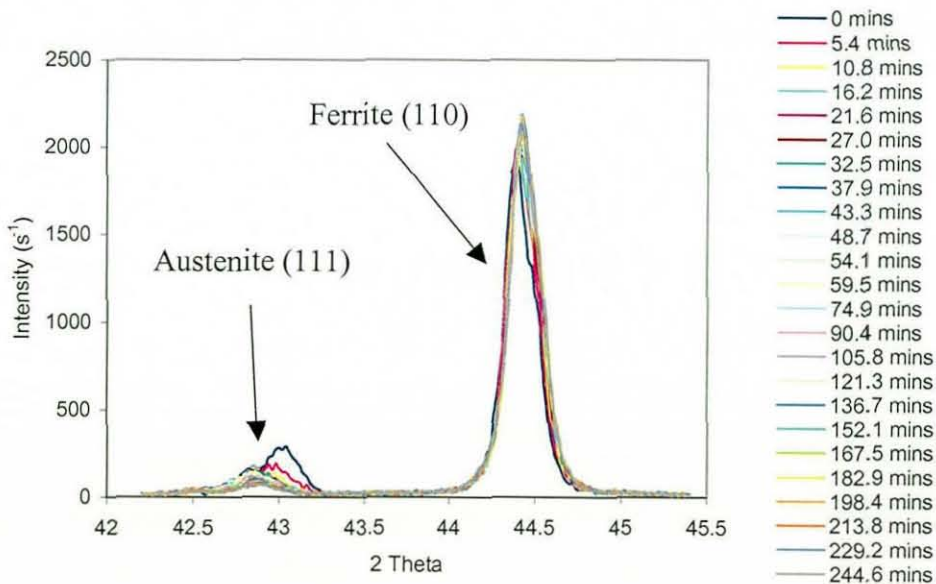
However, the ferrite (110) peaks still have a much greater magnitude than the austenite (111) peaks, suggesting a larger than expected volume fraction of ferrite in the sample. The ferrite peak is also present in the first scan at the austempering temperature, suggesting significant quantities of ferrite form in the sample at very short austempering times (after approximately 4 minutes). These observations were

also made on all the alloy 5 samples regardless of heat treatment, and are against the trend expected for two reasons. Firstly, at the start of austempering, the matrix should be 100% metastable austenite. This is clearly not the case as shown in figure 10.27. Due to the time taken to perform the individual scans the intensity of the ferrite peak is not actually measured until after approximately 4 minutes of austempering. However, this fact alone cannot explain the results shown in figure 10.27. After such a short austempering time this large quantity of ferrite should not be present in the sample. Secondly, the austenite (111) planes have a higher packing density than their ferrite (110) counterparts. Therefore austenite (111) planes should produce a higher diffraction intensity than ferrite (110) planes per unit volume of phase [69]. At the start of austempering the vast majority of the matrix should be metastable austenite. Therefore the austenite (111) planes should produce a very intense diffraction of a much greater magnitude than the ferrite (110) planes. Again, this is not observed in figure 10.27.

After the experiment was completed, the data obtained were used as outlined in section 10.4 to estimate the volume fractions of austenite and bainitic ferrite in the matrix. The results are presented in figure 10.28. As expected from the visual inspection of figure 10.27, the predicted volume fraction of austenite is found to decrease from a volume fraction of just over 0.15 at the start of austempering before reducing steadily again until the experiment was completed. The microstructure model predicted a maximum austenite volume fraction of 0.35 for alloy 5c. Again, the general trend of the data is consistent with the stage 1 and 2 austempering reactions, but the volume fraction of austenite calculated to be present in the sample is not.

It was suspected that as in the previous austempering experiments on alloy 1 that the cooling rate in this sample was not fast enough to prevent the formation of pearlite in the microstructure. After the experiment, the sample was polished so its microstructure could be observed, which is shown in figure 10.29. A small quantity of pearlite was observed in the sample in the matrix. Therefore this would also have contributed to the high intensity of the ferrite peak at the start of austempering. However, the vast majority of the microstructure was typical of an ADI alloy after a prolonged austempering heat treatment, that was undergoing the stage 2 austempering reaction. During stage 2 of austempering, the high carbon austenite breaks down. Carbides precipitate from the austenite, reducing its carbon content. Therefore, as shown in figure 10.29 the matrix transforms to martensite on cooling,

since it is no longer enriched enough with C to remain stable [44]. Importantly, the volume fraction of the martensite (previously austenite at the austempering temperature) in the specimen is much greater than the volume fraction of austenite calculated by the X-ray diffraction integrated intensity results shown in figure 10.28.

Figure 10.28. Predicted volume fraction of austenite in sample 5c during austempering at 400°C.
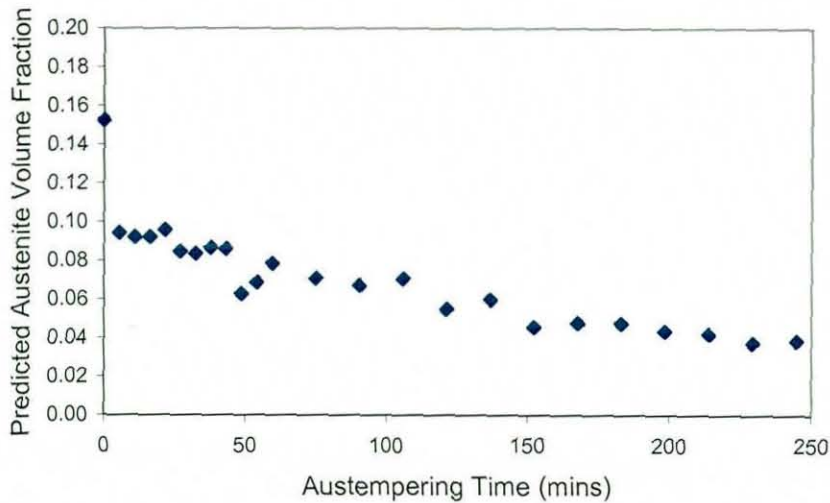
Figure 10.29. An optical micrograph of alloy 5c after completion of the austempering experiment, showing the large volume fraction of martensite (light brown – previously austenite) in the sample.
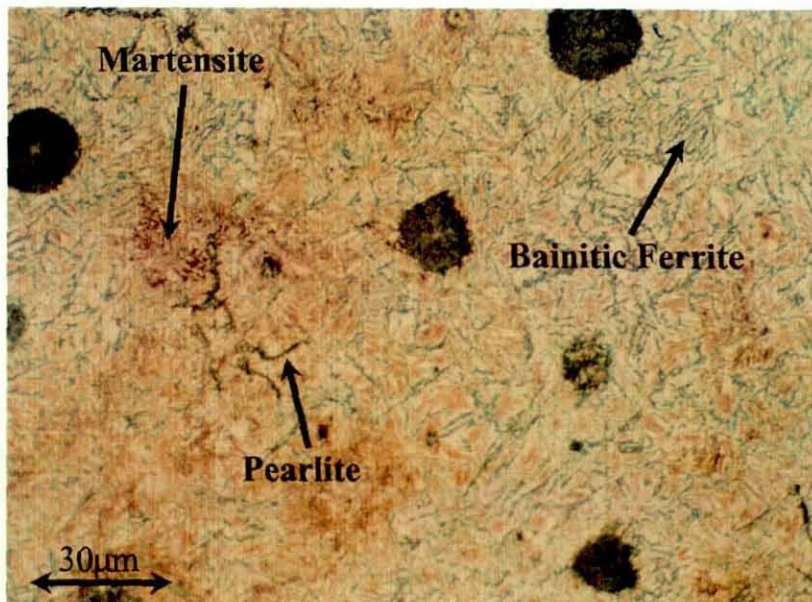
The presence of an oxide film on the samples or decarburisation could be used to explain these strange results. Although a low vacuum pressure of 2.0×10^{-4} mbar was obtained before the experiments were started, slight oxidation of the samples still occurred during the experiments as shown in figure 10.30. These samples are oxidised much less than those of alloys 3, 4 and 6 shown in figures 10.3, 10.5 and 10.15. Bainitic ferrite forms by a displacive mechanism [26;27;33]. The displacive nature of this transformation could result in spallation of the thin oxide film above the newly formed bainitic ferrite phase. However, the oxide which is present over the austenite phase could remain intact. Section 10.6 showed the presence of an oxide film could mask the presence of small quantities of phases in ductile iron alloys. Therefore, the spallation of the oxide film above the bainitic ferrite phase could cause an increase in the diffraction intensity of the ferrite, which would explain the observations made in the current experiments. The oxide film shown in figure 10.30 was again identified as magnesium silicate, which was identified on the sample during austempering and at room temperature.

Figure 10.30. Oxide films on alloy 5 samples.

If decarburisation of the surface layers of the sample occurred during the experiment then some evidence would remain in the surface layers of the sample. Figure 10.31 shows a digital micrograph of the surface of sample 5c. A thin film of ferrite approximately 1µm thick can be seen across some of the sample surface, although it is not present across the whole surface. This ferrite most likely formed on

cooling from the austenitisation temperature. A low C content of the austenite on the surface due to decarburisation during austenitisation would have assisted ferrite formation in these areas [26;33], and therefore explain the observations of the high intensity ferrite peak during the early stages of austempering. Experiments performed on alloy 1 showed that evidence of decarburisation was not found in these alloys after much greater austenitisation times, however, these experiments were performed under a much lower vacuum pressure of 8.0×10^{-5} mbar compared to 2.0×10^{-4} mbar for sample 5c. Therefore it seems the most likely cause of the high intensity ferrite peak observed in the samples during the early stages of austempering is a consequence of decarburisation of a thin layer of the sample surface during austenitisation.

Figure 10.31. A thin intermittent ferrite film on the surface of sample 5c after completion of austempering.
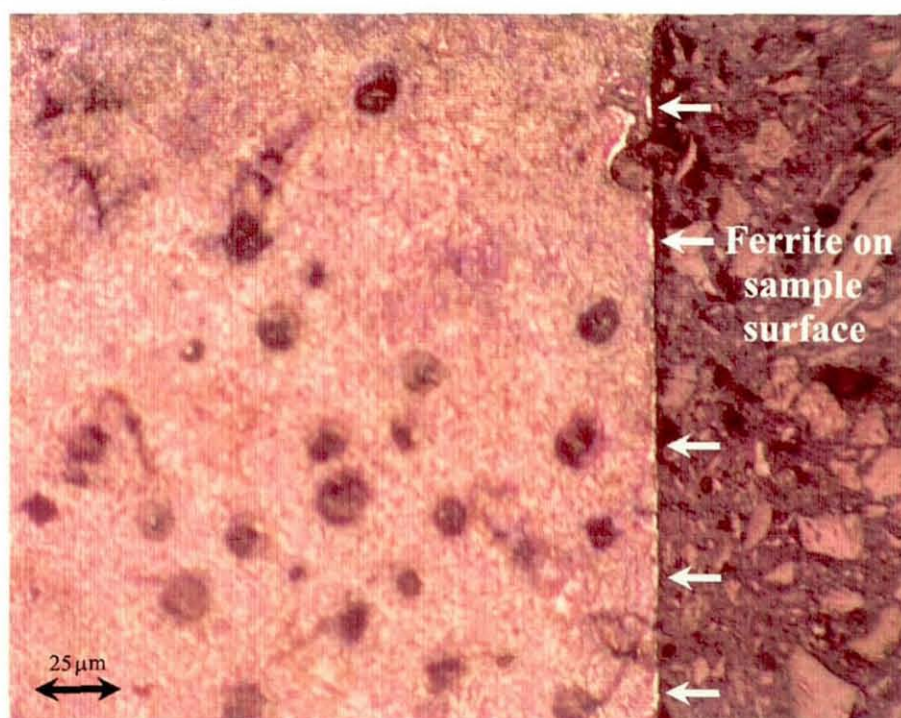
The presence of the ferrite film found on parts of the sample surface reduced the intensity of the austenite diffraction peaks and therefore did not allow accurate matrix volume fractions to be calculated from the integrated peak areas (see section 10.4). Decarburisation of the austenite was thought to occur mainly during

austenitisation due to the higher temperatures the sample was exposed to. However, the possibility of decarburisation during austempering cannot be excluded, and could also account for the large quantity of martensite present in the matrix of sample 5c. If it did occur, it could also influence the austenite lattice parameter. The lattice parameter of the austenite could simply reduce because it contained less C. This could also have a further effect on the stage 1 austempering transformation. Decarburisation of the austenite could produce greater volume fractions of bainitic ferrite in the sample since more austenite would be consumed before the austenite contained the limiting austenite C content X_{T0}. These two effects could also compete during austempering transformation as the austenite would be decarburised and enriched with C at the same time. Therefore it can be seen that although decarburisation was thought to be mainly a process limited to the austenitisation of these samples, the decarburisation of the surface layers during austempering could potentially influence the measurement of the austenite lattice parameter in a number of ways.

It can be seen at this point that the penetration depth into the sample of the diffracted X-rays is important for the results obtained. A software program called AbsorbDX allows such a calculation to be made [158]. Table 10.3 shows the results of these calculations. It can be seen from the table that a larger proportion of the diffracted X-rays are obtained from regions of the sample close to the surface. This is because the absorption of the X-ray increases exponentially with penetration depth[158]. In fact, the total X-ray penetration is approximately 7 μm, but nearly all the X-rays that penetrate over half this depth are absorbed as they try to leave the sample [158]. The ferrite film observed on parts of the surface of alloy 5c was approximately 1 μm thick. Therefore these calculations suggest that its presence on some areas of the surface would account for the diffraction of 75% of the incident X-rays. These results show that even a very thin and intermittent film of ferrite on the sample surface could greatly influence the results obtained during these investigations.

The shift in the austenite (111) peak as it is enriched with C during the austempering process was also monitored during these experiments. This enabled predictions of the austenite C content to be made during austempering, although these predictions should be treated with some caution due to the decarburisation of

the surface layer. Figure 10.32 shows how the austenite lattice parameter in sample 5c varied with austempering time. The lattice parameter rises quickly at first as the austenite becomes enriched with C. It then remains constant (through the processing window, which is short in sample 5c due to the high austempering temperature), as the limiting austenite C content X_{T0} is reached, then after approximately 90 minutes of austempering starts to fall. Again, these observations are consistent with the microstructural changes that occur during austempering in ADI alloys. These data were then converted into predictions of the austenite C content using the same methods detailed in section 10.7.2.

Table 10.3. Calculated penetration depth of diffracted Cu X-rays at 45° into a Fe sample.

Percentage of diffracted X-rays (%)	Calculated penetration depth (μm)
25	0.22
50	0.53
75	1.07
99	3.55

Figure 10.32. Changes in the austenite lattice parameter during austempering in alloy 5c.
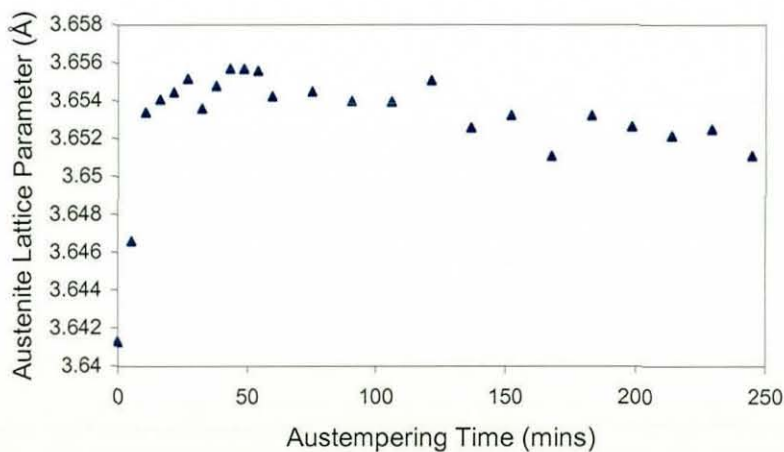
The results of the different predictions of the austenite C content derived from the measured lattice parameters, are shown in figures 10.33-10.35 in sample 5c.

Although there is some scatter in the results, the time of the maximum austenite carbon content was judged to first occur after around 30 minutes of austempering. This value was taken as the time where the austenite C content values start to become constant and maximal, and therefore corresponds to the end of stage 1 of the austempering process. The maximum value of the calculated austenite C content ranged from 1.26-1.65 wt.% C depending on the calculation method (see section 10.7.2). During austempering of ADI alloys, the maximum austenite C content is maintained through the processing window, hence the maximum values are constant for a short period of time. This maximum C value is also known as the limiting austenite C content, $X_{T0,}$ and can be calculated using MTDATA. It was calculated to be 0.992 wt.% C for alloy 5c. This value is significantly lower than all the estimations of the austenite C content from the X-ray diffraction data obtained at high temperature, (however, as stated previously decarburisation could have influenced the calculation of the austenite C content).

Figure 10.33. Calculated austenite C contents using the thermal expansion coefficient estimated by the current author for alloy 5c.
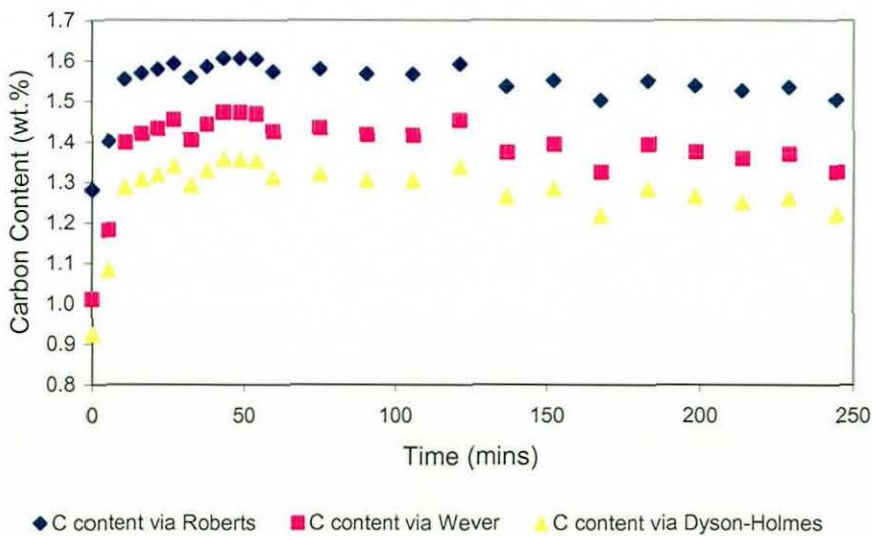
Figure 10.34. Calculated austenite C contents using the thermal expansion coefficient from Bhadeshia *et al.* for alloy 5c[152].
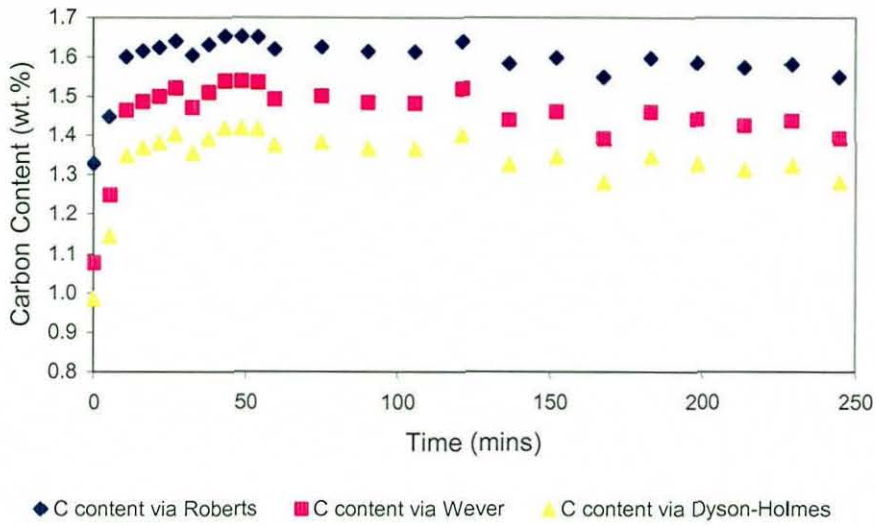
Figure 10.35. Calculated austenite C contents using the thermal expansion coefficient from Choi *et al.* for alloy 5c[153].
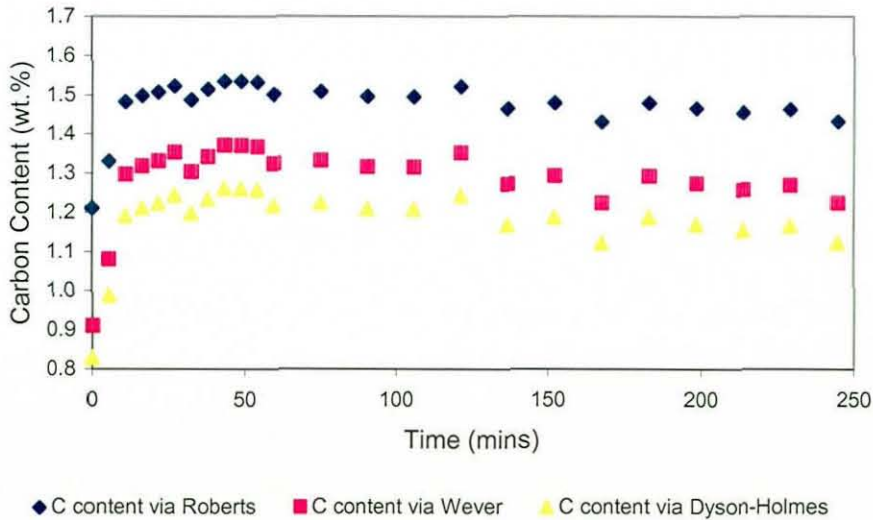
As shown in figure 10.29, the austenite that was present during austempering of alloy 5c has transformed to martensite on cooling to room temperature. Therefore no austenite was detected in the room temperature X-ray diffraction pattern of this sample. However, sample 5f was austenitised at 1000°C and austempered at 300°C. Due to this heat treatment regime, this alloy undergoes the austempering

transformation at a significantly slower rate. Austenite was detected to be present in the room temperature X-ray diffraction pattern of this sample. Figure 10.36 shows the room temperature X-ray diffraction pattern obtained from sample 5f after it was polished. The polishing removed the oxide film and also the decarburised layer from the sample. Figure 10.37 shows the last high temperature X-ray diffraction measurement taken in alloy 5f before it was cooled to room temperature. The difference between the intensity of the austenite and ferrite peaks in comparison to the high temperature X-ray diffraction measurements is clear. The increase in the intensity of the austenite peaks in figure 10.36 supports the theory that the presence of ferrite on the surface of the sample was reducing the intensity of the austenite (111) plane diffraction due to its increased ferrite volume in the surface layers.

Figure 10.36. Room temperature X-ray diffraction trace for alloy 5f after the sample was polished to remove any surface effects present on the sample.
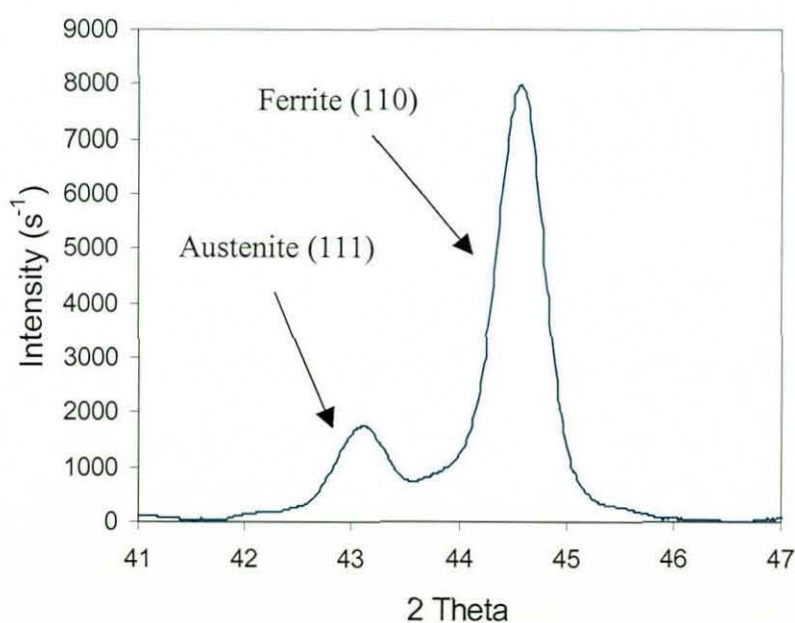
The data obtained from the last high temperature scan on specimen 5f allowed the austenite C content to be calculated again using the different methods outlined in section 10.7.2. The C content of austenite was calculated to range between a minimum value of 1.42 wt.% C using the Dyson and Holmes equation [155] and the Choi *et al.* thermal expansion coefficient [153], and a maximum value of 1.76 wt.% C, using the Roberts equation [150] and the thermal expansion coefficient of

Bhadeshia *et al.* [152], after austempering for 370 minutes. The austenitisation experiments performed in section 10.7 showed that the best estimate for these alloys was most likely that calculated using the Dyson and Holmes equation [155] and the Choi *et al.* thermal expansion coefficient [153]. This calculation produced the lowest value in this case, as it did for all heat treatments. As shown in figure 10.38, after austempering for this time period, the lattice parameter of the austenite in alloy 5f seems to be at a maximum and constant value, suggesting this alloy is in the processing window at this time. Therefore the austenite present in the alloy should contain a C concentration of X_{T0}, its theoretical maximum. The austenite carbon content was calculated using equations 10.12, 10.13 and 10.15 using the room temperature X-ray diffraction data. Table 10.4 compares the austenite C contents calculated from the high temperature and low temperature X-ray diffraction measurements on alloy 5f, with calculations of X_{T0} and X_{T*} made by the microstructure model. $X_{T0'}$ values, which also account for the stored energy of bainitic ferrite, would be slightly greater than those of X_{T0}.

Figure 10.37. The last high temperature X-ray diffraction trace obtained during austempering of sample 5f.
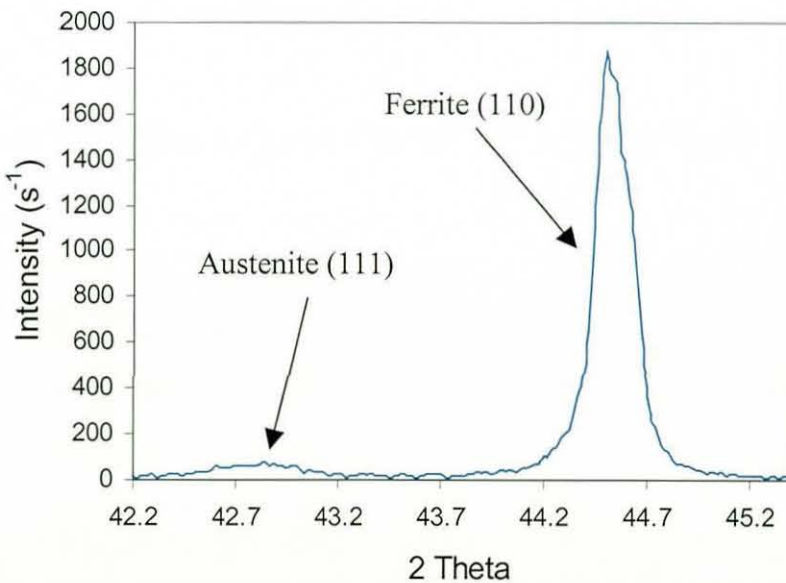
Table 10.4 presents some interesting results. Firstly, there is a slight difference in the measured room temperature and high temperature X-ray diffraction

measurement of the austenite C content. The sample could not be quenched after the completion of the austempering measurements, since it was located in the vacuum chamber of the X-ray diffractometer. Hence the sample was cooled to room temperature at a slower rate of $2°Cs^{-1}$. The sample was also polished to remove the oxide film on the sample. The polishing process would also have removed the decarburised layer. Either of these two processes could explain the difference between the two measurements.

Figure 10.38. Changes in the austenite lattice parameter during austempering of alloy 5 samples austenitised at 1000°C.
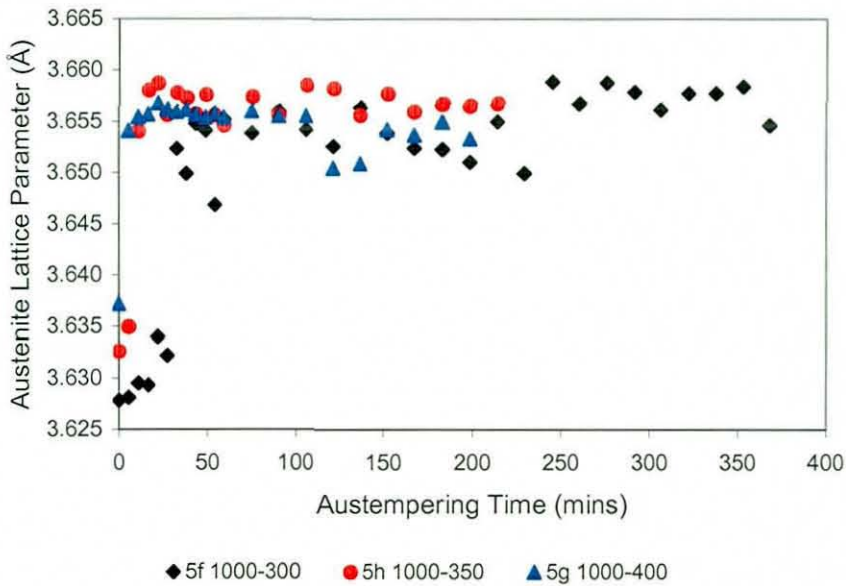
Table 10.4. Comparison of predictions of the austenite C content in sample 5f after austempering for 370 minutes, using room temperature and high temperature X-ray diffraction and model calculations (all wt.%).

Room temperature X-ray diffraction	High temperature X-ray diffraction	Calculated X_{T0}	Calculated X_{T*}
1.64-1.70	1.42-1.76	1.293	2.813

Secondly, all the X-ray diffraction measurements of the austenite C content are higher than the calculated X_{T0} value, which is its theoretical maximum. This is a

common observation in ADI literature [15;21;22;157]. As mentioned previously, decarburisation could explain why the high temperature measurements are higher. However, this could not have influenced the room temperature results since the decarburised layer was removed when the sample was polished. An explanation for the X-ray diffraction measurement of the austenite C content being greater than X_{T0}, was originally given by Le Houillier *et al.* from a study on steels [84]. They stated that upon quenching steels from the isothermal transformation temperature to room temperature, only the austenite that has been substantially enriched with C would be retained in the sample. The rest of the austenite will transform to martensite on cooling. Hence the average austenite C content measured by X-ray diffraction is artificially high due to the formation of martensite from the austenite that was not enriched with C [84]. However, as with many ADI alloys, sample 5f contained no martensite. This suggests that in alloy 5f, the austenite C content is above the calculated X_{T0} value. However, this alloy as with all the heat treated alloy 5 samples did contain a small quantity of pearlite (a volume fraction of less than 0.05) in the matrix. This observation makes these results inconclusive, since the formation of pearlite on cooling between the austenitisation and austempering temperatures could influence the austempering transformation in these alloys, and hence the room temperature austenite C content measurement. An optical micrograph of the structure of alloy 5f is shown in figure 10.39. This shows the microstructure of alloy 5f to be typical of an ADI alloy. However, a small volume fraction of pearlite is observed in the sample.

Finally, although the measured austenite C content was found to be above X_{T0}, it is less than the X_{T*} value which is used in the microstructure model. Chapter 6 demonstrated that inaccuracies in the microstructure model could be related to the precipitation of carbides at low austempering temperatures. Alloy 5f was austempered at 300°C and therefore carbides could well be present in the bainitic ferrite in this alloy. None of the model versions account for the precipitation of carbides, hence carbide precipitation could account for this difference.

High temperature X-ray diffraction experiments were performed on four more alloy 5 samples for the following austenitisation and austempering temperatures, 900-350, 900-300, 1000-400 and 1000-350 (all °C). In all these samples, the intensity of the austenite (111) peaks was found to be much lower than the ferrite (110) peaks.

As previously mentioned this is thought to be a consequence of decarburisation of the surface of the sample.

Figure 10.39. Optical micrograph of alloy 5f after austempering.

Figures 10.38 and 10.40 show the how the austenite lattice parameter in all the alloy 5 samples changed with austempering time. As expected, the largest lattice parameters occur in the samples austempered at lower austempering temperatures. This is because at lower austempering temperatures, more C enrichment of the austenite occurs before stage 1 of the austempering reaction ceases [2;15;44;157]. The austenite in the samples austempered at 300°C also reached their maximum C contents after a greater time, whilst the samples austempered at 400°C reached their maximum values in the shortest time. Again, this is what should be expected, because at higher temperatures, the rate of the stage 1 reaction is faster in ADI alloys [2;15;44].

Figure 10.40. Changes in the austenite lattice parameter during austempering of alloy 5 samples austenitised at 900°C.
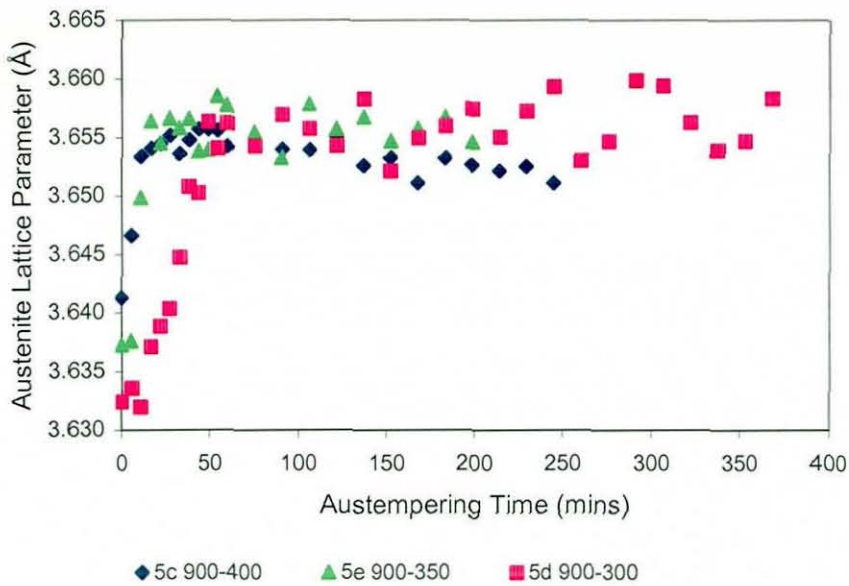
Table 10.5 presents all the most important data obtained during high temperature and low temperature X-ray diffraction measurements from the austenitisation and austempering experiments on the alloy 5 samples. Predictions of the limiting austenite C content X_{T0}, and the overall transformation time for the stage 1 austempering reaction made by the model outlined in chapter 8 are also included. Hence the values shown in the table 10.5 are the maximum range of C^0_γ, X_{T0} and X_{T*} across the 10 shells of the model and the range of stage 1 transformation times for the different shells. The average value of these parameters is also included in the table 10.5.

The experimentally obtained data is also shown via the maximum range of calculated values. The lowest values were always obtained when the C content of austenite was calculated using the Dyson and Holmes equation [155] and the Choi *et al.* thermal expansion coefficient [153], if the measurement was at high temperature. As mentioned previously, these values were thought to be the most accurate for the alloys in the current work. The largest values were always obtained when the C content of austenite was calculated using the Roberts equation [150] and the thermal expansion coefficient of Bhadeshia *et al.* [152], if the measurement was at high temperature.

Table 10.5. Comparison of the most important data obtained from both high and room temperature X-ray diffraction experiments on the alloy 5 samples.

Sample	5c	5e	5d	5g	5h	5f
Austenitisation temperature (°C)	900	900	900	1000	1000	1000
Austempering temperature (°C)	400	350	300	400	350	300
Austenitisation						
Average predicted C_γ^0 (wt.%)	0.647	0.647	0.647	0.904	0.904	0.904
Range of predicted C_γ^0 in 10 shells (wt.%)	0.613-0.762	0.613-0.762	0.613-0.762	0.862-1.040	0.862-1.040	0.862-1.040
Range of measured C_γ^0 values HTXRD (wt.%)	0.67-1.36	0.67-1.36	0.67-1.36	0.83-1.51	0.83-1.51	0.83-1.51
Austempering						
Approximate austempering time to obtain maximum austenite C content (mins)	30	40	60	20	30	90
Model prediction of stage 1 transformation times (mins) in the 10 shells	23.6-32.7	26.4-40.2	40.4-62.0	38.5-53.5	47.8-71.0	76.6-113.9
Max measured austenite C content (HTXRD) (wt.%)	1.65-1.26	1.80-1.37	1.86-1.46	1.68-1.29	1.80-1.48	1.89-1.49
Model average X_{T0} prediction (wt.%) of the 10 shells	0.992	1.144	1.293	0.992	1.144	1.293
Model X_{T0} range (wt.%) in the 10 shells	0.928-1.005	1.080-1.580	1.230-1.305	0.928-1.005	1.080-1.158	1.230-1.305
Model average X_{T*} prediction (wt.%) of the 10 shells	1.802	2.309	2.813	1.802	2.309	2.813
Model X_{T*} range (wt.%) in the 10 shells	1.738-1.815	2.245-2.323	2.750-2.825	1.736-1.815	2.245-2.323	2.750-2.825
Last austenite C content (HTXRD) (wt.%)	1.55-1.12	1.71-1.28	1.85-1.45	1.60-1.19	1.72-1.42	1.79-1.36
Ambient XRD austenite C content (wt.%)	No peak	1.44-1.51	NA	No peak	NA	1.64-1.70

The austenitisation measurements and predictions shown in table 10.5 have been discussed previously in section 10.7.3. Room temperature measurements of the austenite C content were only directly possible on two samples. The samples austempered at 400°C contained no austenite on cooling to room temperature since any of the remaining austenite transformed to martensite, therefore no measurements could be made. Samples 5d and 5h were re-austenitised after austempering and then cooled as fast as possible to ascertain if pearlite was forming in the alloy 5 samples on cooling between the austenitisation and austempering temperatures. These experiments revealed that as suspected a small quantity of pearlite was indeed forming in these samples on cooling between the heat treatments.

As can be seen in the table, all the maximum measurements of the austenite C content during high temperature X-ray diffraction are greater than the X_{T0} prediction, but smaller than X_{T*}, although as previously mentioned, decarburisation could have influenced these measurements. All the measurements also show that the austenite C content increases with a reduction in the austempering temperature as expected theoretically. The time at which the austenite C content first became maximal and constant in the samples gives a good indication of the time needed to completion of the stage 1 austempering reaction in the samples. These times are generally in good agreement with the predicted stage 1 transformation times predicted by the kinetics model, which are also shown in the table 10.5. Finally, where measurements were possible room temperature X-ray diffraction measurements of the austenite C contents are slightly different from their high temperature counterparts. As previously mentioned, this is most likely a result of the slow cooling they were subjected to at the end of austempering. However, they are also shown to be greater than X_{T0}, but some pearlite was observed in all the samples which casts some doubt on the accuracy of these results.

10.8.3 Measuring the length of the sample which maintained a uniform temperature during the experiments

Section 10.3 presented a series of calculations that could be used to find the length of the sample that was exposed to X-rays during these experiments. These calculations were important, since only a small length of the sample is maintained at a uniform temperature during experiments. Hardness tests were performed along the length of sample 5f to establish if the hardness of the section exposed to X-rays was constant. These results are shown in figure 10.41. As can be seen in the figure, a uniform hardness was obtained across the centre of the sample for a length of 30mm, which when compared to the values calculated in table 10.1, is shown to be much greater than the width of the incident X-ray beam over the angular ranges of interest in this work. Hence the current author is confident that during the experiments, X-ray data were only obtained from regions of the samples that were at uniform temperature.

The difference in hardness along the sample is due to the presence of the water cooled clamps at the sample ends (see section 9.4). The peaks in hardness approximately 20 mm from the sample centre is due to the lower austempering temperature these sample regions were subjected to. These regions are closer to the clamps, so maintain a lower temperature at all stages of heat treatment than the centre of the sample. Sample 5f was austempered at 300°C, hence these regions were austempered at a lower temperature and therefore have a higher hardness. Closer still to the water cooled clamps, the hardness falls dramatically. This material on heating to the austenitisation temperature does not transform to austenite because of its close proximity of the water cooled clamps. Instead, the carbides in the pearlite coarsen during the heating and hence its hardness is reduced. Finally, at each end of the sample some material remains in the clamps throughout the experiment and hence the hardness of these areas remains unchanged.

Figure 10.41. Measured hardness profile along the length of alloy 5f.
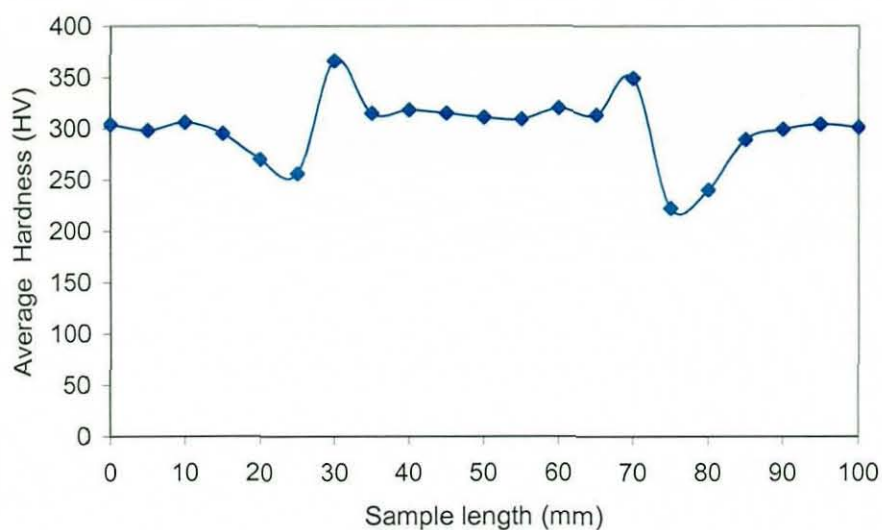
10.9 Summary

This chapter presented the results of high temperature X-ray diffraction experiments, which were performed on ductile iron alloys. At the start of the chapter, the concept of X-ray fluorescence was introduced. When this effect was combined with high temperature X-ray diffraction measurements, it was thought that the resulting intensity of experimental data would not be sufficient to obtain accurate results. Therefore, modifications to the slit configuration of the X-ray diffractometer were performed. These changes boosted the diffraction intensity data without significantly lowering the quality of the data obtained.

The specimen area exposed to incident radiation during the X-ray diffraction experiments was also calculated. Importantly, it was demonstrated that the incident X-ray beam only interacted with a section of the sample that was at a uniform temperature for all the measurements performed in this work. A method was also introduced that enabled the volume fractions of the bainitic ferrite and austenite present in the sample to be calculated from high temperature X-ray diffraction data.

Experiments were performed on alloys 3, 4 and 6 to determine their phase boundary temperatures. Oxidation of the samples during exposure at high temperatures was shown to have an important influence on the results of these

investigations, However, in alloys 4 and 6 reproducible measurements were made on different samples, demonstrating that consistent measurements could be obtained during high temperature X-ray diffraction experiments. The major oxide phases present on the different alloys were also identified.

Austenitisation experiments were performed on alloys 1 and 5. These experiments showed that during austenitisation, the austenite C content reached equilibrium values very quickly at all the temperatures of interest. The austenite lattice parameter was also found to increase with austenitisation temperature due to the higher concentrations of C present in these alloys, which agrees with what should be theoretically expected. Again, reproducibility of the results was demonstrated. Different methods were used to calculate the ambient austenite lattice parameter from the high temperature X-ray diffraction data, and hence estimate the austenite C content. These values were compared to MTDATA estimates of the austenite C content. For both alloys, the most accurate results were obtained when the Dyson and Holmes relationship [155] was used to estimate the austenite C content and the ambient austenite lattice parameter was calculated using the thermal expansion coefficient proposed by Choi *et al.* [153].

In the final section of this work high temperature X-ray diffraction measurements were performed on samples 1 and 5. Due to the limited cooling rate imposed by the X-ray diffractometer temperature control unit (see section 9.4), ADI could not be produced in alloy 1. However, alloy 5 contained higher concentrations of alloying elements. This enabled ADI to be produced in these alloys. The important influence of decarburisation was demonstrated by the results of these investigations, which showed that a thin ferrite film formed on cooling to the austempering temperature after the austenitisation heat treatment due to decarburisation. The presence of this film boosted the diffraction intensity of the ferrite phase during austempering, producing results that were not applicable to the bulk of the sample. The influence of the ferrite film prevented accurate phase volume fraction predictions being calculated from the peak intensity data. However, this did not prevent the austenite lattice parameter and hence the austenite C content from being measured during austempering, (although it is also possible that decarburisation influenced these values).

The austenite C content was shown to increase during austempering before remaining stable through the processing window in all the samples. The experimental

results regarding transformation time were also in agreement with what was expected since the time needed to complete stage 1 of austempering increased as the austempering temperature was reduced. The time that the maximum austenite C content was reached in the samples was also shown to be in good agreement with the stage 1 transformation time predicted by the kinetic model introduced in chapter 8. The samples austempered at lower temperatures were found to contain higher austenite C contents which again is the expected behaviour. However, small quantities of pearlite were observed in all the alloy 5 samples. Therefore some doubt exists as to the accuracy of these results. The calculated room temperature austenite C contents were all shown to be above their theoretical maximum values of X_{T0}, although further work is required in this area.

11 Conclusions

The influence of alloy composition, and both heat treatment temperatures and times, on the resulting microstructure and mechanical properties of ADI alloys has been discussed in chapter 2, highlighting the complex nature of these alloys. Chapter 3 highlighted the concepts behind MTDATA, a computer program used throughout this work that is capable of predicting equilibrium in multi component systems. It was also demonstrated how slave applications, which are powerful computer programs written in Fortran, can be combined with MTDATA enabling more complex phase transformations to be modelled. It was also shown that MTDATA can be used to make accurate predictions of phase boundaries in Fe-C-Si systems.

The microstructural analysis of a chilled cast ductile iron camshaft cam lobe in chapter 4 revealed that the large carbides present in the alloy were cementite. Cementite was found to be present throughout the whole of the cam lobe, although its quantity reduced towards the centre of the component. A model was then developed that was capable of predicting the influence of chemical composition on the chill tendency of ductile iron alloys, via calculations of equilibrium and metastable eutectic temperatures. These predictions were shown to be in agreement with experimental observations on a wide range of irons. When these predictions were combined with Magmasoft cooling curve calculations for the chilled ductile iron cam lobe, it was shown that the resulting microstructure of the cam lobe could be explained by the combination of the cooling curve data with the phase boundary predictions calculated by the model.

In chapter 5 a model capable of predicting the microstructure and simple mechanical properties of ADI alloys, was shown to produce reasonably accurate results when compared to a large range of experimental measurements taken from literature. Chapter 6 analysed these predictions in more detail, showing that inaccuracies in some predictions made by the model could be related to the closure of the processing window and the precipitation of carbides at high and low austempering temperatures respectively.

Chapter 7 showed how the Scheil approach could be used to predict the segregation that occurs upon solidification in ADI alloys. Experimental data obtained using SEM analysis that displayed the total extent of alloying element segregation in the materials was collected. Comparisons of these experimental data to the calculated segregation profile proved them to be accurate. Therefore the influence of

alloying element segregation was successfully incorporated into the microstructure model.

The segregation profiles calculated by the model presented in chapter 7 were used as a basis to predict the local microstructural austempering kinetics in chapter 8. A model originally developed for steels [112;114] was adapted for ADI alloys. Crucially, the model used MTDATA to calculate the local driving force for the transformation, and therefore was capable of accounting for the influence of all the elements in the alloys. The transformation times for stage 1 of austempering were shown to be in good agreement with dilatometry, image analysis and X-ray diffraction measurements. Importantly, the model showed a clear difference in the transformation rate of material as a function of alloying element segregation. This is in agreement with literature observations and is one of the issues that has slowed the adoption by industry of these alloys, since it makes them difficult to heat treat correctly [2;15]. It was also shown how the model could be used to investigate the influence of individual alloying elements on the rate of the austempering transformation.

Chapter 8 also showed that the critical driving force needed for martensite formation to take place can be calculated using a method found in literature [125]. A model was developed that used MTDATA to calculate this driving force as a function of temperature, hence allowing for all of the elements present in ADI alloys. The model then compared the calculated driving force values to the critical driving force, therefore determining the temperature at which it exceeded the critical value. Hence the model could calculate the martensite start temperature as a function of alloy composition. This method for calculating the martensite start temperature was shown to be an improvement over the routine used in the original model when they were both compared to a wide range of measurements obtained from literature, and therefore was incorporated into the model.

The improvements to the microstructure model shown in chapters 7 and 8 were incorporated into a new model version. Hence it can be seen that substantial modifications to the original microstructure model were developed in this work. The improved model for example allows generic investigations to be made on the influence of alloying element segregation on local transformation rates and martensite start temperatures in ADI alloys. These important improvements

demonstrate the models capability to be used as a useful tool in new alloy development or alloy troubleshooting in industry.

Chapter 9 introduced high temperature X-ray diffraction, highlighting the development of this experimental technique from its early stage until the current day. An explanation of some of the testing and improvements that were performed during this work is also included. These developments to the high temperature X-ray diffraction technique had to be performed before any useful experimental data could be obtained. The results of preliminary experiments on ductile iron alloys were also presented, showing how the accurate measurement of temperature was established for future experiments.

Details of high temperature X-ray diffraction experiments were presented in chapter 10. A series of experiments were performed on ductile iron alloys which showed the important influence of oxidation on the results obtained. The formation of oxide films on the sample was shown to mask the presence of small quantities of phases in the samples. Decarburisation during these experiments could also have influenced the results.

The austenitisation heat treatment was monitored using high temperature X-ray diffraction on two ductile iron alloys. These experiments showed that equilibrium was reached between the austenite C content and graphite during austenitisation in a short period of time, at temperatures between 900-1000°C. Good reproducibility was also achieved during these experiments, although decarburisation of the samples during austenitisation could have affected these measurements. Measurement of the austenite lattice parameter during these experiments enabled the austenite C content of the alloys to be estimated as a function of temperature. The estimated values of the austenite C contents were shown to differ in value dependent mainly on the thermal expansion coefficients used to calculate them.

A series of austempering experiments were performed on alloy 5 using high temperature X-ray diffraction. Evidence was presented that showed decarburisation of the surface of the sample during austenitisation resulted in the formation of ferrite across some areas of the sample surface on cooling to the austempering temperature. The role of decarburisation on the results obtained in these investigations was important. It lead to the amplification of the ferrite intensity measurements with respect to those of austenite, due to the large volumes of ferrite in the surface layers. However, the austenite lattice parameter could still be

monitored and hence the austenite C content could be measured as a function of austempering time during the experiments, (although decarburisation could also have influenced these values). The microstructure of the samples below the surface layers was generally typical of that observed in ADI alloys, although a small volume of pearlite was observed in the alloys. However, all the room temperature austenite C contents of the samples were shown to be above the limiting austenite C content X_{T0} as were the high temperature measurements. Further work is required to improve the measurements obtained using this technique.

12 Future Work

Some issues, which could be addressed in future modifications of the microstructure model in the hope of further improving the microstructure predictions are discussed in this chapter. Segregation of alloying elements upon solidification in the current work was modelled using the Scheil approach. A slight improvement could occur if back diffusion was incorporated into the segregation stage of the modelling process, although the method outlined in chapter 7 produced very good results. This would allow elements to diffuse back across the advancing solidification interface, which is not currently allowed in the present model version, therefore produce a more modest segregation profile, which could produce a small improvement in agreement with experimental measurements. The influence of nodule count also plays a role in the degree of segregation observed in ductile iron alloys. A high nodule count reduces the mean inter nodule distance and therefore limits alloying element segregation in ductile iron alloys [159]. Incorporating nodule count information into the segregation predictions should therefore improve model calculations. This could be performed by multiplying the segregation profile obtained by a factor which was inversely proportional to the nodule count, because as the nodule count increases, the severity of segregation reduces [159].

In steels, bainitic ferrite tends to nucleate on prior austenite grain boundaries. However, in ADI alloys as shown in figure 8.1, nucleation of bainitic ferrite also occurs from the interface between the matrix and graphite nodules. Therefore as previously mentioned in section 8.2.2, the transformation kinetics model could be adjusted to incorporate nodule count into the nucleation rate expression.

The kinetic model predictions in the current model are limited to the first stage of austempering only. However, heat treaters are also interested in the time span of the processing window, since this is the time period during austempering where ADI alloys display their optimum mechanical properties. Therefore, an important addition to the current model would be the calculation of the size of the processing window. This concept could be further extended to predictions of austenite dissolution during stage 2 of austempering.

The model does not take into account the cooling rate between the austenitisation and austempering temperatures. As demonstrated in chapter 10, a reasonably fast cooling rate can still result in pearlite formation in ADI alloys. This can be a problem especially in large section castings, where the cooling rate is slower in the centre of large components. Therefore, it would be advantageous to produce a

model that could predict the critical cooling rate needed to avoid pearlite formation in ADI alloys. Models exist that are capable of producing TTT and CCT diagrams for steels [117;156]. However, ADI alloys generally contain much higher C contents than steels and therefore it would have to be investigated whether or not these models were appropriate for ADI alloys.

Another modification to the microstructure model regards the precipitation of carbides during austempering. ADI alloys contain high Si concentrations, which for most austempering regimes suppress carbide precipitation. However, at lower austempering temperatures, the precipitation of carbides does occur [14;40;157]. The carbides reduce the ductility of ADI alloys, so the toughness of the irons is reduced. Therefore their presence in ADI alloys is important, particularly in respects of their mechanical properties, hence modelling of their precipitation could be beneficial for this purpose. However, it is not thought that the precipitation of carbides has much influence on the current microstructure model results regarding phase volume fraction predictions.

Another important issue concerning ADI alloys is the measurement of the austenite C content during austempering. Theoretically, bainitic ferrite formation should cease when the limiting austenite C content, X_{T0} is reached in ADI alloys. However, many X-ray measurements of the austenite C content at the end of the first stage of austempering have shown austenite C contents to above X_{T0} [15;21;22;157]. The most popular explanation for this anomaly is that X-ray diffraction typically over estimates the C content of the austenite. On quenching to room temperature martensite forms from austenite that has not been enriched enough with C. The remaining austenite therefore has an artificially high C content due to the formation of the martensite [84]. This explanation is acceptable for certain alloys, but is not generally applicability for the majority of experimental measurements of the austenite C content, because if ADI alloys are produced from a carefully selected composition and subjected to the correct heat treatment regime then martensite formation should be avoided, or at worst limited to an insignificant volume fraction.

High temperature X-ray diffraction experiments could be a useful tool to test this hypothesis, because in situ measurements of the austenite C content during austempering, would allow a direct comparison to be made with the calculated austenite C content X_{T0}, without any discrepancies from the formation of martensite. However, as shown in chapter 10, the current experimental setup would need to be

modified to allow increased cooling of the sample, or alternatively an alloy specifically designed to have increased hardenability could be used, hence avoiding pearlite formation on cooling to the austempering temperature, before conclusive experimental data could be obtained.

References

1. D.R. Askeland, The Science and Engineering of Materials, Chapman and Hall, 3rd edition, (1988).

2. R. Elliott, Cast Iron Technology, Butterworths, (1988).

3. A. K.Sinha, Ferrous Physical Metallurgy, Butterworths, (1989).

4. J. Hemanth, Effect of Cooling Rate on Dendrite Arm Spacing (DAS), Eutectic Cell Count (ECC) and Ultimate Tensile Strength (UTS) of Austempered Chilled Ductile Iron, *Materials and Design*, Vol. **21**, pp 1-8, (2001).

5. J. Liu and R. Elliott, Numerical Model for Microsegregation in Ductile Iron, *Materials Science and Technology*, Vol. **14**, pp 1127-1131, (1998).

6. J. Liu and R. Elliott, The Influence of Cast Structure on the Austempering of Ductile Iron. Part 2: Assessment of Model Calculations of Microsegregation, *International Journal of Cast Metals Research*, Vol. **12**, pp 75-82, (1999).

7. R. Boeri and F. Weinberg, Microsegregation in Ductile Iron, *AFS Transactions*, Vol. **97**, pp 179-184, (1990).

8. G. Rivera, R. Boeri, and J. Sikora, Revealing and Characterising Solidification Structure of Ductile Cast Iron, *Materials Science and Technology*, Vol. **18**, pp 691-697, (2002).

9. D.J. Moore, T.N. Rouns, and K.B. Rundman, The Relationship Between Microstructure and Tensile Properties in Austempered Ductile Irons, *AFS Transactions*, Vol. **95**, pp 765-774, (1987).

10. A. Rimmer, ADI is Growing, *Materials World*, pp 252-255, (May, 1997).

11. S. Korichi and R. Priestner, High Temperature Decomposition of Austempered Microstructures in Spheroidal Graphite Cast Iron, *Materials Science and Technology*, Vol. **11**, pp 901-907, (1995).

12. J.S. James and R.C. Thomson, Microstructural Modelling of Austempered Ductile Iron, pp 47-60, *Proceedings of Castcon 98*, Bournemouth UK, (1998).

13. M. Croker, ADI-New Solutions to Component Engineering, *Metallurgia (UK)*, Vol. **64**, pp 220-222, (1997).

14. E. Dorazil, B. Barta, E. Munsterova, L. Stransky, and A. Huvar, High-Strength Bainitic Ductile Cast Iron, *AFS International Cast Metals Journal*, Vol. **7**, pp 52-62, (1982).

15. N. Darwish and R. Elliott, Austempering of Low Manganese Ductile Irons Part 1: Processing Window, *Materials Science and Technology*, Vol. **9**, pp 572-585, (1993).

16. H.K.D.H. Bhadeshia, Bainite in Steels, The Institute of Materials, 1st edition, (1992).

17. M. Bahmani and R. Elliott, Effects of Pearlite Formation on Mechanical Properties of Austempered Ductile Iron, *Materials Science and Technology*, Vol. **10**, pp 1068-1072, (1994).

18. R. Harding, Austempered Ductile Iron Components, Advantages, Production, Properties and Specification, Unpublished work, BCIRA, (2000).

19. M. Grech and J.M. Young, Effects of Austenitising Temperature on the Tensile Properties of Cu-Ni Austempered Ductile Iron, *Materials Science and Technology*, Vol. **6**, pp 415-421 (1990).

20. J.S. James, PhD Thesis, The Microstructural Modelling of Austempered Ductile Iron, Loughborough University, (2000).

21. A. Kutsov, Y. Taran, K. Uzlov, A. Krimmel, and M. Evsyukov, Formation of Bainite in Ductile Iron, *Materials Science and Engineering A*, Vol. **273-275**, pp 480-484, (1999).

22. T.N. Rouns and K.B. Rundman, Constitution of Austempered Ductile Iron and Kinetics of Austempering, *AFS Transactions*, Vol. **95**, pp 851-874, (1987).

23. A.S. Hamid Ali and R. Elliott, Austempering of an Mn-Mo-Cu Alloyed Ductile Iron Part 1: Austempering Kinetics and Processing Window, *Materials Science and Technology*, Vol. **12**, pp 679-690, (1996).

24. S. Yazdani and R. Elliott, Influence of Molybdenum on Austempering Behaviour of Ductile Iron: Part 1: Austempering Kinetics and Mechanical Properties of Ductile Irons Containing 0.13%Mo, *Materials Science and Technology*, Vol. **15**, pp 531-540, (1999).

25. M. Yan and W.Z. Zhu, Morphology of Bainitic Plates of Austempered Ductile Iron and Their Effects on Mechanical Properties, *Journal of Materials Science Letters*, Vol. **15**, pp 1044-1047, (1996).

26. H.K.D.H. Bhadeshia, Bainite in Steels, IOM Communications Ltd, 2nd edition, (2001).

27. H.K.D.H. Bhadeshia and J.W. Christian, Bainite in Steels, *Metallurgical Transactions A*, Vol. **21**, pp 767-797, (1990).

28. V. Franetovic, M.M. Shea, and E.F. Ryntz, Transmission Electron Microscopy of Austempered Nodular Iron: Influence of Silicon Content, Austenitizing Time and Austempering Temperature, *Materials Science and Engineering*, Vol. **96**, pp 231-245, (1987).

29. J. Achary and D. Venugopalan, Microstructural Development and Austempering Kinetics of Ductile Iron During Thermomechanical Processing, *Metallurgical and Materials Transactions A*, Vol. **31**, pp 2575-2585, (2000).

30. L. Sidjanin and R.E. Smallman, Metallography of Bainitic Transformation in Austempered Ductile Iron, *Materials Science and Technology*, Vol. **8**, pp 1095-1103, (1992).

31. C.M. Burke, D.J. Moore, and K.B. Rundman, Ausforming Austempered Ductile Iron, *AFS Transactions*, Vol. **106**, pp 91-97, (1998).

32. J. Mallia, M. Grech, and R.E. Smallman, Effect of Silicon Content on Transformation Kinetics of Austempered Ductile Iron, *Materials Science and Technology*, Vol. **14**, pp 452-460, (1998).

33. R.W.K. Honeycombe and H.K.D.H. Bhadeshia, Steels - Microstructure and Properties, Edward Arnold, 2nd edition, (1995).

34. P.F. Wieser, Mechanism of Graphite Formation, Ann Arbor Press, (1967).

35. C.R. Loper, Jr, Inoculation of Cast Iron - Summary of Current Understanding, *AFS Transactions*, Vol. **107**, pp 523-528, (1999).

36. R. Barton, Graphite-Nodule Number and Distribution-Their Effects on Nodular-Graphite Iron Castings, *Foundry Trade Journal*, pp 117-126, (February 1985).

37. J. Desimoni, R. Gregorutti, K. Laneri, J.L. Sarutti, and R.C. Mercader, Influence of the Mn Content on the Kinetics of Austempering Transformation in Compacted Graphite Cast Iron, *Metallurgical and Materials Transactions A*, Vol. **30**, pp 2745-2752, (1999).

38. J. Liu and R. Elliott, The Influence of Cast Structure on the Austempering of Ductile Iron, *International Journal of Cast Metals Research*, Vol. **11**, pp 407-412, (2003).

39. L. Sidjanin, R.E. Smallman, and J.M. Young, Electron Microstructure and Mechanical-Properties of Silicon and Aluminium Ductile Irons, *Acta Metallurgica et Materialia*, Vol. **42**, pp 3149-3156, (1994).

40. W.J. Dubensky and K.B. Rundman, An Electron Microscope Study of Carbide Formation in Austempered Ductile Iron, *AFS Transactions*, Vol. **93**, pp 389-394, (1995).

41. S. Yazdani and R. Elliott, Influence of Molybdenum on Austempering Behaviour of Ductile Iron, Part 4: Austempering Behaviour of Ductile Iron Containing 0.45%Mo, *Materials Science and Technology*, Vol. **15**, pp 896-902, (1999).

42. M. Nili Ahmadabadi, E. Niyama, M. Tanino, T. Abe, and T. Ohide, Chemical Composition and Structural Identification of Eutectic Carbide in 1 Pct Mn Ductile Iron, *Metallurgical and Materials Transactions A*, Vol. **25**, pp 911-918, (1994).

43. M. Nili Ahmadabadi, E. Niyama, and J. Echigoya, Transmission Electron Microscopy Study of High Temperature Bainitic Transformation in 1 wt.% Mn Ductile Iron, *Materials Science and Engineering A*, Vol. **194**, pp 87-98, (1995).

44. J. Aranzabal, I. Gutierrez, J.M. Rodriguez-Ibabe, and J.J. Urcola, The Influence of Heat Treatments on the Microstructure and Toughness of Austempered Ductile Iron, *Materials Science and Technology*, Vol. **8**, pp 263-274, (1992).

45. H.L. Yakel, Crystal Structures of Stable and Metastable Carbides, *International Metals Review*, Vol. **30**, pp 17-40, (1985).

46. M. Gage and P.A. Fallon, Microstructural Characteristics of Bainitic Ductile Irons, *Canadian Metallurgical Quarterly*, Vol. **25**, pp 79-90, (1986).

47. D. Krishnaraj, H.N.L. Narasimhan, and S. Seshan, Structure and Properties of ADI as Affected by Low Alloy Additions, *AFS Transactions*, Vol. **100**, pp 105-112, (1992).

48. B. Bosnjak, B. Radulovic, K. Pop-Tonev, and V. Asanovic, Influence of Microalloying and Heat Treatment on the Kinetics of Bainite Reaction in Austempered Ductile Iron, *Journal of Materials Engineering and Performance*, Vol. **10**, pp 203-211, (2001).

49. N. Darwish and R. Elliott, Austempering of Low Manganese Ductile Irons Part 2: Influence of Austenitising Temperature, *Materials Science and Technology*, Vol. **9**, pp 586-602, (1993).

50. W.D. Callister Jr, Fundamentals of Materials Science and Engineering, Wiley, 5th edition, (2001).

51. N. Darwish and R. Elliott, Austempering of Low Manganese Ductile Irons Part 3: Variation of Mechanical Properties with Heat Treatment, *Materials Science and Technology*, Vol. **9**, pp 882-889, (1993).

52. P. Prasad Rao and S.K. Putatunda, Influence of Microstructure on Fracture Toughness of Austempered Ductile Iron, *Metallurgical and Materials Transactions A*, Vol. **28**, pp 1457-1470, (1997).

53. R. Kazerooni, A. Nazarboland, and R. Elliott, Use of Austenitising Temperature in Control of Austempering of an Mn-Mo-Cu Alloyed Ductile Iron, *Materials Science and Technology*, Vol. **13**, pp 1007-1015, (1997).

54. D.J. Moore, T.N. Rouns, and K.B. Rundman, Structure and Mechanical Properties of Austempered Ductile Iron, *AFS Transactions*, Vol. **93**, pp 705-718, (1985).

55. K.L. Hayrynen, S.M. Loftus, R.L. May, D.J. Moore, and K.B. Rundman, Microstructural Study of Ausformed-Austempered Ductile Iron, *AFS Transactions*, Vol. **103**, pp 157-163, (1995).

56. ASTM A897M, Standard Specification for Austempered Ductile Iron Castings, ASTM International, (1990).

57. A.K. McDonald, Chill-Cast Camshaft Developments, *Foundry Trade Journal*, pp 416-422, (October 1986).

58. R.H. Davies, A.T. Dinsdale, T.G. Chart, T.I. Barry, and M.H. Rand, Application of MTDATA to the Modelling of Multicomponent Equilibria, *High Temperature Materials*, Vol. **26**, pp 251-262, (1989).

59. R.H. Davies, A.T. Dinsdale, J.A. Gisby, J.A.J. Robinson, S.M. Martin, MTDATA - Thermodynamic and Phase Equilibrium Software from the National Physical Laboratory, National Physical Laboratory, (2002).

60. J. Gisby, H. Davies, A. Dinsdale, J. Robinson, P. Quested, and A. Gibbon, MTDATA User Group Meeting Number 12, National Physical Laboratory (2000).

61. N. Saunders and A.P. Miodownik, CALPHAD, Calculation of Phase Diagrams, A Comprehensive Guide, Pergamon, (1998).

62. B. Sundman, TCFE Database, *supplied by TCAB for use with MTDATA*, Version 1.0, (2001).

63. A. Dinsdale, J. Gisby, and J. Robinson, MTDATA Introductory Course, National Physical Laboratory, (2000).

64. J.E. Hillard and W.S. Owen, A Thermal and Microscopic Study of the Iron-Carbon-Silicon System, *Journal of the Iron and Steel Institute*, Vol. **172**, pp 268-282, (1952).

65. P.F. Wieser, C.E. Bates, J.F. Wallace, Mechanism of Graphite Formation in Iron-Silicon-Carbon Alloys, *Malleable Founders Society*, (1967).

66. A. Lapish, Product Development Report, *Report No. 167/ACDI/C060*, Federal Mogul, (1999).

67. A. Lapish, Product Development Report, *Report No. 169/ACDI/C268*, Federal Mogul, (2000).

68. A. Lapish, Visit Report, *Report No. VF/04/99*, Federal Mogul, (1999).

69. B.D. Cullity, Elements of X-ray Diffraction, Addison-Wesley, 2nd edition, (1978).

70. JCPDS Powder Diffraction File, International Centre for Diffraction Data, (2000).

71. T. Bex, Chill Specimen Structure Tells Iron Properties, Part 3 of 3, *Modern Casting*, pp 48, (May 1991).

72. E.J. Kubric, A. Javid, and F.J. Bradley, Investigation of the Effects of C, Si, Mn, S and P on Solidification Characteristics and Chill Tendency of Gray Iron-Part 1: Thermal Analysis Results, *AFS Transactions*, Vol. **105**, pp 573-578, (1997).

73. M. Booth, Thermal Analysis for Composition Determination of Grey Cast Irons, *The British Foundryman*, Vol. **76**, pp 35-45, (1983).

74. R.W. Heine, Carbon, Silicon, Carbon Equivalent, and Thermal Analysis Relationships in Gray and Ductile Cast Irons, *AFS Transactions*, Vol. **81**, pp 462-470, (1973).

75. W. Donald and A. Moore, Significance of Carbon Equivalent Formulae and Their Applications in the Foundry, *Report No. 1128*, BCIRA, (1973).

76. D.M. Stefanescu, F. Martinez, and I.G. Chen, Solidification Behaviour of Hypoeutectic and Eutectic Compacted Graphite Cast Irons, Chilling Tendency and Eutectic Cells, *AFS Transactions* Vol. **91**, pp 205-216, (1983).

77. R.W. Heine. Austenite Liquidus, Carbide Eutectic and Undercooling in Process Control of Ductile Base Iron, *AFS Transactions*, Vol. **103**, pp 199-206, (1995).

78. U. Ekpoom and R.W. Heine, Metallurgical Processing Variables Affecting the Solidification of Malleable Based White Cast Iron, *AFS Transactions*, Vol. **89**, pp 1-14, (1981).

79. Principles of Thermal Analysis and Calorimetry, Edited by P.J. Haines, Royal Society of Chemistry, 1st edition, (2002).

80. R.F. Speyer, Thermal Analysis of Materials, Marcel Dekker, 1st edition, (1994).

81. G. Van der Plaats, The Practice of Thermal Analysis, Mettler Toledo, 1st edition, (1992).

82. Magmasoft Computer Program, Magma GmbH, (2000). http://www.magmasoft.com last viewed September 2003.

83. T. Takahashi, T. Abe, and S. Tada, Effect of Bainite Transformation and Retained Austenite on Mechanical Properties of Austempered Spheroidal Graphite Cast Steel, *Metallurgical Transactions A*, Vol. **27**, pp 1589-1598, (1996).

84. R. Le Hoillier, G. Begin, and A. Dube, A Study of Peculiarities of Austenite During the Formation of Bainite, *Metallurgical Transactions A*, Vol. **2**, pp 2645-2653, (1971).

85. K.W. Andrews, Empirical Formulae for the Calculation of Some Transformation Temperatures, *Journal of the Iron and Steel Institute*, Vol. **203**, pp 721-727, (1965).

86. A.S. Hamid Ali, K.I. Uzlov, N. Darwish, and R. Elliott, Austempering of Low Manganese Ductile Irons Part 4: Relationship Between Mechanical Properties and Microstructure, *Materials Science and Technology*, Vol. **10**, pp 35-40, (1994).

87. A.S. Hamid Ali and R. Elliott, Austempering of Mn-Mo-Cu Alloyed Ductile Iron Part 2: Mechanical Properties, *Materials Science and Technology*, Vol. **13**, pp 24-30, (1997).

88. D.J. Moore, T.N. Rouns, and K.B. Rundman, Effect of Manganese on Structure and Properties of Austempered Ductile Iron: A Processing Window Concept, *AFS Transactions*, Vol. **94**, pp 255-264, (1986).

89. H. Bayati, R. Elliott, and G.W. Lorimer, Influence of Austenitising Temperature on Austempering Kinetics of High Manganese Alloyed Ductile Cast Iron, *Materials Science and Technology*, Vol. **11**, pp 776-786, (1995).

90. J. Aranzabal, I. Gutierrez, and J.J. Urcola, Influence of Heat Treatments on Microstructure of Austempered Ductile Iron, *Materials Science and Technology*, Vol. **10**, pp 728-737 (1994).

91. J. Aranzabal, I. Gutierrez, M. Rodriguez-Ibade, and J.J. Urcola, Influence of the Amount and Morphology of Retained Austenite on the Mechanical Properties of an Austempered Ductile Iron, *Metallurgical and Materials Transactions A*, Vol. **28**, pp 1143-1156, (1997).

92. M. Gagne, The Influence of Manganese and Silicon on the Microstructure and Tensile Properties of Austempered Ductile Iron, *AFS Transactions*, Vol. **93**, pp 801-812, (1985).

93. M. Nili Ahmadabadi, T. Ohide, and E. Niyama, Effects of Successive-Stage Austempering on the Structure and Impact Strength of High-Mn Ductile Iron, *Cast Metals*, Vol. **5**, pp 62-72, (1992).

94. P. Prasad Rao and S.K. Putatunda. Comparitive Study of Fracture Toughness of Austempered Ductile Irons with Upper and Lower Ausferrite Microstructures, *Materials Science and Technology*, Vol. **14**, pp 1257-1265, (1998).

95. S. Yazdani and R. Elliott, Influence of Molybdenum on Austempering Behavior of Ductile Iron Part 3: Austempering Kinetics, Mechanical Properties, and Hardenability of Ductile Iron Containing 0.25%Mo, *Materials Science and Technology*, Vol. **15**, pp 855-895, (1999).

96. R.C. Thomson, J.S. James, and D.C. Putman, Modelling of Microstructural Evolution and Mechanical Properties of Austempered Ductile Iron, *Materials Science and Technology*, Vol. **16**, pp 1412-1419, (2000).

97. C.H. Young and H.K.D.H. Bhadeshia, Strength of Mixtures of Bainite and Martensite, *Materials Science and Technology*, Vol. **10**, pp 209-214, (1994).

98. W.C. Leslie, Iron and its Dilute Substitutional Solid Solutions, *Metallurgical Transactions*, Vol. **3**, pp 5-26, (1972).

99. G. Langford and M. Cohen, Calculation of Cell-Size Strengthening of Drawn Wire, *Metallurgical Transactions*, Vol. **1**, pp 1478-1480, (1970).

100. S.B. Singh and H.K.D.H. Bhadeshia, Estimation of Bainite Plate Thickness in Low-Alloy Steels, *Materials Science and Engineering A*, Vol. **245**, pp 72-79, (1998).

101. S.A. Khan and H.K.D.H. Bhadeshia, The Bainite Transformation in Chemically Heterogeneous 300M High-Strength Steel, *Metallurgical Transactions A*, Vol. **21**, pp 859-875, (1990).

102. L. Nastac and D.M. Stefanescu, Modelling of Microsegregation in SG Cast Iron, *AFS Transactions*, Vol. **101**, pp 933-938, (1993).

103. J. Mallia and M. Grech, Effect of Silicon Content on Impact Properties of Austempered Ductile Iron, *Materials Science and Technology*, Vol. **13**, pp 408-414, (1997).

104. R.E. Reed-Hill, Physical Metallurgy Principles, PWS-KENT, 3rd edition, (2001).

105. D.A. Porter and K.E. Easterling, Phase Transformations in Metals and Alloys, Chapman and Hall, (1992).

106. Energy-Dispersive X-ray Microanalysis, Edited by D. Vaughan, Kevex Corporation, (1993).

107. K.L. Hayrynen, D.J. Moore, and K.B. Rundman, Heavy Section Ductile Iron: Production and Microsegregation, *AFS Transactions*, Vol. **96**, pp 619-632, (1988).

108. L.V. Kostyleva, V.A. Ilyinski, and A.A. Zhukov, Microsegregation of Silicon in Iron-Carbon Alloys, *Cast Metals*, Vol. **5**, pp 109-113 (1992).

109. A.A. Zhukov, Thermodynamics of Microsegregation and Influence of Elements on Structure of Unalloyed and Alloyed Cast Iron, *Metal Science*, Vol. **12**, pp 521-524, (1978).

110. I. Minkoff, *The Physical Metallurgy of Cast Iron*, John Wiley and Sons, (1983).

111. H.K.D.H. Bhadeshia, Bainite: Overall Transformation Kinetics, *Journal de Physique*, Vol. **43**, pp 443-448, (1982).

112. G.I. Rees and H.K.D.H. Bhadeshia, Bainite Transformation Kinetics Part 1 Modified Model, *Materials Science and Technology*, Vol. **8**, pp 985-993, (1992).

113. G.I. Rees and H.K.D.H. Bhadeshia, Bainite Transformation Kinetics Part 2 Non-Uniform Distribution of Carbon, *Materials Science and Technology*, Vol. **8**, pp 994-996, (1992).

114. N.A. Chester and H.K.D.H. Bhadeshia, Mathematical Modelling of Bainite Transformation Kinetics, *Journal de Physique IV*, Vol. **7**, pp 41-46, (1997).

115. N.A. Chester, Mathematical Modelling of Microstructural Development in Continuously Annealed High-Strength Steels, PhD Thesis, University of Cambridge, (1997).

116. L. Vassileva, Private Communication to Prof. R.C. Thomson, (1995).

117. Materials Algorithms Project Website, Phase Transformations Research Group, University of Cambridge and National Physical Laboratory, Teddington, UK, (2003).
http://www.msm.cam.ac.uk/map *last viewed September 2003.*

118. ASTM E562-89, Standard Test Method for Determining Volume Fraction by Systematic Manual Point Count, ASTM International, (1992).

119. D.T. Llewellyn and R.C. Hudd, Steels Metallurgy and Applications, Butterworth-Heinemann, 3rd edition, (1998).

120. H.K.D.H. Bhadeshia, Driving Force for Martensitic Transformation in Steels, *Metal Science*, Vol. **15**, pp 175-177, (1981).

121. H.K.D.H. Bhadeshia, Thermodynamic Extrapolation and Martensite-Start Temperature of Substitutionally Alloyed Steels, *Metal Science*, Vol. **15**, pp 178-180, (1981).

122. C. Zener, Kinetics of the Decomposition of Austenite, *Transactions of the Metals Society of the AIME*, Vol. **167**, pp 550-595, (1946).

123. J.C. Fisher, The Free Energy Change Accompanying the Martensite Transformation in Steels, *Metals Transactions*, Vol. **185**, pp 688-690, (1949).

124. G. Ghosh and G.B. Olson, Kinetics of F.C.C. > B.C.C. Heterogeneous Martensitic Nucleation-1, The Critical Driving Force for Athermal Nucleation, *Acta Metallurgica et Materialia*, Vol. **42**, pp 3361-3370, (1993).

125. T. Cool and H.K.D.H. Bhadeshia, Prediction of Martensite Start Temperature of Power Plant Steels, *Materials Science and Technology*, Vol. **12**, pp 40-44, (1996).

126. T. Cool, MAP_STEEL_MS Computer Program, Materials Algorithms Project Website, Phase Transformations Research Group, University of Cambridge and National Physical Laboratory, Teddington, UK, (1996). http://www.msm.cam.ac.uk/map/steel/programs/ms-b.html last viewed September 2003.

127. Atlas of Time-Temperature Diagrams for Irons and Steels, ASM International, (1991).

128. K.G. Tembwe, Microstructure Modelling of Cast Iron Camshafts, MSc Thesis, Loughborough University, (1996).

129. R. Jenkins, X-ray Fluorescence Spectrometry, John Wiley and Sons, 2nd edition, (1999).

130. M. von Laue, *Jahrbuch der Radioaktivität und Elektronik*, Vol. **9**, pp 308, (1912).

131. W.L. Bragg, *Proceeding of the Cambridge Philosophy Society*, Vol. **17**, pp 43, (1912).

132. A. Westgren, Roentgen Spectrographic Investigations of Iron and Steel, *Journal of the Iron and Steel Institute*, Vol. **103**, pp 303-325, (1921).

133. K. Becker, *Zeithschrift für Physik*, Vol. **40**, pp 37, (1927).

134. H.J. Goldschmidt, High Temperature Methods, Chapter 9 of X-ray Diffraction by Polycrystalline Materials, Edited by H.S.Peiser, H.P.Rooksby, A.J.C.Wilson, Chapman and Hall, pp 249-264, (1960).

135. Z.S. Basinski, W. Hume-Rothery, F.R.S. Sutton, and A.L. Sutton, The Lattice Expansion of Iron, *Proceedings of the Royal Society, Series A*, Vol. **229**, pp 459-467, (1955).

136. H.J. Goldschmidt, Selected Applications of High Temperature X-ray Studies in the Metallurgical Field, *Advances in X-ray Analysis*, Vol. **5**, pp 191-212, (1962).

137. H.J. Goldschmidt, A High Temperature X-ray Study on High-speed Steel, *Journal of the Iron and Steel Institute*, Vol. **186**, pp 68-85, (1957).

138. H.J. Goldschmidt, An X-ray High Temperature Oxidation Study on Iron-Copper, *Journal of the Iron and Steel Institute*, Vol. **196**, pp 390-393, (1960).

139. N. Ridley and H. Stuart, Partial Molar Volumes from High-Temperature Lattice Parameters of Iron-Carbon Austenites, *Metal Science Journal*, Vol. **4**, pp 219-222, (1970).

140. H. Esser and G. Müller, *Archiv Eisenhüttenwesen*, Vol. **7**, pp 265, (1933).

141. E. Caudron, H. Buscail, R. Cueff, V.A.C. Haanappel, Y.P. Jacob, F. Riffard, and M.F. Stroosnijder, In-situ High Temperature X-ray Characterization of Yttrium Implantation Effect on Pure Iron Oxidation at 700 deg C, *Materials Science Forum*, Vol. **371-372**, pp 817-824 (2001).

142. E. Caudron and H. Buscail, In-situ High Temperature X-ray Diffraction Characterization of Yttrium Implanted Low Carbon Steel and Pure Iron, *Materials Chemistry and Physics (Switzerland)*, Vol. **64**, pp 29-36, (2000).

143. S. Li., N. Xu., J. Shi., M.Z.C. Hu, and E.A. Payzant, In-situ High Temperature X-ray Diffraction of Mixed Conducting Perovskite Type Oxides, *Journal of Materials Science Letters*, Vol. **20**, pp 1631-1633, (2001).

144. S. Assmann, M. Ermrich and K. Kunzmann, High Temperature X-ray Diffraction of a Low Fusing Dental Ceramic, *Journal of Materials Science*, Vol. **36**, pp 5403-5406, (2001).

145. A. Bodin, L. Woning, J. Sietsma, and S. van der Zwaag, In-situ High Temperature X-ray Diffraction on the Austenite-Ferrite Transformation in Low Carbon Steels, *ISIJ International*, Vol. **42**, pp 94-99, (2002).

146. Perrys Chemical Engineer's Handbook, McGraw-Hill, 7th edition, (2002).

147. O. Kubaschewski and B.E. Hopkins, Oxidation of Metals and Alloys, Butterworths, 2nd edition, (1967).

148. J.S. Sheasby, W.E. Boggs, and E.T. Turkdogan, Scale Growth on Steels at 1200C: Rationale of Rate and Morphology, *Metal Science*, Vol. **18**, pp 127-136, (1984).

149. K. Sachs and C.W. Tuck, Surface Oxidation of Steel in Industrial Furnaces, *Werkstoffe und Korrosion*, Vol. **21**, pp 945-954, (1970).

150. C.S. Roberts, Effect of Carbon on the Volume Fractions and Lattice Parameters of Retained Austenite and Martensite, *Journal of Metals*, Vol. **5**, pp 203-204, (1953).

151. N.N. Aleksandrov and N.I. Klochnev, Production Technology and Properties of Heat-Resisting Cast Iron, Israel Program for Scientific Translations, (1965).

152. H.K.D.H. Bhadeshia, S.A. David, J.M. Vitek, and R.W. Reed, Stress Induced Transformation to Bainite in Fe-Cr-Mo-C Pressure Vessel Steel, *Materials Science and Technology*, Vol. **7**, pp 686-698, (1991).

153. S.D. Choi, S. Kim, and J.H. Je, Annealing Behaviour of Retained Austenite in Low Carbon Steel: Real Time Synchrotron X-ray Scattering Studies, *Journal of Materials Science Letters*, Vol. **21**, pp 353-355, (2002).

154. F. Wever, *Archiv Eisenhüttenwesen*, Vol. **21**, pp 367, (1950).

155. D.J. Dyson and B. Holmes, Effect of Alloying Additions on the Lattice Parameter of Austenite, *Journal of the Iron and Steel Institute*, Vol. **277**, pp 469-474, (1970).

156. S. Suresh Babu, (2003).
http://ssbabu.ms.ornl.gov/index.html last viewed September 2003.

157. M.A. Yescas and H.K.D.H. Bhadeshia, Model for the Maximum Fraction of Retained Austenite in Austempered Ductile Cast Iron, *Materials Science and Engineering A*, Vol. **333**, pp 60-66, (2002).

158. AbsorbDX Computer Program, Bruker AXS, (2000).
www.bruker-axs.com last viewed September 2003.

159. R.W. Heine, Nodule Count: The Benchmark of Ductile Iron Solidification, *AFS Transactions*, Vol. **101**, pp 879-884, (1993).